Title
Controlled quantum-state-resolved chemistry to enable quantum logic with molecular ions

Author
Mills, Michael Charles

Publication Date
2020

Peer reviewed|Thesis/dissertation

UNIVERSITY OF CALIFORNIA
Los Angeles

Controlled quantum-state-resolved chemistry to enable quantum logic with molecular ions

A dissertation submitted in partial satisfaction
of the requirements for the degree
Doctor of Philosophy in Physics

by

Michael Charles Mills

2020

ABSTRACT OF THE DISSERTATION

Controlled quantum-state-resolved chemistry to enable quantum logic with molecular ions

by

Michael Charles Mills
Doctor of Philosophy in Physics
University of California, Los Angeles, 2020
Professor Eric R. Hudson, Chair

This dissertation describes experiments performed in the MOTion trap, a hybrid atom–ion trap comprised of a magneto-optical trap (MOT) and a linear Paul trap with an integrated time-of-flight mass spectrometer (ToF-MS). We aim to sympathetically cool the vibrational and rotational degrees of freedom of a $BaCl^+$ molecular ion by overlapping a cold (~ 4 mK) Ca MOT. This sympathetic cooling can prepare a molecular ion in its rovibrational quantum ground state, providing a method for state preparation for applications in molecular ion quantum logic. While collisions between the molecular ion and the cold atoms can cool the internal degrees of freedom, chemical reactions are also possible for electronically excited atoms. As such, we study these excited-state atom–ion reactions at low temperature < 1 K and develop tools to control these collisions. We make the first experimental observation of reaction blockading, an effect that suppresses excited-state reactions at low temperature, and develop a method to reverse this suppression if desired with the addition of a catalyst laser, providing a means to optically control such reactions.

Beyond its intended purpose of studying and achieving sympathetic cooling, we find that this apparatus is a powerful tool for chemical studies. By imaging the ions, we can

observe reactions occurring one atom at a time. We can precisely tune the collision energy or temperature down to the mK regime to as high as ∼10 K using techniques described in this dissertation, allowing controlled interrogation of these low-temperature reactions. Further, using lasers to address electronic transitions, we can precisely control the quantum state of the reactants, and we can measure the reaction products with the ToF-MS. A testament to the value of this apparatus is the study of $BaOCa^+$ described in this dissertation. Using the tools of the MOTion trap, we were able to identify the production of $BaOCa^+$, the first observation of a mixed hypermetallic oxide, and determine the path of reaction as $BaOCH_3^+ + Ca(4s4p\ ^3P_J) \rightarrow BaOCa^+ + CH_3$.

In addition to developing control of these atom–ion interactions towards sympathetic cooling of molecular ions, we also work towards further developing new quantum logic schemes for molecular ions, such as dipolar quantum logic, dipole–phonon quantum logic (DPQL), and electric-field gradient gates (EGGs). Specifically, we propose a class of molecules particularly well-suited for DPQL, the alkaline earth monoxide cations, that can also be added to existing atomic ion experiments with minimal additional experimental complexity. We further develop the techniques for DPQL and propose methods for single- and two-qubit gates, outlining a path towards universal quantum computation with molecular ions.

The dissertation of Michael Charles Mills is approved.

James Rosenzweig

Paul Hamilton

Wesley C. Campbell

Eric R. Hudson, Committee Chair

University of California, Los Angeles

2020

To Allison,

for your support and your patience

TABLE OF CONTENTS

LIST OF FIGURES

10.7 **Simulation of a frequency sweep to prepare the $|\mathrm{ee}\rangle$ state.** We begin with all normal mode frequencies below $\omega_{\mathrm{mol}}^{(1)}$ and $\omega_{\mathrm{mol}}^{(2)}$ in the motional ground state for all normal modes. We then increase the single-molecule trap frequency ω_0 linearly at a rate of $\dot{\omega}_0 = 3.0 \times 10^9$ rad/s^2 until both the antisymmetric and symmetric stretch mode frequencies pass through $\omega_{\mathrm{mol}}^{(1)}$ and $\omega_{\mathrm{mol}}^{(2)}$. (a) With equal splittings ($\omega_{\mathrm{mol}}^{(1)} = \omega_{\mathrm{mol}}^{(2)}$), we select an arbitrary single-molecular-excitation initial state $|\psi_{\mathrm{mol}}(0)\rangle = \sqrt{\frac{2}{3}}\,|\mathrm{ef}\rangle + \sqrt{\frac{1}{3}}\,e^{i\pi/4}\,|\mathrm{fe}\rangle$. (b) With equal splittings, we start with $|\psi_{\mathrm{mol}}(0)\rangle = |\mathrm{ff}\rangle$. In this plot, the average excitations for molecules (1) and (2) are overlapping within the thickness of the line. (c) $\omega_{\mathrm{mol}}^{(1)} = \omega_{\mathrm{mol}}^{(2)} + 2\pi \cdot 20$ kHz and $|\psi_{\mathrm{mol}}(0)\rangle = \sqrt{\frac{2}{3}}\,|\mathrm{ef}\rangle + \sqrt{\frac{1}{3}}\,e^{i\pi/4}\,|\mathrm{fe}\rangle$. Far away from resonance, $\left|\omega_{\mathrm{mol}}^{(1)} - \omega_{\mathrm{mol}}^{(2)}\right| \gg |J_{12}|$, and the amplitude of oscillation between $|\mathrm{fe}\rangle$ and $|\mathrm{ef}\rangle$ is small. As one of the normal mode frequencies approaches resonance, the coupling strength J_{12} increases, and the previously stated limit is no longer valid. In this regime, there are nontrivial oscillations between $|\mathrm{fe}\rangle$ and $|\mathrm{ef}\rangle$. (d) $\omega_{\mathrm{mol}}^{(1)} = \omega_{\mathrm{mol}}^{(2)} + 2\pi \cdot 20$ kHz and $|\psi_{\mathrm{mol}}(0)\rangle = |\mathrm{ff}\rangle$. Again, the average excitations for molecules (1) and (2) are overlapping within the thickness of the line. In every case shown, sweeping the frequency such that the antisymmetric and symmetric stretch mode frequencies pass through $\omega_{\mathrm{mol}}^{(1)}$ and $\omega_{\mathrm{mol}}^{(2)}$ removes any molecular excitation and prepares the molecular state in $|\mathrm{ee}\rangle$. Additionally, if the initial molecular state is $|\psi_{\mathrm{mol}}(0)\rangle = |\mathrm{ff}\rangle$, such a sweep will yield two phonons in the antisymmetric stretch mode—as this is the first mode to sweep through resonance—regardless of the difference in molecular splittings. 238

LIST OF TABLES

ACKNOWLEDGMENTS

First and foremost, I want to thank my family. Without their constant support and shared enthusiasm for math and science, I would have never made it. I would especially like to thank my wife Allison. It takes a special level of love and support to pick up your life and move to a new city so I could pursue my passion in physics. You have always been the light at the end of the tunnel after a long day in the lab. You've helped me through the hard times and enriched the good times. Without your support, none of this would have been possible. Your enduring patience through this long program is very much appreciated, and I hope the wait was worth it! I can't wait to start the next chapter of our lives together!

I also want to thank my advisor, Eric Hudson, for taking a chance on me. Prior to grad school, I had no experimental AMO experience. In fact, entering grad school, I wasn't sure which field I wanted to pursue. During my UCLA prospective student visit, however, when I toured Eric and Wes's labs and heard about their research, I knew right away AMO was the field for me. I'm extremely grateful Eric was willing to take me under his wing and patiently teach a clueless kid the ways of AMO. He was always happy to take time out of his very busy schedule to help give me the intuitive understanding of a concept that I probably should've already understood instead of just pointing me to an external reference. Additionally, Eric is a master of experiment choice and design, allowing us to work on extremely exciting cutting-edge science without requiring exorbitant resources. I have had the privilege of working on many projects at the forefront of the field with a high science-to-engineering ratio. This has made my grad school experience extremely enjoyable and rewarding, and I have Eric to thank for that.

Beyond Eric, I've had great mentorship from my labmates. Although my time with them was limited, Steven Schowalter (aka Dr. Schowtime) and Alex Dunning were great resources when I first joined the lab. I'm sure I was annoying, but constantly bugging them to ask how and why things were done a certain way was extremely beneficial for my practical

understanding of the lab and the underlying science. I also owe a big thanks to them and their predecessors for all their pioneering work on the experiment which I was able to build on. I was truly standing on the shoulders of giants.

Through much of my grad school experience, Prateek Puri (Teek), was my main labmate, and I could not have asked for a better partner. Teek was there from the beginning of my time at UCLA and helped teach me about MOTs, ion traps, and vegan food. We were a dynamic duo with complementing skills and work styles (and sometimes schedules), and together we were able to accomplish some great things. We were always able to bounce ideas off each other and discuss topics freely and openly, and for that I am very grateful. Teek, your determination, work ethic, and guidance pushed me to be a better scientist, and for that I am extremely grateful. In addition to the great science we've been able to learn and do together, it was always a fun time in and out of the lab with you. Even during a long data-taking session, our conversations kept me sane, even if my rambling about Michigan sports pushed you towards insanity. Outside of the lab, you've been a great partner as well. Whether it's your masterful icing techniques involving 'oysters' or exploring new cities like Barcelona with you at conferences, we've definitely had some times that I'll never forget.

Once Teek graduated, Hao Wu joined the lab as a postdoc, and has been an absolutely invaluable asset to the MOTion experiment. Hao dove head first into the experiment, and has mastered it in an impressively short time. His dedication is unmatched and the results speak for themselves. Hao has been an amazing labmate, and as we continue to evolve the MOTion trap, his experiences have already given him more confidence than I have in feeling comfortable making experimental changes. He is not afraid to get his hands dirty and figure out how everything works, and that is exactly what is needed. Before working with him, I was concerned about graduating and passing the torch to the next generation, but now I know there is nothing to worry about—if anything, I think the experiment will run even more efficiently with Hao in charge. Additionally, with Grant and Clayton leading the charge for the new trap for DPQL and EGGs, I am very optimistic about the future of the MOTion

lab and I look forward to seeing exciting results soon!

Christian Schneider has also been an amazing resource throughout my time at UCLA. He is a seemingly unending source of knowledge, and was always our first line of defence against ignorance. Whenever there was a topic or technique Teek and I didn't fully understand, we could go straight to Christian, and almost every time, we'd leave having understood what we were confused about and more. He was also never shy to help us gain hands-on experience, showing us exactly how things are done—and you know if Christian is showing you how to do it, it's the correct way and not just a sloppy way.

Elizabeth West has been a valuable asset to the lab as well. Like Christian, it seems she has an endless cache of knowledge and encyclopedic expertise. Elizabeth was always there with good advice when we had a question, and was always willing to give us tips (or let us know that what we had been referring to as "squishy blue stuff" was actually called sorbothane and told us about its useful properties).

In fact, the entire UCLA AMO department has been an amazing community to be a part of. I've learned so much from you all (special shoutout to David, JJ, OJ, Tony, and Adam) and had so much fun along the way. Whether it was learning from each other at our weekly Journal Club meetings, borrowing each other's equipment, benefiting from the wide range of expertise of the UCLA AMOers, building camaraderie at conferences by staying at the UCLA Airbnb houses, hanging out after work at Barney's or Q's, or recording our first intramural basketball win, the AMO community has been a family for these past six years and made my time at UCLA an absolute pleasure.

VITA

2011–2014	Undergraduate Researcher under Prof. August Evrard. Department of Physics, University of Michigan, Ann Arbor, MI.
2014	*Outstanding Achievement in Physics Award*. Department of Physics, University of Michigan, Ann Arbor, MI.
2014	B.S.E., Engineering Physics, *summa cum laude*. University of Michigan, Ann Arbor, MI.
2014–2015	Teaching Assistant, Department of Physics and Astronomy, University of California, Los Angeles, CA.
2015–present	Graduate Student Researcher under Prof. Eric R. Hudson, Department of Physics and Astronomy, University of California, Los Angeles, CA.
2016	M.S., Physics, University of California, Los Angeles, CA.
2019–2020	*Dissertation Year Fellowship*. University of California, Los Angeles, CA.

PUBLICATIONS

M. Mills, H. Wu, E. C. Reed, L. Qi, K. R. Brown, C. Schneider, M. C. Heaven, W. C. Campbell, and E. R. Hudson, "Dipole–phonon quantum logic with alkaline-earth monoxide and monosulfide cations," *Phys. Chem. Chem. Phys.* **22**, 24964–24973 (2020).

M. Mills, P. Puri, M. Li, S. J. Schowalter, A. Dunning, C. Schneider, S. Kotochigova, and

E. R. Hudson, "Engineering excited-state interactions at ultracold temperatures," *Phys. Rev. Lett.* **122**, 233401 (2019).

M. Li, M. Mills, P. Puri, A. Petrov, E. R. Hudson, and S. Kotochigova, "Reaction blockading in a reaction between an excited atom and a charged molecule at low collision energy," *Phys. Rev. A.* **99**, 062706 (2019).

P. Puri, M. Mills, I. Simbotin, J. A. Montgomery. Jr, R. Côté, C. Schneider, A. G. Suits, and E. R. Hudson, "Reaction blockading in a reaction between an excited atom and a charged molecule at low collision energy," *Nat. Chem.* **11**, 615–621 (2019).

P. Puri, M. Mills, E. P. West, C. Schneider, and E. R. Hudson, "High-resolution collision energy control through ion position modulation in atom–ion hybrid systems," *Rev. Sci. Instrum.* **89**, 083112 (2018).

P. Puri, M. Mills, C. Schneider, I. Simbotin, J. A. Montgomery. Jr, R. Côté, A. G. Suits, and E. R. Hudson, "Synthesis of mixed hypermetallic oxide $BaOCa^+$ from laser-cooled reagents in an atom–ion hybrid trap," *Science* **357**, 1370–1375 (2017).

M. Mills, P. Puri, Y. Yu, A. Derevianko, C. Schneider, and E. R.. Hudson, "Efficient repumping of a Ca magneto-optical trap," *Phys. Rev. A.* **96**, 033402 (2017).

A. E. Evrard, M. Mills, D. Winn, K. Jones, J. Tritz, and T. A. McKay, "Problem roulette: Studying introductory physics in the cloud," *Am. J. Phys.* **83**, 76 (2015).

CHAPTER 1

Introduction

The first description of a quantum computer was proposed by Paul Benioff in 1980 [Ben80]. This followed the work of Poplavskii [Pop75], pointing out that quantum systems cannot be efficiently simulated on a classical computer, and the work of Holevo [Hol73], showing that n quantum bits (qubits) carry more information than can be described by n classical bits. Further, Bennett and Brassard proposed in 1984 a quantum key distribution scheme "BB84" [BB84], taking advantage of the fact that measuring a quantum state disturbs it to produce a secure way to communicate a private key, sparking interest in quantum information theory and quantum cryptography. This interest grew exponentially after Peter Shor, in 1994, proposed Shor's algorithm, a quantum computing algorithm for factoring prime numbers efficiently, which is a classically intractable problem. Because this problem is hard to solve on a classical computer, RSA-based encryption, which uses a public encryption key that is the product of two large prime numbers, is extremely popular for securing communications over the internet. As such, Shor's algorithm signaled to the field that quantum computing has the potential to be very powerful in real-world applications. This marked the beginning of many breakthroughs in the field of quantum computing, such as Grover's algorithm in 1996 and Shor's proposal for a method to perform quantum error correction [Sho95], providing a path towards fault-tolerant quantum computing.

Since these theoretical breakthroughs, significant effort as been made to create an experimental realization of a quantum computer. Tremendous progress as been demonstrated, especially in the past decade, both in experimental labs and in recently developed commercial

quantum computers. Current implementations have tens of qubits with $> 99\%$ gate fidelities [AAB19, PDF20]. Among these systems, the two most well-established platforms are superconducting qubits and trapped-ion qubits. In this dissertation, we focus on trapped-ion qubits.

Trapped-ion qubits have demonstrated the highest-fidelity quantum operations of all quantum systems [BHL16, HAB14, GTL16, CHC20], making them especially promising candidates for quantum computing. Scaling these systems to high qubit number, however, has proven to be difficult [BCM19]. In a typical trapped-ion quantum computer, the qubits are single atomic ions (Yb^+, Ba^+, and Ca^+ are popular choices) that are coupled to each other by their shared motion in an ion trap. In this dissertation, we explore the idea of using *molecular* ions instead of atomic ions as qubit candidates. The internal structure of a molecule is much more complex than that of an atom, as the constituent atoms of a molecule can vibrate or rotate relative to each other. This additional complexity makes these molecules more difficult to control; the optical cycling transitions used to laser-cool and manipulate atoms generally do not exist in molecules due to decays to different vibrational states. Although the complicated structure makes molecules more difficult to control, it also results in features that are not present in atoms. We aim to capitalize on these features to develop and demonstrate quantum logic schemes using molecular ions which may be scalable.

It was proposed in 2002 that *neutral* polar molecules could be used as a qubit [DeM02]. By using a static electric field with a spacial gradient to induce an electric dipole moment, the molecules could be individually addressed and be coupled through the dipole–dipole interaction. Such a scheme would not be suitable for trapped polar molecular ions though; to sustain a time-averaged electric field in one direction, a molecular ion would be accelerated in that direction due to its charge and not be spatially trapped. In reality, such a static electric field applied to a trapped ion would only push the ion off the trap center until the average electric field from the ion trap was equal in magnitude and opposite in direction to the applied field, resulting in the time-averaged total electric field to be zero. The techniques

from neutral molecules are not in general directly applicable to trapped molecular ions, but the presence of the ion trap and the shared motion with co-trapped ions allows for new and exciting techniques to be implemented.

Some recently proposed quantum logic techniques for polar molecular ions are dipolar quantum logic [HC18], dipole–phonon quantum logic (DPQL) [CH20, MWR20], and electric-field gradient gates (EGGs) [HC20]. Dipolar quantum logic, similar to the proposal for neutral molecules, takes advantage of the dipole–dipole interaction between two polar molecular ions. Instead of a static dipole moment caused by a static electric field, these molecular ions have an oscillating dipole moment, for example, at the rotational oscillation frequency. Identical molecular ions oscillate at the same frequency, enabling a net dipole–dipole interaction and providing a path to entangle two qubits. As this technique relies on oscillating fields, the dipoles are dynamically decoupled from the electric field noise of the environment, including the ion trap, resulting in two-qubit gates that are insensitive to trap heating and do not require ground-state cooling. DPQL exploits the interaction between the normal modes of motion in an ion trap with the oscillation of a molecular ion dipole moment at a similar frequency. In this way, it is possible to transfer quantum information between the phonon modes of an ion trap and the internal state of a polar molecular ion. This interaction opens up a wide toolbox of techniques, discussed further in Chapter 10. EGGs utilize applied microwave electric fields with spatial gradients, which can drive motional sidebands in a molecular ion. Using these EGGs, it is possible to perform a two-qubit gate similar to a Mølmer–Sørensen gate [MS99] that is even more insensitive to the phonon number and can be driven purely by microwave fields.

In order to take advantage of these promising quantum logic schemes, we must first develop the necessary control of the molecular ions. Specifically, we aim to sympathetically cool trapped polar molecular ions with a co-located magneto-optical trap (MOT) in a hybrid atom–ion trap. As our apparatus overlaps a MOT and an ion trap, we refer to it as the MOTion trap, described in detail in Chapter 2. By sympathetic cooling with a MOT, we

can prepare a molecular ion in its rovibrational ground state, a desirable starting point for a quantum logic operation involving the internal states of the molecular ion. Specifically, we use $BaCl^+$ molecular ions, which can be co-trapped with laser-cooled Ba^+ ions to sympathetically cool the translation, and a Ca MOT with a temperature of ~ 4 mK to sympathetically cool the vibration and rotation of the $BaCl^+$ molecular ions.

One reason the combination of $BaCl^+$ and Ca is amenable to sympathetic cooling is that any possible reaction products of $BaCl^+ + Ca$ are higher in energy than the reactants, and these endothermic reactions will never occur at experimental temperatures as long as Ca is in its electronic ground state. As Ca is laser-cooled, however, it spends some time in excited states, which can be reactive with $BaCl^+$. As such, it is critical to understand these potentially destructive excited-state atom–ion collisions, especially at low temperature < 1 K. To this end, much of the work in this dissertation focuses on such interactions. We develop methods to precisely tune the atom–ion collision energy and use these techniques to demonstrate for the first time an effect known as reaction blockading that suppresses these potentially destructive reactions at sub-Kelvin temperatures. Further, we develop optical control of these reactions, giving us the ability to effectively turn this reaction blockading effect off or on with the addition or omission of a catalyst laser. In addition to applications towards sympathetic cooling, the MOTion trap allows the study of such reactions with a precise control of the collision energy and quantum state of the reactants, which can be interesting for physical chemistry or chemical physics studies. As an example of such a study, we present in this dissertation the study of $BaOCa^+$. Using the tools of the MOTion trap, we were able to identify this molecule as the first observed mixed hypermetallic oxide and determine its specific path to formation.

Additionally, in preparation for new generations of the experiment, we further develop the toolkit of techniques available to polar molecular ion qubits. To this end, in Chapter 10, we build on the original proposal for DPQL [CH20] and identify a class of molecules, alkaline earth monoxides, that appear to be especially promising for DPQL. These molecules have

suitable structure and can be easily produced in many existing atomic ion experiments. Finally, this dissertation concludes with an outlook on the direction of future work to be performed in this experiment.

CHAPTER 2

Experimental Apparatus

This chapter provides an overview of the experimental apparatus utilized over the course of my studies. I discuss the principles of operation, design choices and technical details, and expand on certain experimental considerations for operating the apparatus and analyzing the data collected. Specifically, I describe the linear Paul trap (LPT) used to trap ions, the magneto-optical trap (MOT) used to trap neutral atoms, the time-of-flight mass spectrometer (ToF-MS or ToF) used to measure the relative amounts of different species in the ion trap, the controlled gas leak system used to study various reactions or create controlled amounts of molecules, and the various lasers used in this dissertation. Much of the apparatus has been described in detail in the dissertations of Steven Schowalter and Prateek Puri [Sch16, Pur19], from which I have borrowed some figures. For that and for the guidance they have given me, I am grateful.

2.1 The MOTion Trap: Experimental Overview

The experiments described in this dissertation were performed in a hybrid MOT-ion trap, dubbed the MOTion trap. In this MOTion trap, a linear Paul trap (LPT) is constructed inside a vacuum chamber, shown alongside the ToF schematically in Figure 2.1. Two current-carrying anti-Helmholtz coils are placed above and below the vacuum chamber, shown in Figure 2.2. The current in these coils runs in opposite directions, creating the magnetic field gradients required for the MOT.

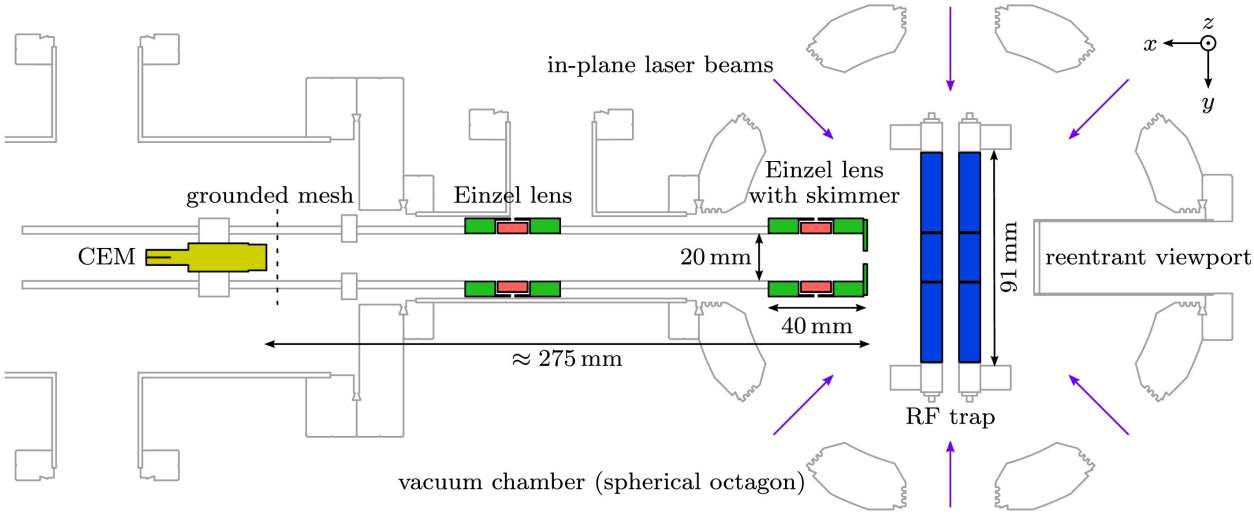

Figure 2.1: **Schematic of ToF and LPT.** Shown is a top-down view of the ToF and LPT inside the vacuum chamber. This figure is borrowed from Ref. [SSY16].

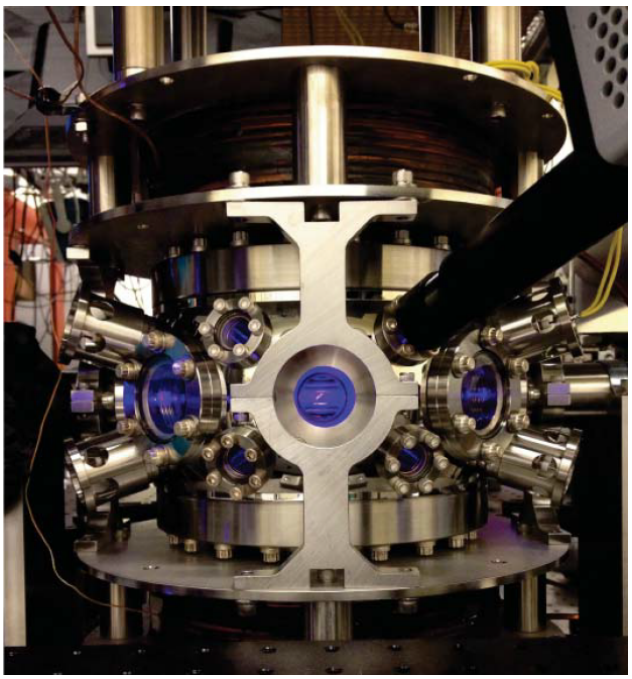

Figure 2.2: **Photograph of MOT coils above and below vacuum chamber.** This image shows the MOT coils mounted above and below the vacuum chamber housing the LPT. This figure is borrowed from Ref. [Sch16].

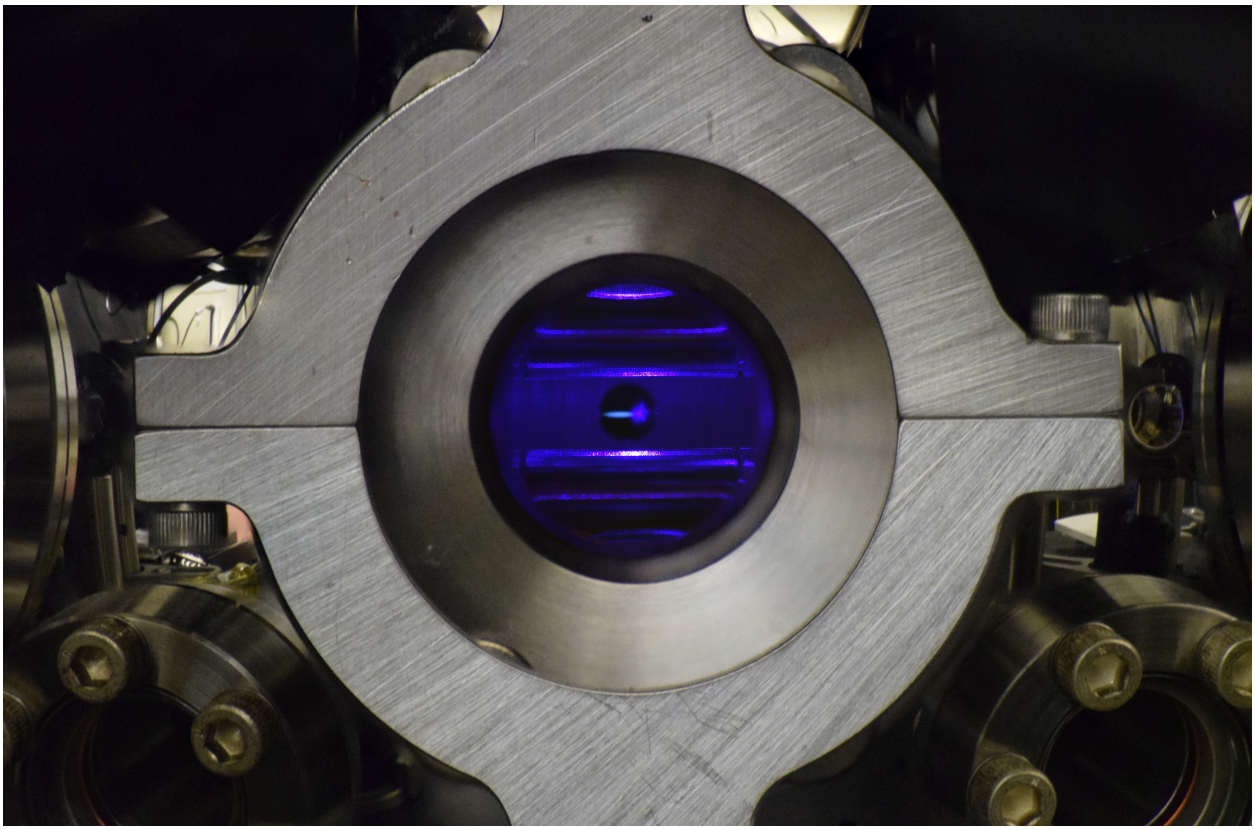

Figure 2.3: **Photograph of MOT and ions in MOTion trap.** Looking inside the reentrant viewport of the vacuum chamber, one can see the LPT rods. At the center of the trap, fluorescence from a crystal of Ba^+ ions is visible (teal prolate spheroid) next to fluorescence from a Ca MOT (violet sphere). Behind the atoms and ions, the black circle is the entrance to the ToF.

2.2 Ion Trap

The theory of ion trapping has been well documented in numerous sources. Ref. [BMB98] is a particularly helpful source. I begin this section with a brief review of relevant aspects of ion trapping theory. I then describe the linear Paul trap (LPT) used in this experiment and the electronics that drive it. This discussion is followed by an overview of the techniques used to laser-cool Ba^+ and Yb^+ and image the laser-cooled ions. I conclude with a discussion of several useful techniques for ion selectivity in the LPT.

2.2.1 Theory

Earnshaw's theorem [Ear48] states that charged particles cannot be stably trapped by an electrostatic potential. For such an electrostatic trap to exist, the ion must feel a restoring force in all directions. An ion of charge q feels an electrostatic force of $q\vec{E}$ where $\vec{E}$ is the electric field. In order for a positively charged ion to feel a restoring force in all directions, it would require $\vec{\nabla} \cdot \vec{E} < 0$, resulting in a local minimum of the electric potential. However, Gauss's law states that in free space $\vec{\nabla} \cdot \vec{E} = 0$, which can be rewritten as Laplace's equation $\nabla^2 V = 0$ where V is the electric potential. While a local minimum in the electric potential is not possible, a saddle point is. For example, in 2D, a saddle point would be confining along one direction and anti-confining in the other direction. Such a 2D saddle point can be realized at the center of a four-rod LPT, illustrated in Figure 2.4. If the trap rods are assumed to be infinitely long hyperbolic cylinders, one could ground the two rods along the y axis at $V = 0$ and apply an rf potential of the form $V_0 \cos(\Omega t)$. The resulting electric potential in the trap $V(x, y, t)$ is

$$V(x, y, t) = \frac{V_0}{2}\left(1 + \frac{x^2 - y^2}{r_0^2}\right)\cos(\Omega t) \tag{2.1}$$

where r_0 is the distance from the center of the trap to one of the rods. For cylindrical rods of finite length, the solution is similar to Equation 2.1, especially near the center of the trap. At any given time, an ion would feel a restoring force towards the center of the trap along one dimension, and an anti-restoring force along the other dimension. However, with appropriate parameters, this time-varying potential results in a harmonic pseudopotential that confines along both the x and y dimensions [Pau90].

To confine the ions in the z direction, one can add endcaps along the z axis, each endcap being a distance z_0 from the center of the trap. By applying an dc voltage U_z to these

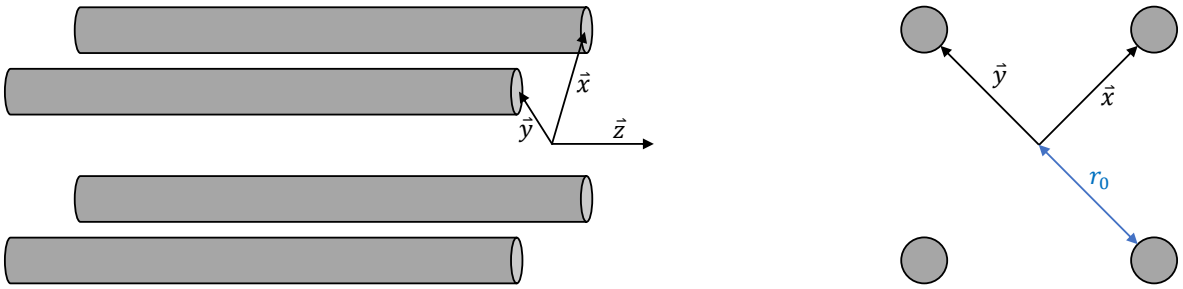

Figure 2.4: **Illustration of a linear Paul trap.** Shown is an illustration of a four-rod linear Paul trap (excluding endcap electrodes). (a) side view. (b) axial view.

endcaps, one produces a potential

$$U(x,y,t) = \frac{\kappa U_z}{z_0^2}\left(z^2 - \frac{1}{2}(x^2+y^2)\right) \tag{2.2}$$

near the center of the trap, where κ is a factor depending on the geometry of the endcaps with the constraint $\kappa < 1$. This dc potential confines the ions axially, but anti-confines them in the radial direction. This anti-confinement is overwhelmed by the confining pseudopotential from the rf potential $V(x,y,t)$, resulting in a confinement in all directions.

For an ion of mass m and charge Q, the equations of motion in such an ion trap are given by the Mathieu equation

$$\ddot{u_i} + (a_i + 2q_i\cos(\Omega t))\frac{\Omega^2}{4}u_i = 0 \tag{2.3}$$

where $\vec{u} = u_x\hat{x} + u_y\hat{y} + u_z\hat{z}$ is the ion position,

$$a_x = a_y = -\frac{1}{2}a_z = -\frac{4Q\kappa U_z}{mz_0^2\Omega^2}, \tag{2.4}$$

and

$$q_x = -q_y = \frac{2QV_0}{mr_0^2\Omega^2}, \qquad q_z = 0. \tag{2.5}$$

The variables q_i and a_i are known as the Mathieu q and a parameters, or are sometimes simply referred to as the q and a parameters. The solutions to Equation 2.3 are known

as Mathieu functions. Until recently, there were no closed-form analytical solutions to the Mathieu equations. Recent work [Dan20], however, has identified two linearly independent, closed-form solutions to the Mathieu equations, allowing one to construct a general analytical solution as a linear combination of these two solutions. In the limit $q_i \ll 1$ and $a_i \ll 1$, a simple approximate solution exists of the form

$$u_i(t) \approx u_{i0} \cos(\omega_i t + \phi_i) \left(1 + \frac{q_i}{2} \cos(\Omega t)\right) \tag{2.6}$$

where u_{i0} is the amplitude of the secular oscillations, ϕ_i is a phase set by the initial conditions, and

$$\omega_i \approx \frac{\Omega}{2} \sqrt{a_i + \frac{1}{2} q_i^2} \tag{2.7}$$

is the frequency of secular oscillations. The motion described by Equation 2.6 can be broken up into two components. The first is a secular oscillation of the ion at frequency ω_i with amplitude u_{i0}. This component is due to the ion oscillating in the harmonic pseudopotential created by the combined dc and rf electric field. The second component is known as "micromotion" and is a faster oscillation at frequency Ω with a time-varying amplitude $u_{i0} \cos(\omega_i t + \phi_i) \frac{q_i}{2}$. This oscillation is due to the direct effect of the rf electric field, which oscillates at frequency Ω. The approximate solution is plotted alongside the full solution in Figure 2.5 for a variety of q parameter values, each with $a = 0$. For increasing q values, the approximation of Equation 2.6 has a decreasing agreement with the full solution.

Equation 2.6 is valid for ideal trapping conditions. Realistically, slight imperfections such as a stray electric field or a phase difference between the two rf rods results in a modified trajectory. Such a trajectory will have a larger micromotion oscillation amplitude, called "excess micromotion" [BMB98]. As an example, we can consider the effect of a stray electric field. This electric field will cause a force on the trapped ion which will be balanced out by the force from the harmonic pseudopotential. The resulting equilibrium position will be displaced by some distance from the trap null. As the rf electric field increases linearly

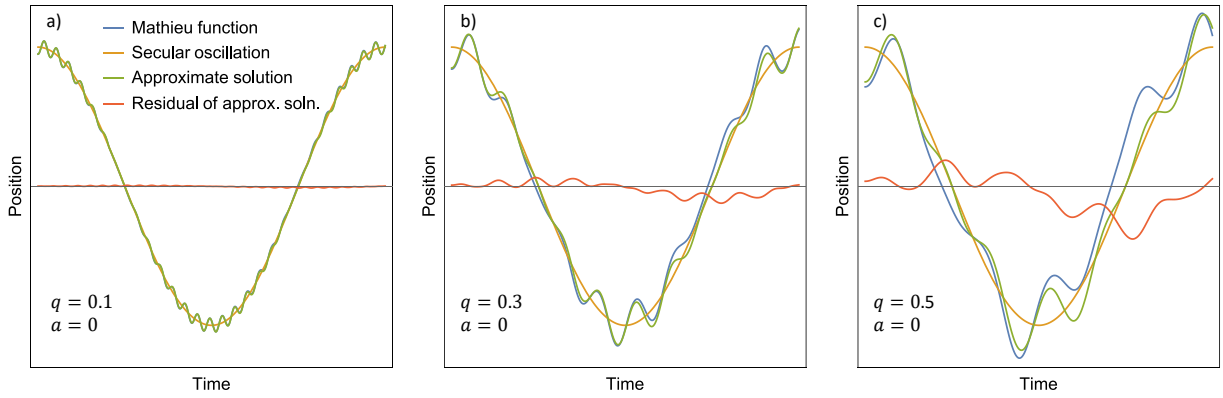

Figure 2.5: **Simulated trajectories in an ion trap.** A solution to the Mathieu equation is compared to the approximate low-q solution and the secular oscillation for (a) $q = 0.1$, (b) $q = 0.3$, and (c) $q = 0.5$.

in amplitude with a radial displacement from the center of the ion trap, the micromotion oscillation amplitude also scales with the radial displacement.

Even under ideal trapping conditions with no excess micromotion, a trapped ion will not be stable for all values of q and a [DB00]. For example, if the q parameter is small, the rf field that creates the radial harmonic pseudopotential will be relatively weak. If the a parameter is large in this example, the endcap voltage will be large, causing a dc potential that pushes an ion radially away from the trap axis. If the a parameter is large enough, this dc "anti-trapping" force can overwhelm the trapping force from the pseudopotential, resulting in an instability, and the ion will exit the trap. The stability diagram for a linear Paul trap is shown in Figure 2.6, where the shaded region represents combinations of the q and a parameters that result in stable trapping of a single ion.

When multiple ions are present in the ion trap, each ion will feel a harmonic pseudopotential as well as the ion–ion repulsion due to the presence of the other ions in the trap. The total potential energy of a configuration of ions in the pseudopotential approximation is given by

$$U = \sum_i \left[\frac{1}{2} m_i (\omega_{x,i}^2 x_i^2 + \omega_{y,i}^2 y_i^2 + \omega_{z,i}^2 z_i^2) + \frac{Q_i}{4\pi\epsilon_0} \sum_{j \neq i} \frac{Q_j}{|\vec{r}_i - \vec{r}_j|} \right] \tag{2.8}$$

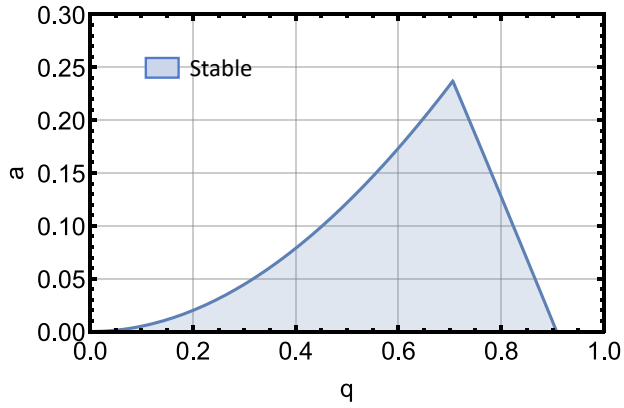

Figure 2.6: **Mathieu stability diagram for a single ion**. For a linear Paul trap, the shaded area represents combinations of the q and a parameters that result in a stably trapped ion.

where i, j are indexes of individual ions, m_i is the mass of ion i, $\omega_{x,i}$, $\omega_{y,i}$, and $\omega_{z,i}$ are the harmonic pseudopotential secular frequencies of ion i in the x, y, and z dimension, respectively, $\vec{r_i} = x_i\hat{x} + y_i\hat{y} + z_i\hat{z}$ is the position of ion i relative to the trap center, Q_i is the charge of ion i, and ϵ_0 is the permittivity of free space. If the ions are laser-cooled, they will tend to align themselves in the configuration with the lowest total potential energy. For sufficiently low temperatures, these ions form a "Coulomb crystal." Typically, in an LPT, $\omega_{x,i} \approx \omega_{y,i}$ and $\omega_{z,i} \lesssim \frac{1}{5}\omega_{x,i}$, and when several ions are loaded in the ion trap and laser-cooled, the ions align themselves along the axis, as the radial potential is more tightly trapping than the axial potential. An image of such an ion chain with 11 $^{138}Ba^+$ ions is shown in the top panel of Figure 2.7. If more ions are added to the chain or if the axial secular frequency is increased, it will become energetically favorable for the ions to form a "kinked" ion chain, with ions near the center of the chain exhibiting a "zig-zag" pattern. An example of this configuration for 12 Ba^+ ions is shown in the middle panel of Figure 2.7. It should be noted that the axial secular frequency for this chain was higher than the value in the top panel, otherwise there would not be such a dramatic difference in the geometry between 11 and 12 ions. For a large number of ions, a 3D crystal will be formed, roughly ellipsoidal in shape, with the size of each dimension scaling with the inverse of the secular frequency in that

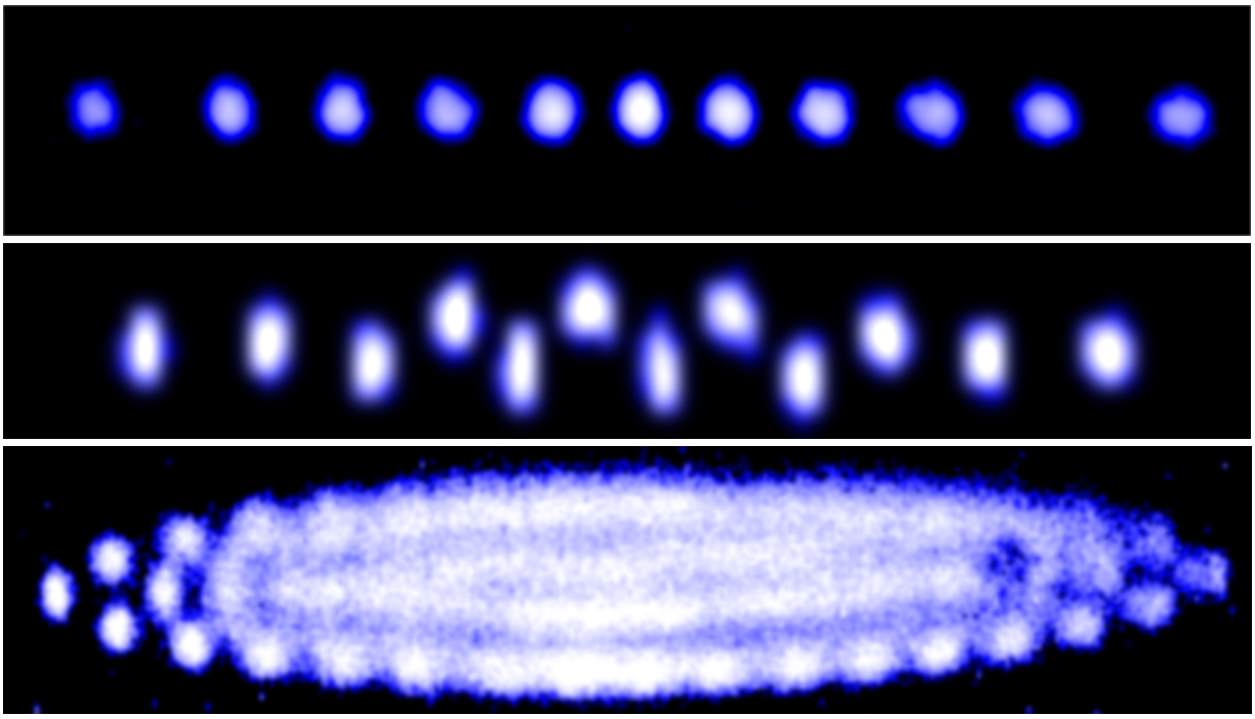

Figure 2.7: **Coulomb crystal images.** Shown are images of multiple trapped and laser–cooled $^{138}Ba^{+}$ ions in various configuration. In the top panel, a linear chain is shown. In the middle panel, a kinked chain is shown. In the bottom panel, a 3D crystal is shown.

dimension. Such a crystal is shown in the bottom panel of Figure 2.7. For large crystals, the density of ions is roughly constant within the crystal. For ions of identical mass m and charge Q, the density is

$$\rho = \frac{\epsilon_0 m}{Q^2}(\omega_x^2 + \omega_y^2 + \omega_z^2) \tag{2.9}$$

where ϵ_0 is the permittivity of free space.

2.2.2 Design

The LPT used in this experiment is made of four segmented rods. The schematic for this trap with dimensions is shown in Figure 2.8, and a photograph of the LPT inside the (opened) vacuum chamber is shown in Figure 2.9. The distance between the radial center of the trap and the edge of one of the four rods is $r_0 = 6.85$ mm. Instead of traditional endcaps, the outer

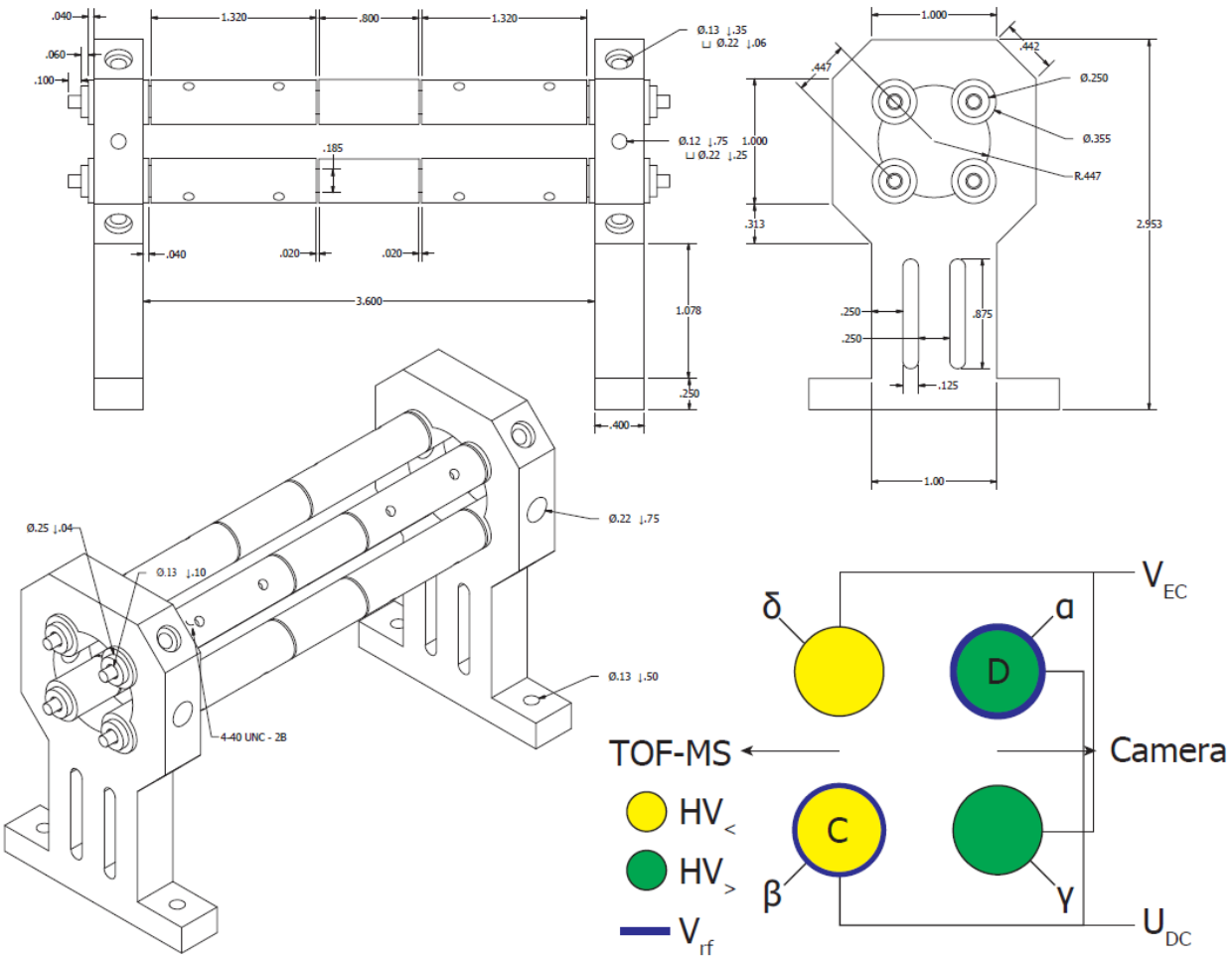

Figure 2.8: **LPT schematic.** A schematic showing the dimensions of the LPT used in this experiment is presented. All units displayed are in inches. In the bottom right, an illustration of an axial view of the 4 trapping rods are shown, labeling the rods α, β, γ, and δ for reference. This figure is borrowed from Ref. [Sch16].

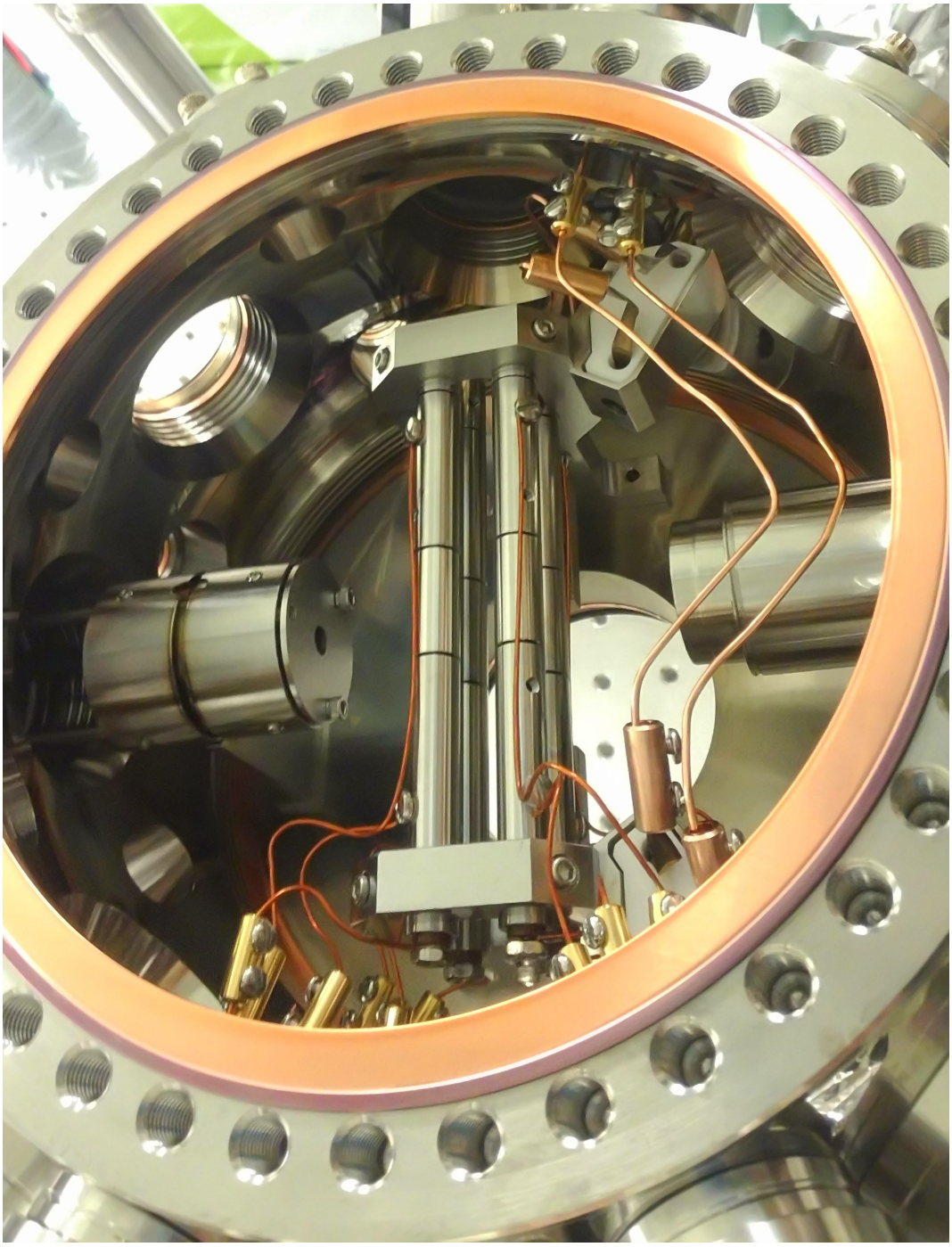

Figure 2.9: **Photograph of the LPT inside the opened chamber.** Inside the opened chamber, the four segmented rods of the LPT are visible. To the left of the LPT is the entrance to the ToF. To the right of the LPT is the reentrant viewport to image the ions.

Parameter	Description	(Typical) Value
r_0	Characteristic radial size	6.85 mm
z_0	Characteristic axial size	10.2 mm
κ	Geometric factor for endcaps	0.022
V_0	Amplitude of rf voltage	$\sim$175 V
Ω	Frequency of rf voltage	$2\pi\cdot$680 kHz
U_z	Endcap voltage	$\sim$20 V

Table 2.1: **A summary of relevant LPT parameters.** Here the most important parameters of the LPT are listed, along with fixed or typical values, when applicable.

segments of the rods are used to provide the endcap voltage. The distance from the axial center of the trap to the axial position where one of these segments starts is $z_0 = 10.2$ mm. The geometric factor for this endcap configuration with our trap geometry is $\kappa \approx 0.022$. An rf voltage of amplitude $V_0 \sim 175$ V and frequency $\Omega = 2\pi \cdot 680$ kHz is applied to rods α and β as labeled in Figure 2.8. A dc bias voltage can be added to all the trap rods in order to correct for any stray electric fields, minimizing the excess micromotion.

2.2.3 Electronics

The rf voltages to drive each of the LPT rod segments are first generated by direct digital synthesis (DDS) devices. With these DDS devices, which each have four output channels, one is able to set the amplitude, frequency and phase of each of the generated rf voltages. In this way, one is able to independently set the rf parameters for each of the rod segments independently. These DDS devices are synchronized with a shared 500 MHz reference clock—additionally, cable lengths for each output are similar to minimize any timing errors. The amplitude, frequency, and phase of these DDS devices are managed by a micro-controller, which can be controlled by the lab computer via a serial-to-USB or through the lab Wi-Fi network.

This micro-controller also allow one to set the dc voltages for the endcaps and for shimming voltages, set the HV for ToF pulsing, and synchronize the timing of the trap loading and the HV pulsing for the ToF. For trap loading, the rf for the rods is turned off briefly.

Figure 2.10: **MOTion electronics control interface.** A screenshot of the interface for the micro-controllers used to control the LPT rf, dc, and HV pulses and their timings is shown.

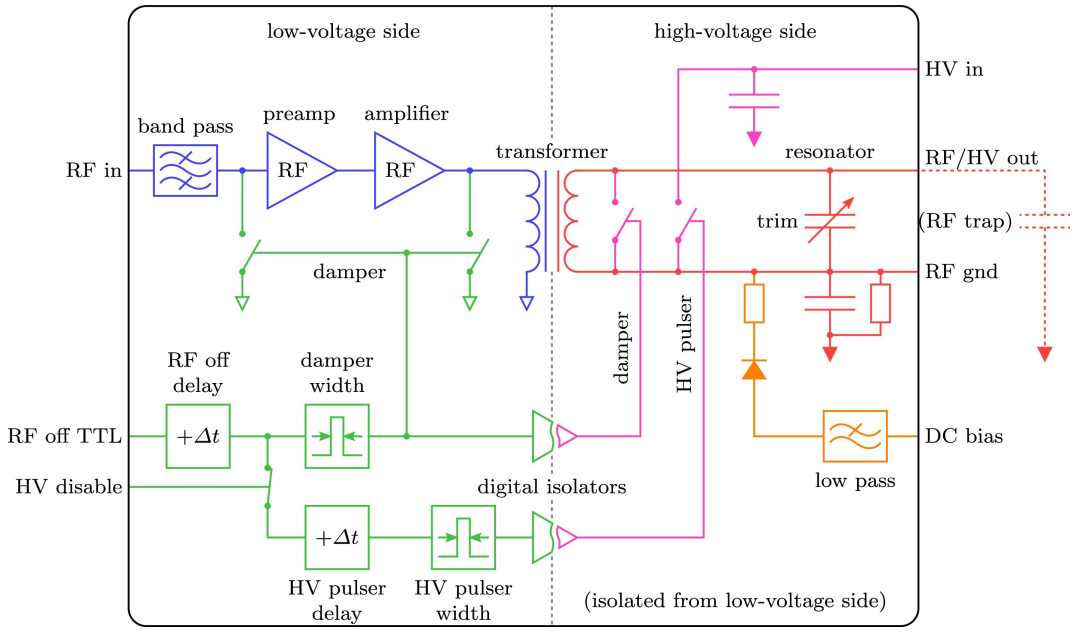

Figure 2.11: **Diagram of LPT drive board.** A diagram of the circuit to drive one of the rod segments is shown. The circuit is separated into two isolated sides, the low-voltage side with the rf input, preamplifier, amplifier, and TTL control, and the high-voltage side, where the rf output can be combined with dc voltages for micromotion compensation as well as HV for ejecting ions into the ToF. This figure was borrowed from Ref. [SSY16]

After an ablation laser pulse used for generating ions, there is some delay time to allow the ions to reach the center of the trap, and the rf is turned on again to trap these ions generated from the ablation. For ToF pulsing, the timing of the HV pulsing is synchronized with the rf so the phase of the rf is the same for each pulse, with the rod voltages increasing smoothly from rf to HV. A screenshot of the interface for this controller is shown in Figure 2.10.

The rf output from the DDS devices must be amplified to the ~ 175 V amplitude required for the LPT. To accomplish this, the rf output from the DDS devices passes through a drive board. The schematic for one of these drive boards is shown in Figure 2.11, and a photograph of three of these drive boards is shown in Figure 2.12. Each drive board is on a printed-circuit board (PCB) and sets the output for a single rod segment. The drive board is separated into two isolated sides, a low-voltage side (left side in Figure 2.11 and right side in Figure 2.12) and a high-voltage side (right side in Figure 2.11 and left side in Figure 2.12). The drive

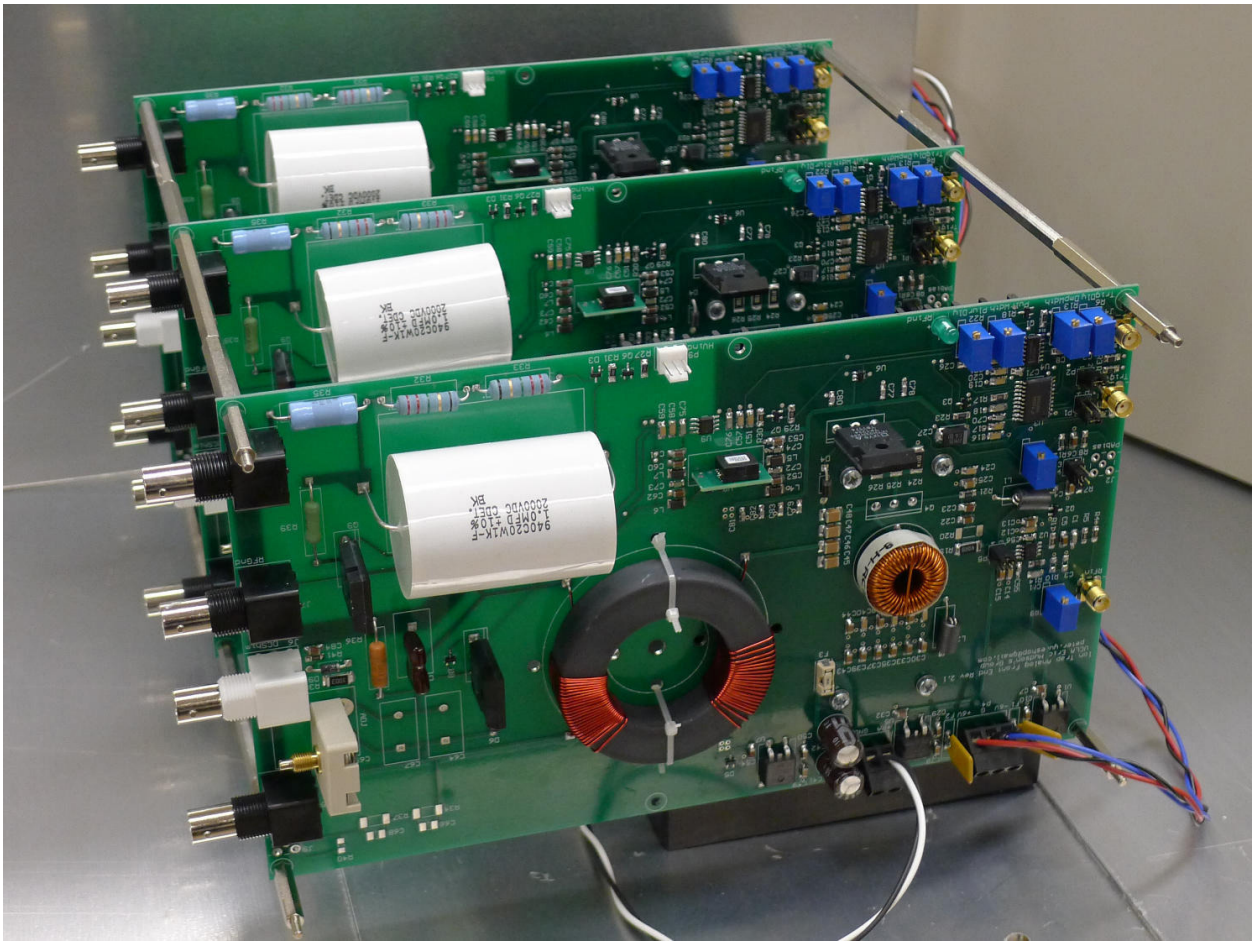

Figure 2.12: **Photograph of LPT drive board.** Shown is a photograph of three LPT drive boards, one for each segment of one rod. This figure was borrowed from Ref. [SSY16]

boards are described in detail in Refs. [SSY16, Sch16]. On the low-voltage side, the rf input generated by the DDS passes through an RC-bandpass filter, and is amplified by a preamplifier and an amplifier. The amplified signal passes to the high-voltage side through a transformer, and with the connection to the trap rod forms an LC-resonator. For rods α and β, the resonance is $\sim 2\pi \cdot 680$ kHz. For rods γ and δ, the resonance is $\sim 2\pi \cdot 1.8$ MHz. In a typical experiment, only the α and β rods are used for rf trapping. A trim capacitor allows one to fine-tune the resonance frequency. The dc bias voltages and the HV pulsing voltages are also added on the high-voltage side. To allow for a fast turn-off of the trap rf, dampers are implemented to minimize the ring-down time.

2.2.4 Laser-Cooling of Ba^+

To cool the trapped Ba^+ ions to temperatures below 1 K, we utilize Doppler cooling. At its core, Doppler cooling takes advantage of the velocity-dependent absorption of photons by an atom or ion. By illuminating the ions with a laser nearly resonant with an electric dipole transition in the ion, but with frequency slightly below resonance, the ions will be more likely to absorb photons from the laser if the velocity of the ion opposes the wave vector of the laser. In this way, the momentum kick from absorbing a photon causes a net force that opposes the motion of the ion, slowing the ion down on average. After absorbing a photon, the ion can emit a similar photon via spontaneous emission. This emission will be random in direction, giving the ion a random momentum kick opposing the emitted photon direction. As such, this momentum kick will, on average, not slow down or speed up the ion. If the ion undergoes stimulated emission from the laser rather than spontaneous emission, the stimulated emission will give a momentum kick that tends to speed up the ion, reversing the effect of the absorption. Thus, if there is no spontaneous emission, there will not generally be a force opposing the motion. The rate at which spontaneous emission occurs, known as the scattering rate, is paramount to the Doppler-cooling process.

The scattering rate of an ion with an electric dipole transition with natural linewidth

Γ and resonance frequency ω_0 illuminated by a laser with frequency ω and Rabi frequency $\Omega = \frac{\vec{d}\cdot\vec{E}}{\hbar}$, where $\vec{d}$ is the transition dipole moment, $\vec{E}$ is the electric field of the laser, and $\hbar$ is the reduced Planck constant, is

$$R_{\text{scat}} = \frac{\Gamma}{2}\frac{\Omega^2/2}{\delta^2 + \Omega^2/2 + \Gamma^2/4} \tag{2.10}$$

where $\delta = \omega - \omega_0 + \vec{k}\cdot\vec{v}$ is the detuning of the laser including the Doppler shift $\vec{k}\cdot\vec{v}$, where k is the wave vector of the laser and v is the velocity of the atom [FFF05]. The average force due to this scattering is then

$$\vec{F}_{\text{scat}} = \hbar\vec{k}R_{\text{scat}} = \hbar\vec{k}\frac{\Gamma}{2}\frac{\Omega^2/2}{(\omega - \omega_0 + \vec{k}\cdot\vec{v})^2 + \Omega^2/2 + \Gamma^2/4} \tag{2.11}$$

since the average force from spontaneous emission will be zero.

This velocity-dependent scattering force is plotted in Figure 2.13 for a one-dimensional example with a red-detuned laser, with a frequency less than the resonance frequency. Figure 2.13a shows the scattering force as a function of the velocity for a laser propagating in the $-\hat{x}$ direction. A similar plot is shown in Figure 2.13b for a laser propagating in the $\hat{x}$ direction. If both lasers are present at the same time, the scattering force as a function of velocity is shown in Figure 2.13c. Here, for low speed, there is a scattering force that opposes the velocity, resulting in a damping "molasses" force that can be linearly approximated as $\vec{F}_{\text{molasses}} = -\alpha\vec{v}$ where α is some damping constant. Additionally, this force is zero for zero velocity; each opposing laser balances the force of the other one. For ions in the pseudopotential of an ion trap, it is possible however to generate a damping force with a single laser without accelerating an ion as its velocity approaches zero. We can understand this by doing the following *gedankencalculation* (we won't actually do the math, but we can imagine that we had). For an ion on the harmonic pseudopotential of an ion trap, depicted in Figure 2.13d, the ion will be located at the center of the trap. With a single cooling laser in the $\hat{x}$ direction, the scattering force as a function of velocity can be thought of as the

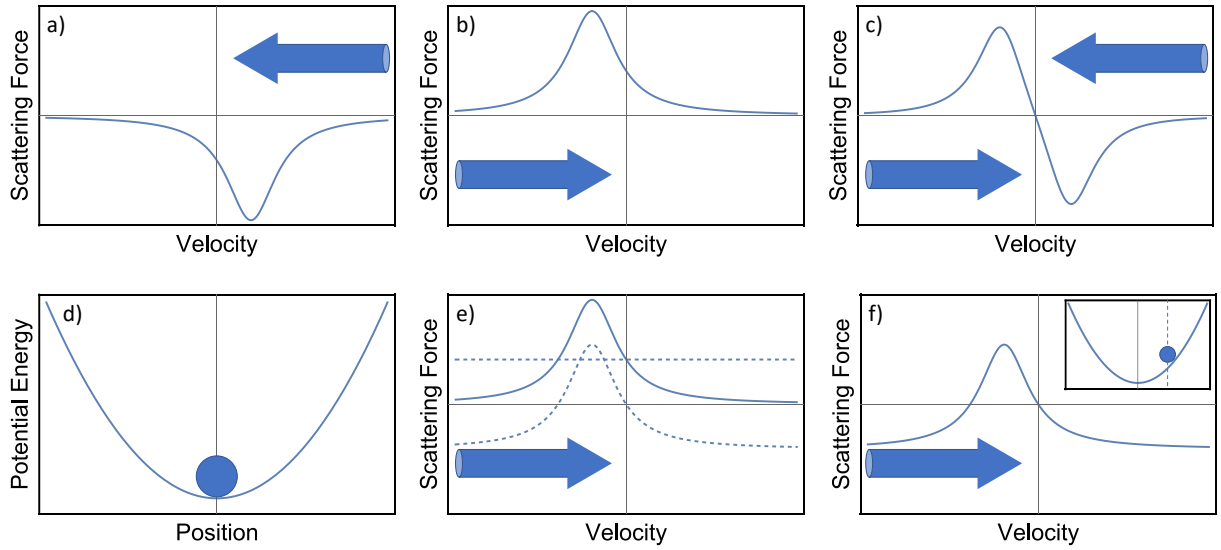

Figure 2.13: **One-dimensional scattering force.** The scattering force along the $\hat{x}$ direction from a red-detuned laser is plotted as a function of ion velocity for (a) a laser propagating in the $-\hat{x}$ direction, (b) a laser propagating in the $\hat{x}$ direction, (c) two lasers, one propagating in each direction. In (c) for sufficiently low speed, there is a net force that opposes the velocity. For an ion in an ion trap, the harmonic pseudopotential is plotted in (d) as a function of ion position. (e) A single laser propagating in the $\hat{x}$ direction can be broken up into two components, shown as dashed lines, including a constant force and a force that opposes the velocity at low speeds. (f) Shown in the inset, the constant-force-component shown in (e) acts to push the ion off the trap null to a new equilibrium position, shown as a vertical dashed line. The remaining force on the ion opposes the velocity for sufficiently low speed.

sum of two components, as illustrated in Figure 2.13e. One component is a constant force, and the second component is a velocity-dependent force that is zero for an ion with zero velocity. The constant force component acts to push the ion off the center of the trap to a new equilibrium position, depicted as a vertical dashed line in the inset of Figure 2.13f. This effect is known as radiation pressure. The other component, shown in the main plot of Figure 2.13f, provides a force that opposes the velocity of the ion for low speed. Similarly to the case in Figure 2.13c, this force can be approximated at low speed as $\vec{F}_{\text{molasses}} = -\alpha\vec{v}$, providing a damping force which reduces the temperature of the ion.

Doppler cooling is not without its limits. Specifically, the temperature to which one can

cool an atom or ion is not absolute zero, but is a finite temperature known as the *Doppler cooling limit* [FFF05]. This can be understood by looking at sources of heating on the atom or ion. One such heating source is the fact that random spontaneous emissions will give momentum kicks in a random direction, leading to a heating term. Another source of heating is due to the random absorption of photons. We previously examined the scattering force, which is simply the average force due to the absorption of photons, $\vec{F}_{\text{scat}} = \langle \vec{F}_{\text{abs}} \rangle$. The random deviations of this absorption force adds another heating term. Taking these heating and cooling terms into consideration, one expects the steady-state temperature during Doppler cooling (in the limit of a weak cooling beam) to be

$$T = \frac{\hbar\Gamma}{4k_{\text{B}}} \frac{1 + (2\delta/\Gamma)^2}{-2\delta/\Gamma} \tag{2.12}$$

where Γ is the natural linewidth of the transition, k_{B} is the Boltzmann constant, and $\delta = \omega - \omega_0$ is the laser detuning [FFF05]. Equation 2.12 ignores any heating from the constant force from a single beam. One can choose a detuning of $\delta = -\Gamma/2$ to minimize this temperature, resulting in the Doppler cooling limit

$$T_{\text{D}} = \frac{\hbar\Gamma}{2k_{\text{B}}}. \tag{2.13}$$

For $^{138}\text{Ba}^+$, we utilize the $6p\ ^2P_{1/2} \leftarrow 6s\ ^2S_{1/2}$ transition, driven by a laser with wavelength $\lambda = 493$ nm, referred to as the cooling laser. The $\text{Ba}^+(^2P_{1/2})$ state has a lifetime of $\tau = 7.9$ ns, with a linewidth of $\Gamma = 1/\tau = 2\pi \cdot 20.3$ MHz [ACK19]. The $\text{Ba}^+(^2P_{1/2})$ state can decay both to the $\text{Ba}^+(^2S_{1/2})$ state (with an Einstein A coefficient of $A_{sp} = 2\pi \cdot 14.8$ MHz) and to the $\text{Ba}^+(^2D_{3/2})$ state (with an Einstein A coefficient of $A_{sp} = 2\pi \cdot 5.4$ MHz) [ACK19]. The $\text{Ba}^+(^2D_{3/2})$ state has a lifetime of ~ 82 s, so the population must be removed from this state to avoid optical pumping into this state. To accomplish this, we add a 650 nm repumping laser to drive the $6p\ ^2P_{1/2} \leftarrow 5d\ ^2D_{3/2}$ transition. The relevant levels in $^{138}\text{Ba}^+$ are shown in Figure 2.14.

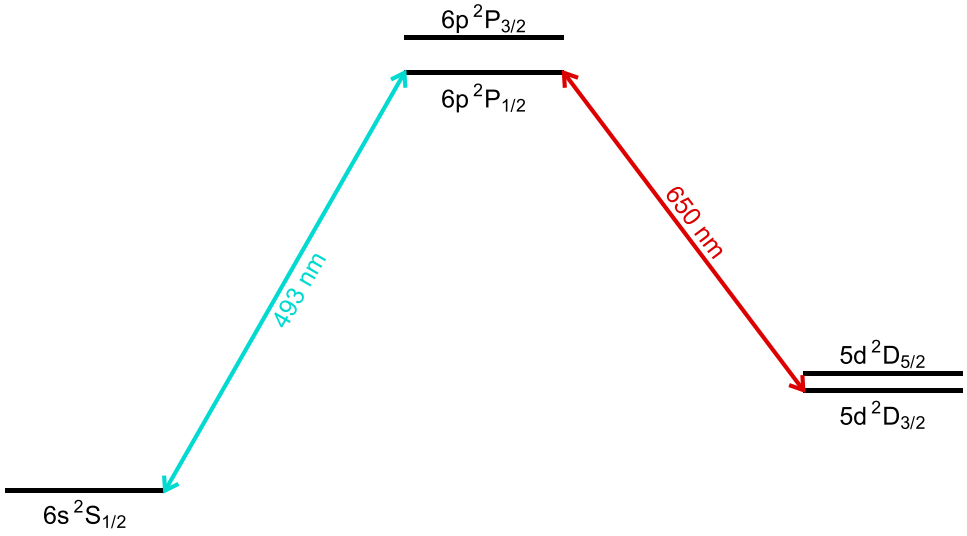

Figure 2.14: **Level scheme for ^{138}Ba$^+$.** The levels of ^{138}Ba$^+$ relevant for laser cooling are shown, with arrows representing the 493 nm cooling laser and the 650 nm repumping laser.

As the cooling and repump lasers both address the same upper state, the Ba$^+$($^2P_{1/2}$) state, there is an added level of complexity. When the detuning of the 493 nm cooling laser is the same as the detuning of the 650 nm repump laser, a coherent superposition of Ba$^+$($^2S_{1/2}$) and Ba$^+$($^2D_{3/2}$) is formed that is not addressed by the lasers and therefore not laser-cooled. This phenomenon is known as coherent population trapping (CPT) and is an example of electromagnetically induced transparency (EIT). To reduce this effect, a magnetic field ~ 6 G is introduced to destabilize the dark states [BB02]. The ^{138}Ba$^+$ level structure in the presence of this magnetic field is presented in Figure 2.15, where the Zeeman sublevels are shown splitting from each state.

Due to the complication of the CPT, an Einstein-rate-equation model will not accurately predict the state populations during laser cooling. To accurately model the state populations, one must compute the time evolution of the atomic density matrix $\hat{\rho}$ including all eight Zeeman sublevels using the Liouville equation

$$\frac{\partial}{\partial t}\hat{\rho} = \left[\hat{\mathcal{H}}, \hat{\rho}\right] + \hat{\mathcal{R}} \tag{2.14}$$

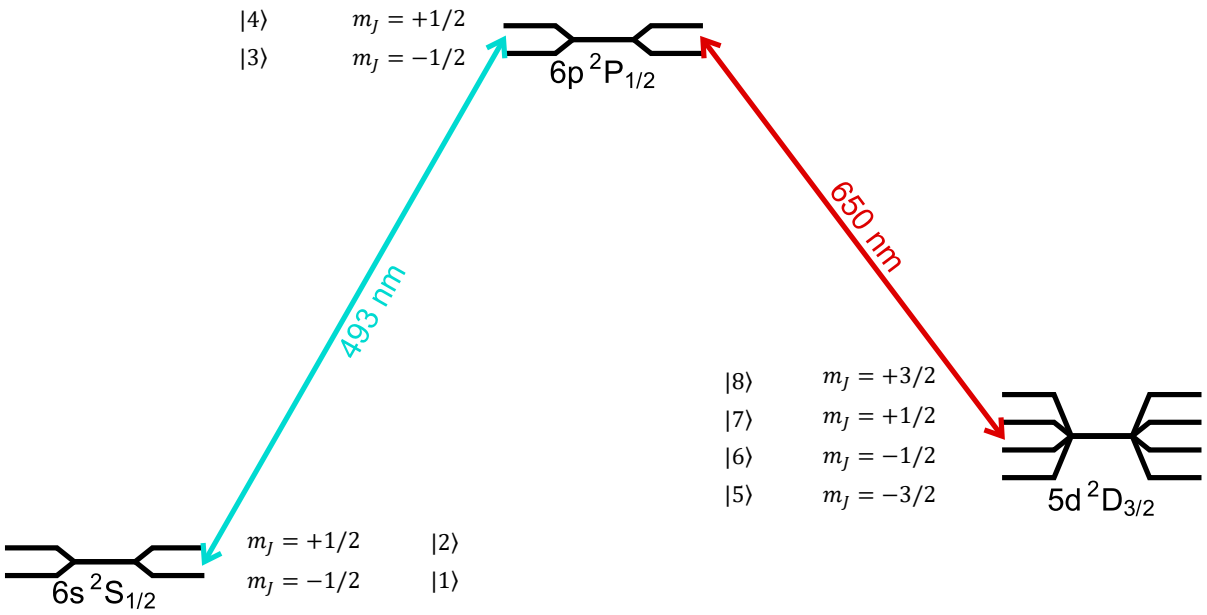

Figure 2.15: **Eight-level model of $^{138}Ba^+$.** The $^{138}Ba^+$ level scheme is shown including the Zeeman sublevels included in the eight-level model.

where $\hat{\mathcal{H}}$ is the Hamiltonian and $\hat{\mathcal{R}}$ is a relaxation matrix that models the decoherence [DPG15]. A Wolfram Mathematica [Inc] code was created to model this behavior. In this eight-level model the states are ordered according to their labeling in Figure 2.15. The full Hamiltonian from this code under the rotating wave approximation (RWA) is shown in matrix form in Figure 2.16, where $\Delta 1$ is the detuning of the 493 nm cooling laser, $\Delta 2$ is the detuning of the 650 nm repump laser, $\Omega 1$ is the Rabi frequency of the 493 nm cooling laser, $\Omega 2$ is the Rabi frequency of the 650 nm repump laser, and $\omega_B = \mu_B|\vec{B}|/\hbar$ is the Larmor frequency, where μ_B is the Bohr magneton and $\vec{B}$ is the magnetic field. The relaxation matrix is shown in Figure 2.17, where Γ is the natural linewidth of the $Ba^+(^2P_{1/2})$ state, $\Gamma 1$ is the Einstein A coefficient between the $Ba^+(^2P_{1/2})$ and $Ba^+(^2S_{1/2})$ states, $\Gamma 2$ is the Einstein A coefficient between the $Ba^+(^2P_{1/2})$ and $Ba^+(^2D_{3/2})$ states, such that $\Gamma = \Gamma 1 + \Gamma 2$ with associated decoherence rate $\gamma = \Gamma/2$. The linewidths of the lasers are taken to be γl, and γp $= \gamma + \gamma$l.

$$\mathcal{H} = \begin{pmatrix} (\Delta 1 - \omega B)\,\hbar & 0 & -\frac{\Omega 1\,\hbar}{\sqrt{3}} & 0 & 0 & 0 & 0 & 0 \\ 0 & (\Delta 1 + \omega B)\,\hbar & 0 & \frac{\Omega 1\,\hbar}{\sqrt{3}} & 0 & 0 & 0 & 0 \\ -\frac{\Omega 1\,\hbar}{\sqrt{3}} & 0 & -\frac{\omega B\,\hbar}{3} & 0 & \frac{\Omega 2\,\hbar}{2\sqrt{2}} & -\frac{\Omega 2\,\hbar}{\sqrt{6}} & -\frac{\Omega 2\,\hbar}{2\sqrt{6}} & 0 \\ 0 & \frac{\Omega 1\,\hbar}{\sqrt{3}} & 0 & \frac{\omega B\,\hbar}{3} & 0 & \frac{\Omega 2\,\hbar}{2\sqrt{6}} & -\frac{\Omega 2\,\hbar}{\sqrt{6}} & -\frac{\Omega 2\,\hbar}{2\sqrt{2}} \\ 0 & 0 & \frac{\Omega 2\,\hbar}{2\sqrt{2}} & 0 & \Delta 2\,\hbar - \frac{6\,\omega B\,\hbar}{5} & 0 & 0 & 0 \\ 0 & 0 & -\frac{\Omega 2\,\hbar}{\sqrt{6}} & \frac{\Omega 2\,\hbar}{2\sqrt{6}} & 0 & \Delta 2\,\hbar - \frac{2\,\omega B\,\hbar}{5} & 0 & 0 \\ 0 & 0 & -\frac{\Omega 2\,\hbar}{2\sqrt{6}} & -\frac{\Omega 2\,\hbar}{\sqrt{6}} & 0 & 0 & \Delta 2\,\hbar + \frac{2\,\omega B\,\hbar}{5} & 0 \\ 0 & 0 & 0 & -\frac{\Omega 2\,\hbar}{2\sqrt{2}} & 0 & 0 & 0 & \Delta 2\,\hbar + \frac{6\,\omega B\,\hbar}{5} \end{pmatrix}$$

Figure 2.16: **Eight-level Hamiltonian for $^{138}Ba^{+}$.** The Hamiltonian in the rotating wave approximation (RWA) is shown for the eight-level model of $^{138}Ba^{+}$.

$$\mathcal{R} = \begin{pmatrix} \Gamma 1\left(\frac{\rho 33}{3} + \frac{2\,\rho 44}{3}\right) & -\frac{\Gamma 1\,\rho 34}{3} & -\gamma p\,\rho 13 & -\gamma p\,\rho 14 & -\gamma l\,\rho 15 & -\gamma l\,\rho 16 & -\gamma l\,\rho 17 & -\gamma l\,\rho 18 \\ -\frac{\Gamma 1\,\rho 43}{3} & \Gamma 1\left(\frac{2\,\rho 33}{3} + \frac{\rho 44}{3}\right) & -\gamma p\,\rho 23 & -\gamma p\,\rho 24 & -\gamma l\,\rho 25 & -\gamma l\,\rho 26 & -\gamma l\,\rho 27 & -\gamma l\,\rho 28 \\ -\gamma p\,\rho 31 & -\gamma p\,\rho 32 & -\Gamma\,\rho 33 & -\Gamma\,\rho 34 & -\gamma p\,\rho 35 & -\gamma p\,\rho 36 & -\gamma p\,\rho 37 & -\gamma p\,\rho 38 \\ -\gamma p\,\rho 41 & -\gamma p\,\rho 42 & -\Gamma\,\rho 43 & -\Gamma\,\rho 44 & -\gamma p\,\rho 45 & -\gamma p\,\rho 46 & -\gamma p\,\rho 47 & -\gamma p\,\rho 48 \\ -\gamma l\,\rho 51 & -\gamma l\,\rho 52 & -\gamma p\,\rho 53 & -\gamma p\,\rho 54 & \frac{\Gamma 2\,\rho 33}{2} & \frac{\Gamma 2\,\rho 34}{2\sqrt{3}} & 0 & 0 \\ -\gamma l\,\rho 61 & -\gamma l\,\rho 62 & -\gamma p\,\rho 63 & -\gamma p\,\rho 64 & \frac{\Gamma 2\,\rho 43}{2\sqrt{3}} & \Gamma 2\left(\frac{\rho 33}{3} + \frac{\rho 44}{6}\right) & \frac{\Gamma 2\,\rho 34}{3} & 0 \\ -\gamma l\,\rho 71 & -\gamma l\,\rho 72 & -\gamma p\,\rho 73 & -\gamma p\,\rho 74 & 0 & \frac{\Gamma 2\,\rho 43}{3} & \Gamma 2\left(\frac{\rho 33}{6} + \frac{\rho 44}{3}\right) & \frac{\Gamma 2\,\rho 34}{2\sqrt{3}} \\ -\gamma l\,\rho 81 & -\gamma l\,\rho 82 & -\gamma p\,\rho 83 & -\gamma p\,\rho 84 & 0 & 0 & \frac{\Gamma 2\,\rho 43}{2\sqrt{3}} & \frac{\Gamma 2\,\rho 44}{2} \end{pmatrix}$$

Figure 2.17: **Relaxation matrix for the eight-level model of $^{138}Ba^{+}$.** The relaxation matrix is shown for the eight-level model of $^{138}Ba^{+}$.

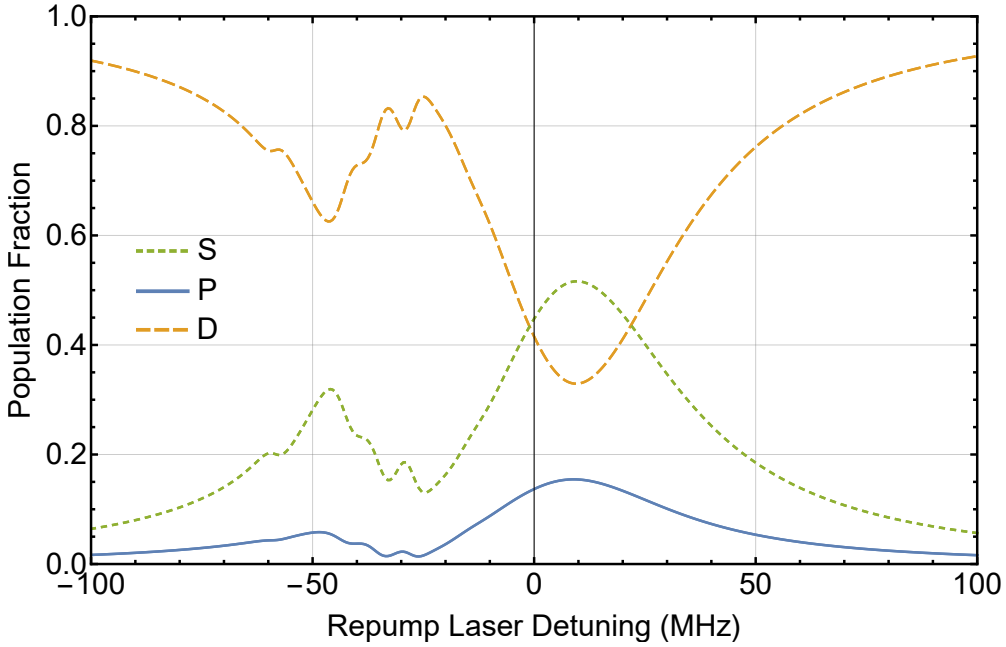

Figure 2.18: **Eight-level model simulation results.** For typical experimental parameters, the simulated population fractions of the $Ba^+(^2S_{1/2})$, $Ba^+(^2P_{1/2})$, and $Ba^+(^2D_{3/2})$ states are plotted as a function of the 650 nm repump laser detuning. The $Ba^+(^2P_{1/2})$ state population fraction is especially low when the repump laser detuning is close to the cooling laser detuning, set to −30 MHz. Relatively small bumps and dips are visible due to the different shifts of the Zeeman sublevels.

This eight-level model is implemented for typical experimental parameters. Instead of examining the time-varying dynamics of Equation 2.14, we are instead interested in the steady-state population fractions in the $Ba^+(^2S_{1/2})$, $Ba^+(^2P_{1/2})$, and $Ba^+(^2D_{3/2})$ states. To find these values, we set

$$\frac{\partial}{\partial t}\hat{\rho} = 0 \tag{2.15}$$

for a given set of experimental parameters. As an example, the simulated steady-state population fractions are plotted as a function of the 650 nm repump laser detuning for typical experimental parameters in Figure 2.18. The expected fluorescence one expects to observe from a laser-cooled Ba^+ ion—and consequently the rate at which the ion can undergo a cooling cycle—is proportional to the $Ba^+(^2P_{1/2})$ state population. As such, the $Ba^+(^2P_{1/2})$ state population fraction is of particular importance for laser cooling. In this

simulation, the 493 nm cooling laser has a detuning of -30 MHz. As a result, the simulation results show a dip in the $Ba^+(^2P_{1/2})$ state population when the repump laser detuning is near the cooling laser detuning due to the CPT effect. This dip in fluorescence is a feature that is observed in the lab when the 650 nm laser detuning is scanned over a large range. Additionally, smaller peaks and dips are visible due to the different shifts of the Zeeman sublevels. Another feature shown in Figure 2.18 that may not be initially intuitive is the relatively high population fraction in the $Ba^+(^2D_{3/2})$ state. For large repump detunings, this makes sense due to optical pumping into the $Ba^+(^2D_{3/2})$ state and inefficient repumping out of that state. Even for small detunings, the $Ba^+(^2D_{3/2})$ state population can be larger than the $Ba^+(^2S_{1/2})$ state population. This is, in part, due to the fact that the $Ba^+(^2D_{3/2})$ has more Zeeman sublevels that can be populated. The relative intensities of the cooling and repump lasers are also an important factor as well.

To optimize the laser-cooling of Ba^+, there are many variables to consider. With the parameters in Figure 2.18, varying only the repump laser detuning, one may aim to maximize the fluorescence by selecting a repump laser detuning $\sim +10$ MHz. Using this detuning, one may not achieve the best cooling. As the number of photons absorbed by the repump laser is not negligible compared to the photons absorbed by the cooling laser, the blue-detuned repump laser can actually act as a heating source. One may find that sacrificing some fluorescence to have a red-detuned repump beam may result in better cooling. In reality, one is not limited to only changing the repump laser detuning. In general, varying the detuning of both lasers, the intensity of both lasers, the polarization of both lasers, and the magnetic field strength all have important effects on the effectiveness of the laser cooling. While modeling these parameters using such an eight-level model can be helpful to develop an understanding and intuition of various effects, it is generally advisable to vary these parameters in the lab—and to try varying multiple parameters at once, since they are quite convoluted due to the CPT—in order to achieve a desirable result.

One must also consider the goal one is trying to achieve with the laser cooling. The ideal

parameters for reaching the lowest possible Doppler-limited temperature with an already cold ion will be significantly different than the ideal parameters for cooling a large sample of hot Ba^+ ions into a crystal quickly. Many of the experiments performed in this dissertation involve utilizing large Ba^+ crystals with ~ 1000 ions. In this case, we have found it beneficial to use cooling and repump beams with high intensity $I \gg I_{\text{sat}}$, where I_{sat} is the saturation intensity for a transition. This high intensity broadens the cooling and repump transition. With this high intensity and significant red-detuning on the cooling and repump lasers, it is possible to cool a large velocity class of ions, including the hot ions produced by ablation loading, at a small cost to the laser-cooled temperature. At other times, we have used chains with $\lesssim 10$ ions, and desired high fluorescence. Under these circumstances, it is beneficial to use less intensity and smaller detunings.

With a single cooling and repump laser along the axis of the ion trap, the axial motion will be cooled efficiently. The radial motion, however, will not be directly cooled by these lasers. There is some mixing of the motional modes; that is to say, radial excitations have a tendency to excite axial modes to some extent. The excitation that is transferred to an axial mode can be laser-cooled. In this way, all three normal modes for an ion can be laser-cooled, albeit inefficiently, with a laser only along the axis of one of these modes. It is more efficient, however, to directly laser-cool all modes rather than relying on remixing. One can add a slight angle to the axial laser beam to have a small projection along the radial directions. Alternatively, a radial beam can be added that more efficiently cools the radial modes. The experiments performed in this dissertation typically use such a radial beam for more efficient cooling.

2.2.5 Laser-Cooling of Yb^+

In addition to Ba^+, Yb^+ is utilized in this dissertation. For the experiments performed, typically only $^{174}Yb^+$ and $^{172}Yb^+$ are used. These isotopes do not have hyperfine structure, making laser-cooling simpler. As shown in Figure 2.19, we utilize a 369 nm cooling laser

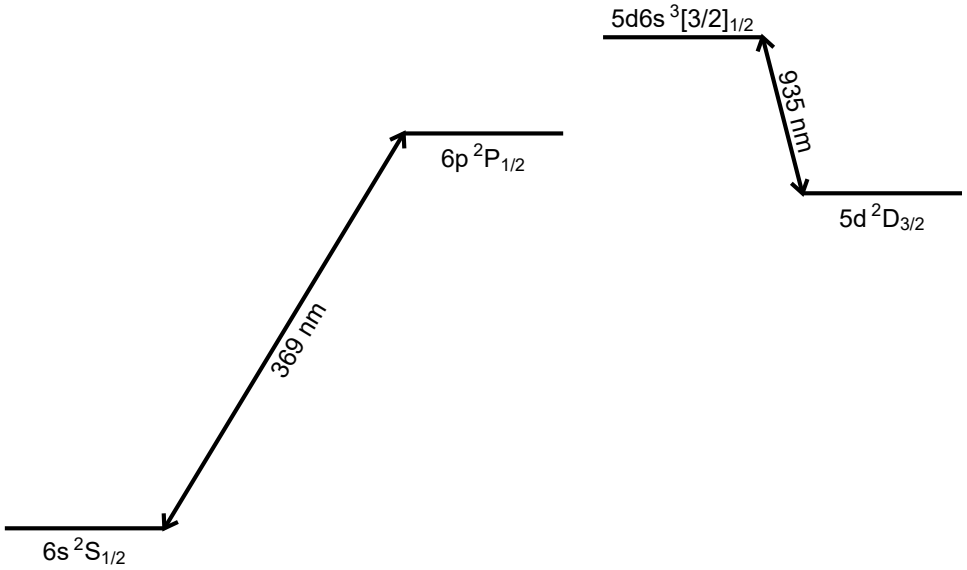

Figure 2.19: **Level scheme for Yb^+.** Relevant states and transitions are shown for laser–cooling Yb^+. The 369 nm cooling laser drives the $6p\ ^2P_{1/2} \leftarrow 6s\ ^2S_{1/2}$ transition. The $Yb^+(^2P_{1/2})$ state can decay to the $Yb^+(^2D_{3/2})$ state. To prevent accumulation in this state, a 935 nm repump laser drives the $5d6s\ ^3[3/2]_{1/2} \leftarrow 5d\ ^2D_{3/2}$ transition. The $Yb^+(^3[3/2]_{1/2})$ state can decay to the ground $Yb^+(^2S_{1/2})$ state.

to drive the $6p\ ^2P_{1/2} \leftarrow 6s\ ^2S_{1/2}$ transition. The $Yb^+(^2P_{1/2})$ state has a natural linewidth of $2\pi \cdot 19.6$ MHz, and will decay to the $Yb^+(^2S_{1/2})$ state with 99.5% chance and to the $Yb^+(^2D_{3/2})$ state with 0.5% chance [OYM07]. To prevent the population from accumulating in the $Yb^+(^2D_{3/2})$ state, a 935 nm repump laser is utilized, driving the $5d6s\ ^3[3/2]_{1/2} \leftarrow 5d\ ^2D_{3/2}$ transition. The $Yb^+(^3[3/2]_{1/2})$ state has a linewidth of $2\pi \cdot 4.2$ MHz and decays to the $Yb^+(^2S_{1/2})$ state with 98.2% chance and to the $Yb^+(^2D_{3/2})$ state with 1.8% chance.

2.2.6 Imaging

To image the ions, an electron-multiplying charged-coupled device (EMCCD) is used. The EMCCD used to image the ions in this experiment is an Andor Luca-R EMCCD. The sensor of this camera has 1000 × 1000 pixels, each with a 8 μm × 8 μm size. A lens tube holding an imaging objective lens is inserted into the reentrant flange such that the lens is $\sim$ 50 mm

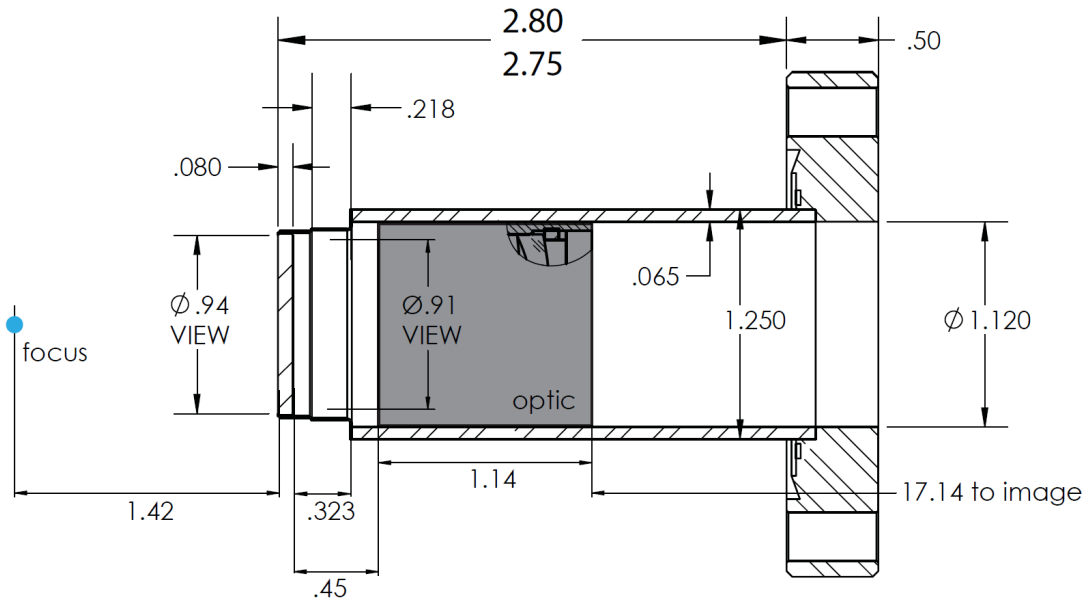

Figure 2.20: **Reentrant imaging system.** A schematic shows the objective lens, labeled "optic" in the reentrant viewport of the vacuum chamber. Relevant dimensions are shown in inches. This figure is borrowed from Ref. [Sch16].

from the center of the ion trap, as shown in Figure 2.20. This lens forms an image ~ 17 inches away, where the camera sensor is located, resulting in a magnification of ~ 8. As a result, the image seen on the camera represents an area roughly 1 mm $\times$ 1 mm in size, with each pixel representing 1 μm $\times$ 1 μm. The path from the objective lens to the camera sensor is completely enclosed to prevent scatter from ambient light, and includes a 2 inch adjustable mirror to align the light path precisely onto the sensor. The entire reentrant imaging system is placed on a translation stage, allowing for precise control of the focus of the imaged ions.

To increase the signal-to-noise ratio for the imaging system, an optical band-pass filter is inserted in the imaging path, blocking most ambient light while passing a high fraction of the ion fluorescence. A filter wheel holding as many as six different optical filters allows one to easily switch between these filters. For Yb^+ ion imaging, a band-pass filter near 369 nm is used. For Ba^+ ion imaging, a band-pass filter either near 493 nm or 650 nm can be used. While these band-pass filters allow fluorescence from the ion to pass, they also allow scattered light from the lasers to pass, which can add noise to the image. Of the two

filters for Ba^+, the 650 nm filter is typically used. This filter enables the use of a 493 nm radial cooling beam without added scatter noise on the image due to the extra beam path.

2.2.7 Loading

To load the ions, we rely on ablation of a target to produce a plume of ions. Ablation works by utilizing a high-energy, tightly focused pulse of laser light to produce a plasma on the surface of a material. In this dissertation, a pressed, annealed $BaCl_2$ powder target is used to generate Ba^+ and $BaCl^+$ ions, and a Yb metal target is used to produce Yb^+ ions. A Continuum Minilite II laser is utilized for the ablation in this experiment. This laser is a Q-switched Nd:YAG laser that produces a $\sim$ 5 ns pulse of energy $\sim$ 2 mJ at a wavelength of 1064 nm. When the ablation loading, the rf voltage to the LPT is turned off, allowing the ions generated to easily reach the center of the ion trap. Some time later, when many ions are expected to be in the trapping volume, the rf voltage of the LPT is turned on, resulting in ions being trapped. One downside of ablation loading is that the ions created from ablation can stick to the trap rods and other surfaces, which can lead to patch charges that can push the ions off the trap center, leading to excess micromotion.

Additionally, some molecular ion species can be generated from chemical reactions between currently trapped ions and a background gas. To generate these molecular ions, we also have the capability to leak in a gas in a controlled manner. The details of this system are presented in Section 2.5. We often use this system to leak in CH_3Cl, which reacts with Ba^+ to form $BaCl^+$. In this way, we can load $BaCl^+$ ions with greater control than is possible with ablation loading. Other gases have also been leaked into the vacuum chamber to study chemical reactions that occur with an ion.

2.2.8 Species Selection Techniques

Once a large cloud of ions is loaded from the ablation sequence, it is desirable to select only a subset of those trapped ions to keep. For example, one may want to perform an experiment with only Ba^+ ions. If Ba^+ and $BaCl^+$ ions are loaded from the ablation, one must be able to eject the $BaCl^+$ ions without ejecting the Ba^+ ions. Here, it is possible to take advantage of the stability of ions in an ion trap. We can understand this by examining Figure 2.21, where the Mathieu stability diagram is plotted for various ions of different masses as a function of the rf and dc voltages applied to two diagonally opposed rods. Regions of stability are shown as shaded areas. If one uses $V_{\mathrm{rf}} = 175$ V, as is typically done in experiment, one can add a dc voltage to two diagonally opposed rods to generate a Mathieu a parameter that is high enough to make $BaCl^+$ unstable, but not high enough to make Ba^+ unstable. As shown in Figure 2.21, this is true for $V_{\mathrm{dc}} \sim 20$ V, where out of the three displayed ions, only Ba^+ is stable. In the experiment, we use this technique to eject $BaCl^+$ ions while keeping the Ba^+ ions by ramping the dc voltage up to this value and ramping it back down to its original value. We refer to this technique as an a-ramp. In general, an a-ramp will only eject masses higher than the ion one would like to keep. For high q parameters, this is not necessarily true, but the experiment does not typically access such high q values.

Also shown in Figure 2.21 is Ca^+, which can be produced in the ion trap during an experiment due to ionization of the Ca atoms in the MOT. To prevent these ions from building up during an experiment, we use an rf voltage high enough that Ca^+ ions are unstable. As shown in Figure 2.21, this is true for $V_{\mathrm{rf}} = 175$ V.

It is often desirable to select only a single isotope of an ion, typically the isotope used for laser-cooling. Often times, isotopes of lower mass than the target isotope exist, and a-ramping will not be viable to eliminate these unwanted isotopes—even if this were not true, it is difficult to achieve a mass-selectivity of ~ 1 amu using an a-ramp. Another method to eliminate species from the ion trap is to heat an ion species out of the trap. This can

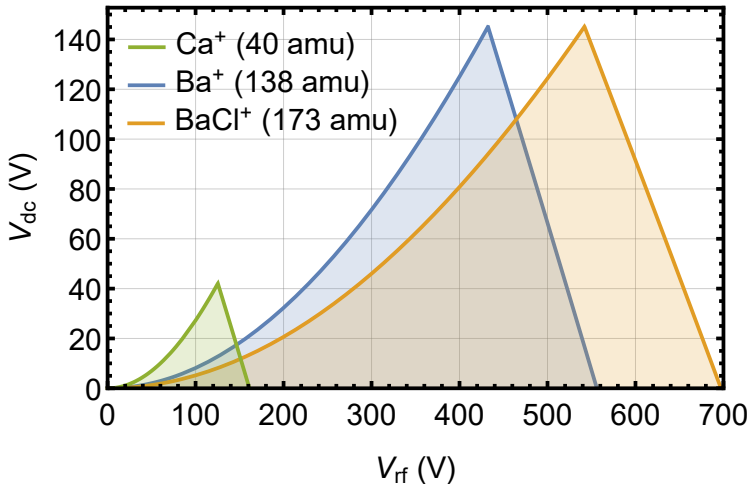

Figure 2.21: **Mathieu stability diagram for several ion species.** Instead of plotting the stability for varying Mathieu a and q parameters, which are different for different ion masses, the stability diagrams are plotted for several ion species of interest for varying rf and dc voltages applied to the center rod segments. Regions of stability are shown as shaded areas.

be accomplished by laser-heating a specific isotope of an ion that one is laser-cooling (by using a blue-detuned laser rather than a red-detuned laser), however the isotope shifts for laser-cooling transitions are often larger than can be easily shifted and may require extra equipment such as an electro-optic modulator (EOM). For this reason, we do not typically implement this technique.

Instead, we heat the ions electrically. This can be accomplished either through "tickling" or parametric heating. The first method, known as tickling, can be accomplished by applying an electric field to the ions that oscillates at their secular frequency in the harmonic pseudopotential of the LPT. As ions of different masses have different secular frequencies, it is possible to resonantly heat ions of a certain mass very efficiently, while not heating other ions efficiently.

The other method, known as parametric heating, is what is typically used in this experiment. Parametric heating occurs when there is a quadrupolar ac electric field in addition to the rf trapping field. When the frequency of this auxiliary ac field is similar to twice

the secular frequency, the ions can be resonantly excited and heated. For ions with some motional damping, such as by laser-cooling, it has been shown that ions under the effect of such parametric heating exhibit Mathieu trajectories with modified q and a parameters, and the stability of the modified trajectory is dependent on the damping coefficient and the amplitude of the auxiliary quadrupolar ac electric field applied [ZRS02]. That is, for a given damping coefficient, there will be some critical quadrupolar ac field amplitude that will result in an unstable trajectory, heating the ion out of the trap. We utilize this effect in Ba^+ to eliminate all isotopes other than the $^{138}Ba^+$ that is actively laser-cooled. The $^{138}Ba^+$ ions are being laser-cooled, and will have a greater damping constant than the other Ba^+ isotopes, which only undergo sympathetic cooling. We observe the range of frequencies over which we observe parametric heating for a single mass is larger than the frequency difference due to the difference in masses of the Ba^+ isotopes. As such, we are able to generate an auxiliary ac quadrupolar field by driving rods γ and δ (far off resonance from their LC-resonator frequency of 1.8 MHz) in a manner that can parametrically heat all Ba^+ isotopes. As the $^{138}Ba^+$ damping constant is greater than the damping constant for all other isotopes, we are able to adjust the amplitude of the auxiliary field until only $^{138}Ba^+$ is remaining. Additionally, since $^{138}Ba^+$ is the heaviest stable isotope of Ba^+, one can select a parametric heating frequency that preferentially heats lower-mass isotopes to some degree more than $^{138}Ba^+$.

Another method to eject some ions from the LPT is to reduce the endcap voltages until the axial trap depth is low enough that some ions will be ejected from the trap. With cooling and repump lasers propagating in only one direction axially, the "bright" laser-cooled ions will feel a radiation pressure pushing them to one side of the chain. This will typically result in the bright ions pushed to one side and the "dark" ions on the other side. By lowering the endcap on side with the dark ions more than the other endcap, one can preferentially eject the dark ions, sometimes resulting in an isotopically pure sample. In our experience, we observe that this technique can work well to generate an isotopically pure sample with low

ion number ($\lesssim$ 20 ions), but if a larger crystal is desired, the parametric heating technique more easily produces an isotopically pure sample with large ion number.

In addition to producing a pure sample of the laser-cooled isotope of the desired ion, it is often beneficial to load a specific number of ions or a specific crystal size. For $^{138}Ba^{+}$ ions, the typical procedure for accomplishing this is as follows: First, after ablation, large number of Ba^{+} and $BaCl^{+}$ ions are present. An a-ramp is performed that eject the $BaCl^{+}$ without ejecting the Ba^{+}. To eliminate the dark isotopes of Ba^{+}, the parametric heating technique is performed, leaving a large crystal of pure $^{138}Ba^{+}$. To eliminate enough ions that results in the desired number of ions, either a-ramping or endcap ramping is performed. For larger crystals ($\gtrsim$ 100 ions), typically an a-ramp with amplitude large enough to eject a small fraction of Ba^{+} ions is utilized. With multiple repeated a-ramps, the crystal can be whittled down to the desired size. When the goal is a countable ion chain or small crystal ($\lesssim$ 20 ions), either repeated a-ramps or an endcap ramp are utilized.

2.3 Magneto-Optical Trap

In this section, a brief overview of the theory of the magneto-optical trap (MOT) is provided. Further details of the theory are available in literature [FFF05]. This discussion is followed with the design of the Ca MOT used in this experiment as well as specific details related to the magneto-optical trapping of Ca. Further, I provide details of the *magnetic* trapping of Ca atoms due to the magnetic fields generated for the Ca MOT. This section is concluded with a description of the imaging system used to detect and measure the Ca MOT.

2.3.1 Theory

The optical molasses technique described in Section 2.2.4 can effectively cool an atom by providing a scattering force that opposes the velocity, but this force is independent of the position of the atom, allowing the atom to randomly walk away from its initial position. In

order to spatially trap atoms in addition to cooling them, a magneto-optical trap (MOT) can be utilized. A MOT takes advantage of the shift of the resonance frequency of an atomic transition due to the Zeeman effect in the presence of a magnetic field. If the magnetic field varies with position, the scattering force is then position-dependent. By appropriately choosing a magnetic field configuration and laser polarization and detuning, a spatially trapping force can be realized.

Specifically, a quadrupolar magnetic field is generated by driving two coils equidistant from the center of the MOT with current flowing in opposite directions, as shown in Figure 2.22. The direction of the current flowing in each of the coils is depicted by yellow arrows. The quadrupolar magnetic field lines are drawn as white lines. Three orthogonal, counter-propagating pairs of circularly polarized lasers are illustrated in violet, with straight arrows indicating the direction of propagation and circular arrows representing the direction of the circular polarization for each beam. Note that, as shown to be necessary in later discussion, the horizontal, radial cooling beams have left-handed circular polarization (LHCP), and the vertical, axial beams have right-handed circular polarization (RHCP).

The most common and most straightforward type of MOT is known as a type-1 MOT. In a type-1 MOT, the cooling transition involves a ground state with angular momentum J and an excited state with angular momentum $J' = J+1$. The advantage of a type-1 MOT is that circularly polarized light can drive transitions to the stretched excited state without any "dark states" in the ground-state manifold that are not addressed by the cooling laser. In the following discussion, the case of $J = 0$ and $J' = 1$ is considered, as this is representative of the levels of the Ca MOT used in this dissertation.

The magnetic field produced by the coil configuration shown in Figure 2.22, referred to as anti-Helmholtz coils, takes the form

$$\vec{B}(x, y, z) = \alpha(-x\hat{x} - y\hat{y} + 2z\hat{z}) \tag{2.16}$$

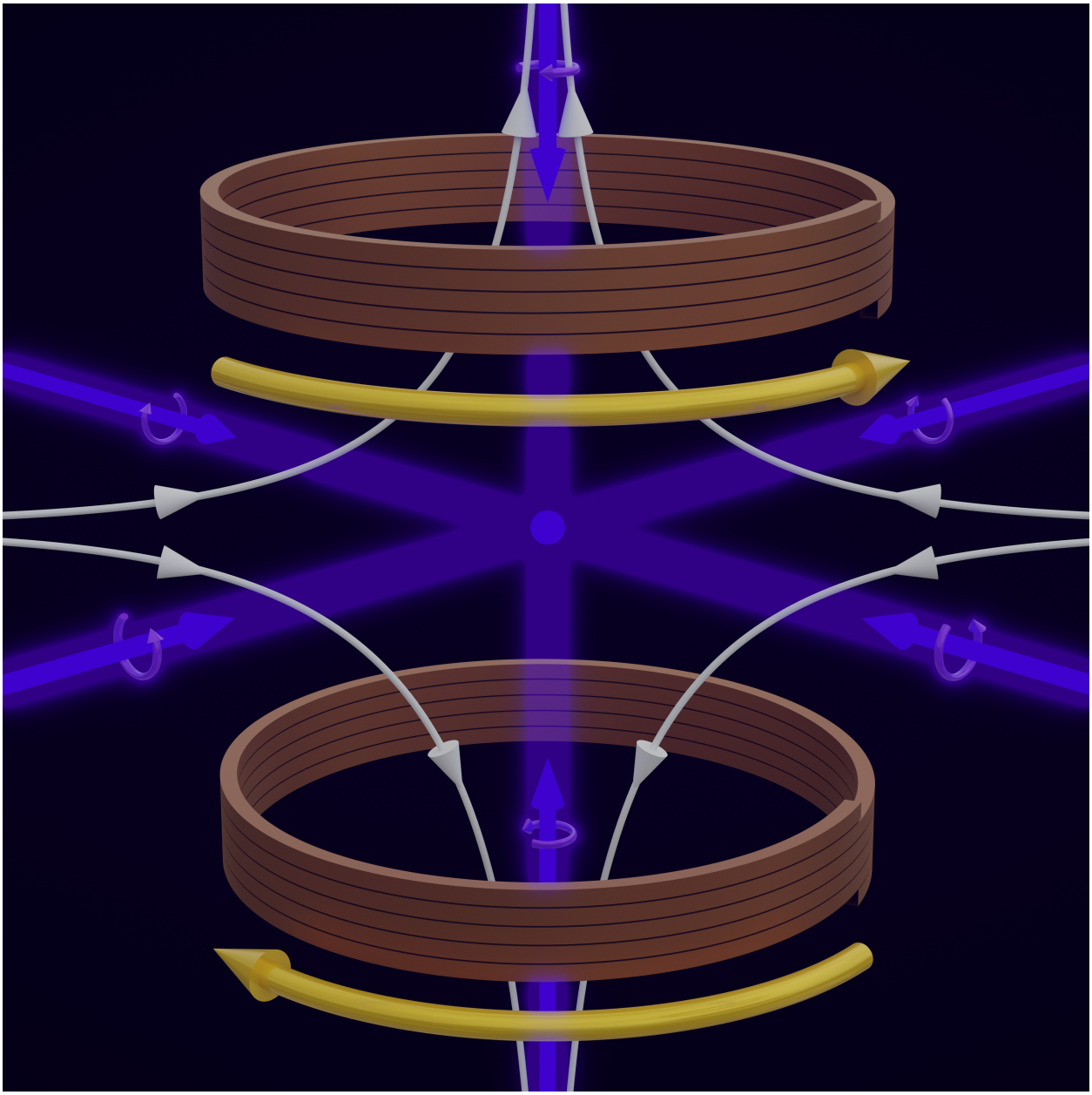

Figure 2.22: **MOT illustration.** A 3D rendering is shown of the anti-Helmholtz coils above and below the MOT with yellow arrows indicating the direction of the current. White arrows represent the magnetic field lines generated by these coils. The three pairs of counter-propagating cooling beams are shown in violet, with straight arrows representing the propagation direction and circular arrows representing the circular polarization of each beam.

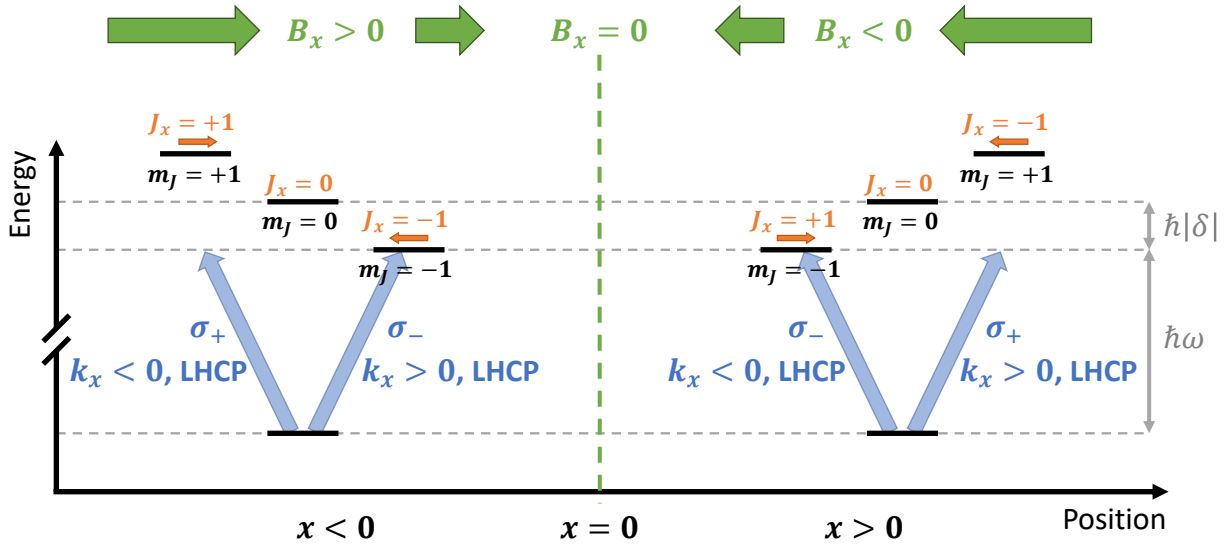

Figure 2.23: **MOT level splitting.** The Zeeman splitting of the excited state is shown for $x < 0$ with $B_x > 0$ as well as for $x > 0$ with $B_x < 0$. The angular momentum projection along the $+\hat{x}$ direction is shown in orange, and the projection along the magnetic field direction is shown in black. On either side of $x = 0$, the σ_- light is closer to resonance than the σ_+ light, and the laser beam with the direction of propagation opposing the displacement has a larger scattering force. Thus, with LHCP beams, a restoring force is realized.

where $\hat{x}$ and $\hat{y}$ are defined as the two horizontal, radial directions, $\hat{z}$ is the vertical, axial direction, and α is some constant depending on the geometry, current, and number of winds in each coil. The magnetic field at the origin is 0 and varies linearly with position. The resulting Zeeman shift of the ground and excited state due to this field is illustrated in 1D along the x-axis in Figure 2.23. Note that the excited-state angular momentum projected along the $+\hat{x}$ direction (labeled J_x in orange text) is not always the same as the angular momentum projected along the magnetic field quantization axis (labeled m_J in black text). For positions $x < 0$, the magnetic field component along the $+\hat{x}$ direction $B_x > 0$, and the excited-state Zeeman sublevel with $J_x = -1$ is the $m_J = -1$ state. For positions $x > 0$, $B_x < 0$ and the excited-state Zeeman sublevel with $J_x = +1$ is the $m_J = -1$ state. The effect of adding two counter-propagating, red-detuned lasers with LHCP along the x-axis is shown by blue arrows. For $x < 0$, the beam propagating in the $+\hat{x}$ direction drives the σ_- transition, which becomes near-resonance due to the Zeeman splitting. The beam propagating in the

$-\hat{x}$ direction drives the σ_+ transition, but is far off-resonance due to the Zeeman splitting, resulting in a relatively low scattering rate. For $x > 0$, the opposite is true, with the beam propagating in the $-\hat{x}$ direction driving the closer-to-resonance σ_- transition. In either case, the σ_- transition will be driven more than the σ_+ transition, and the scattering force will oppose the displacement of the atom, pushing it towards $x = 0$, resulting in a trapping force. If, instead, a counter-propagating pair of beams with RHCP were chosen, the resulting force would be anti-trapping, pushing the atom away from the null.

If the cooling laser is detuned from the transition by $\delta = \omega - \omega_0$, the effective detuning including the Zeeman shift (and excluding the Doppler shift) for the laser propagating in the $+\hat{x}$ direction with LHCP is

$$\delta' = \delta - \beta_x x \tag{2.17}$$

where

$$\beta_x = \frac{g\mu_\mathrm{B}}{\hbar}\frac{\mathrm{d}B_x}{\mathrm{d}x} \tag{2.18}$$

where g is the Landé g-factor of the excited state, μ_B is the Bohr magneton, and $\hbar$ is the reduced Planck constant. The average scattering force for the laser propagating in the $+\hat{x}$ direction is

$$\vec{F}_\mathrm{scat}^{(+\hat{x})} = \hbar\vec{k}R_\mathrm{scat} = \hbar k\frac{\Gamma}{2}\frac{\Omega^2/2}{(\omega - \omega_0 - \beta_x x)^2 + \Omega^2/2 + \Gamma^2/4}\hat{x} \tag{2.19}$$

where $\vec{k}$ is the laser wave vector, Γ is the natural linewidth of the transition, and Ω is the Rabi frequency. Similarly, for the laser propagating in the $-\hat{x}$ direction, the scattering force is

$$\vec{F}_\mathrm{scat}^{(-\hat{x})} = \hbar\vec{k}R_\mathrm{scat} = -\hbar k\frac{\Gamma}{2}\frac{\Omega^2/2}{(\omega - \omega_0 + \beta_x x)^2 + \Omega^2/2 + \Gamma^2/4}\hat{x}. \tag{2.20}$$

The scattering force as a function of atom position due to each laser individually as well as due to the presence of both lasers is shown in Figure 2.24. With a pair of counter-propagating beams with LHCP, a restoring force of the form $F = -k_\mathrm{spring}x$ is realized for positions near the center of the trap, where k_spring is a spring constant. Along with the optical molasses

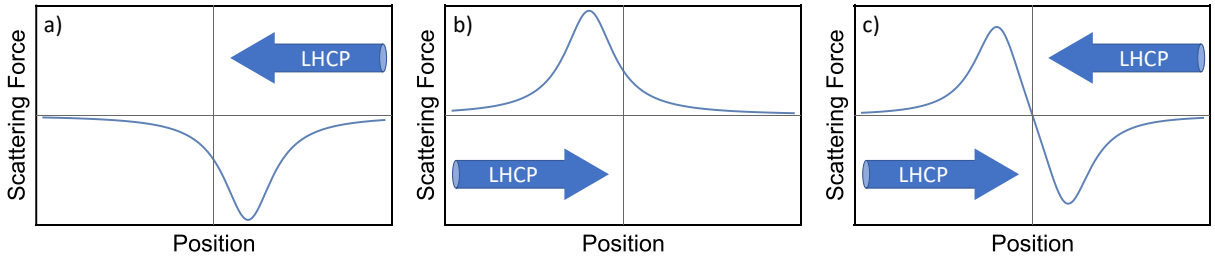

Figure 2.24: **Scattering force for MOT beams.** The scattering force is calculated and plotted as a function of position for (a) a single laser with LHCP propagating in the $-\hat{x}$ direction, (b) a single laser with LHCP propagating in the $+\hat{x}$ direction, and (c) both lasers present. With both lasers present, a restoring force is realized near $x = 0$.

from these laser beams, the atoms will be both trapped at the center of the MOT and cooled to low temperature. One should note that in the vertical, axial $\hat{z}$ direction, the sign of the magnetic field is the same as the sign of the displacement, and RHCP beams must be used.

2.3.2 Design

The magnetic field required for the MOT is generated by the anti-Helmholtz coils illustrated in Figure 2.25. Square 4 mm $\times$ 4 mm copper wire (with a 2 mm diameter hole at the center for water cooling) is used. This wire is wrapped around a support 100 times, with a 10 $\times$ 10 pattern. The inner radius is 6.1 cm from the vertical axis of the MOT, with the closest edge 8.6 cm away vertically. Each coil is driven with $\sim$ 100 A current by a HP-6683A power supply. Additionally, a HP-6033A power supply is used to drive a bias current through the top coil, allowing one to control the position of the magnetic field zero or to create a bias magnetic field which is useful for laser-cooling Ba^+ ions. With 100 A current driven through the coils, a magnetic field gradient of 60 G/cm is produced in the axial $\hat{z}$ direction with -30 G/cm in the radial $\hat{x}$ and $\hat{y}$ directions is generated.

With 100 A current, the voltage drop over the coils is $\gtrsim$ 20 V, resulting in a power draw of $>$ 2 kW. Due to this heat load, the coils must be actively cooled. To accomplish this, water is pumped through each coil via the hole in the center of the wire. The water is pumped

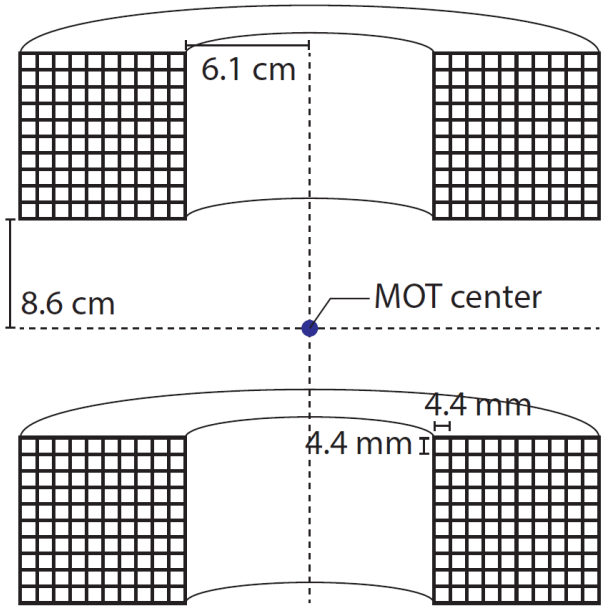

Figure 2.25: **Anti-Helmholtz coil geometry.** A schematic of the coils used to generate the magnetic field for the MOT is shown. Each coil consists of 100 windings. This figure is borrowed from Ref. [Sch16].

through the coils at a pressure of 270 PSI and drops to 40 PSI after passing through the coil. The temperature of the coils is measured using thermocouples attached to the coils that are read by a Omega CN9600 temperature controller. If the temperature exceeds a setpoint, the temperature controller shorts the interlock pins on the HP-6683A power supply, disabling it. Typical temperatures are as high as ~ 65 °C.

The Ca atoms are supplied by an AlfaVakuo AlfaSource (previously known as Alvatec Alvasource) getter. This getter is comprised of a stainless steel tube that contains a source of high-purity Ca in an argon atmosphere, sealed by indium metal. Once the getter is installed in the chamber and vacuum pressures are reached, the getter can be opened, exposing the Ca to the chamber. This is accomplished by running current through the getter to heat it enough so that the indium seal melts and exposes the Ca. The melting of the indium seal can be detected by measuring the vacuum pressure. Once the seal breaks, a spike in the pressure will occur due to the argon being released into the chamber. Such a spike can be

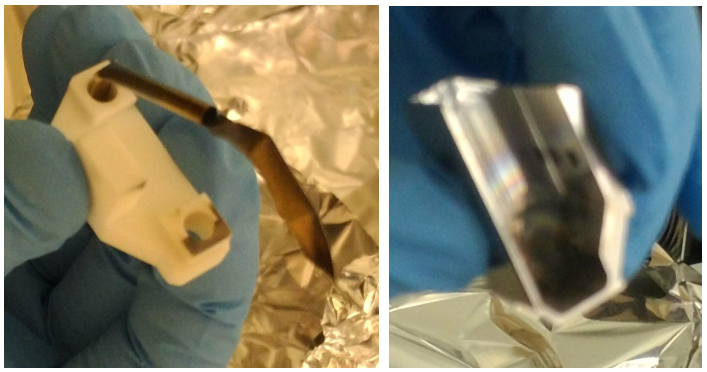

Figure 2.26: **Ca getter and housing.** (left) A photograph of the getter tube is shown with the MACOR housing. (right) A photograph of the mount for the getter is shown. This mount attaches to the LPT.

seen in Figure 2.27. The current through the getter was slowly increased in steps of 0.5 A until a large spike was observed on both a NEXTorr ion pump located near the trap as well as an RGA located farther away through a path with low conductance, resulting in a smaller measured spike. Once the getter seal has been broken, the getter can release Ca atoms by running a current through it. This current, ∼4–5 A, heats the getter, causing Ca vapor to be sprayed out of the hole in the getter tube towards the center of the MOT.

2.3.3 Magneto-Optical Trapping of Ca

Experiments performed in this dissertation use a ^{40}Ca MOT. A level scheme for ^{40}Ca is shown in Figure 2.28. The 423 nm cooling laser drives the $4s4p\ ^1P_1 \leftarrow 4s^2\ ^1S_0$ transition. The $4s4p\ ^1P_1$ state has a lifetime of 4.5 ns and decays back to the ground with high probability. Roughly 1 in 10^5 decays from the $4s4p\ ^1P_1$ state will decay to the $3d4s\ ^1D_2$ state. The $3d4s\ ^1D_2$ state has a lifetime of 1.71 ms [HR86], and decays to the $4s4p\ ^3P_1$ and $4s4p\ ^3P_2$ states, which have a lifetime of 0.331 ms and 118 minutes, respectively [HR86, Der01]. These long-lived states are not in the laser-cooling cycle and may leave the MOT before decaying back to the ground state. To remediate this loss, a 672 nm repump laser is typically used, driving the $4s5p\ ^1P_1 \leftarrow 3d4s\ ^1D_2$ transition. The $4s5p\ ^1P_1$ state can decay to the ground state. It is noted that the $4s5p\ ^1P_1$ state also has decay pathways leading to the metastable

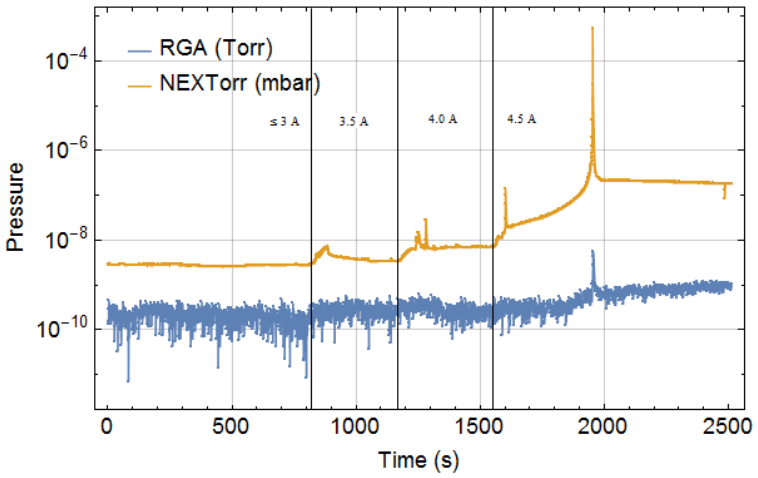

Figure 2.27: **Breaking the indium seal on a getter.** The current driven through an unopened getter was increased in steps of 0.5 A up to 4.5 A until a spike in the vacuum pressure was measured due to the indium seal breaking, releasing the argon gas inside.

$4s4p\ ^3P_J$ states, and other repump transitions may be used which are more efficient. This is discussed further in Chapter 4.

The Ca atoms emitted from the getter source are $\sim$ 1000 K and need to be cooled so that enough can be captured by the MOT of trap depth $<$ 10 K. To accomplish this, two 423 nm "slowing" beams are used, red detuned by 4Γ and 10Γ, where $\Gamma = 2\pi \cdot 34.6$ MHz is the natural linewidth of the cooling transition. The propagation direction of the slowing beams opposes the direction of the hot atoms emitted from the getter.

2.3.4 Fluorescence Imaging

To image the MOT, we use two EMCCD cameras. These cameras are located at two of the 1.33" CF flanges. Relative to the reentrant viewport, these viewports are located 22.5° horizontally away in either direction, and both of them are 16° above the horizontal plane. Two cameras are used rather than one in order to locate the position of the MOT relative to the ions. Further details on the position identification are presented later. These cameras allow one to image the MOT using either fluorescence or absorption imaging.

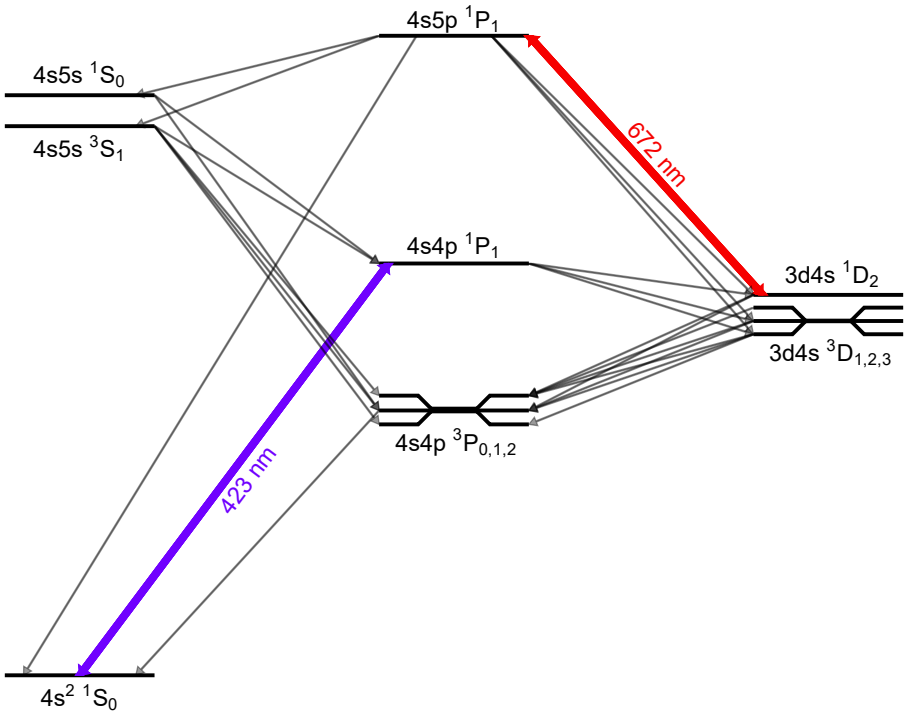

Figure 2.28: **Level scheme of Ca.** A level scheme is shown for ^{40}Ca. The 423 nm cooling laser is shown as a violet arrow and the 672 nm repump laser is shown as a red arrow. The thin gray arrows represent spontaneous decay channels.

Fluorescence imaging takes advantage of the scattered light at 423 nm from spontaneously decaying Ca($4s4p\ ^1P_1$) atoms. Fluorescence imaging is useful for observing not only the position and size of the MOT, but also can give some information about the population fraction in the $4s4p\ ^1P_1$ state. If the atom number and spatial profile is the same for two cases, but the fluorescence is brighter for one case than the other, one knows there must be a larger $4s4p\ ^1P_1$ state population for the case with more fluorescence.

2.3.5 Absorption Imaging

In addition to fluorescence measurement, we can also measure the MOT using absorption imaging. For absorption imaging, a weak laser resonant with the $4s4p\ ^1P_1 \leftarrow 4s^2\ ^1S_0$ transition is shone directly into one of the cameras through a path that crosses the center of the

MOT. A short exposure time of 10 μs is used by using the first order output of an AOM, which can be quickly shut on or off. We compare one such image with the MOT present—we first shut off all cooling lasers to allow the MOT atoms to decay to the ground state—to one without the MOT present. When the MOT is present, some of the laser light will be absorbed by the Ca atoms, reducing the light that reaches the camera.

With no MOT present, the laser will have some intensity distribution which can generically be labeled $I_0(x, y)$ where x and y are the coordinates on the camera image. The MOT density profile is expected to be

$$\rho_{\mathrm{MOT}}(x, y, z) = \rho_0 \exp\left\{\left[-\frac{x^2}{w_x^2} - \frac{y^2}{w_y^2} - \frac{z^2}{w_z^2}\right]\right\} \tag{2.21}$$

where ρ_0 is the peak density, and w_x, w_y, and w_z are the MOT waists in the x, y, and z directions, respectively. When the MOT is present, it will absorb some of the light, and the resulting image will have an intensity profile

$$I(x, y) = I_0(x, y) \exp\left\{\left[-\int_{z=-\infty}^{\infty} \sigma \rho_{\mathrm{MOT}}(x, y, z) \mathrm{d}z\right]\right\} \tag{2.22}$$

where σ is the absorption cross section

$$\sigma = \left(\frac{2j_2 + 1}{2j_1 + 1}\right)\left(\frac{\lambda^2}{2\pi}\right)\left(\frac{A_{21}}{\Gamma}\right) \tag{2.23}$$

where j_1 is the angular momentum of the $4s^2\ {}^1S_0$ state ($j_1 = 0$), j_2 is the angular momentum of the $4s4p\ {}^1P_1$ state ($j_2 = 1$), λ is the wavelength of the $4s4p\ {}^1P_1 \leftarrow 4s^2\ {}^1S_0$ transition, Γ is the natural linewidth, and A_{21} is the Einstein A-coefficient for the $4s4p\ {}^1P_1 \leftarrow 4s^2\ {}^1S_0$ transition (in this case, $A_{21} = 0.99999\Gamma$).

Comparing the intensity measured with the MOT to the intensity measured without the

MOT, one gets the ratio

$$\frac{I(x,y)}{I_0(x,y)} = \exp\left\{\left[-\int_{z=-\infty}^{\infty} \sigma\rho_{\mathrm{MOT}}(x,y,z)\mathrm{d}z\right]\right\}. \tag{2.24}$$

If one were to take the two images and divide one by the other, this is the expected result. For convenience, we define a signal parameter S given by

$$S(x,y) \equiv -\ln\left[\frac{I(x,y)}{I_0(x,y)}\right] = \int_{z=-\infty}^{\infty} \sigma\rho_{\mathrm{MOT}}(x,y,z)\mathrm{d}z. \tag{2.25}$$

Plugging in the MOT density profile from Equation 2.21,

$$S(x,y) = \sigma\rho_0\sqrt{\pi}w_z \exp\left\{\left[-\frac{x^2}{w_x^2} - \frac{y^2}{w_y^2}\right]\right\}. \tag{2.26}$$

At this point, one knows the form $S(x,y)$ should take, and one has the calculated 2D $S(x,y)$ from the image data comparing the two images. With this method, one will not be sensitive to measuring w_z, since the camera image is only 2D. One can make the assumption that the MOT is relatively spherically symmetric and set $w_z = \frac{1}{2}(w_x + w_y)$. By fitting the measured $S(x,y)$ to Equation 2.26, one can determine the fitted peak density ρ_0 as well as the x and y waists w_x and w_y. In software, however, we have observed that fitting functions with two dimensions can be inconsistent or unreliable at times. Instead, we make the fitting more robust by breaking the problem down into two one-dimensional fits. We do this by integrating the signal over one dimension or the other. We define the one-dimensional signals $S_x(x)$ and $S_y(y)$ as

$$S_x(x) \equiv \int_{y=-\infty}^{\infty} S\mathrm{d}y = \sigma\rho_0\pi w_y w_z \exp\left\{\left[-\frac{x^2}{w_x^2}\right]\right\} \tag{2.27}$$

and

$$S_y(y) \equiv \int_{x=-\infty}^{\infty} S\mathrm{d}x = \sigma\rho_0\pi w_x w_z \exp\left\{\left[-\frac{y^2}{w_y^2}\right]\right\}. \tag{2.28}$$

We then typically fit the experimental $S_x(x)$ to fit parameters w_x and amplitude S_{x0}, where $S_{x0} = \sigma\rho_0\pi w_y w_z$. Similarly, we fit the experimental $S_y(y)$ to fit parameters w_y and amplitude S_{y0}, where $S_{y0} = \sigma\rho_0\pi w_x w_z$. The peak MOT density should then be given by

$$\rho_0 = \frac{S_{x0}}{\sigma\pi w_y w_z} = \frac{S_{y0}}{\sigma\pi w_x w_z}. \tag{2.29}$$

While the last two terms should theoretically be equal, the fits of the experimental data typically show small deviations, and we estimate ρ_0 as the average of these two values.

2.3.6 MOT–Ion Overlap

One key parameter necessary for studying interactions between the MOT and the trapped ions is the overlap between the two species. To measure the overlap, we first must know the location of the trapped ions. To do this, we use the two MOT cameras to observe the fluorescence from the ions, and mark the coordinates of the center of the ions for each camera. We then know if the MOT is located on these same coordinates on both cameras, the center of the MOT is aligned with the center of the ions. If the MOT is not perfectly aligned, one must know the position of the center of the MOT to calculate the decreased overlap factor due to the misalignment. We define the x-axis as the LPT axis (north is $+\hat{x}$ and south is $-\hat{x}$ in the lab), the y-axis as the axis with the reentrant viewport and the ToF (west is $+\hat{y}$ and east is $-\hat{y}$ in the lab), and the z-axis is defined as the vertical axis (up is $+\hat{z}$ and down is $-\hat{z}$). Camera 1 is located $\theta = 22.5°$ to the left of the reentrant viewport and $\phi = 16°$ above the horizontal plane. Camera 1 is located $\theta = 22.5°$ to the right of the reentrant viewport and $\phi = 16°$ above the horizontal plane. Both cameras are pointed towards the center of the trap. The coordinates on camera 1 where the ions were located is defined as the null for that camera image, and any difference in position from this null labeled x'_{cam1} and y'_{cam1}. Camera 2 has similar definitions for x'_{cam2} and y'_{cam2}. For camera 1, an object at the trap null $(x, y, z) = (0, 0, 0)$ produces an image on the

camera at $(x_{01}, y_{01}, z_{01}) = (-R\cos\phi\sin\theta, -R\cos\phi\cos\theta, R\sin\phi)$ where R is the distance to the camera. An object away from the trap null produces an image at a slightly different location, which can be determined knowing x'_{cam1}, y'_{cam1}, θ, and ϕ. This small difference in position $(\Delta x_1, \Delta y_1, \Delta z_1)$ is given by

$$\begin{aligned}
\Delta x_1 &= x'_{\text{cam1}}\cos\theta + y'_{\text{cam1}}\sin\phi\sin\theta \\
\Delta y_1 &= -x'_{\text{cam1}}\sin\theta + y'_{\text{cam1}}\sin\phi\cos\theta \\
\Delta z_1 &= y'_{\text{cam1}}\cos\phi.
\end{aligned} \tag{2.30}$$

Similarly, for camera 2, we have

$$\begin{aligned}
\Delta x_2 &= x'_{\text{cam2}}\cos\theta - y'_{\text{cam2}}\sin\phi\sin\theta \\
\Delta y_2 &= x'_{\text{cam2}}\sin\theta + y'_{\text{cam2}}\sin\phi\cos\theta \\
\Delta z_2 &= y'_{\text{cam2}}\cos\phi
\end{aligned} \tag{2.31}$$

with a base position of $(x_{02}, y_{02}, z_{02}) = (R\cos\phi\sin\theta, -R\cos\phi\cos\theta, R\sin\phi)$.

For camera 1, if we measure the center of the MOT at coordinates x'_{cam1} and y'_{cam1}, we can surmise that the position of the MOT should lie on a ray defined by a point at $(x, y, z) = (x_{01}+\Delta x_1, y_{01}+\Delta y_1, z_{01}+\Delta z_1)$ propagating in the direction $\vec{r}_1 = \hat{x}\cos\phi\sin\theta + \hat{y}\cos\phi\cos\theta - \hat{z}\sin\phi$. A similar ray can be defined for camera 2 based on x'_{cam2} and y'_{cam2}. The theoretical intersection of these rays should give the actual 3D position of the center of the MOT. Often, based on an experimental measurement, these two rays will not precisely intersect. Instead, one can find the nearest crossing of these two rays, where the distance between them is minimized. Averaging the position of each ray at this point gives a reasonably accurate determination of the MOT position relative to the center of the ions in 3D, labeled $(x_{\text{MOT}}, y_{\text{MOT}}, z_{\text{MOT}})$, where (0,0,0) corresponds to the center of the ions. This position is

estimated by

$$\begin{aligned} x_{\mathrm{MOT}} &= \sec\Phi\left(\frac{x'_{\mathrm{cam1}}+x'_{\mathrm{cam2}}}{2}\right) \\ y_{\mathrm{MOT}} &= -\csc\Phi\left(\frac{x'_{\mathrm{cam1}}-x'_{\mathrm{cam2}}}{2}\right)\cos\phi \\ z_{\mathrm{MOT}} &= \csc\Phi\left(\frac{x'_{\mathrm{cam1}}-x'_{\mathrm{cam2}}}{2}\right)\sin\phi+\sec\phi\left(\frac{y'_{\mathrm{cam1}}+y'_{\mathrm{cam2}}}{2}\right) \end{aligned} \tag{2.32}$$

where

$$\Phi = \frac{\cos^{-1}\left[1-2\sin^2\theta\cos^2\phi\right]}{2} \tag{2.33}$$

is half of the angle between the two cameras. For our experimental parameters of $\theta = 22.5°$, $\phi = 16°$, and $\Phi = 21.5836°$, the result is

$$\begin{aligned} x_{\mathrm{MOT}} &= 1.0754\left(\frac{x'_{\mathrm{cam1}}+x'_{\mathrm{cam2}}}{2}\right) \\ y_{\mathrm{MOT}} &= -2.6131\left(\frac{x'_{\mathrm{cam1}}-x'_{\mathrm{cam2}}}{2}\right) \\ z_{\mathrm{MOT}} &= 0.7493\left(\frac{x'_{\mathrm{cam1}}-x'_{\mathrm{cam2}}}{2}\right)+1.0403\left(\frac{y'_{\mathrm{cam1}}+y'_{\mathrm{cam2}}}{2}\right). \end{aligned} \tag{2.34}$$

Once the position center of the MOT relative to the center of the ions is known, an overlap factor can be calculated knowing the spatial distribution of each species. The spatial distribution of the ions can vary depending on whether the ions are in a chain, a large crystal, or a large cloud. We generically define this distribution $\rho_{\mathrm{ion,norm}}(x,y,z)$ in a way that is integral-normalized such that $\int \rho_{\mathrm{ion,norm}}\mathrm{d}^3\vec{r} = 1$. We define the MOT density distribution to be amplitude-normalized such that the maximum value is 1 and takes the form

$$\rho_{\mathrm{MOT,norm}}(x,y,z) = \exp\left\{\left[-\frac{(x-x_{\mathrm{MOT}})^2}{w_x^2}-\frac{(y-y_{\mathrm{MOT}})^2}{w_y^2}-\frac{(z-z_{\mathrm{MOT}})^2}{w_z^2}\right]\right\}. \tag{2.35}$$

The overlap Θ is then defined as

$$\Theta = \int \rho_{\text{ion,norm}}(x,y,z)\rho_{\text{MOT,norm}}(x,y,z)\mathrm{d}^3\vec{r}. \tag{2.36}$$

The overlap factor can range from 0 to 1. Additionally, the Greek letter Θ makes an excellent choice for the overlap factor, since it looks like a MOT that is well-overlapped with an ion chain. In certain atom–ion reaction rate calculations, there is a dependence on the density of the neutral species. In these calculations, the average atomic density on the ions can be written as $\rho = \Theta\rho_0$, where ρ_0 is the peak density of the MOT.

2.3.7 Lifetime

One important characteristic of a MOT is its lifetime τ_{MOT}. This parameter describes, on average, how long an atom will remain in the MOT. The atom can exit the MOT due to collisions with a background gas or by falling into a long-lived dark state that is not addressed by the cooling laser, resulting in a lack of trapping that allows the atom to leave the MOT region. For a constant MOT loading rate R_{load} (units atoms/s), there is a loss rate $R_{\text{loss}} = \frac{N_{\text{MOT}}}{\tau_{\text{MOT}}}$ where N_{MOT} is the number of atoms in the MOT. The differential equation equation governing the number of the atoms in the MOT at time t is

$$\frac{\mathrm{d}}{\mathrm{d}t}N_{\text{MOT}} = R_{\text{load}} - R_{\text{loss}} = R_{\text{load}} - \frac{N_{\text{MOT}}}{\tau_{\text{MOT}}}. \tag{2.37}$$

With an initial condition of 0 atoms in the MOT, the solution to Equation 2.37 is

$$N_{\text{MOT}}(t) = \tau_{\text{MOT}}R_{\text{load}}\left(1 - \mathrm{e}^{-t/\tau_{\text{MOT}}}\right). \tag{2.38}$$

An example of such a lifetime measurement is shown in Figure 2.29. With a 453 nm repump laser, the fluorescence of the MOT is measured as a function of time after turning the cooling and repump lasers on. These experimental data are fitted to Equation 2.38, and the fitted

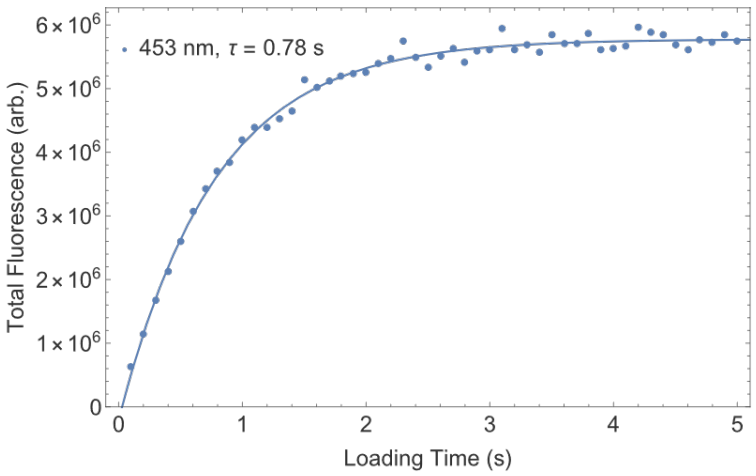

Figure 2.29: **MOT lifetime measurement.** Using a 453 nm repump laser, the lifetime of the MOT is measured by observing the MOT fluorescence as a function of time after turning on the cooling and repump lasers and fitting the data to Equation 2.38.

τ_{MOT} is 0.78 s.

2.3.8 Temperature

The temperature of a MOT can be measured by the ballistic expansion after turning off the cooling lasers. Simply speaking, once there is no trapping or cooling force, the atoms will simply drift away at the velocity they had when the lasers were turned off. If the atoms were cold, this velocity will be low; if the atoms were hot, this velocity will be high. Thus, by measuring the spatial extent of the atom cloud as a function of time, the temperature of the MOT can be determined. Specifically, we measure the spread of the atom cloud along only one direction, the $\hat{x}$ direction, which is the axial dimension of the ion trap. When the MOT is laser-cooled and reaches steady-state temperatures, the spatial profile in the $\hat{x}$ direction is

$$\rho(x, t = 0) \propto \exp\left\{\left[-\frac{x^2}{w_x(t = 0)^2}\right]\right\} \tag{2.39}$$

where $w_x(t = 0) = w_{x0}$ is the MOT waist in the $\hat{x}$ direction at the time when the MOT lasers are shut off ($t = 0$). These atoms have some thermal distribution of velocity v determined by

the temperature T that causes the position of the atoms to drift in time. Some time later, the spatial distribution of the atomic cloud is

$$\begin{aligned}\rho(x,t) &\propto \int \exp\left\{\left[-\frac{(x+vt)^2}{w_{x0}^2}\right]\right\}\exp\left\{\left[-\frac{mv^2}{2k_{\mathrm{B}}T}\right]\right\}\mathrm{d}v \\ &\propto \exp\left\{\left[-\frac{x^2}{w_{x0}^2+2\frac{k_{\mathrm{B}}T}{m}t^2}\right]\right\}\end{aligned} \tag{2.40}$$

where m is the atomic mass and k_{B} is the Boltzmann constant. The entire denominator in the exponent in the second line of Equation 2.40 can be considered as a time-dependent MOT waist $w_x(t)$ such that

$$w_x(t) = \sqrt{w_{x0}^2 + 2\frac{k_{\mathrm{B}}T}{m}t^2}. \tag{2.41}$$

By measuring the expanding waist as a function of time, the experimental data can be fit to Equation 2.41 with T as a free parameter to fit a value for the MOT temperature T.

As this technique requires the free expansion of the atoms, fluorescence detection cannot be used to measure the waist, as fluorescence only occurs when the MOT is actively laser-cooled. Instead, we use absorption imaging to determine the waist of the atomic cloud after some free expansion time t. By repeating this experiment many times and varying t, the data can be fit to Equation 2.41 to determine the MOT temperature T. The results of an example of such a measurement are shown in Figure 2.30. The fitted initial waist is $w_{x0} = 0.46$ mm and the fitted temperature is $T = 4.5$ mK.

The measured temperature is noticeably higher than the Doppler limit (< 1 K for Ca). With strong cooling laser intensity, the minimum temperature will be higher, but this effect is not enough to explain the temperature difference observed for our Ca MOT. In fact, this observation of a higher-than-expected temperature is typical of other alkaline-earth MOTs, where the $J = 0$ ground state precludes the possibility of Sisyphus cooling [OBF99, LBS03, XLS02, XLH03]. The higher temperature must indicate some source of heating. A reasonable explanation for this heating term was not offered until 2005, in Ref. [CMK05].

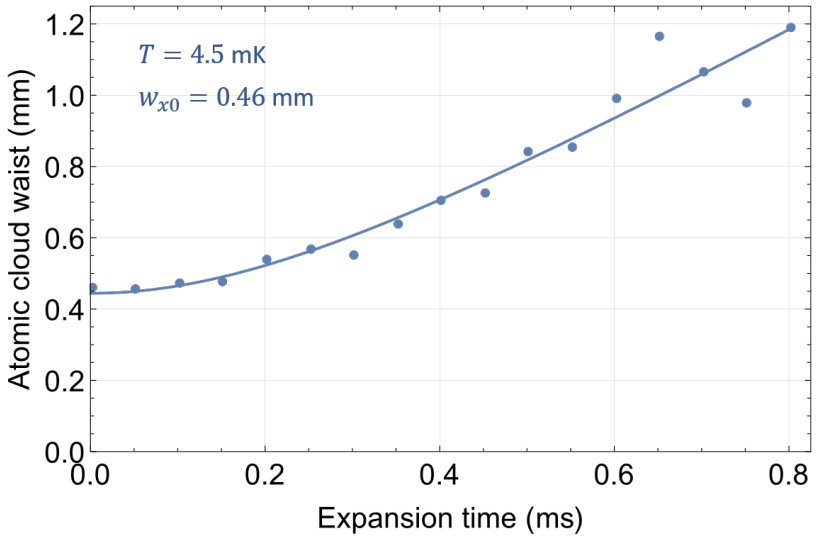

Figure 2.30: **Measurement of MOT temperature by ballistic expansion.** The results of an experiment to measure the MOT temperature using the ballistic expansion technique is shown. The measured MOT temperature is $T = 4.5$ mK.

The explanation can be understood in the following way. Imagine a 1D MOT with an equilibrium position at $x = 0$. If there were an imbalance in the intensities of the two counter-propagating cooling beams, there would be a constant force added to the restoring force of the trap due to this imbalance. That extra constant force would push the MOT off its original equilibrium position to a new equilibrium position $x' \neq 0$. In a realistic laser beam, there will be small fluctuations in the intensity pattern. These fluctuations result in local, microscopic force imbalances. As an atom in a MOT traverses the trapping volume, it will feel randomly varying forces due to these microscopic imbalances. That varying force effectively gives the atom random velocity kicks, resulting in a heating term.

2.3.9 Metastable States

Another important feature of a Ca MOT one must consider is the existence of metastable states. While the $3d4s\ ^1D_2$ state is metastable with a lifetime of 1.71 ms [HR86], one can use a repump laser to prevent a buildup of population in this state. Additionally, the $4s4p\ ^3P_J$ states are metastable. The $4s4p\ ^3P_1$ state is the shortest-lived state among these, with

a lifetime of 0.331 ms. The $4s4p\ ^3P_0$ and $4s4p\ ^3P_2$ states have lifetimes of many minutes, which is much longer than the time it takes for an atom to drift outside of the MOT trapping volume. Thus, any atoms that fall into these states will almost surely be lost from the trap, leading to a loss channel that decreases the lifetime of the MOT. Even atoms that fall into the $4s4p\ ^3P_1$ state may be lost, depending on the MOT temperature and size of the trapping volume.

One may be interested in determining how likely it is that an atom in the $4s4p\ ^3P_1$ state will decay to the ground state and be re-cooled by the lasers instead of being lost. To estimate this, we define a parameter called the "dark lifetime," which describes the amount of time, on average, an atom can remain dark and still be re-trapped when it falls to the ground state and becomes bright again. The restoring force for the MOT does not extend to infinity. Thus, for a given temperature, there will be some critical distance r_c where if a dark atom exceeds this distance, even if the atom becomes bright again the MOT will not recapture the atom. After some time being dark, the probability that an atom is outside this radius gives the probability that the atom will be lost. From the previous section, we know the time-dependent probability density function for the position of an atom that has been dark for time t is

$$\rho(t) \propto \exp\left\{\left[-\frac{r^2}{w(t)^2}\right]\right\} \tag{2.42}$$

where r is the radial distance from the center of the MOT and $w(t)$ is the time-dependent MOT waist (assumed to be spherically symmetric), given by

$$w(t) = \sqrt{w_0^2 + \frac{2k_\mathrm{B}T}{m}t^2} \tag{2.43}$$

where w_0 is the initial MOT waist, m is the atomic mass and k_B is the Boltzmann constant.

The fraction of atoms one can expect to recapture at time t is then given by the probability

$$\begin{aligned} P(r_c, t) &= \frac{\int_0^{r_c} \rho(t) \mathrm{d}^3\vec{r}}{\int_0^{\infty} \rho(t) \mathrm{d}^3\vec{r}} \\ &= \mathrm{erf}\left[\frac{r_c}{w(t)}\right] - \frac{2r_c \exp\left\{[-\frac{r_c^2}{w(t)^2}]\right\}}{\sqrt{\pi} w(t)}. \end{aligned} \tag{2.44}$$

This probability can be measured in the lab—and the capture radius r_c determined—by the following procedure:

1. Perform ballistic expansion experiment to determine w_0 and T
2. Make a stable MOT
3. Take a fluorescence image
4. Turn off cooling beams and slowing beams
5. After some amount of "dark" time t, turn the cooling beams back on, but leave the slowing beams off (to minimize the amount of new atoms loaded in)
6. Wait some amount of time for MOT to contract back to its normal size ($\sim$10 ms)
7. Take fluorescence image to determine the amount of atoms recaptured in the MOT
8. Repeat steps 2–7 for various values of t
9. Plot the resulting fraction recaptured (by comparing before and after images) as a function of dark time
10. Fit the results using Equation 2.44, allowing for the capture radius r_c to be a free parameter

We performed such an experiment on September 25, 2017. It should be noted that the initial MOT waist w_0, temperature T, and capture radius r_c all change based on cooling laser

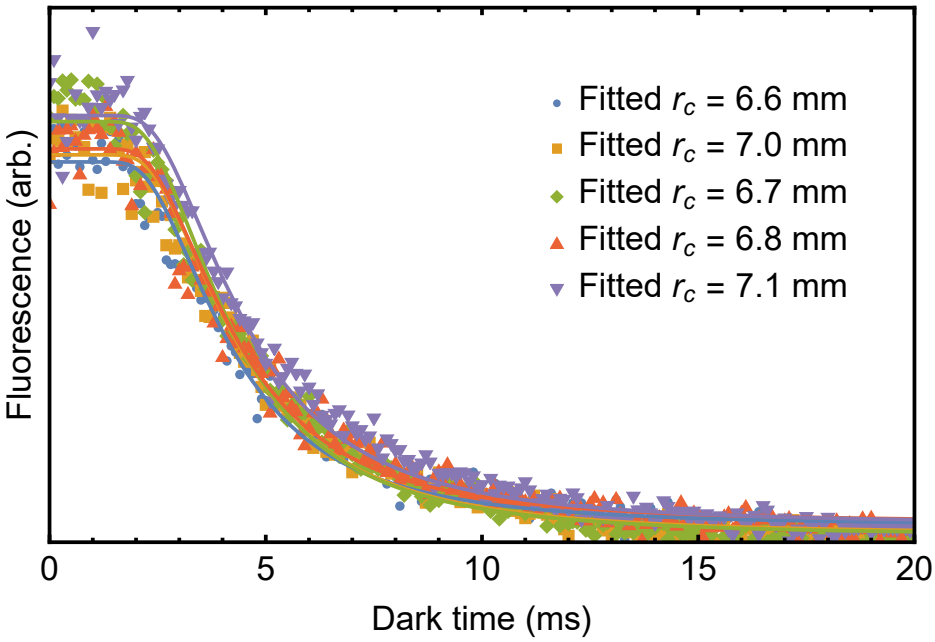

Figure 2.31: **Dark lifetime experimental data.** The results of an experiment detailed in this section are presented. After a variable "dark time" with the MOT lasers turned off, the cooling beams (but not the slowing beams) are turned back on, and the resulting MOT fluorescence is measured. Fluorescence data are shown as points, and fits to Equation 2.44 are shown as lines. Each data point represents a measurement detailed by steps 2–7.

power, detuning, and alignment, so the results of this experiment are not completely general. Rather, they give a representative example of experimental conditions. Ballistic expansion measurements yielded $w_0 = 0.466$ mm and $T = 5.15$ mK. Steps 2–10 were repeated five times, and the fitted values of r_c are shown in Figure 2.31. As expected from Equation 2.44, almost no atoms are lost for short dark times ($\lesssim 2$ ms). Intuitively, this is due to the fact that the initial MOT waist ($w_0 = 0.466$ mm) is much smaller than the average capture radius ($r_c = 6.9$ mm), and based on the MOT temperature ($T = 5.15$ mK), it takes some amount of time to reach a similar size. This technique is essentially a release-recapture measurement. In a typical release-recapture measurement, the capture radius r_c is known and the MOT temperature T is determined. Here, we instead first measure the MOT temperature, and use this information to determine the capture radius.

Based on these experimental results, one would expect an atom decaying into the $4s4p\,^3P_1$

state (with a lifetime of 0.331 ms), to most likely decay to the ground state, where it can be laser-cooled, before exiting the MOT region. This information is valuable when simulating the behavior of the MOT. Additionally, the presence of these dark, metastable atoms can be important to certain reactions (see Chapter 5). Additionally, the overlap factor Θ determined for the MOT will not necessarily be accurate for these metastable states; these states are not laser-cooled, and ballistically expand according to their "dark time." To determine the average overlap for a dark, metastable state, we must consider the time-dependent peak density $\rho_0(t)$ and waist $w(t)$ of these atoms. The waist for a given dark time can be determined by Equation 2.41, and the peak density can be determined from this waist; as the dark atom spatial distribution ballistically expands, its peak density decreases. In a reaction, the relevant quantity to consider is the product of the overlap and the peak density. The average value for this quantity for these states can be determined by

$$\langle \Theta(t)\rho_0(t) \rangle = \int_0^{t_f} \Theta(t)\rho_0(t)\mathrm{d}t \tag{2.45}$$

where t_f is the final time considered. For $4s4p\ ^3P_1$, one can estimate the average product of overlap and density using t_f =0.331 ms, which is the average lifetime of the state. For a more thorough analysis, one could perform an integral of Equation 2.45 over all possible values of t_f, weighted by the probability density function for the lifetime of the $4s4p\ ^3P_1$ state. For the $4s4p\ ^3P_0$ or $4s4p\ ^3P_2$ states, one can use $t_f = \infty$. As $w(t) \to \infty$, $\Theta(t) \to 1$. According to Equation 2.41, for large dark time, the waist increases linearly with time. As the peak density scales as $w(t)^{-3}$, $\rho_0(t) \propto t^{-3}$ and the integral converges.

For $4s4p\ ^3P_1$ and $4s4p\ ^3P_2$, the effects described thus far do not offer a complete explanation of realistic experimental behavior. One effect so far neglected is the magnetic trapping of certain Zeeman sublevels of the atoms in these states due to the magnetic field produced by the anti-Helmholtz coils. This effect is discussed in detail in the following subsection.

2.3.10 Magnetic Trapping of Metastable Ca Atoms

The magnetic field produced by the MOT coils is

$$\vec{B}(x,y,z) = \alpha\left(-(x-x_0)\hat{x} - (y-y_0)\hat{y} + 2(z-z_0)\hat{z}\right) \tag{2.46}$$

where $\alpha \approx 30$ G/cm is a constant depending on the coil geometry and current, and the position (x_0, y_0, z_0) is the location of the magnetic field zero. The null position (0,0,0) is defined as the center of the ions. Typically, $x_0 = y_0 = 0$, and $z_0 \sim$1 mm in order to minimize the CPT effects on the Ba^+ ions. The metastable atoms in this magnetic field have a potential energy of

$$V_{\text{mag}} = -\vec{\mu}\cdot\vec{B} = \frac{\mu_{\text{B}} g}{\hbar}\vec{J}\cdot\vec{B} = \frac{\mu_{\text{B}} g}{\hbar} m_J B \tag{2.47}$$

where $\vec{\mu}$ is the magnetic moment of the atom, μ_{B} is the Bohr magneton, g is the Landé g-factor, $\hbar$ is the reduced Planck constant, and $\vec{J}$ is the angular momentum of the atom.

The $4s4p\ ^3P_0$ state has $J = 0$ and cannot be trapped by this effect. The $4s4p\ ^3P_1$ state does interact with the magnetic field, but the lifetime is short, so we focus on the $4s4p\ ^3P_2$ state in this discussion. The Zeeman sublevels with a positive projection of $\vec{J}$ along the magnetic field direction ($m_J = +1$ and $m_J = +2$) have a lower potential energy for a lower magnitude of the magnetic field, and are "low-field-seeking," feeling a force towards the magnetic field zero. These sublevels will be attracted to the magnetic field zero and can be trapped. Similarly, $m_J = -1$ and $m_J = -2$ will be high-field-seeking, and will be anti-trapped, pushed away from the magnetic field zero. The sublevel $m_J = 0$ feels no force due to this effect.

The spatial distribution of these magnetically trapped atoms can be determined from

Equation 2.47 and takes the form

$$\rho(x,y,z) \propto \exp\left\{\left[-\sqrt{\frac{(x-x_0)^2+(y-y_0)^2+4(z-z_0)^2}{w^2}}\right]\right\} \tag{2.48}$$

where w is some characteristic waist. To measure this experimentally, absorption imaging can be used. As the $4s4p\ ^3P_2$ state does not absorb at 423 nm, these atoms first must be pumped to the ground state. To accomplish this, we drive the $4s4d\ ^3D_2 \leftarrow 4s4p\ ^3P_2$ transition at 446 nm. The $4s4d\ ^3D_2$ state decays to the $4s4p\ ^3P_1$ state with high probability (75.8% calculated), with most of the remaining probability decaying back to the $4s4p\ ^3P_2$ state (24.0% calculated) [MPY17]. After pumping for a short time, the vast majority of the magnetically trapped atoms are in the ground $4s^2\ ^1S_0$ state. Before the atoms significantly ballistically expand, an absorption image is performed.

Compared to Subsection 2.3.5, a slightly different treatment must be made when analyzing absorption image data from a magnetic trap, due to the different spatial distribution. The signal parameter S for a magnetic trap is

$$S = w\sigma\rho_0 \frac{\sqrt{(x-x_0)^2+(y-y_0)^2}}{w} \mathrm{K}_1\left[\frac{\sqrt{(x-x_0)^2+(y-y_0)^2}}{w}\right] \tag{2.49}$$

where $\mathrm{K}_1[x]$ is the modified Bessel function of the second kind, σ is the absorption cross section, and ρ_0 is the peak density. The resulting one-dimensional signals $S_x(x)$ and $S_y(y)$ are

$$S_x(x) = \pi\sigma\rho_0 w^2 \left(1+\frac{|x|}{w}\right) \exp\left\{\left[-\frac{|x|}{w}\right]\right\} \tag{2.50}$$

and

$$S_y(y) = \pi\sigma\rho_0 w^2 \left(1+\frac{|y|}{w}\right) \exp\left\{\left[-\frac{|y|}{w}\right]\right\}. \tag{2.51}$$

Due to the relatively low density and number of atoms in the magnetic trap, we have observed that it is difficult to directly measure the atoms through absorption imaging in

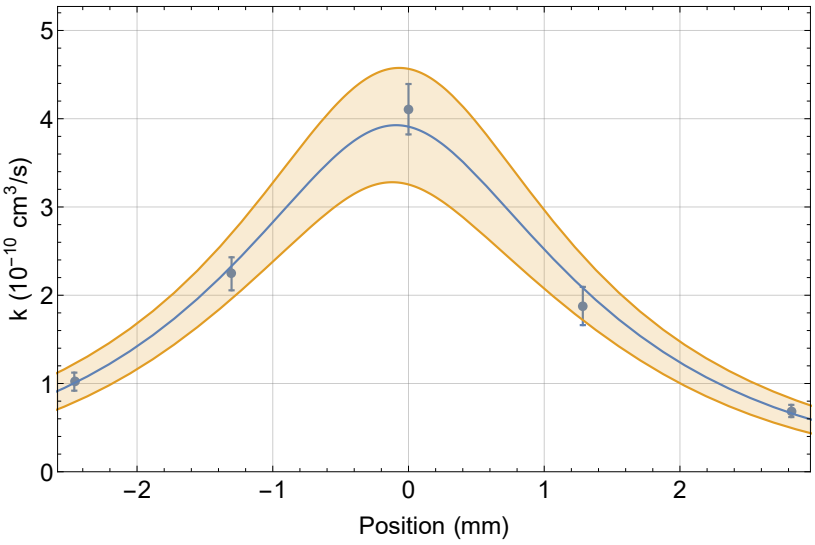

Figure 2.32: **Ion reaction rate with magnetically trapped atoms as a function of position.** The reaction between magnetically trapped Ca($4s4p\,^3P_2$) atoms and $BaCl^+$ ions is measured as a function of the ion axial position. This spatially varying rate is a measurement of the spatial extent of the magnetic trap.

this way. To measure the spatial extent, we instead observe reactions between the magnetic trap and $BaCl^+$ molecular ions and vary the position of the ions. The results of such an experiment, where the ion position is varied along the LPT axis, are shown in Figure 2.32. The fitted magnetic trap waist is $w \approx 1$ mm.

To determine the total number of atoms in the magnetic trap we use fluorescence imaging. First, the MOT cooling and slowing beams are extinguished, then we wait long enough that the MOT dissipates and only the magnetically trapped $4s4p\ ^3P_2$ atoms remain. Then, the MOT cooling lasers, but not the slowing lasers are turned on simultaneously with the 446 nm pumping beam. The $4s4p\ ^3P_2$ atoms are optically pumped into the $4s4p\ ^3P_1$ state which decay to the ground state and are laser-cooled. The fluorescence of the laser-cooled atoms are then measured. To calibrate this fluorescence measurement, we compare the MOT fluorescence with an absorption image to be able to convert from fluorescence to the number of atoms measured by absorption imaging—which is more reliable for the normal MOT. Based on the resulting fluorescence, and knowing what the capture radius of the MOT is,

the total number of magnetically trapped atoms can be estimated. Additionally, by varying the delay time after the MOT has been extinguished, the lifetime of the magnetic trap can be measured. This lifetime has been observed to vary day-to-day somewhat, but is typically ~ 1 s.

2.4 Time-of-Flight Mass Spectrometer

The time-of-flight mass spectrometer (ToF-MS or simply ToF) integrated with our ion trap is an invaluable tool, allowing one to simultaneously measure the relative amounts of different species in the trap by their mass-to-charge ratio. The apparatus has been described in detail in Refs. [SCR12, SSC14, SSY16]. In this chapter I describe the principles of operation, overview the technical details of the ToF system, and elaborate on experimental considerations for the operation of the ToF and analysis of its measurements.

2.4.1 Principles of Operation and Design

The basic principle of time-of-flight mass spectrometry is simple: one imparts a mass-dependent velocity on the particles of interest, and measures the arrival time of each particle at a detector some distance away. As different masses will arrive at the detector at different times, one can compare the detector signal at various arrival times to determine the relative amounts of particles of each mass. Specifically, in our system, we are interested in measuring the masses of the ions in our ion trap. As these are charged particles, we can impart a mass-dependent velocity by accelerating the ions through a potential difference ΔV. The electric potential energy $q\Delta V$ will be converted to kinetic energy $\frac{1}{2}mv_{\mathrm{f}}^2$, where q is the electric charge of the ion, m is the mass of the ion, and v_{f} is the final velocity imparted on the ion. Then, the velocity of the ions is given by

$$v_{\mathrm{f}} = \sqrt{\frac{2q\Delta V}{m}} \tag{2.52}$$

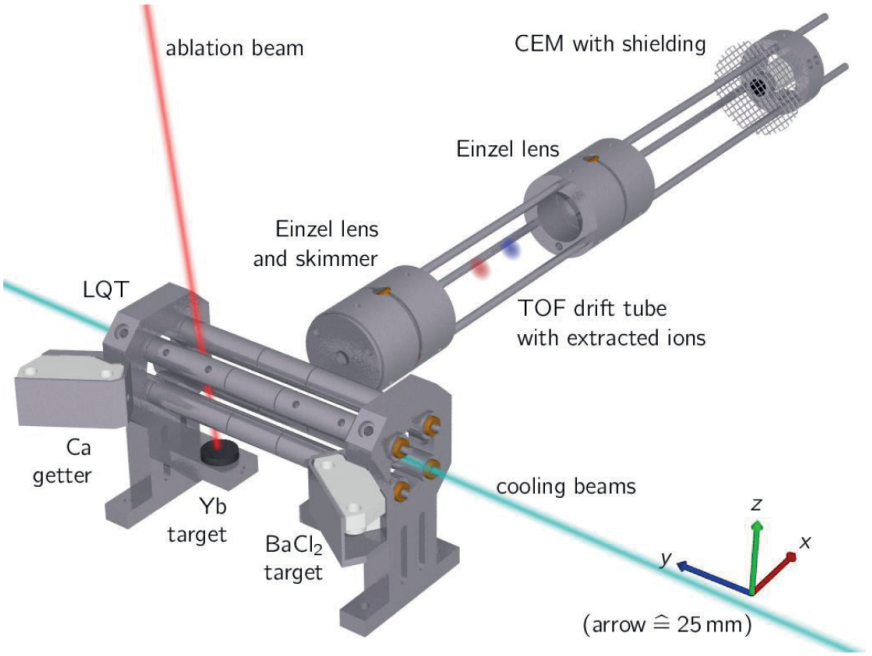

Figure 2.33: **ToF-MS schematic.** A 3D rendering of the ToF-MS integrated with the ion trap. Ions are ejected radially from the ion trap into the ToF drift tube.

resulting in a mass-dependent velocity.

A 3D rendering of the ToF design used in this experiment is shown in Figure 2.33. A simple implementation of ToF-MS would be to simply set the back two rods (the rods furthest from the ToF drift tube) to some high voltage, and set the front two rods (the rods closest to the ToF drift tube) to zero voltage. The ions would be accelerated to a velocity given by Equation 2.52, where ΔV would be the voltage at the position of the ions (approximately halfway between the back and front rods). While this implementation would be simple, there are several drawbacks. Firstly, ions at different radial positions are accelerated through varying potential differences. Ions closer to the back rods would end up with a higher final velocity than the ions closer to the front rods. It is possible to select a specific voltage difference such that the difference in velocity is compensated by the difference in total path lengths for the different ions. In general, however, the required voltage difference to compensate for this effect is problematic for other design constraints.

Secondly, the ejected ions will have some divergence due to initial conditions and ion–ion repulsion. As a result, not all ions will hit the active area of the detector.

To solve the first problem, a two-stage acceleration scheme can be implemented [WM55]. For our apparatus, shown in Figure 2.33, this can be accomplished by applying a voltage V_{back} to the back rods, applying a voltage $V_{\text{front}} < V_{\text{back}}$ to the front rods, and grounding the skimmer, setting the skimmer voltage to $V_{\text{skimmer}} = 0$. By adjusting the voltage difference between V_{front} and V_{back} relative to the difference between V_{front} and V_{skimmer}, the Wiley–McLaren condition specified in Ref. [WM55] can be satisfied, ensuring that the arrival time is insensitive to the initial ion position. Additionally, we control the voltage of the front two rods separately to fine-tune the ion trajectory. Specifically, the back rods (rods α and γ) are at voltages $V_\alpha = V_\gamma = 1386$ V. The voltage on the top front rod (rod δ) is set to $V_\delta = 1209$ V, and the voltage on the bottom front rod (rod β) is set to $V_\beta = 1195$ V.

To solve the second problem, spherical Einzel lenses can be added to the drift tube. Spherical Einzel lenses create a cylindrically symmetric electrostatic potential that focuses a beam of ions without changing the energy of the beam. These lenses are analogous to spherical lenses used to focus a beam of light. Specifically, we use two spherical Einzel lenses. The first Einzel lens roughly collimates the ion beam; however, the axial and radial divergence of the beam are different, so the Einzel lens voltage must be chosen that the approximate collimation is sufficient for both dimensions. The second Einzel lens causes the ion beam to be slightly converging, in order to maximize the probability that an ion will hit the CEM detector. Specifically, the first Einzel lens voltage is set to $V_{\text{EL1}} = 940$ V, and the second Einzel lens voltage is set to $V_{\text{EL2}} = 610$ V.

In summary, by ejecting ions radially, the ions are accelerated by the voltage difference between the back two rods and the front two rods, then are accelerated by the voltage difference between the front rods and the skimmer. After passing through the skimmer, the ions are guided through the drift tube ($\sim$275 mm) by the Einzel lenses until they arrive at the channel electron multiplier (CEM), which is shielded from the drift tube by a stainless

Component	Typical Voltage (V)
Back rods (α and γ)	1386
Top front rod (δ)	1209
Bottom front rod (β)	1195
First Einzel lens	940
Second Einzel lens	610

Table 2.2: **Typical ToF-MS voltages.** Typical values are listed for the high-voltage pulsing on the trap rods upon ejection as well as the constant voltages on the Einzel lenses.

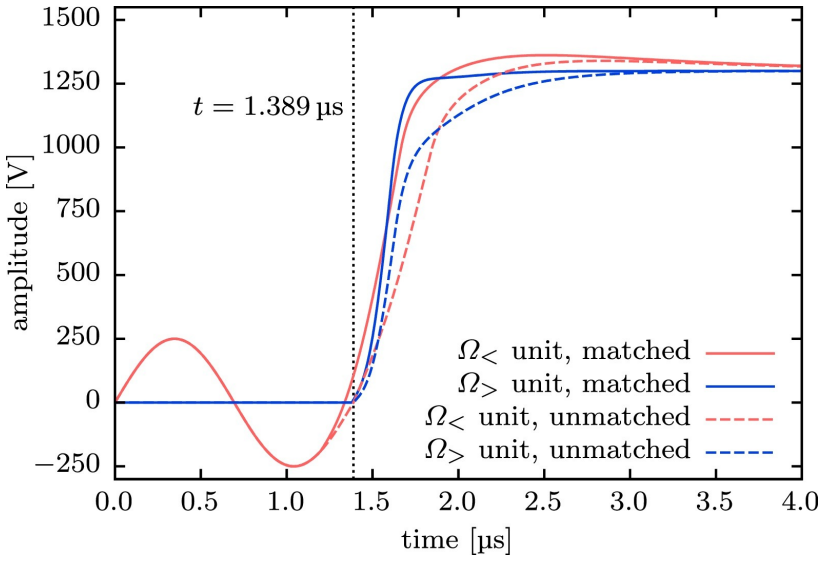

Figure 2.34: **ToF phase matching.** The voltages during a ToF pulse are simulated for two rods, one with rf and one grounded. The rf phase at which the HV pulse begins must be chosen such that the voltage from a grounded rod and an rf rod rise in a similar manner. This figure is borrowed from Ref. [SSY16].

steel mesh. The CEM is a PHOTONIS brand MAGNUM 5901 detector.

2.4.2 Electronics

The electronics for the ToF have been described in detail in Ref. [SSY16]. In this section, I focus on several pragmatic aspects of the electronics. The circuit to add the HV ToF pulse is shown in Figure 2.12. The HV pulse is added to the trap rods on the isolated, HV side of the MOTion drive boards. During a ToF sequence, it is important to turn off the rf and

begin the HV pulse at a precise phase of the rf voltage, so the rod voltages are smoothly ramped up to HV. This is shown in Figure 2.34, where the simulated voltages of two rods are shown for good matching parameters and less ideal matching parameters. When the proper rf phase to begin the ToF HV pulse is chosen, the voltage of an initially grounded rod matches closely with the voltage of an initially rf rod. These voltages can be measured by capacitive pickoffs on the vacuum feedthrough PCBs. These pickoffs allow measurement of the combined rf and HV going directly to the trap rods, with a probe ratio of ∼1000:1. By monitoring these voltages on an oscilloscope, one can optimize the phase and amplitude of the ToF pulses to ensure proper matching. If these voltages are not matched well, the ion trajectory can be perturbed.

2.4.3 Single-Ion Detection

To determine the single-ion ToF detection efficiency experimentally, one can simply laser-cool a single $^{138}Ba^{+}$ ion, eject it into the ToF, and look for a signal. As shown in Figure 2.35, one can distinguish between a detection event or a lack thereof by setting a threshold on the signal voltage. If the signal exceeds this threshold during the time interval where a $^{138}Ba^{+}$ signal is expected, the ion has been detected; otherwise, it has not been detected. Such an experiment was performed on May 19, 2017. During this experiment, the CEM voltage was set to 1700 V. With 45 trials of ejecting a single $^{138}Ba^{+}$ ion into the ToF, there were 15 detection events using a detection threshold of 3 mV, resulting in a $(33 \pm 7)\%$ single-ion detection efficiency. For the 15 trials where an ion was detected, the mean integrated background-subtracted ToF signal from 10.11–10.13 μs was 1.64×10^{-11} V·s with a standard deviation of 1.06×10^{-11} V·s and a standard error of 0.27×10^{-11} V·s. For the 30 trials where no ion was detected, the mean integrated background-subtracted ToF signal from 10.11–10.13 μs was 0.15×10^{-11} V·s with a standard deviation of 0.42×10^{-11} V·s and a standard error of 0.08×10^{-11} V·s.

On Monday, February 11, 2019, upon arriving at the lab in the morning, a scroll pump

failure was observed, leading to a vacuum pressure of order 1 mbar in the chamber. The vacuum pressure was at this elevated value for an unknown amount of time, as high as 60 hours depending on when during the weekend the scroll pump failure occurred. It should be noted that on the night of Sunday, February 10, Prateek Puri dreamt that the chamber had been vented, perhaps warranting further study of this premonition. After this event, the CEM detector became less sensitive to an ion signal. A possible explanation for this is that the elevated pressure in the chamber led to carbon or oxygen contamination of the CEM detector, resulting in a decreased signal amplitude. After this date, the single-ion detection efficiency of the ToF was noticeably changed and found to be dependent on the CEM voltage. The single-ion ToF detection efficiency was measured on July 13, 2020 for several CEM voltage settings. With the CEM at 1700 V, for 9 single-ion attempts, no ions were observed. With 95% confidence, we can limit the single-ion detection efficiency to $< 28\%$. With 1900 V CEM voltage, again on 9 attempts, no ions were detected, limiting the single-ion detection efficiency to $< 28\%$ with 95% confidence. With 2100 V CEM voltage, 20 single-ion ToF ejections were performed, and on 5 of those attempts, an ion was detected, yielding a single-ion ToF detection efficiency of $(25 \pm 10)\%$. In order to improve the statistics, data were taken using small chains of two $^{138}Ba^{+}$ ions. Assuming the ions each have the same chance of detection and that the presence of one ion does not effect the other, we can use these results to derive a single-ion detection efficiency. Using these two-ion chains, 20 ToF ejections were performed, and on 13 of these trials, at least one ion was detected, giving a two-ion detection chance of $(65 \pm 11)\%$. From this chance, we can derive the single-ion detection efficiency, determined to be $(41 \pm 10)\%$. If one makes the assumption that the single-ion detection efficiency can be accurately derived from the two-ion experiment, one can combine these two results, yielding a total single-ion detection efficiency of $(33 \pm 7)\%$ with a CEM voltage of 2100 V. Using a similar technique, the detection efficiency of a five-ion chain is measured at a CEM voltage of 1900 V. The five-ion chain resulted in the detection of at least one ion on 4 attempts out of a total of 10 attempts, yielding a five-

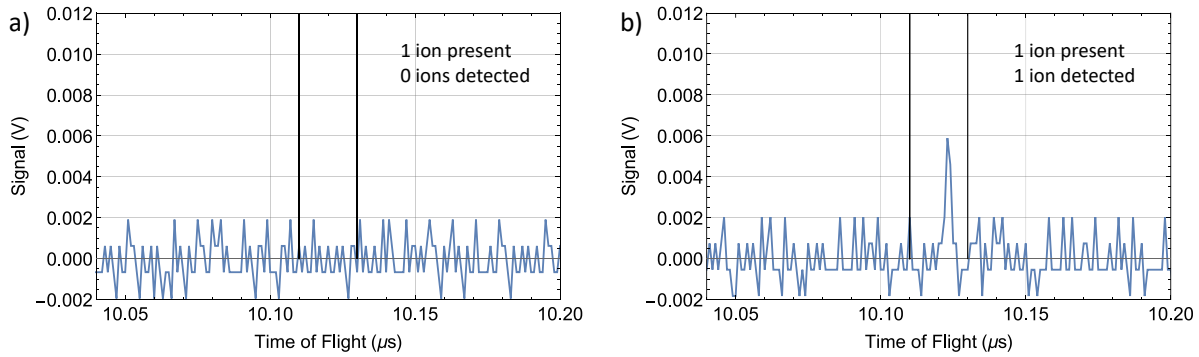

Figure 2.35: **Single-ion ToF signal.** For a single laser-cooled $^{138}Ba^{+}$ ion, a typical ToF signal upon ejection is shown for a CEM voltage of 1700 V. The expected arrival time for a $^{138}Ba^{+}$ ion is between the two vertical black lines. (a) The ion was not detected. (b) The ion was detected. A detection event is defined as a voltage peak clearly above the noise.

ion detection chance of $(40 \pm 16)\%$. From this, the single-ion ToF detection efficiency is determined to be $(10 \pm 5)\%$ with a CEM voltage of 1900 V. The single-ion ToF detection efficiency was measured for a CEM voltage of 2300 V on March 6, 2019. With 41 single-ion ToF ejections, an ion was detected on 11 trials, resulting in a single-ion detection efficiency of $(27 \pm 7)\%$ with a CEM voltage of 2300 V. Of the trials where an ion was detected, the mean integrated background-subtracted signal was 1.87×10^{-10} V·s with a standard deviation of 0.88×10^{-10} V·s and a standard error of 0.28×10^{-10} V·s. This average integrated signal is $\sim 10\times$ larger than the signal measured in 2017 at a lower voltage of 1700 V.

2.4.4 Detector Saturation

The CEM detector ideally provides a constant gain factor, resulting in an output current that is linear with the number of ions detected per unit time. In reality, for large signals, the detector can saturate and the gain factor will be reduced. This saturation can lead to a nonlinearity in the measured signal as a function of ion number. Each ion has charge e and will generate a current on the CEM that is amplified and measured as a voltage pulse on an oscilloscope. The integral of the current as a function of time yields the total charge, and thus the integrated oscilloscope voltage signal versus time is a measurement of the total

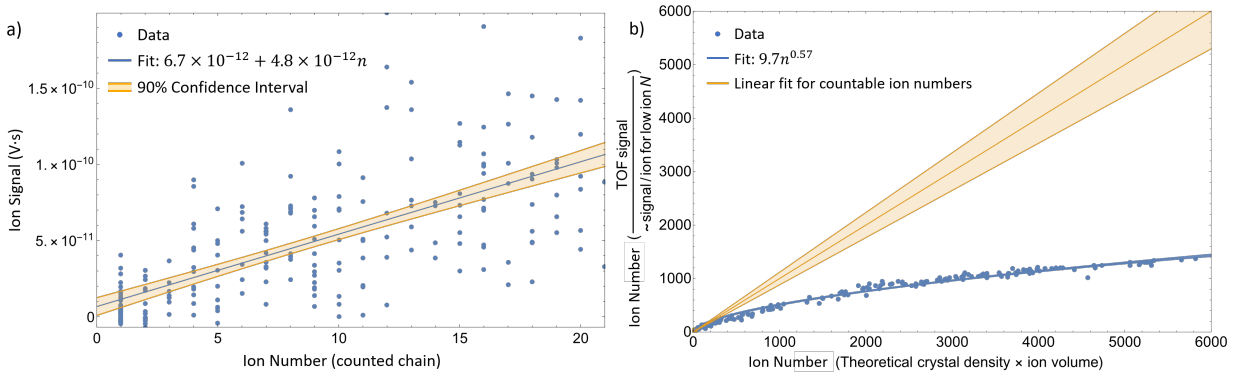

Figure 2.36: **ToF signal for small and large ion crystals.** (a) The integrated ion signal from the ToF as a function of ion number for countable chains. (b) Using the linear fit from (a) to normalize the ToF signal, the number of ions determined by the ToF signal is plotted as a function of the number of ions determined by the crystal volume times the theoretical crystal density for large crystals. The detector saturation causes the data points to fall below the linear fit in yellow.

ion number detected by the ToF. If the saturation is dependent on the output current, as is typical for these detectors, the saturation effect is not constant over a voltage pulse—the effect is more important at the peak of the pulse than it is at the lower-amplitude edges of the pulse. Thus, the saturation effect is not a function of the ion number, but rather the voltage. Comparing two ToF pulses of the same ion number, a hotter sample with a peak widely distributed in time with a lower peak amplitude will not be as affected by the saturation as a cold sample with a shorter time width and a higher peak amplitude.

On May 19, 2017, we attempted to measure the effect of this saturation and correct for it. We make the assumption that the measured voltage at each time step is independent of the measurement at any other time step. That is to say that there is no "dead time" after a large pulse that leads to decreased sensitivity after a large voltage signal. To begin, we measured the integrated ToF signal as a function of ion number for countable ion chains. With low ion number, the saturation effects should be minimized, so this measurement gives a baseline of what the integrated signal should be per ion. A total of 225 trials were performed with ion number varying from 1–20. The results are shown in Figure 2.36a. Any offset for ion

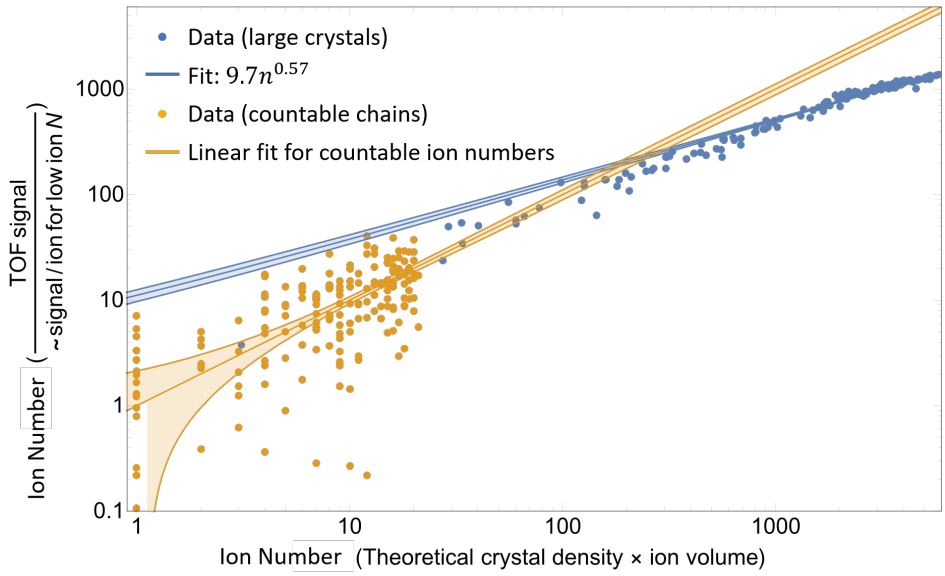

Figure 2.37: **ToF signal as a function of ion number for countable chains and large crystals.** The integrated ion signal for countable chains and large crystals is shown together on a log-log plot. For crystals with ion number $\gtrsim 100$ ions, detector saturation leads to an underestimation of the ion number.

number $n = 0$ can be attributed to imperfect background subtraction of the oscilloscope voltage. Once this baseline is measured, we determine that each ion should produce an additional 4.8×10^{-12} V·s integrated ion signal.

To measure the effect of the saturation, we must use large crystals that are not countable. Instead of relying on counting the ions, we use the fact that a large crystal should have a constant density that can be calculated based on the secular frequency. Using this theoretical frequency and using the camera image to estimate the crystal volume, the total number of ions in a large crystal can be estimated. The ion number of a large crystal can now be measured by the ToF by dividing the integrated signal by 4.8×10^{-12} V·s—although this method is subject to saturation effects—and additionally by observing the volume and multiplying by the theoretical density. We compare these two methods in Figure 2.36b, plotting the ion number determined from the ToF signal as a function of the ion number determined from the ion volume and density. The linear fit from Figure 2.36a is shown

in yellow with the 90% confidence bands. With no saturation, the data should follow this line. A power-law fit is included with the data to guide the eye. For a large crystal of ~ 6000 ions, the saturation leads us to underestimate the ion number by a factor of > 4. The data for countable chains and for large crystals are shown together on a log-log plot in Figure 2.37. For crystals with ion number $\gtrsim 100$ ions, the saturation of the detector leads to an underestimation of the ion number.

To correct for this saturation, we must find a "correction function" to perform on the measured voltage that results in the large-crystal data following the linear fit of the countable-chain data. To reiterate, we cannot use a correction function that acts on the integrated ion signal; we must use a function that acts on the measured voltage. To test a candidate for a correction function, the data is re-analyzed including the correction function acting on the voltage. The results of the large-crystal data are then plotted against the linear fit for the countable-chain data, similar to Figure 2.37. A power-law fit of the form an^b, where a and b are free parameters, is performed on the large-crystal data. If the correction function is perfect, the fit will yield $a = 1.0$ and $b = 1.0$.

The form of the correction function was arbitrarily chosen to be

$$V_{\text{cor}} = \exp\{[c_1 V^{c_2}]\} \tag{2.53}$$

where V_{cor} is the corrected voltage signal, V is the original voltage, and c_1 and c_2 are free parameters. By setting $c_1 = 41.9543$ and $c_2 = 1.9765$, the resulting data for large crystals fits well with the linear fit based on the countable chains. The results are plotted in Figure 2.38. Using this correction function, a high degree of linearity is achieved. A power-law fit to the large-crystal data yields $1.00002n^{1.00031}$. An example of this correction function acting on the voltage signal from the ToF is shown in Figure 2.39, where a peak from $^{138}Ba^+$ is shown both with and without the correction function acting on the voltage. For low voltage, the correction function has little effect. For higher voltage, the correction function leads to a

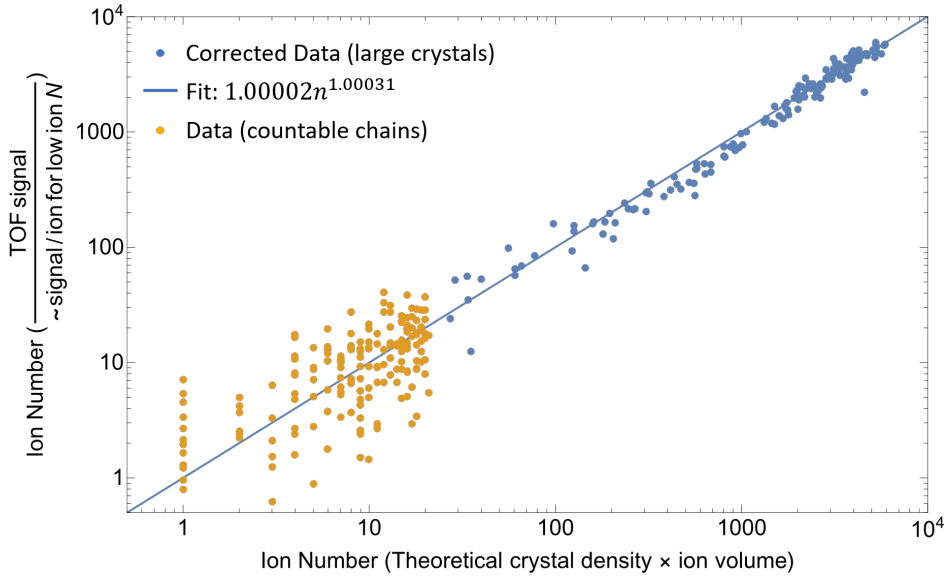

Figure 2.38: **Corrected ToF signal.** Using the correction function given by Equation 2.53, the ion number determined by the ToF signal matches well with the ion number determined by the ion volume and theoretical crystal density.

significant change in the voltage.

While this correction function performs well, the gain of the detector may change somewhat over time, and using a different CEM voltage results in a different correction function being ideal. As such, these results are not completely global. To ensure the highest accuracy, a new calibration should be done when the CEM voltage is changed.

2.4.5 Mass Calibration

To determine the mass of an unknown ion species based on its arrival time, the ToF must first be calibrated with known masses. To accomplish this, we use the known species of Ba^+, $BaOH^+$, and $BaCl^+$, the last of which has two main isotopologues from the main isotopes of Cl. The fitted arrival time (in units μs) as a function of the ion mass (in units Dalton) is

$$t_{\mathrm{ToF}} = 0.75\sqrt{m} + 1.30 \tag{2.54}$$

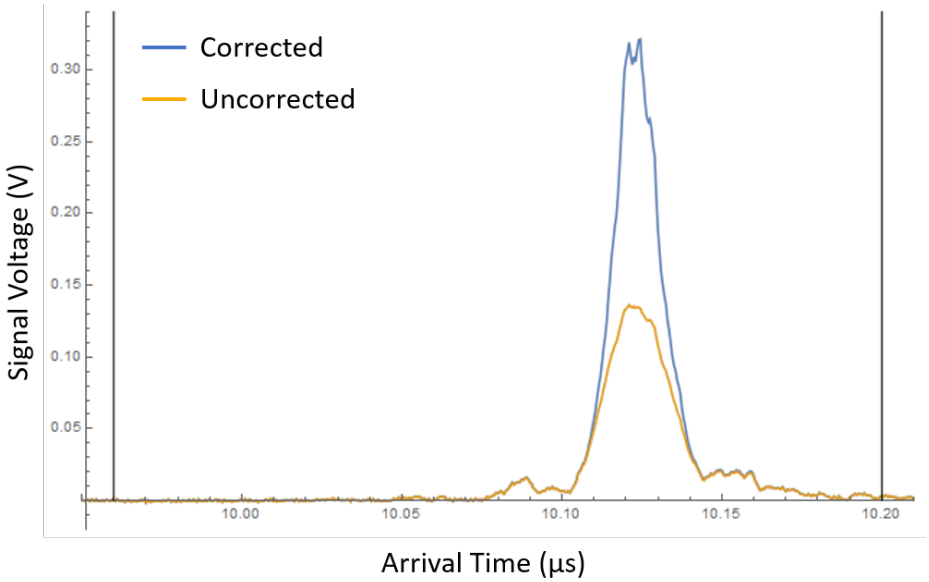

Figure 2.39: **Corrected ToF voltage.** Using the correction function given by Equation 2.53, an example ToF signal is shown for a $^{138}Ba^{+}$ peak. For low voltage, the correction function makes almost no change. For higher voltage, the correction is significant.

where m is the ion mass and 0.75 and 1.30 are fitted values of free parameters. By inverting this equation, one can find the mass of an unknown species based on its arrival time t_{ToF}.

2.5 Controlled Gas Leak System

It is often beneficial to have the ability to leak a gas into the chamber in a controlled way. To this end, a controlled gas leak system has been added to the chamber. This system is shown schematically in Figure 2.41. This system consists of a primary and secondary side.

On the primary side, the gas of interest—typically CH_3Cl—is present at a pressure $\sim$ 10mbar. This pressure is monitored by a Pirani gauge (MKS 103170014SH). A scroll pump (Agilent IDP-3) is present on the primary side to pump down before introducing the CH_3Cl to enable a high-purity gas. The scroll pump is not typically active outside of this initial procedure. As CH_3Cl is a toxic gas, a gas sampling bag is attached to the output of the scroll pump to capture any pumped CH_3Cl. Additionally, a lecture bottle of N_2 is present

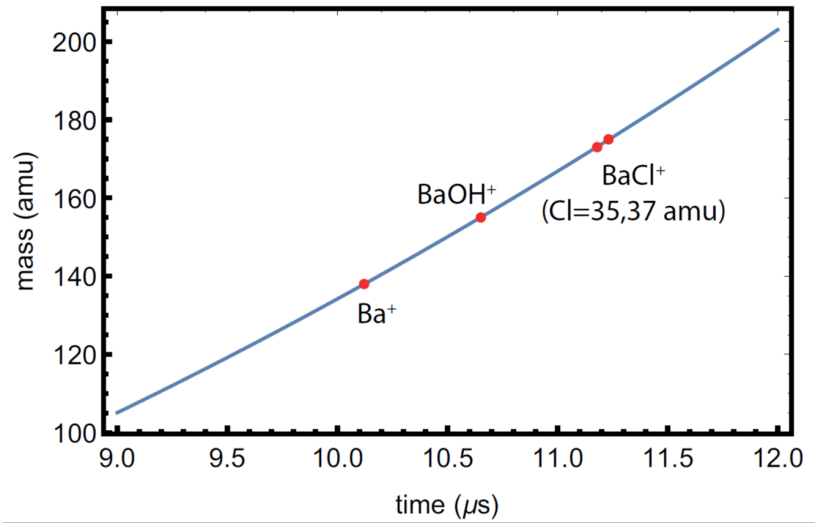

Figure 2.40: **ToF mass calibration.** To calibrate the mass-dependent arrival time of the ToF, the known ion species of Ba^+, $BaOH^+$, and $BaCl^+$ are used.

to allow one to purge any remaining CH_3Cl from the primary side if necessary.

The secondary side is connected to the main chamber with the MOTion trap by a gate valve. In this way, the entire controlled gas leak system can be baked before opening to the main chamber. A turbomolecular pump (Agilent TwisTorr 304FS), backed by a scroll pump (Agilent SH-100), is present to pump excess gas from the secondary side and to bring the controlled gas leak system to pressure $\sim 10^{-7}$ mbar before opening the gate valve to the MOTion chamber. To measure the total pressure on the secondary side is a hot cathode gauge (MKS 100005980). To measure the relative quantities of different gases, a residual gas analyzer (RGA) is also present in the secondary side (SRS RGA200).

Connecting the primary and secondary side is a piezoelectric gas doser (Oxford Applied Research PLV1000). This device essentially acts as a leak valve where the opening is actuated by a piezoelectric crystal stack, which, when extended, lifts a ceramic plunger that otherwise seals the valve. This stack is tightened on the housing with a specific force applied by a nut on the back. Applying too much force causes the doser to be constantly open. Ideally, this nut is tightened so that the force is not enough to open the valve, but is close. Then, by

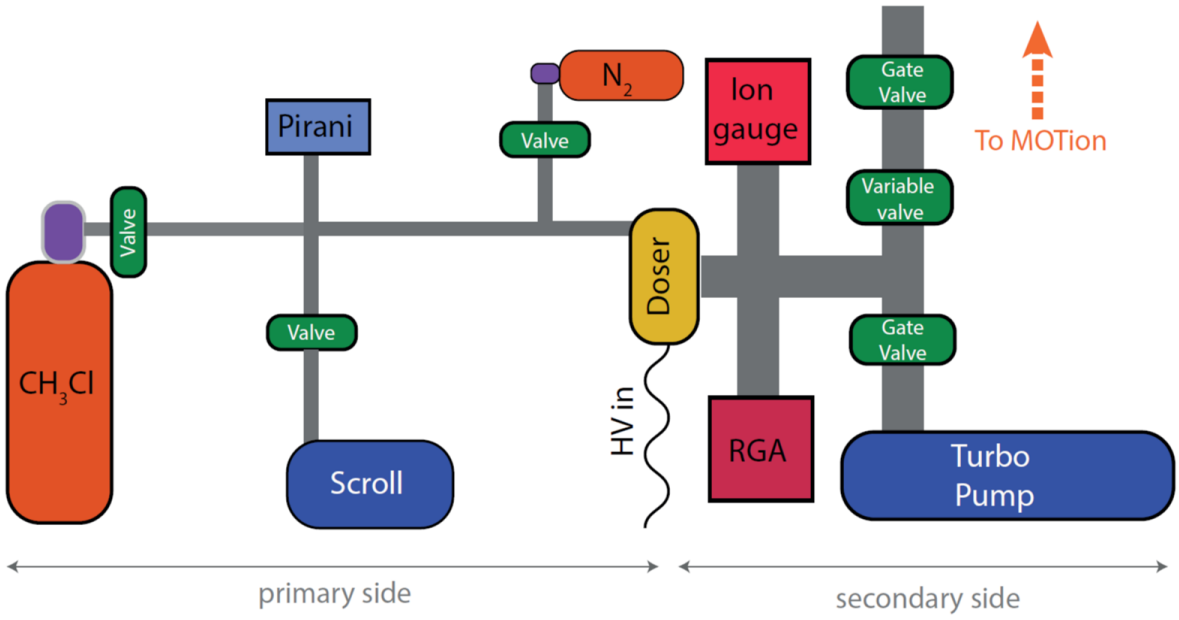

Figure 2.41: **Controlled gas leak system schematic.** An illustration of the controlled gas leak system is shown. For its typical use of forming $BaCl^+$ with reactions between Ba^+ and CH_3Cl, the primary side consists of $\sim$ 10 mbar pressure of nearly pure CH_3Cl. A piezoelectric gas doser allows a controlled amount of CH_3Cl to be leaked to the secondary side to the MOTion trap.

applying a voltage ($<$ 1000 V) to the piezo stack, the valve will open some amount that is controlled by the input voltage, enabling a controlled gas leak rate.

This controlled gas leak system is highly configurable in that the gas can be easily switched out without breaking vacuum. This system is useful for studying chemical reactions in the chamber, but the most common use is for controlled formation of $BaCl^+$. As such, the remaining discussion focuses on leaking CH_3Cl, although the techniques and analysis can be easily extended to other gases of interest.

A typical experiment begins by loading a pure $^{138}Ba^+$ crystal of a desired size using the techniques laid out in Subsection 2.2.8. Then, a controlled amount of CH_3Cl is leaked into the chamber to produce the desired fraction of $BaCl^+$. Sample data for such a procedure are presented in Figure 2.42, where the fractions of Ba^+ and $BaCl^+$, measured by the ToF, are shown as a function of the amount of CH_3Cl leaked into the chamber. The amount of CH_3Cl

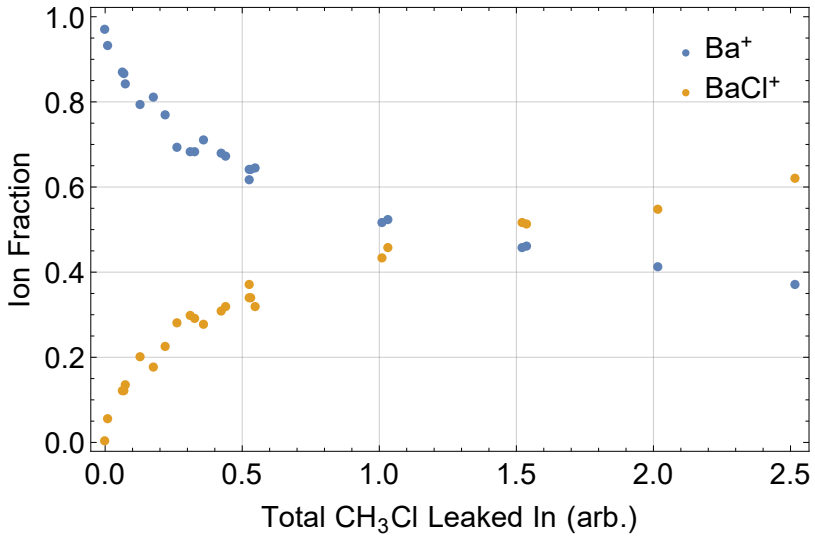

Figure 2.42: **$BaCl^+$ loading curve.** Starting with a pure $^{138}Ba^+$ sample, the Ba^+ and $BaCl^+$ fractions are plotted for various amounts of CH_3Cl leaked into the chamber.

is measured by monitoring the partial pressure at mass 50 amu on the RGA. The RGA measures this pressure at a rate of 2 Hz, and the integrated signal as a function of time gives a total amount of gas leaked into the MOTion chamber. The units on the horizontal axis of Figure 2.42 are actually in 10^{-4} Torr·s, but they have been labeled as arbitrary because the pressure at the RGA is significantly higher than the pressure at the ions, likely by a factor of ~ 100. Even though the precise pressure at the location of the ions is not know, measuring the pressure at the RGA allows the loading of a repeatable fraction of $BaCl^+$. During the leak, typically a constant RGA pressure is held by varying the voltage on the piezo stack to maintain a steady leak rate. This constant leak rate is held until the desired amount of gas has been leaked in, typically on the order of 30 s. Once the target gas amount has been leaked in, the voltage on the piezo is set to zero and the leak is stopped. Typically, it is wise to wait $\sim$10 s after the leak stops to allow any residual gas to be pumped away. Once the leak is completed, a sample with a well-known fraction of $BaCl^+$ is produced. As a ToF measurement can only be performed once during a single experiment, as it is destructive, it is often important to have a well-known $BaCl^+$ fraction at the beginning of an experiment. For this reason, the controlled gas leak system is a very valuable tool in the MOTion trap.

2.6 Lasers

This section is laser-focused.

2.6.1 Homebuilt ECDL Lasers

Many lasers in this experiment are homebuilt external-cavity diode lasers (ECDLs) arranged in a Littrow configuration [HWS01]. The design for each of these lasers is essentially identical. In this configuration, a single-mode laser diode is collimated using an aspheric lens, and the output is directed at a holographic diffraction grating. The grating is aligned so the $m = -1$ order is directed straight back at the laser diode, providing optical feedback. The grating and the back side of the laser diode form an external cavity, with a free spectral range (FSR) typically of order 10 GHz and linewidth typically $\lesssim 1$ MHz. The gain curve of the internal laser-diode cavity set by the front and back surface typically has FSR $\gtrsim 100$ GHz. Combining these two gain curves along with the frequency selectivity of the grating, a single mode can become dominant. The frequency of this single mode is then determined by the length of the external cavity and the grating angle. The frequency of the laser can then be controlled by precise tuning of the grating angle, which is achieved by a piezoelectric actuator (Thorlabs AE0203D08F) integrated into an optomechanical mount (LINOS Lees mount or Thorlabs Polaris mount). The output $m = 0$ order from the grating is reflected by a mirror rigidly attached to the grating mount so the alignment of the output light is insensitive to grating angle to a large degree. In this setup, the laser diode and grating are mounted to an aluminum base which is inside an aluminum enclosure that can be sealed by a rubber gasket. The entire enclosure is placed on a sorbethane sheet which rests on a metal block which sits on sorbethane on the optical table.

Both the laser diode and the aluminum baseplate are temperature-controlled using Peltier thermo-electric coolers (TECs). The laser diode typically needs to be actively cooled to prevent overheating, and the temperature needs to be stable for a stable frequency. The

Laser	Wavelength(s)	Use(s)
Homebuilt ECDL	493 nm	Ba^+ cooling (old)
Homebuilt ECDL	650 nm	Ba^+ repump (old)
Toptica DL pro	493 nm	Ba^+ cooling (new)
Toptica DL pro	650 nm	Ba^+ repump (new)
Homebuilt ECDL	369 nm	Yb^+ cooling
Homebuilt ECDL	935 nm	Yb^+ repump
Homebuilt ECDL	672 nm	Ca repump
Homebuilt ECDL	453 nm	Ca repump
Homebuilt ECDL	446 nm	$Ca(4s4p\ ^3P_2)$ depopulator
Toptica TA-SHG 110	423 nm	Ca cooling
M2 SolStis ECD-X	350–500 nm & 700–1000 nm	Various
Spectra Quanta-Ray	1064/532/355/266 nm	PDL pumping or other
Sirah Cobra Stretch	205–280 nm	Various
Continuum Minilite II	1064 nm	Ablation
AdTech FP QCL	4200–4340 nm	$BaCl^+$ vibrational transition
Thorlabs FP QCL	4360–4450 nm	$BaCl^+$ vibrational transition
Daylight Solutions QCL	3800/7530 nm	$BaCl^+$ vibrational transitions

Table 2.3: **Summary of lasers.** The lasers used in this experiment are listed with their typical wavelengths and primary uses.

baseplate needs to be temperature stabilized to prevent the baseplate from changing the cavity length with temperature drifts—it should be noted that even if the baseplate does not change length, the cavity is sensitive to the temperature and pressure of the air as well. The temperatures of these two components are measured with thermistors and require a temperature controller to maintain a stable temperature. In addition to a temperature controller, these lasers require a low-noise current supply and a piezo driver to vary the voltage (typically 0–150 V) on the piezo to change the grating angle to finely tune the laser frequency. These electronics are typically controlled by either a MOGLabs laser controller or voltage, current, and temperature controllers developed in-house by Christian Schneider and Peter Yu. Wavelength Electronics temperature controllers are also utilized at times. The frequency of these lasers is measured by a HighFinesse WSU-2 wavelength meter.

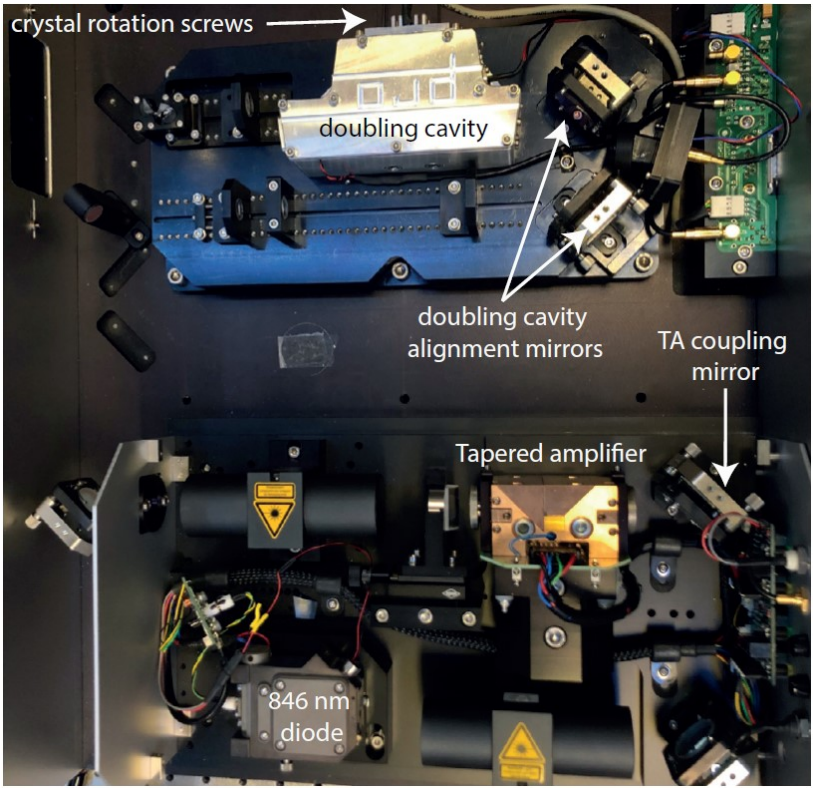

Figure 2.43: **Toptica TA-SHG 110 photograph.** A photograph inside the enclosure of the Toptica TA-SHG 110 is shown. The 846 nm light is amplified by a tapered amplifier and doubled to 423 nm by a bowtie doubling cavity.

2.6.2 Toptica DL pros

The Ba^+ lasers were upgraded to Toptica DL pros in 2019. These lasers are similar in principle to the homebuilt ECDLs, but they offer higher stability than the homebuilt laser design. The control of these lasers is done by Toptica DLC diode laser controllers.

2.6.3 Toptica TA-SHG 110

The Ca MOT cooling laser is generated by a Toptica TA-SHG 110 system. A photograph inside the enclosure of this laser is shown in Figure 2.43. This system begins with an 846 nm laser diode that passes through an optical isolator, then through tapered amplifier (TA) that amplifies the 846 nm laser power to ~ 2 W, followed by another optical isolator. This

light passes through a bowtie doubling cavity with a BBO doubling crystal that doubles the frequency to produce ~ 250 mW of 423 nm light. The doubling cavity is locked by a Toptica PID 110 controller, which modulates the voltage on a piezo on one of the doubling cavity mirrors.

The frequency of the 423 nm laser is locked using a saturated-absorption lock illustrated in Figure 2.44. A portion of the output of the TA-SHG 110 is picked off to be used for the saturated-absorption lock. This is the beam path that passes through the first polarizing beamsplitter (PBS). The relative power used for this beam path is controlled by a half-wave plate (1/2 WP). This beam passes through a 10% beamsplitter and 10% of the beam power is reflected through a Ca vapor cell, illustrated by the lightest beam path. This weak beam acts as the probe beam in the saturated-absorption lock. The remaining beam power is reflected by two mirrors and transmits through another PBS. It is then deflected through a quarter-wave plate (1/4 WP) and passes through an acousto-optic modulator (AOM) labeled "Lock AOM" and the $m = -1$ order is selected and reflected back through the AOM. This beam then passes through the AOM again, and the red-shifted $m = -1$ order of this beam then travels back through the beam path of the incoming beam. This beam traveling in the reverse direction was red-shifted twice by the AOM. For a typical incoming beam frequency of $\omega_0 + 88$ MHz, where ω_0 is the the Ca $4s4p\ ^1P_1 \leftarrow 4s^2\ ^1S_0$ resonance frequency, and an AOM frequency of 88 MHz, the outgoing beam has a frequency of $\omega_0 - 88$ MHz. As this beam passed through a 1/4 WP twice, it will now be reflected by the PBS instead of transmitted. This beam acts as the pump beam in the saturated-absorption lock and is overlapped with the probe beam.

As the name suggests, a saturated-absorption lock relies on the absorption of an atomic species being saturated by a laser. In this case, we consider the overlapped weak probe beam and intense pump beam. In the absence of the pump beam, the probe beam passes through the Ca vapor cell and is absorbed by the Ca atoms if the laser frequency is near resonance. Specifically, the typical frequency of the probe beam will be $\omega_0 + 88$ MHz, so the laser will

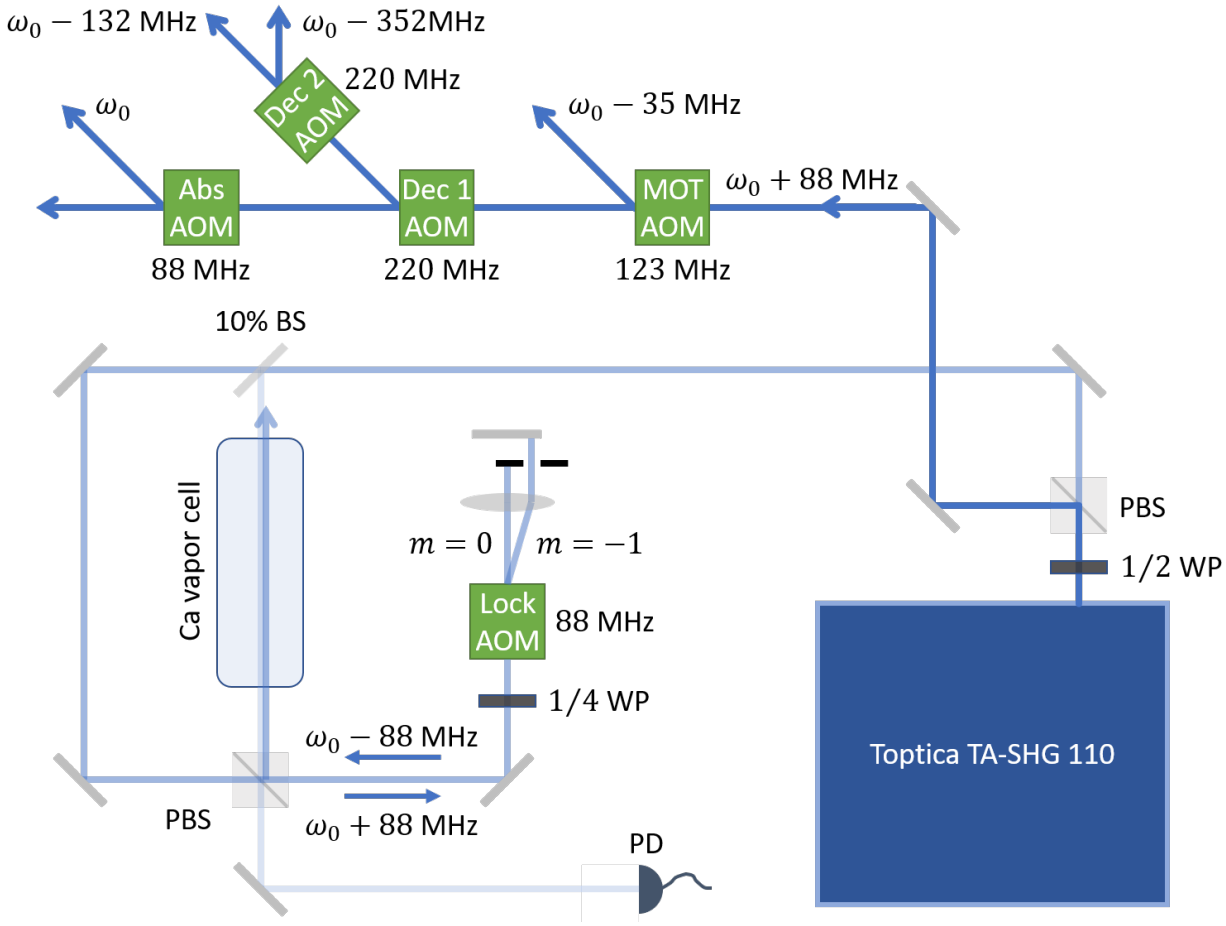

Figure 2.44: **Toptica TA-SHG 110 Laser schematic with saturated-absorption lock and relevant AOMs.** The beam path is illustrated for the 423 nm laser. The dark path represents the main beam path. The medium path corresponds to the light picked off to use in the saturated-absorption lock, including the pump beam. The lightest path is a fraction of light picked off from the medium path used for the probe beam in the saturated-absorption lock. The frequency of different beam paths are labeled, where ω_0 refers to the Ca $4s4p\ ^1P_1 \leftarrow 4s^2\ ^1S_0$ transition resonance. Typical AOM frequencies are listed next to the respective AOMs.

specifically only dress a certain velocity class of Ca atoms—those whose velocity along the laser propagation direction is enough so the Doppler shift cancels out the laser detuning. The power of the probe laser is reduced due to this absorption. If the pump beam is overlapped with the probe beam (with opposite propagation direction), then it will also be absorbed by the same velocity class of atoms only if the pump beam detuning is equal in magnitude but opposite in sign to the probe beam, in this case, $\omega_0 - 88$ MHz. When this is the case, the pump beam, with a significantly higher intensity than the probe beam, will saturate the atoms of this specific velocity class, and the probe beam will no longer be strongly absorbed. As a result, the transmitted probe beam will have more power than if the pump beam was not present. This only happens when the detunings of the pump beam is equal in magnitude and opposite in sign to the probe beam, and given the AOM frequency of 88 MHz, the pump beam will always red-detuned of the probe beam by 2×88 MHz. This means that the only 423 nm output frequency from the Toptica TA-SHG 110 that results in the probe beam *not* being strongly absorbed by the atoms in the Ca vapor cell is $\omega_0 + 88$ MHz. This feature is measured using a photodiode (PD) and used to lock the frequency of the output to $\omega_0 + 88$ MHz.

The frequencies required for the various MOT beams are then generated using AOMs. These AOMs are also illustrated in Figure 2.44. The first AOM (MOT AOM), generates the frequency required for the cooling beams of the MOT, with a detuning of roughly -1Γ from the transition frequency. The deceleration beams are generated by the next two AOMs (Dec 1 and Dec 2 AOMs). These produce the deceleration beams required to slow the hot Ca atoms emitted by the getter and have detunings of roughly -4Γ and -10Γ. The final AOM (Abs AOM) is for absorption imaging. This AOM is set to the same frequency as the saturated-absorption lock AOM to produce resonant light for absorption imaging.

2.6.4 M2 SolStis ECD-X

The M2 SolStis ECD-X laser is a tunable Ti:sapphire laser (Ti:sapph) with an optional bowtie doubling cavity. The Ti:sapph cavity is pumped by a Lighthouse Photonics Sprout G laser, which produces ~ 15 W of laser power at 532 nm. The frequency of the Ti:sapph is coarsely tuned by an intracavity birefringent filter, which can be tilted to change the allowed frequency with a precision on the order of 500 GHz. For more precise tuning, an etalon within the Ti:sapph cavity can be tuned by a piezo to vary the frequency on the order of 100 MHz. Even finer tuning can be performed by a piezo element to vary the length of the cavity. This piezo can be adjusted to lock the frequency of the laser to ~ 1 MHz. If a further reduction in linewidth is necessary, the laser can be coupled into a reference cavity that is able to narrow the linewidth to the ∼kHz level. Typically, this last step is not necessary for the experiments performed in this dissertation. The output can be tuned using these methods over a range of roughly 700–1000 nm with an output power > 2 W.

Additionally, the output frequency can be doubled to 350–500 nm by an attached bowtie doubling cavity with replaceable doubling crystals. Each crystal has a tuning range of ~ 20 nm of the doubled wavelength. The power of the doubled light can reach as high as 1 W.

While this laser does not have a singular purpose, it has been an extremely valuable tool. With an appropriate doubling crystal (if necessary), this laser can typically provide more-than-ample laser power at any wavelength in its range with $\lesssim 1$ hour of tuning. At various times, this laser has been used near the Ba^+ cooling frequency, near the Yb^+ cooling frequency to allow us to simultaneously cool two isotopes, near the Ca cooling frequency to enable control of ultracold ion–neutral interactions, as well as 10 other transitions in Ca, enabling the study of $4s4p\ ^3P_J$ reactions and efficient repump transitions.

2.6.5 Spectra Quanta-Ray

A Spectra Physics Quanta-Ray Lab-170 Series laser is also utilized in this dissertation. This laser is a Q-switched Nd:YAG pulsed laser. The fundamental output of the Quanta-Ray produces a 10 ns pulse with energy ∼750 mJ at a wavelength of 1064 nm with a repetition rate of 10 Hz. A harmonic generation unit housed inside the laser head allows for the frequency of this fundamental output to be doubled to 532 nm (with a pulse energy of $\sim$ 350 mJ) or tripled to 355 nm (with a pulse energy of $\sim$ 150 mJ). Additionally, an external BBO doubling crystal allows the doubling of the frequency of the 532 nm output to 266 nm (with a pulse energy of $\sim$ 50 mJ).

2.6.6 Sirah Cobra Stretch

For a tunable pulsed laser source in the UV, a Sirah Cobra Stretch pulsed dye laser (PDL) is used. This PDL can be pumped by 355 nm or 532 nm pulsed light from the Spectra Physics Quanta-Ray. The wavelength is determined by the laser dye used and the alignment of the gratings in the PDL enclosure. This light is then doubled by one of two BBO doubling crystals. One has an effective range of 205–215 nm doubled light and the other has a range of 215–280 nm. In this way, pulse energies of a few mJ can be produced at a 10 Hz repetition rate over the range of 205–280 nm. This laser is especially useful for driving the A $^1\Pi \leftarrow$X $^1\Sigma^+$ photodissociation transition in $BaCl^+$, which varies over this wavelength range depending on the initial vibrational state of $BaCl^+$.

2.6.7 Continuum Minilite II

The ablation loading of Ba^+, $BaCl^+$, and Yb^+ are achieved using a Continuum Minilite II laser. This is a pulsed, Q-switched Nd:YAG laser that outputs up to 15 mJ per pulse at a wavelength of 1064 nm with a pulse width of 5–7 nm. Typically, the power is kept < 2 mJ to prevent additional coating of the electrodes due to the ablation plume. In addition to

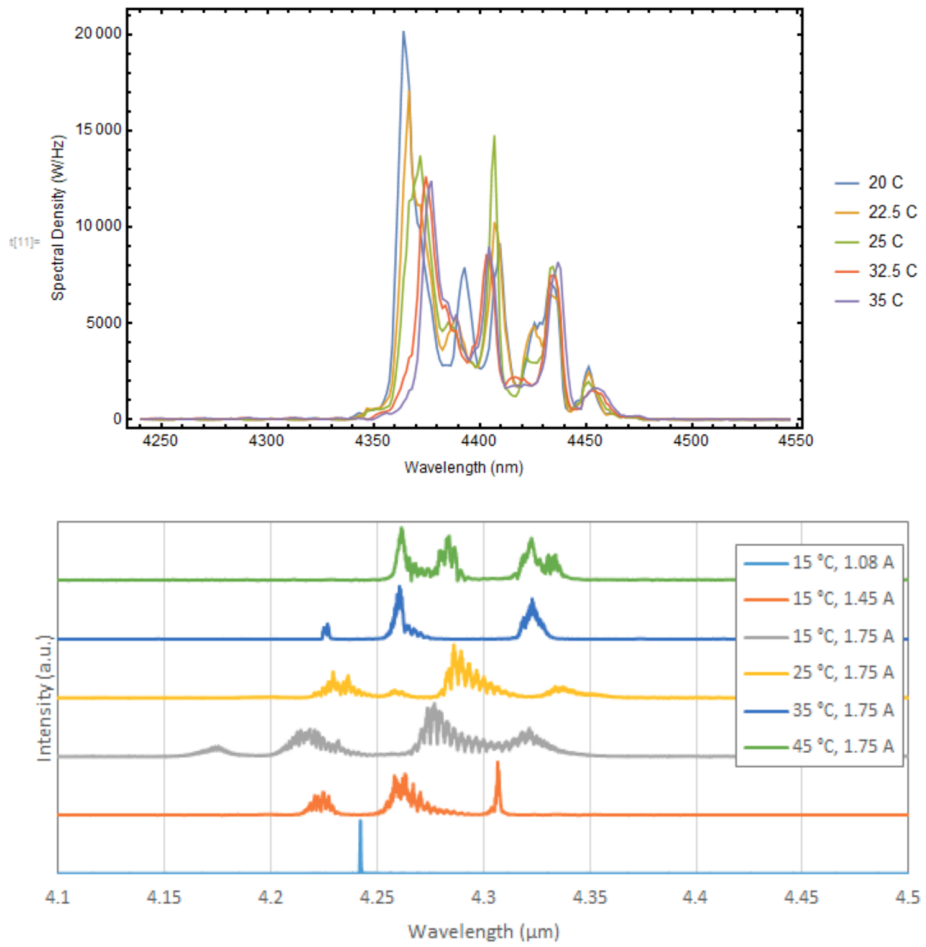

Figure 2.45: **Fabry–Perot quantum cascade laser spectra.** The spectra for both the Thorlabs (top) and Adtech (bottom) QCLs are shown for various temperatures and currents.

ablation, the Minilite flashlamps are used as a reference for timing sequences.

2.6.8 Fabry-Perot Quantum Cascade Lasers

To attempt to drive a vibrational overtone transition (v=7 ← v=0) in the ground electronic state of $BaCl^+$, two Fabry–Perot quantum cascade lasers (FP-QCLs or QCLs) were used. These QCLs are capable of producing high powers (100s of mW) in the mid-infrared (MIR) wavelengths by forming a Fabry–Perot resonator with a quantum cascade material to form a gain medium. One QCL was an AdTech Optics HHL-14-48HP that was loaned from

AdTech. The other QCL is a Thorlabs brand QCL in a two-tab C-mount. These QCLs have a spectrally broad output that varies with temperature and drive current. Example spectra are shown in Figure 2.45. The AdTech QCL has a range of roughly 4200–4340 nm, and the Thorlabs QCL has a range of roughly 4360–4450 nm.

2.6.9 Daylight Solutions QCL

To produce a MIR source with a narrow linewidth and high spectral density, a Daylight Solutions laser system was purchased (M1038-PC-QCL-J0162). This laser is capable of generating $\gtrsim$100 mW power with a linewidth $\lesssim$ 10 MHz with a tuning range of 3650–3850 nm, near the vibrational overtone transition (v=8 $\leftarrow$ v=0) in the ground electronic state of $BaCl^+$. This laser was later modified by Daylight Solutions to generate $\sim$80 mW power at wavelengths of $\sim$7500–8000 nm, near the vibrational overtone transition (v=4 $\leftarrow$ v=0) in the ground electronic state of $BaCl^+$.

CHAPTER 3

Ion–Neutral Interactions

As this experiment relies on the sympathetic cooling of the molecular ions by the neutral atoms in the Ca MOT, ion–neutral interactions are at the core of this dissertation. Simply put, this chapter aims to answer two questions: how often do the atoms and ions collide, and what happens when they collide? As we are primarily concerned with collisions that must reach short range, a semi-classical long-range capture model is typically sufficient to estimate the ion–neutral collision rate. Once an atom and ion reach short range, we are interested in two possibilities: either the atom will sympathetically cool the ion or there will be some reaction. The latter can be destructive for sympathetic cooling, but can be interesting from a chemistry perspective.

3.1 Long-Range Capture Models

To undergo an inelastic or reactive collision, the atom and ion must reach short range. By calculating the rate at which they will reach short range, the maximum rate of these collisions can be determined. The rate at which these species reach short range can be estimated by semi-classical capture models that calculate the rate at which an atom and ion would collide based on the long-range attractive potential. The long-range potential can be expressed as a series expansion in powers of $1/R$

$$V(R) = \sum_n V_n(R) = \sum_n -\frac{C_n}{R^n} \tag{3.1}$$

where R is the distance between the atom and the ion and C_n are long-range coefficients ($C_n > 0$ for attractive potentials).

For many charged–neutral collisions, the dominant potential is the charge-induced dipole potential given by

$$V_4 = -\frac{C_4}{R^4} \tag{3.2}$$

and is referred to as the C_4 interaction or the Langevin interaction [Lan05]. The magnitude of the C_4 coefficient for an atom with polarizability α and a singly-charged ion with fundamental charge e is given by

$$C_4 = \frac{\alpha}{2}\frac{e^2}{(4\pi\epsilon_0)^2} \tag{3.3}$$

where ϵ_0 is the permittivity of free space. For a C_4 interaction including the centrifugal barrier, the total effective potential [CD00] is

$$V_{\text{eff}}(R) = \frac{\hbar^2\ell^2}{2\mu R^2} - \frac{C_4}{R^4} \tag{3.4}$$

where $\hbar$ is the reduced Planck constant, ℓ is the quantized orbital angular momentum of the collision complex such that $\hbar\ell = \mu v b$ where v is the collision velocity, b is the collision impact parameter defined as the distance of closest approach if the colliding partners followed a straight-line trajectory, and $\mu = \frac{m_\text{i} m_\text{n}}{m_\text{i}+m_\text{n}}$ is the reduced mass of the system for ion mass m_i and neutral mass m_n. Each partial wave with angular momentum ℓ will have a different effective potential curve as a function of R. For a collision energy E, the atom and ion will reach short range if $E > V_{\text{eff,max}}$ where $V_{\text{eff,max}} = V_{\text{eff}}(R_{\text{max}})$ is the maximum of the effective potential, which occurs at distance R_{max}.

To determine the value of R_{max} and $V_{\text{eff,max}}$, one sets the derivative of $V_{\text{eff}}(R)$ to zero to

determine $R_{\max}$, which will yield $V_{\text{eff,max}}$.

$$\begin{aligned} \frac{\mathrm{d}}{\mathrm{d}R}V_{\text{eff}} = 0 &= -\frac{\hbar^2\ell^2}{\mu R_{\max}^3} + 4\frac{C_4}{R_{\max}^5} \\ \rightarrow R_{\max} &= \sqrt{\frac{4C_4\mu}{\hbar^2\ell^2}} \end{aligned} \tag{3.5}$$

Using this calculated value of $R_{\max}$, the maximum value of the effective potential is then given by

$$V_{\text{eff,max}} = V_{\text{eff}}(R_{\max}) = \frac{\hbar^4\ell^4}{16\mu^2 C_4} \tag{3.6}$$

for any value of ℓ. For some value of collision energy E, there will be some maximum value of ℓ defined as $\ell_{\max}$ such that $E > V_{\text{eff,max}}$. This is given by

$$\begin{aligned} E &> \frac{\hbar^4\ell^4}{16\mu^2 C_4} \\ \rightarrow \ell_{\max} &= \left(\frac{16\mu^2 C_4 E}{\hbar^4}\right)^{1/4}. \end{aligned} \tag{3.7}$$

Collisions with angular momentum $\ell < \ell_{\max}$ will result in a short-range collision, and collisions with angular momentum $\ell > \ell_{\max}$ will not overcome the centrifugal barrier and will not reach short range.

From $\ell_{\max}$, one can calculate $b_{\max} = \frac{\hbar\ell_{\max}}{\mu v}$ which gives the maximum impact parameter that will result in a short-range collision for a collision energy $E = \frac{1}{2}\mu v^2$. Using this maximum impact parameter, one can define the velocity-dependent short-range collision cross section as

$$\begin{aligned} \sigma_4(v) &= \pi b_{\max}^2 \\ &= \frac{2\pi}{v}\sqrt{\frac{2C_4}{\mu}}. \end{aligned} \tag{3.8}$$

Often, it is convenient to define a thermal rate coefficient $k(T)$ that gives the collision rate per unit atomic density for a given collision temperature T. This rate coefficient for the C_4

interaction is given by

$$k_4(T) = \int_{v=0}^{\infty} v f(v) \sigma_4(v) \mathrm{d}v \tag{3.9}$$

where $f(v)$ is the Maxwell–Boltzmann speed distribution

$$f(v) = 4\pi \left(\frac{\mu}{2\pi k_\mathrm{B} T} \right)^{3/2} v^2 \exp\left\{ \left[-\frac{\mu v^2}{2 k_\mathrm{B} T} \right] \right\} \tag{3.10}$$

where k_B is the Boltzmann constant. For the case of the C_4 interaction, the product $v\sigma_4(v)$ in the integrand of Equation 3.9 is velocity-independent, resulting in a temperature-independent rate, known as the Langevin rate constant, given by

$$k_4 = 2\pi \sqrt{\frac{2C_4}{\mu}} = \frac{e}{2\epsilon_0} \sqrt{\frac{\alpha}{\mu}}. \tag{3.11}$$

A similar treatment can be performed for different C_n interactions, yielding $k_n(T)$ for each of these interactions. The C_4 interaction is unique in that it results in a rate coefficient that is independent of temperature, which is not true for other interactions. Such calculations are presented in Ref. [ZW17]. Other than the C_4 interaction, the C_3 interaction is the most important term in the experiments performed in this dissertation. A C_3 interaction arises from the interaction of an ion with a neutral atom with a quadrupole moment. This can be important for collisions with excited-state Ca atoms with a quadrupole moment, as discussed in Chapter 7.

3.2 Reactions

As the sympathetic cooling of the molecular ions in this experiment relies on collisions with neutral atoms, any possible reactions must be considered that can destroy the molecular ion. These reactions can be broken up into two groups: charge-exchange (CEX) reactions of the form $A^+ + B \rightarrow A + B^+$ and chemical reactions of the form $AB^+ + C \rightarrow A^+ + BC$

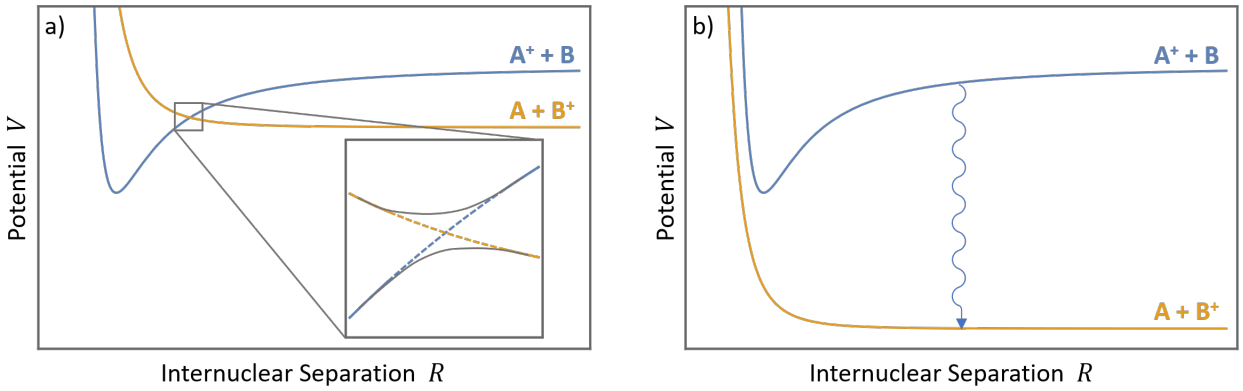

Figure 3.1: **CEX reaction pathways.** (a) For two Born–Oppenheimer (BO) potential curves that cross, there is a breakdown of the BO approximation that results in an avoided crossing, shown in the inset with the BO potentials shown as dashed lines and the adiabatic potentials are shown as solid lines. If the atom–ion pair reaches short range, it can transfer from one BO potential curve to the other, resulting in a CEX reaction. (b) A radiative CEX occurs when the collision complex emits a photon and transfers from the higher BO potential to the lower potential.

for example. Either of these can destroy the $BaCl^+$ molecular ions in this experiment. In addition to the motivations regarding sympathetic cooling, the study of these reactions are of interest as the MOTion trap used in this experiment has access to sub-Kelvin atom–ion interactions with a high level of control of the electronic states of the reactants. As such, certain experiments are possible in this trap that are not accessible to more traditional charged–neutral studies such as flowing afterglow (FA) [FFS69], selected ion flow tubes (SIFT) [AS76], and reaction kinetics in uniform supersonic flow (*cinétique de réaction en ecoulement supersonique uniforme*, CRESU) [RDM84] experiments.

3.2.1 Charge-Exchange Reactions

A CEX reaction is an inelastic collision between two collision partners where the chemical composition remains the same, but an electron is transferred from one species to another. This reaction can proceed by two mechanisms, shown in Figure 3.1. In Figure 3.1a, two Born-Oppenheimer (BO) potentials are shown as a function of internuclear separation between

the two collision partners. At short range, these two BO potentials cross. Due to coupling between these two potentials, the BO approximation [BO27] breaks down near the location of this crossing, leading to an avoided crossing depicted in the inset, where the dashed lines represent the BO potentials and the solid lines represent the adiabatic potentials. This coupling can lead to a transfer from one BO potential to the other, resulting in a CEX reaction. A CEX reaction can also proceed by a radiative process, illustrated in Figure 3.1b. In this example, the collision pair $A^+ + B$ emits a photon and transfers from the upper BO potential to the lower one, resulting in a product of $A + B^+$.

3.2.2 Chemical Reactions

In a chemical reaction, the chemical composition of the reactants changes, not just the charge. In reactions observed in this experiment, typically three or more atoms are involved in these reactions. As such, the potential energy curves are no longer a function of just one coordinate, but rather depend on the distance between each nucleus and all other nuclei. For example, in a reaction such as $AB^+ + C \rightarrow A^+ + BC$, the potential energy is a function of the distance between A and B, defined as R_{AB}, as well as the similarly defined distances R_{AC} and R_{BC}. A BO potential curve is then replaced by a multi-dimensional potential energy surfaces (PES). In the example above, for an exothermic, barrierless reaction, it is possible for the products and reactants to be on the same PES, just with different values of R_{AB}, R_{AC}, and R_{BC}. This would correspond to the collision complex essentially "rolling down a hill" of the PES, rearranging its constituents in a manner with lower potential energy, imparting kinetic energy on the products. As the product PES is the same as the reactant PES in this example, this reaction does not depend on the breakdown of the BO approximation. In a realistic chemical reaction, however, there will likely be avoided crossings of the different PESs, resulting in a breakdown of the BO approximation. Additionally, similar to a CEX reaction, radiative processes can play a role.

3.3 Sympathetic Cooling

In this dissertation, we aim to sympathetically cool $BaCl^+$ molecular ions using collisions with a cold Ca MOT. Molecules have additional complexity compared to atomic species in that there are not only translational degrees of freedom, but internal vibrational and rotational degrees of freedom that must be controlled. Specifically, we aim to produce a significant fraction of population in the ground rovibrational state.

3.3.1 Motional Cooling

While the translation of the $BaCl^+$ molecular ions can be sympathetically cooled by co-trapped, laser-cooled Ba^+ ions, the effect of the cold buffer gas of Ca on the motion of the ions is both complicated and interesting. Due to ion–ion heating [CSR13] and micromotion interruption [CSH14], the behavior is dependent on both the number of ions and the initial temperature of the ions. Micromotion interruption describes the process by which the ion trap can do work on an ion during a collision, causing heating to occur. This can be understood by considering an elastic collision between an atom and an ion. In free space, the ion has some position $\vec{r}_i$ and momentum $\vec{p}_i$ before the collision, and by the conservation of energy and momentum, the momentum after the collision $\vec{p}_f$ can be determined—the final position $\vec{r}_f$ does not change during the instantaneous collision. The trajectory of the ion then just proceeds in a straight line according to its new momentum, and the total energy of the ion is just its kinetic energy given by $\frac{p^2}{2m}$. In an ion trap, however, the ion is not in free space. Rather, it is following a Mathieu trajectory. So $\vec{r}_i$ and $\vec{p}_i$ are given by its initial Mathieu trajectory, and the ion begins with potential and kinetic energy. After the collision, the position remains the same, but the new momentum $\vec{p}_f$ puts it on a different Mathieu trajectory. Even if the collision completely stops the ion, setting $\vec{p}_f = 0$, this final position and momentum represents a point on a Mathieu trajectory. This Mathieu trajectory can have a higher total energy than the initial trajectory, leading to a heating of the ion by this

micromotion interruption effect.

In Ref. [SDC16], Steven Schowalter and colleagues explored this complicated system in great detail both theoretically and experimentally. They found that the non-laser-cooled ions do not simply equilibrate at the temperature of the neutral species, as one would naïvely expect. In fact, there is a bifurcation of the reached temperature. For ions initially above a certain temperature, they equilibrate to a certain temperature; similarly, ions initially below a certain temperature equilibrate to a different, lower temperature. These equilibrium temperatures are also dependent on the number of ions present. In this way, purely sympathetic cooling of the motion of ions may not be feasible for initially hot ions. For this reason, we use co-trapped, laser-cooled Ba^+ ions to sympathetically cool the translation of the $BaCl^+$ molecular ions.

3.3.2 Vibrational Cooling

While the co-trapped, laser-cooled Ba^+ ions provide sympathetic translational cooling to the $BaCl^+$ molecular ions, they provide almost no sympathetic cooling of the internal degrees of freedom such as the vibration and rotation [OZW06]. To sympathetically cool these degrees of freedom, a neutral buffer gas can be used. Without relying on laser-cooled neutral atoms, ^{3}He is a natural choice. This method, however, can only reach temperatures as low as $\sim$ 300 mK, which may not be cold enough to cool to the rotational ground state of certain molecules. Additionally, the vibrational cooling efficiency of such atoms is low [FDH85, FKB99]. Instead, we use laser-cooled Ca atoms to sympathetically cool these degrees of freedom. Due to the significantly higher polarizability of Ca compared to He, the vibrational cooling rate was predicted to be very efficient based on a semi-classical argument [Hud09]. This prediction was experimentally verified [RSS13], and a detailed, quantum mechanical close-coupling calculation [SHG16] confirms this efficiency and predicts that this high efficiency is general to other laser-coolable atoms, as they tend to have high polarizabilities.

3.3.3 Rotational Cooling

Rotational cooling differs from vibrational cooling in that the rotational degrees of freedom can be cooled efficiently by collisions with a He buffer gas, as has been demonstrated in Refs. [HVK14, HLC15]. This can be qualitatively understood by the amount of time a collision takes compared to the period of rotation or vibration. For a typical molecule, the rotational constant B_e is on the order of 10 GHz, giving a rotational period of ~ 0.1 ns. For vibration, the spacing is on the order of 10 THz, giving a vibrational period of ~ 0.0001 ns. For a 4 K He buffer gas, the mean velocity is $\sim$ 50 m/s. For a molecular internuclear separation of ~ 5 a_0, the He atom would traverse this distance in ~ 0.001 ns, faster than a rotational period, but slower than a vibrational period. Classically, one would expect that if the collision is much faster than a rotational period, the rotation can be affected by the collision. For the vibration, however, the collision is slower than a period, so the effect gets somewhat washed out or averaged out over a vibrational period. This is only a classical picture of the collision—in fact, using this picture only, one would expect a Ca collision to be worse at cooling vibration, so it clearly has its limits—but it offers some intuition as to why these cooling efficiencies are so different.

The slow time scale of the rotation, however, is also the reason why He buffer gas cooling may be insufficient to reach the rotational ground state. As the rotational splitting is on the order of 10 GHz, the temperature would need to be $\ll 1$ K to have a high probability of being in the rotational ground state. For this reason, buffer gas cooling with He is not suitable for high-fidelity preparation in the rotational ground state. Alternatively, direct optical preparation in the ground rotational state has been achieved by driving vibrational transitions in the mid-IR wavelength range in HD^+[SRD10, SBH12] and MgH^+ [SHS10]. This technique, however, requires molecule-specific lasers and is not easily generalizable to a broader class of molecular ions due to the laser wavelengths required for other molecules (For $BaCl^+$, the $v = 1 \leftarrow v = 0$ transition is $\sim 30,000$ nm). Instead, we rely on sympathetic cooling of the $BaCl^+$ rotational states by the Ca MOT. This sympathetic cooling has the

advantage of not requiring any molecule-specific lasers and the low temperature of the MOT $\sim$ 4 mK is low enough to produce a high probability of populating the rotational ground state.

CHAPTER 4

Efficient Repumping of a Ca Magneto-Optical Trap

During the study performed in Chapter 5, we explored the level structure of Ca in detail, especially regarding the many paths by which atoms can "leak" out of the MOT cooling cycle by populating the $4s4p\ ^3P_J$ metastable states. This leakage limits the lifetime of the Ca MOT, and much of the leakage occurs (directly or indirectly) from the $4s5p\ ^1P_1$ state populated by the 672 nm repump laser. This fact led us to explore alternative repumping transitions in Ca, demonstrating several transitions that result in less leakage to these $4s4p\ ^3P_J$ states, yielding a longer MOT lifetime and higher atomic density. This chapter is a version of our group's publication "Efficient repumping of a Ca magneto-optical trap."

We investigate the limiting factors in the standard implementation of the Ca magneto-optical trap. We find that intercombination transitions from the $4s5p\ ^1P_1$ state used to repump electronic population from the $3d4s\ ^1D_2$ state severely reduce the trap lifetime. We explore seven alternative repumping schemes theoretically and investigate five of them experimentally. We find all five of these schemes yield a significant increase in trap lifetime and consequently improve the number of atoms and peak atom density by as much as $\sim 20\times$ and $\sim 6\times$, respectively. One of these transitions, at 453 nm, is shown to approach the fundamental limit for a Ca magneto-optical trap with repumping only from the dark $3d4s\ ^1D_2$ state, yielding a trap lifetime of $\sim$5 s.

4.1 Introduction

The magneto-optical trap (MOT) [RPC87] is an integral part of atomic and molecular physics, where it is the starting point for a variety of experiments including precision tests of fundamental physics [HJH15], studies of quantum many-body physics [KTL16], and production of ultracold molecules [RSS13, BMN14]. At present, atomic MOTs have been constructed for atoms within Groups 1, 2, 6, 12, and 18, as well as the lanthanides. Extension to atoms in other Groups is often limited by the availability of appropriate laser technology for driving the necessary cooling transitions and complications due to the electronic structure of the atom. For example, if there are multiple electronic states below the upper electronic state of the primary laser cooling transition, then radiative decay into these lower levels can severely reduce, and even eliminate, the laser cooling force. For these reasons, the Group 1 atoms, with their lone optically active, unpaired electron, provide the simplest, and often best performing, MOTs.

Nonetheless, the same 'complications' that can limit the laser cooling process often host interesting and useful phenomena. A prime example of this is the presence of ^3P states of Group 2(-like) atoms, which, while detrimental to the performance of a standard MOT, allow the construction of next-generation optical atomic clocks that can outperform the Cesium standard [LBY15]. One such MOT of this type is the Ca MOT. Calcium MOTs have been utilized in atomic optical clock experiments using the 657 nm $^3P_1 \leftarrow {}^1S_0$ intercombination line [SDS04, DSL05, WOH06] and have significant appeal due to their simplicity of construction as portable optical frequency standards [Vut15]. However, despite this appeal, the details of the Ca electronic structure lead to relatively poor performance of Ca MOTs, including a short trap lifetime limited by optical pumping into dark states and a low achievable peak atomic density. This is one reason other Group 2(-like) atoms such as Sr, Yb, and Hg have become more popular choices for optical frequency standards [LBY15, DK11].

Given the potential of Ca as a portable frequency standard, as well as its utility in our own experiments as a sympathetic coolant for molecular ions [RSS13], we have performed a detailed combined experimental and theoretical study of Ca MOT operation. Specifically, relativistic many-body calculations are performed for the first 75 energy levels of the Ca atom, providing reliable electronic structure and transition matrix elements for this multi-electron atom. The results of this calculation are incorporated into a rate equation model for the populations in the Ca atom, which is used to evaluate specific repumping schemes and identify seven promising transitions. In total, we experimentally investigate five alternative repumping schemes and find that all of them yield Ca MOTs with lifetimes and atom numbers improved by $\sim 10\times$ over the traditional scheme described in Ref. [GH01]. The best of these schemes, which utilizes repumping to a highly configuration-mixed state with a 453 nm repumping laser, produces a Ca MOT with lifetime, number, and density improved over the standard MOT by $\sim 25\times$, $\sim 20\times$, and $\sim 6\times$, respectively.

In the remainder of this chapter, we first present the details of the relativistic many-body calculation of the Ca energy levels and the resulting rate equation model of the Ca populations. We then use this rate equation model to explain the poor performance of the traditional Ca MOT. From this work, we propose seven alternative MOT operation schemes and experimentally investigate five of them. We characterize the differences in these MOT operation schemes, reporting the achievable MOT lifetimes, density, and trapped atom numbers, as well as the necessary repumping laser frequencies. We conclude with discussion of the ideal repumping scheme for Ca MOT operation and possible extension to other Group 2(-like) atoms.

4.2 Relativistic Many-Body Calculations of Atomic Structure

The analysis of MOT performance requires estimates of electric-dipole transition rates between the 75 lowest-energy levels of Ca, including both spin-allowed and spin-forbidden

States		ΔE, cm^{-1}		A_{if}, $10^8\,s^{-1}$		
Initial	Final	CI+MBPT	NIST	CI+MBPT	Exp.	Deviation (%)
$4s4p\ ^1P_1$	$4s^2\ ^1S_0$	23491	23652.304	2.170	2.182(12) [ZBR00]	-0.5(5)
$4p^2\ ^1S_0$	$4s4p\ ^1P_1$	18846	18133.972	0.778	0.754(21) [Smi88]	3.2(2.9)
$4p^2\ ^1D_2$	$4s4p\ ^1P_1$	17691	17067.543	0.576	0.683(11) [HWW85]	-16(1)
$3d4p\ ^1D_2$	$3d4s\ ^1D_2$	13901	13985.779	0.341	0.358(9) [SR81]	-4.7(2.4)
$4snp\ ^1P_1$	$4s^2\ ^1S_0$	44383	43933.477	0.325	0.284(39) [PRT76]	14(16)
$4s4f\ ^1F_3$	$3d4s\ ^1D_2$	19943	20493.953	0.312	0.31(6) [LH87]	1(19)
$4s7p\ ^1P_1$	$4s^2\ ^1S_0$	46975	45425.358	0.130	0.148(21) [LH87]	-12(12)
$4s7s\ ^1S_0$	$4s4p\ ^1P_1$	21724	20624.234	0.068	0.113(5) [Smi88]	-40(3)
$4s4d\ ^1D_2$	$4s4p\ ^1P_1$	14169	13645.983	0.160	0.154(4) [Smi88]	3.9(2.7)
$4s6d\ ^1D_2$	$4s4p\ ^1P_1$	22324	21337.526	0.057	0.080(3) [Smi88]	-29(3)
$4s5p\ ^1P_1$	$3d4s\ ^1D_2$	14259	14881.981	0.130	0.147(3) [SR81]	-12(2)
$4s6p\ ^1P_1$	$4s^2\ ^1S_0$	41788	41679.008	0.092	0.157(22) [PRT76]	-41(8)
$4s6s\ ^1S_0$	$4s4p\ ^1P_1$	17451	17038.131	0.014	0.052(4) [Smi88]	-73(2)
$4s4p\ ^1P_1$	$3d4s\ ^1D_2$	1041	1802.670	0.0000534	0.0000368(100) [LH87]	45(39)
$4s4p\ ^3P_1$	$4s^2\ ^1S_0$	15180	15210.063	0.0000274	0.0000302(7) [HR86]	-9.3(2.2)
$3d4p\ ^1F_3$	$3d4s\ ^1D_2$	18651	18688.259	0.057	0.165(7) [SR81]	-65(1)

Table 4.1: **Comparison of CI+MBPT transition energies ΔE (cm^{-1}) and rates A_{if} (10^8 s^{-1}) with NIST-recommended transition energies.** For comparison, 16 out of the available 111 experimental transition rates along with their uncertainties.

(intercombination) transitions. While the energy levels are well established, transition rates among the first 75 lowest-energy states (811 possible channels) are not known completely, although there are a number of theoretical and experimental determinations. The earlier theory work provides oscillator strengths for spin-allowed transitions for levels up to $4s10s$, $4s9p$, $4s6d$, and $4s5f$, respectively [Mit93, BF94, LH96, HLH99]. Most of these calculations are non-relativistic with a limited number of low-lying levels treated with *ab initio* relativistic methods. The data on transition probabilities for intercombination transitions and transitions involving the $4s6f$ states are scarce [PKR01, SJ02, FT03]. In literature, 111 experimental transition rates are available [ZBR00, Smi88, Kos64, SR81, PRT76, LH87, ALB09, HWW85, HP86, HR86, KRR16, Mor04, SO75, UHF83, UHF82]. The incompleteness of transition rate data motivated us to generate a full set of the 811 required transition rates. To this end we used methods of relativistic many-body theory. *Ab initio* relativistic calculations are necessary as the analysis requires inclusion of transition amplitudes that are non-relativistically forbidden.

Calcium is an atom with two valence electrons outside a tightly bound core. We employ a systematic formalism that combines advantages of both the configuration interaction (CI) method and many-body perturbation theory (MBPT), the CI+MBPT method [DFK96]. The CI+MBPT method has been used extensively for evaluation of atomic properties (see, e.g., Ref. [DP11] for optical lattice clock applications and references therein). Relativistic effects are included exactly, as the formalism starts from the Dirac equation and employs relativistic bi-spinor wave functions throughout the entire calculation. In our treatment, the CI model space is limited to excitations of valence electrons. Contributions involving excitations of core electrons are treated within MBPT. In this approach, we first solve for the valence electron orbitals and energies in the field of the core electrons. The one-electron effective potential includes both the frozen-core Dirac-Hartree-Fock (DHF V^{N-2}) and self-energy (core-polarization) potentials. The self-energy correction is computed using second-order MBPT diagrams involving virtual core excitations. At the next step, the computed one-electron valence orbitals are used to diagonalize the atomic Hamiltonian in the model space of two valence electrons within the CI method. The CI Hamiltonian includes the residual (beyond DHF) Coulomb interaction between the valence electrons and their core-polarization-mediated interaction. The latter was computed in the second-order MBPT. This step yields two-electron wave-functions and energies. Finally, with the obtained wave-functions we calculated the required electric-dipole matrix elements. In calculations of transition rates we used experimental energy intervals and the computed CI+MBPT matrix elements.

We used two independent CI+MBPT implementations: (i) by the Reno group (see the discussion of the earlier version in Ref. [Der01]) and (ii) a recently published package [KPS15]. The practical goal of the calculations was not to reach the highest possible accuracy, but rather to generate the large amount of data needed for the transition array involving the 75 lowest-energy levels. An additional computational challenge was the inclusion of high angular momenta states, e.g., the $4s5g\ ^3G$ state. The Reno code was run on a large basis

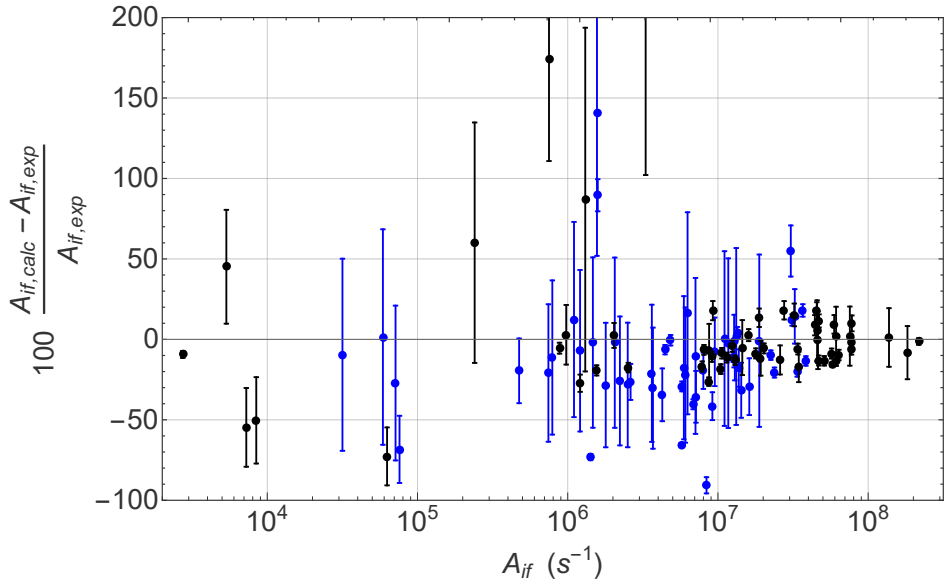

Figure 4.1: **Comparison of the calculated CI+MBPT transition rates with 111 available experimental data.** Transitions involving a state with orbital angular momentum $l \geq 3$ or principal quantum number $n \geq 6$ are shown in blue. All other transitions are shown in black. Error bars correspond to the experimental error.

set but without including core-polarization-mediated interaction in the CI Hamiltonian due to considerable computational costs. The production runs with the package of Ref. [KPS15] employed a smaller basis set (due to code limitations) but treated the correlation problem more fully. Our final values combine the outputs of the two codes. The bulk of the results comes from the package of Ref. [KPS15]. These results are augmented with the rate data involving $4s8s$ states from the Reno code due to the limited number of roots in the package of Ref. [KPS15].

We assessed the quality of the calculations by comparing the CI+MBPT energies with the NIST recommended values [KRR16] and CI+MBPT transition rates with 111 available experimental values (see subset in Table 4.1) [ZBR00, Smi88, Kos64, SR81, PRT76, LH87, ALB09, HWW85, HP86, HR86, KRR16, Mor04, SO75, UHF83, UHF82]. The CI+MBPT energy intervals for tabulated transitions agree with NIST values to better than 1000 cm^{-1}. To quantify the error of the CI+MBPT transition rates, we calculate the relative deviation

from the experimental values, $E_{if} = 100\frac{A_{if,calc}-A_{if,exp}}{A_{if,exp}}$, with standard errors corresponding to the experimental errors (see Figure 4.1). The weighted root mean square of E_{if} yields an estimate of the error of the CI+MBPT transition rates. We determine this error for two subsets of transitions: The first includes all transitions involving a state with orbital angular momentum $l \geq 3$ or principal quantum number $n \geq 6$, where both faithful numerical representation and inclusion of correlations are important, and yields an average error of 48%. The second subset includes all other transitions and has an average error of 13%. This difference in error is reflective of the computational difficulty of obtaining transition rates for these subsets of transitions. For some transitions, the deviation of our theoretical transition rates from experiment is large; to remedy this, we replace our calculated transition rates with experimental values when the deviation is greater than twice the experimental error or the experimental error is less than our expected error. In the supplementary material, we provide the complete data set that includes all 811 calculated transitions, as well as a data set augmented by experimental values.

4.3 Rate Equation Model of Ca Electronic State Populations

Using the 811 calculated CI+MBPT transition rates augmented by experimental transition rates as previously described, we create a rate model including the first 75 excited states of calcium. As an example, the differential equation for state i with a monochromatic laser driving from state i to state k is given by

$$\frac{\mathrm{d}}{\mathrm{d}t}N_i = \sum_{j>i} A_{ji}N_j - \sum_{j<i} A_{ij}N_i - \frac{N_i}{\tau_{Loss}} + A_{ki}\frac{\pi^2c^3}{\hbar\omega_{ik}^3}\frac{I_\mathrm{L}}{2\pi c}\frac{\Gamma_k}{(\omega_{ik}-\omega_\mathrm{L})^2+\frac{\Gamma_k^2}{4}}\left(N_k - \frac{2j_k+1}{2j_i+1}N_i\right) \tag{4.1}$$

where N_i is the number of atoms in state i, A_{ij} is the decay rate of state i to j, τ_{Loss} is the time in which an uncooled atom drifts outside of the MOT region (for our parameters, this value is 1.7 ms for the $4s4p\ ^3P_0$ and $^3P_2$ states and ∞ otherwise), c is the speed of light in

a vacuum, $\hbar$ is the reduced Planck constant, ω_{ik} is the angular transition frequency between state i and k, ω_{L} (I_{L}) is the angular frequency (intensity) of the applied laser, Γ_k is the natural linewidth of state k, and j_i is the total angular momentum quantum number of state i [FFF05].

To determine the effect of the errors in the CI+MBPT transition rates on the lifetime of the MOT, we randomly vary each of the 811 transition rates according to their expected error. Using these modified transition rates, we numerically solve the coupled differential equations to extract a MOT lifetime. We repeat this process 1000 times and report the mean and the standard deviation of the resulting MOT lifetimes.

4.4 Evaluation of the Standard Ca MOT Operation

The standard implementation of a Ca MOT is formed by laser cooling on the strong $4s4p\ ^1P_1 \leftarrow 4s^2\ ^1S_0$ transition at 423 nm in the presence of an anti-Helmholtz magnetic field with gradient of 60 G/cm in the axial direction. This transition incurs loss from the laser cooling cycle primarily due to decay from the $4s4p\ ^1P_1$ state to the $3d4s\ ^1D_2$ state. This $^1D_2$ state, as shown in Figure 4.2, decays to the $4s4p\ ^3P_1$ (83% branching) and $^3P_2$ (17% branching) states with a total lifetime of 1.71 ms [HR86]. The $^3P_1$ state decays to the ground state with a lifetime of 0.331 ms, while the $^3P_2$ state has a lifetime of 118 minutes, leading to loss from the laser cooling cycle [HR86, Der01]. This loss, which is proportional to the $4s4p\ ^1P_1$ state population, limits the lifetime of the Ca MOT and according to the rate model with our experimental parameters leads to a MOT lifetime of 27(5) ms. As detailed later, we experimentally observe a MOT lifetime of 29(5) ms in this configuration.

To extend the MOT lifetime, a repumping laser is usually added to drive the $4s5p\ ^1P_1 \leftarrow 3d4s\ ^1D_2$ transition at 672 nm in order to return electronic population in the $3d4s\ ^1D_2$ level to the laser cooling cycle before it decays to the $4s4p\ ^3P_1$ and $^3P_2$ states [KS92]. In this configuration, the rate equation model predicts that the MOT lifetime is increased to

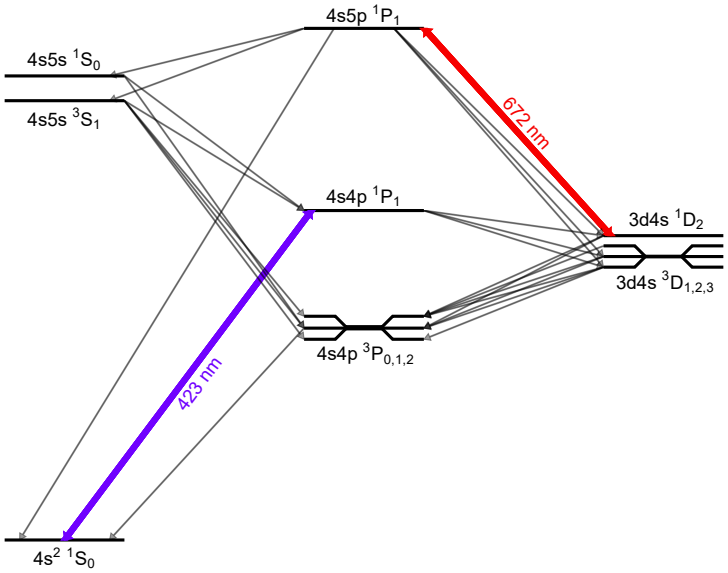

Figure 4.2: **Relevant level structure for operation of a standard calcium MOT.** Laser cooling is accomplished on the 423 nm $4s4p\ ^1P_1 \leftarrow 4s^2\ ^1S_0$ transition. Atoms that decay to the $3d4s\ ^1D_2$ state are repumped back into the cooling cycle via the 672 nm $4s5p\ ^1P_1 \leftarrow 3d4s\ ^1D_2$ transition, while those in the long-lived $4s4p\ ^3P_{0,2}$ states are lost from the MOT.

86(18) ms for our experimental parameters. As detailed later, we experimentally observe a MOT lifetime of 93(6) ms in this configuration.

Interestingly, it is often assumed that the lack of a further increase in the MOT lifetime with this repumping scheme is due to an incomplete depletion of the $3d4s\ ^1D_2$ state, which is in turn due to unfavorable branching ratios in the $4s5p\ ^1P_1$ state [KS92]; this state decays primarily back to the $3d4s\ ^1D_2$ state and only weakly back in the cooling cycle. However, the rate equation model reveals that the MOT lifetime is actually limited by the decay of the $4s5p\ ^1P_1$ state to the $4s5s\ ^3S_1$, $3d4s\ ^3D_1$, and $3d4s\ ^3D_2$ states, all of which decay primarily to the $4s4p\ ^3P_{0,1,2}$ states, as shown in Figure 4.2 and first pointed out in Ref. [OBF99]. Specifically, according to the theoretical calculations, the $4s5p\ ^1P_1$ state decays indirectly to the lossy $4s4p\ ^3P_0$ and $^3P_2$ states at a total rate of 8×10^4 s^{-1}, while the $3d4s\ ^1D_2$ state decays to the $4s4p\ ^3P_2$ state at a rate of only 80 s^{-1}. With this understanding, the natural question arises: *Is there an alternative repumping scheme that would suppress the loss into*

these triplet states?

4.5 Evaluation of Alternative Ca MOT Operation Schemes

The ideal repumping laser out of the $3d4s\ ^1D_2$ state would quickly transfer population from the $^1D_2$ state back into to the cooling cycle with perfect efficiency. With this idealized scheme, the rate model predicts a lifetime of 3.0(4) s with our MOT parameters. This lifetime is limited by the decay of the $4s4p\ ^1P_1$ state to $3d4s\ ^3D_1$ and $^3D_2$ states and is thus dependent on the $4s4p\ ^1P_1$ state population; lowering the $4s4p\ ^1P_1$ state population by decreasing 423 nm cooling laser intensity while maintaining reasonable MOT performance can extend the lifetime by $\sim 2\times$. Since this lifetime is similar to lifetimes set by other effects in most systems, such as collisions with background gas, it is likely unnecessary for the majority of applications to employ a more complicated multi-laser repumping scheme out of the ^{3}P states like that used in Sr [LBY15], especially since the longer lifetime of the $3d4s\ ^1D_2$ and $4s4p\ ^3P_1$ in Ca make this scheme less efficient.

Therefore, for this work we choose to only explore single-laser repump transitions from the $3d4s\ ^1D_2$ state with high branching ratios back into the laser cooling cycle. With this metric, we find that within the first 75 electronic states, there are seven reasonable alternative repumping transitions from the $3d4s\ ^1D_2$ state, shown in Figure 4.3, which go to states in the $^1P_1$ and $^1F_3$ manifolds. Using the rate equation model with our standard MOT parameters, we calculate the expected MOT lifetimes for these transitions, which are limited by optical pumping into the $^3P_{0,2}$ states, and present the results in Table 4.2.

Of these seven transitions, five are accessible by lasers available to us and we explore them using a standard six beam Ca MOT described in Ref. [RSS13]. Briefly, in this system, laser cooling is provided by driving the $4s4p\ ^1P_1 \leftarrow 4s^2\ ^1S_0$ cooling transition with a total laser intensity of 63 mW/cm^2 detuned 34.4 MHz below resonance. The Ca MOT is loaded from an oven source placed ~ 3.5 cm away from the MOT. Atoms from the oven are decelerated

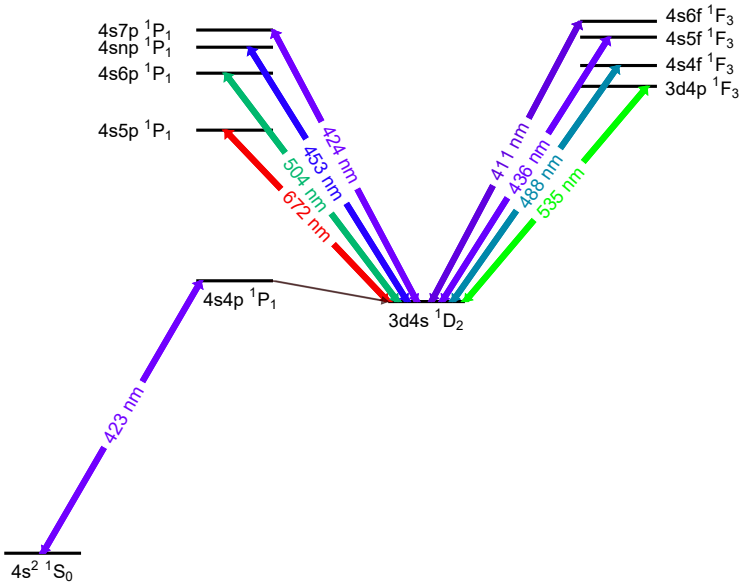

Figure 4.3: **Simplified calcium electronic level structure showing the eight repumping transitions considered here.** All transitions except the 504 nm and 535 nm have been studied experimentally. The overall best Ca MOT performance is found when pumping to a highly configuration-mixed state, labeled as $4snp\ ^1P_1$, using the 453 nm $4snp\ ^1P_1 \leftarrow 3d4s\ ^1D_2$ transition.

by two 'deceleration beams' with intensities 110 mW/cm^2 and 53 mW/cm^2 and detunings below resonance of 109 MHz and 318 MHz, respectively. The 672 nm traditional Ca MOT repump laser has an intensity of 11 mW/cm^2.

For each single-beam repumping scheme, we characterize the MOT performance by measuring the MOT density, lifetime, and temperature. The density is measured using absorption imaging on the $4s4p\ ^1P_1 \leftarrow 4s^2\ ^1S_0$ transition. The MOT lifetime, τ, is extracted by using fluorescence imaging to observe the number of trapped atoms, N, as the MOT is loaded from the oven at rate R and fitting the data to the form $N(t) = R\tau\left(1 - e^{-t/\tau}\right)$. The temperature, T, is found from the ballistic expansion of the Ca atoms after the MOT trapping beams are extinguished. For this measurement, the e^{-1} waist of the cloud is extracted from absorption images taken after a variable time of expansion, and T is extracted by fitting this data to the form $w(t > 0) = \sqrt{w(t = 0)^2 + \frac{2k_B T t^2}{m}}$, where k_B and m are the Boltzmann

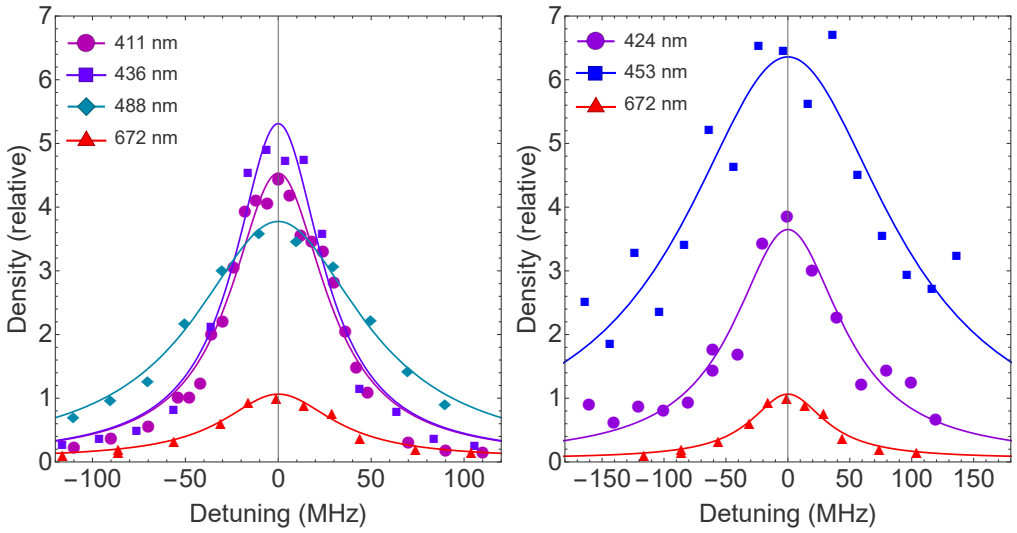

Figure 4.4: **Measured calcium MOT density as a function of repumping laser detuning.** (a) $^1F_3$ and (b) $^1P_1$ repump transitions. Experimental data are shown by points, while Lorentzian fits are shown as lines. All measured densities are scaled to the peak MOT density achievable with the standard 672 nm repumping scheme.

constant and the mass of the Ca atom, respectively. The results of these measurements are shown in Figure 4.4, Figure 4.5, and Table 4.2. All of the experimentally explored alternative repumping schemes produce significantly denser MOTs at roughly the same temperature with longer lifetimes.

Somewhat surprisingly, repumping to $^1F_3$ states leads to similar or sometimes better MOT performance than repumping to $^1P_1$ states. Population promoted to the $^1F_3$ states quickly decays to states with term $^1D_2$, which in turn primarily decay to the $4s4p\ ^1P_1$ state. During this cascade, there is less decay into states of triplet character as compared to decays from some of the $^1P_1$ repumping states. Thus, despite the more complicated repumping pathway, repumping to the $^1F_3$ states can be very effective.

The relative performance of the $^1F_3$ repumping schemes can be explained by their branching pathways into lossy triplet states. The total MOT loss rate due to loss from an upper repump state is given by $\frac{\mathrm{d}}{\mathrm{d}t}N = -\Gamma_i f_{\mathrm{Loss}} N_i$, where N is the total number of atoms in the MOT, N_i is the number of atoms in the upper repump state, Γ_i is the natural linewidth of

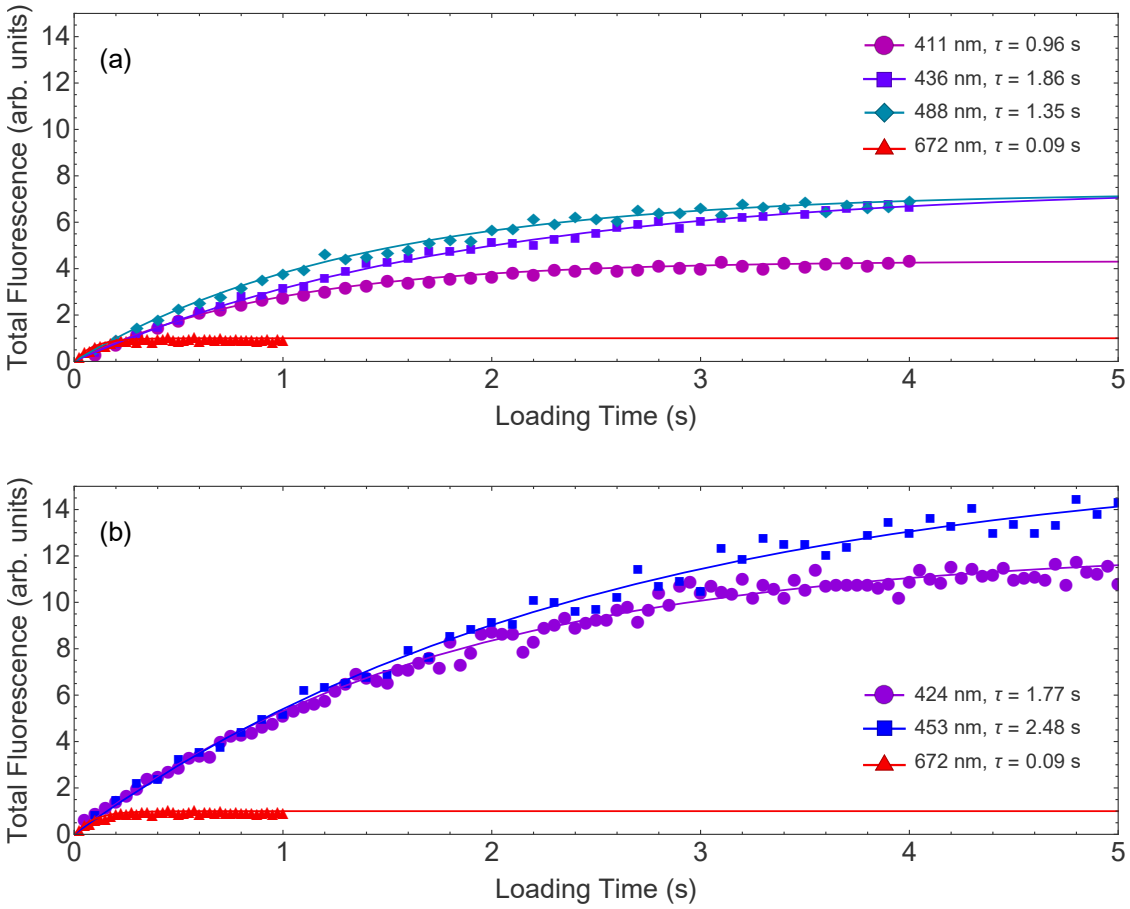

Figure 4.5: **Measured Ca MOT loading curves.** (a) $^1F_3$ and (b) $^1P_1$ repump transitions. MOT fluorescence is plotted as a function of time elapsed after the cooling lasers are turned on; curves fitted to $N(t) = R\tau\left(1 - e^{-t/\tau}\right)$ are shown alongside the data.

the upper repump state, and f_{Loss} is the fraction of decays which lead to decay into the triplet states directly or indirectly. Of the three $^1F_3$ repump transitions experimentally tested, we approximate the relative values of N_i by comparing the average number of repump transition cycles required before decay into another state. We use the calculated linewidths Γ_i along with the most significant loss pathways to estimate f_{Loss}.

Summarizing from Figure 4.6, the $4s4f\ ^1F_3$ state decays with $\sim 17\%$ branching into the $4s4d\ ^1D_2$ state, which has a branching of $\sim 0.2\%$ into the $4s4p\ ^3P_2$ state. The $4s5f\ ^1F_3$ state decays to the $4s4d\ ^1D_2$, $4p^2\ ^1D_2$, and $4s5d\ ^1D_2$ states with $\sim 8\%$, $\sim 3\%$, and $\sim 8\%$ branching, respectively. The $4p^2\ ^1D_2$ state decays to triplet states with $\sim 0.3\%$ branching,

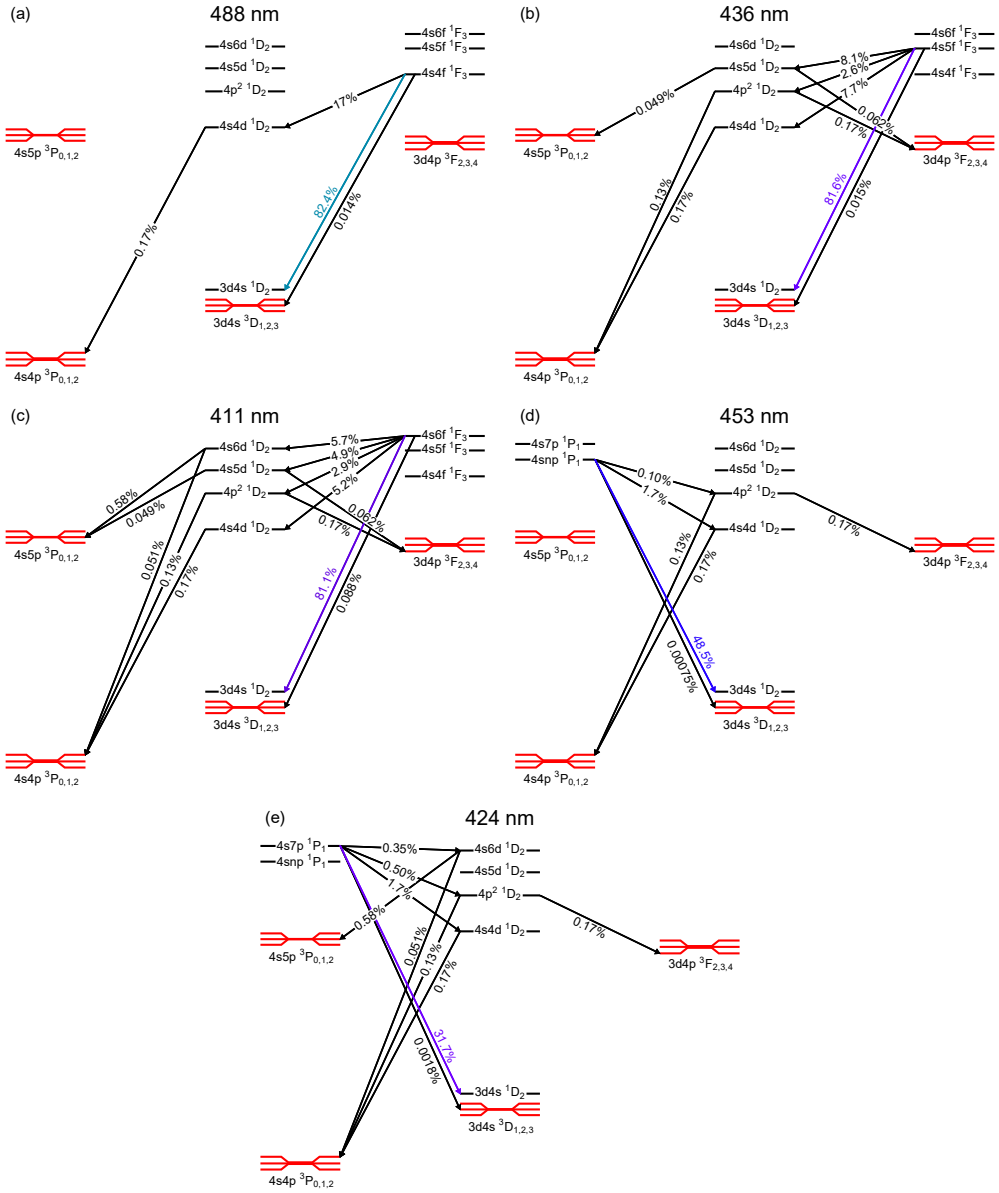

Figure 4.6: **Simplified electronic energy level structures illustrating the main loss channels for the experimentally tested repumping schemes.** $^1F_3$ repumps are shown in (a), (b), and (c), and $^1P_1$ repumps are shown in (d) and (e). Here we show only the most significant pathways into lossy triplet states, shown in red. The omitted decays dominantly return to the main cooling cycle. Using only these branching ratios and the natural linewidths of the upper states, one can compare the approximate relative MOT lifetimes for each transition. This simple model reproduces the lifetime ordering of the more comprehensive 75-level rate equation model and also matches experimental results.

State	λ (nm)	f (THz)	ρ_0 (cm^{-3})	N (atoms)	τ, model (s)	τ, exp. (s)	T (mK)	Ca^+ Production (relative)
$4s5p\ ^1P_1$	672	446.150837(13)	$7.5(7)\times10^9$	$3.7(3)\times10^6$	0.086(18)	0.093(6)	4(1)	$\equiv 1$
$3d4p\ ^1F_3$	535	–	–	–	0.14(11)	–	–	–
$4s6p\ ^1P_1$	504	–	–	–	2.3(3)	–	–	–
$4s4f\ ^1F_3$	488	614.393495(22)	$2.1(2)\times10^{10}$	$2.7(2)\times10^7$	0.73(16)	1.35(6)	5(1)	0.9(1)
$4snp\ ^1P_1$	**453**	**662.057231(22)**	$\mathbf{5.0(5)\times10^{10}}$	$\mathbf{7.8(7)\times10^7}$	**2.4(3)**	**2.48(8)**	**5(1)**	**0.8(1)**
$4s5f\ ^1F_3$	436	688.180929(22)	$2.8(3)\times10^{10}$	$2.8(3)\times10^7$	0.99(15)	1.86(7)	4(1)	1.4(2)
$4s7p\ ^1P_1$	424	706.783089(10)	$2.9(3)\times10^{10}$	$5.9(5)\times10^7$	2.2(3)	1.77(6)	5(1)	1.7(2)
$4s6f\ ^1F_3$	411	729.478413(22)	$2.5(2)\times10^{10}$	$1.6(1)\times10^7$	0.45(10)	0.96(3)	4(1)	3.1(4)
Ideal	–	–	–	–	3.0(4)	–	–	–

Table 4.2: **Summary of the repump performances.** Each row of this table lists the calculated and measured properties of an individual repumping scheme, with the most efficient repump transition to the $4snp\ ^1P_1$ state in bold. We attribute deviations between the model prediction for the MOT lifetime and the measured lifetime to inaccuracies in the calculated transition rates. These inaccuracies are expected to be higher for the high-lying F-states, in agreement with the larger deviations seen between model and data for these states. The experimental errors include statistical and systematic uncertainties.

and the $4s5d\ ^1D_2$ state decays to triplet states with $\sim 0.1\%$ branching. The $4s6f\ ^1F_3$ state decays with branching ratio $\sim 5\%$, $\sim 3\%$, $\sim 5\%$, and $\sim 6\%$ into the $4s4d\ ^1D_2$, $4p^2\ ^1D_2$, $4s5d\ ^1D_2$, and $4s6d\ ^1D_2$ states respectively, the last of which decays with $\sim 0.6\%$ branching into the $4s5p\ ^3P_1$ state. Using this method with only the branching ratios shown in Figure 4.6 and the natural linewidths of the upper repump states, we predict that the lifetime of the MOT τ_{488}, τ_{436}, τ_{411}, using a 488 nm, 436 nm, or 411 nm repump should obey the relaton: $\tau_{436} > \tau_{488} > \tau_{411}$. This agrees with the observed MOT lifetimes. For the same reason, we expect repumping to the $3d4p\ ^1F_3$ state with a 535 nm laser will exhibit poor performance. One can use this method to quickly estimate relative performances of potential repump transitions without developing a comprehensive rate model.

Similarly, the MOT performance when repumping to the $4s6p\ ^1P_1$ and $4s7p\ ^1P_1$ states relative to the traditional $4s5p\ ^1P_1$ state is understood by their primary branching ratios into triplet states. The $4s6p\ ^1P_1$ state decays with $\sim 0.006\%$ branching into the $3d4s\ ^3D_2$ state, and the $4s7p\ ^1P_1$ state decays with $\sim 0.002\%$ branching into the $3d4s\ ^3D_2$ state, while the $4s5p\ ^1P_1$ state decays with $\sim 0.9\%$ branching into the $3d4s\ ^3D_1$, $3d4s\ ^3D_2$, and $4s5s\ ^3S_1$

states.

Interestingly, the best MOT performance, in terms of number, density, and lifetime, is achieved by repumping to a highly configuration-mixed state, which we label as $4snp\ ^1P_1$. Our calculations find this state is primarily composed of the mixture $4s7p$ (43%), $4p3d$ (28%), and $4s8p$ (13%). The high performance of this repumping transition arises from two facts. First, its primary branching ratio to triplet states is $\sim 0.001\%$ and the lowest of all repumping transitions explored here. Second, it exhibits a very high branching ratio of $\sim 43\%$ directly back to ground $4s^2\ ^1S_0$ state.

Because the lifetime of the MOT when operating with the 453 nm repump ($\sim$ 2.5 s) is close to the idealized limit set by intercombination transitions from the $4s4p\ ^1P_1$ state (3 s), we vary the intensity of the 423 nm cooling laser to measure the lifetime of the MOT as a function of the $4s4p\ ^1P_1$ state population. Figure 4.7 shows our results alongside the predicted lifetime from the rate model and the calculated limit of $0.24/\rho_{pp}$ s^{-1} set by the decay from the $4s4p\ ^1P_1$ state indirectly to the lossy $4s4p\ ^3P_0$ and $^3P_2$ states – here ρ_{pp} is the population fraction in the $4s4p\ ^1P_1$ state. Our results show that the lifetime of the MOT in this scheme approaches this fundamental limit for any Ca MOT with a single repump out of the $3d4s\ ^1D_2$ state. Therefore, repumping at 453 nm provides nearly the optimum performance for any imaginable single-repump scheme in Ca.

Trapping calcium atoms in a MOT also provides us with a cold sample convenient for metastable state spectroscopy. We take advantage of this as well as the effect a repump laser has on the total number of atoms and fluorescence of a MOT to measure the transition energies of several repump transitions. Using a low repump laser intensity to minimize power broadening, we measure MOT fluorescence on the $4s4p\ ^1P_1 \leftarrow 4s^2\ ^1S_0$ transition as we scan a given repump frequency. As the repump laser comes into resonance, the number of atoms in the MOT and the fluorescence drastically increase. We use a HighFinesse Angstrom WS Ultimate 2 wavelength meter calibrated to the Ca $4s4p\ ^1P_1 \leftarrow 4s^2\ ^1S_0$ transition via a saturated absorption lock to measure the absolute frequency [SMD11]. Our results are

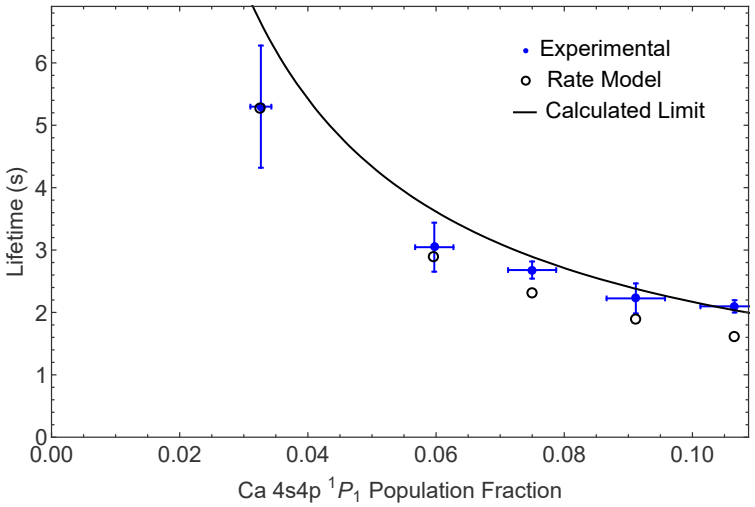

Figure 4.7: **Measured Ca MOT lifetime as a function of $4s4p\ ^1P_1$ state population with a 453 nm repump.** The measured lifetimes are shown alongside the rate model predictions and a curve representing the fundamental limit for any single repump laser scheme in a Ca MOT. This limit is the result of decay from the $4s4p\ ^1P_1$ state indirectly to the $4s4p\ ^3P_0$ and $^3P_2$ states and is found as $0.24/\rho_{pp}$ s^{-1}, where ρ_{pp} is the population fraction of the Ca $4s4p\ ^1P_1$ state.

shown in Table 4.2, where the reported uncertainties account for the following potential errors: the absolute accuracy of the wavelength meter, the error in the Lorentzian fits, the Zeeman effect for a $M_J = \pm 1$ transition, the DC Stark effect, the AC Stark effect, and the uncertainty in the Ca $4s4p\ ^1P_1 \leftarrow 4s^2\ ^1S_0$ transition frequency.

4.6 Ca^+ Production

Due to its relatively light mass and high ionization potential, Ca is especially useful in hybrid atom–ion traps as a sympathetic coolant [RSS13]. However, as was recently identified [SRK11, SDC16], Ca MOT operation can produce Ca^+ and Ca_2^+ through multi-photon and photo-associative ionization, respectively. These ions then produce an unwanted heat load during the sympathetic cooling process. While techniques exist to cope with these nuisance ions [SDC16], it is advantageous to keep their production rate as low as possible. Therefore, we use time of flight mass spectrometry [SCR12, SSC14, SSY16] to measure the

density normalized Ca^+ production rate for each of the tested repump lasers and compare to the Ca^+ production rate with a 672 nm repump. As shown in Table 4.2, we find that the largest Ca^+ production rate occurs with the 411 nm repump, a factor of 3.1 compared to the Ca^+ production rate with the 672 nm repump. The 453 nm repump, which resulted in the MOT with the longest lifetime, highest density, and largest number of atoms also yields the lowest Ca^+ production rate.

4.7 Summary

In summary, we propose seven alternatives to the traditional 672 nm repumping scheme for a Ca MOT and experimentally explore five of them. We find that all five produce significant improvements in MOT density and lifetime. Three of these repumping transitions appear particularly convenient from a technological perspective since they occur at wavelengths that are accessible by diode lasers, *i.e.* 453 nm, 424 nm, and 411 nm – with the middle transition of this list occurring at nearly the same wavelength as the cooling transition in Ca. The overall best MOT performance occurs for repumping at 453 nm on the $4snp\ ^1P_1 \leftarrow 3d4s\ ^1D_2$ transition and results in a $\sim 6\times$ and $\sim 25\times$ improvement in density and lifetime, respectively, over the standard scheme. According to our rate model, this lifetime is near the maximum theoretical lifetime that can be achieved in a Ca MOT with a single repump laser from the $3d4s\ ^1D_2$ state.

In all cases, the relative performance of the different repumping schemes can be understood by their branching into triplet states. Electronic population in these states typically ends up in either the $4s4p\ ^3P_0$ or $^3P_2$ state, which due to their long spontaneous emission lifetimes are lost from the MOT. For this reason, if a Ca MOT lifetime beyond that of ~ 5 s is desired it would be necessary to add additional lasers to repump from the $4s4p\ ^3P_0$ and $4s4p\ ^3P_2$ states as is done in Sr [LBY15]. If the MOT is not limited by other factors such as background gas collisions, we estimate this would extend the lifetime to ~ 29 s. If a further

increase in the lifetime is required, it would be necessary to repump from the $4s4p\ ^3P_1$ state, which would completely close the laser cooling cycle. However, even if these lasers are added, given the longer lifetime of the $3d4s\ ^1D_2$ state as compared to its analogue in Sr, it will likely be necessary to retain the 453 nm repump for optimal MOT operation.

Finally, due to their similar atomic structure it may be possible to apply this repumping scheme in other Group 2(-like) atoms. For example, in Sr MOTs we speculate that repumping on the $5s8p\ ^1P_1 \leftarrow 4d5s\ ^1D_2$ transition at 448 nm may be beneficial since it would return population from the $4d5s\ ^1D_2$ more quickly than in the typically employed scheme and thereby increase the achievable optical force. A likely less efficient, but perhaps technologically simpler repumping pathway would be to drive the $5s6p\ ^1P_1 \leftarrow 4d5s\ ^1D_2$ transition at 717 nm. In both of these cases, however, it may be necessary to retain the lasers used to repump population from the $5s5p\ ^3P_0$ and $^3P_2$ states as the larger spin–orbit mixing in Sr increases the parasitic intercombination transitions from *e.g.* the $5s5p\ ^1P_1$ state.

CHAPTER 5

Synthesis and Reaction Study of $BaOCa^+$

Hybrid atom–ion traps such as the MOTion trap described in this dissertation offer access to a new regime of charged–neutral chemistry previously not attainable. As both the ions and neutrals can be cooled to the millikelvin regime, the collision temperature accessible to hybrid traps is orders of magnitude lower than traditional methods [FFS69, AS76, RDM84]. Additionally, the cooling and repump lasers allow for optical control of the internal electronic states of the reactants. One interesting example of chemistry we were able to perform in the MOTion trap is the synthesis and study of $BaOCa^+$. Using the atomic physics toolkit available to us, we were able to produce and detect $BaOCa^+$, which is the first molecule of its kind ever observed, and determine the reaction pathway through which it can be formed. This chapter is a version of our group's publication "Synthesis of mixed hypermetallic oxide $BaOCa^+$ from laser-cooled reagents in an atom–ion hybrid trap."

Hypermetallic alkaline earth (M) oxides of formula MOM have been studied under plasma conditions that preclude insight into their formation mechanism. We present here the application of emerging techniques in ultracold physics to the synthesis of a mixed hypermetallic oxide, $BaOCa^+$. These methods, augmented by high-level electronic structure calculations, permit detailed investigation of the bonding and structure as well as the mechanism of its formation via the barrierless reaction of Ca $4s4p\ ^3P_J$ with $BaOCH_3^+$. Further investigations of the reaction kinetics as a function of collision energy over the range 0.005 kelvin (K) to 30 K and of individual Ca fine-structure levels compare favorably with calculations based on long-range capture theory.

5.1 Introduction

Molecules usually contain their constituent atoms in well-defined ratios predicted by classical theories of valence. Hypervalent species, however, are well known and provide an opportunity to look more deeply into chemical bonding [NSG02] and to anticipate and predict new chemical species and structures that may have exotic or useful properties [UOY10]. An interesting class of hypervalent molecules is the hypermetallic alkaline earth (M) oxides of form MOM. Theory reveals the bonding in these linear molecules to be the donation of an electron from each metal atom to the central O atom, resulting in a system in which the central atom is closed-shell, inhibiting coupling between the radical centers on the terminal metal atoms. As a result, the singlet-triplet splitting is very small, and its prediction is sensitive to the level of theory applied. The hypermetallic alkaline earth oxide BeOBe and its cation have recently been investigated by Heaven and coworkers using a range of spectroscopic tools, augmented with high-level electronic structure calculations [MBH09, ABH11]. For BeOBe, the singlet was found to be the ground state, just 243 cm^{-1} below the triplet. Theoretical predictions of bonding and structure have also been reported for MgOMg [OBS11], CaOCa [OBS12], and SrOSr [OJS13].

Given these properties, MOM molecules and their cations provide an opportunity to benchmark quantum chemical calculations and explore bonding in molecules containing M atoms in the +1 oxidation state, which have recently been produced and are expected to be useful for inorganic synthesis [GJS07]. For mixed hypermetallic oxides MOM′, dramatic effects on the electronic structure, single-triplet splitting, and excited-state spectra may be expected to result from breaking the metal atom symmetry, leading to unusual inorganic diradicaloid systems [Abe13]. In addition, for the mixed cations the asymmetric hole distribution affects both the dipole moment and bonding. All of these properties could be tuned through choice of metal atoms for applications such as nonlinear optics or materials science or as synthetic intermediates [NC15]. One challenge to such investigations is to develop a

means to synthesize these molecules under controlled conditions and probe the pathways leading to their formation. Cations are a natural first target for such investigations because they can be manipulated and detected with great ease and sensitivity.

Emerging techniques in ultracold physics are now being adapted to the study of chemical systems, bringing new capabilities to probe reaction dynamics and mechanisms [EDV15, DKW11, Hud16]. Recently, a study of the reaction of conformers of 3-aminophenol with laser-cooled Ca^+ ions revealed a fascinating dependence on the conformational state [CDK13]; quantum state-resolved collisions between OH and NO [KWS12], as well between $N2^+$ and Rb [HW12], have been observed; and quantum effects were found to have a major impact on state-resolved KRb reactions [ONW10]. Reactions involving polyatomic reagents are a compelling target for such studies because these techniques may be used to cool these species into a limited number of quantum states as well as provide precise control over reaction conditions. Here, we describe use of a magneto-optical atom trap coupled to an ion trap and time-of-flight mass spectrometer to synthesize a mixed hypermetallic alkaline earth oxide, $BaOCa^+$. These methods, augmented with high-level electronic structure calculations, permit detailed investigation of the properties of this molecule as well as the mechanism of its formation via the barrierless reaction of Ca (^3P_J) with $BaOCH_3^+$.

5.2 Experimental Apparatus

Several aspects of the experimental apparatus were crucial to the feasibility of this study. The hybrid ultracold atom–ion trap, dubbed the MOTion trap (Figure 5.1a) [RSS13, SDC16], consists of a radiofrequency linear quadrupole ion trap (LQT), colocated magneto-optical trap (MOT) of Ca atoms, and a radially coupled time-of-flight mass spectrometer (ToF) [SCR12, SSC14]. Because of the spatial overlap of the atoms and ions, ultracold collisions between the two species and the chemical reactions and quantum phenomena that they give rise to can readily be observed.

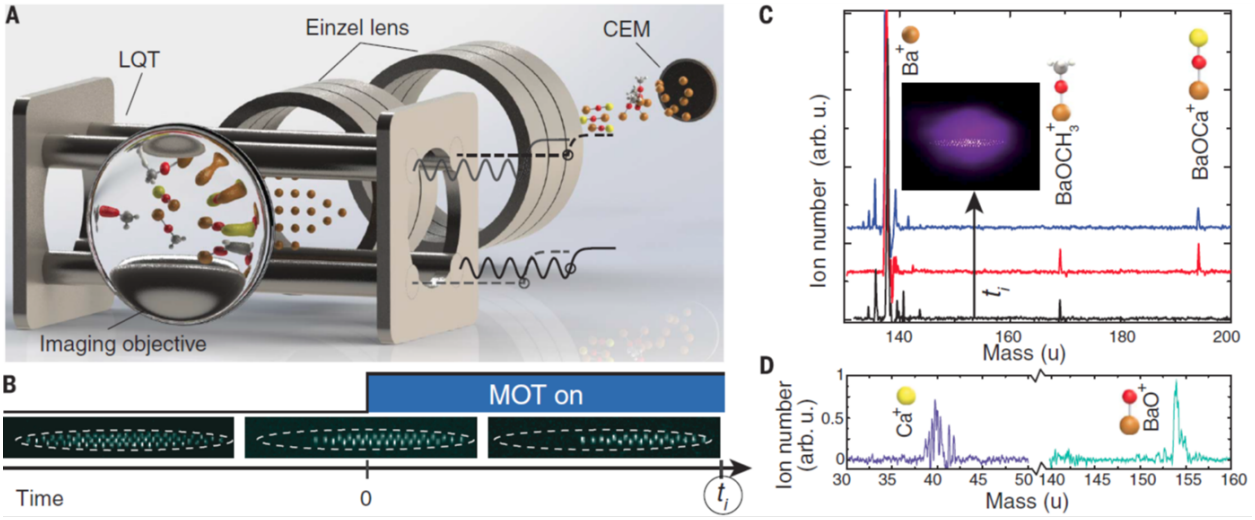

Figure 5.1: **Experimental schematic and sample data acquisition.** (a) A schematic of the experimental apparatus, including the LQT, the high-voltage pulsing scheme (shown as solid and dashed lines), and the ToF. (b) An illustrative experimental time sequence that depicts initialization of a Ba^+ crystal, production of $BaOCH_3^+$ (visualized as dark ions in the crystal) through reactions with methanol vapor, and subsequent MOT immersion. (c) Sample mass spectra obtained after ejecting the LQT species into the ToF after various MOT immersion times, t_i. (Inset) A superimposed fluorescence image of an ion crystal immersed in the Ca MOT. (d) Mass spectra of photofragmentation products collected after inducing photodissociation of $BaOCa^+$. The identified photofragments were used to verify the elemental composition of the product.

The collision energy of the trapped ions and atoms in this study, defined as E/k_B, where E is the kinetic energy of the collision complex and k_B is the Boltzmann constant, ranged from 0.005 K to 30 K, depending on the size of the ion crystal loaded into the LQT. A standard Ba^+ crystal was used as a sympathetic coolant for other trapped ions (Figure 5.1b). In a typical experimental sequence, Ba^+ ions were initially loaded into the LQT through laser ablation of a $BaCl_2$ target. From this initial sample, a small number of $BaOH^+$ and $BaOCH_3^+$ ions were created by the reaction of Ba^+ with CH_3OH [DSL93] introduced into the vacuum chamber at a pressure of $\sim 10^{-10}$ torr. The $BaOCH_3^+$ molecules were translationally cooled by the Ba^+ crystal. Recent studies [RSS13] indicate that collisions with the ultracold Ca atoms of the MOT should also cool their rotational-vibrational internal degrees of freedom; however, absent spectroscopy of $BaOCH_3^+$, we assume an internal temperature of <300 K, bounded

by the temperature of our vacuum chamber. Once a sufficient number of $BaOCH_3^+$ molecules were produced, $BaOH^+$ ions could be removed from the LQT by resonantly exciting their motion at a mass-specific secular frequency; afterward, the purified sample was immersed in a radius $r \approx 0.6$ mm cloud of 3 million Ca atoms at 0.004(2) K (numbers in parentheses are 1-σ errors) (Figure 5.1b). After a variable immersion time, t_i, the voltages of the LQT were adjusted [SSY16] to eject the ions into the ToF, yielding mass spectra (Figure 5.1c).

The ToF spectra indicated the formation of a reaction product with mass-to-charge ratio m/z of 193(1) unified atomic mass units (u), which is consistent with that of $BaOCa^+$ (193.9 u). We confirmed the assignment by introducing a photodissociating laser into the LQT and analyzing the dissociation fragments of the molecule. Depending on which dissociation pathway was resonant with the laser, fragments were detected with mass-to-charge ratios of either 40(1) or 153.7(3) u, which is consistent with Ca^+ and BaO^+, respectively (Figure 5.1d).

5.3 Electronic Structure Calculations

To aid in the interpretation of the experimental results, electronic structure calculations were performed for the $Ca + BaOCH_3^+ \rightarrow BaOCa^+ + CH_3$ reaction [SSY16, FTS09]. Optimized geometries for $BaOCH_3^+$ and $BaOCa^+$ and their fragments were obtained from density functional theory (DFT) by using the triple-z correlation consistent basis sets (cc-pwCVTZ on calcium and barium and ccpVTZ on hydrogen, carbon, and oxygen) and the B3LYP density functional. Coupled cluster theory including single and double excitations with perturbative triples, denoted CCSD(T), was used to estimate thermochemical energy differences.

To check the validity of the DFT geometries for this problem, the CCSD(T) energies of the stationary points were recalculated at geometries obtained from second-order Møller-Plesset (MP2) theory, and the changes in thermochemical energy differences were less than 1 kcal/mol. DFT and MP2 offer different approaches to the electron correlation problem, but they predict geometries of generally comparable accuracy. Discrepancies between the two

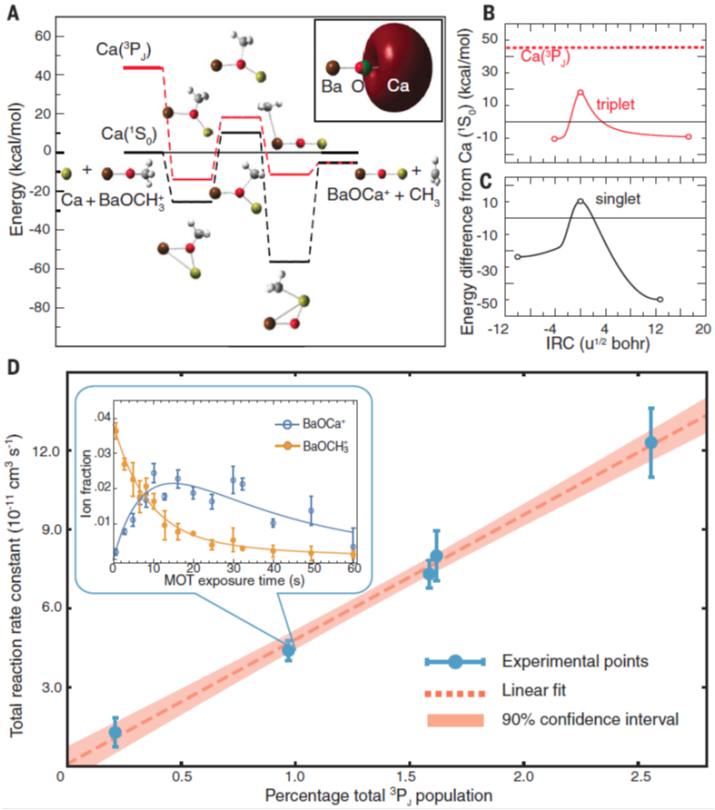

Figure 5.2: **$BaOCa^+$ production mechanism.** (a) Energy of stationary points along the Ca $^1S_0$ (black) and ^3P_J (red) reaction pathways calculated at the CCSD(T)/cc-pV5Z level of theory. The corresponding energies for the singlet pathway in kcal/mol are, from left to right, 0, -25.5, 10.2, -56.4, and -5.3, and for the triplet pathway are 43.5, -13.9, 18.1, -11.3, and -5.3. The presence of a barrier in the Ca $^1S_0$ pathway precludes reaction at low temperature, whereas the transition state in the triplet pathway is well below the energy of the reactants and does not prevent the exothermic reaction to $BaOCa^+$ and CH_3. The geometries of the complexes at each stationary point are shown below the singlet pathway and above the triplet pathway. (Inset) The linear geometry of the $BaOCa^+$ molecule and its open-shell highest occupied molecular orbital. Energy along the IRC for both the (b) singlet and (c) triplet surfaces calculated at the B3LYP/cc-pVTZ level of theory. The circles correspond to the stationary points in (a), and all energies are given with respect to the ground-state reactants. (d) Experimental total reaction rates plotted as a function of aggregate triplet Ca population, presented alongside a linear fit to the data (weighted by the reciprocal of the standard error squared) and its corresponding 90% confidence interval band. Experimental uncertainties are expressed at the 1-σ level. (Inset) The temporal evolution of both $BaOCH_3^+$ and $BaOCa^+$ amounts, normalized by initial Ba^+ number, in the LQT as a function of MOT exposure time as well as the solutions of differential equations globally fit to ∼250 kinetic data points in order to extract reaction rate constants, with a reduced χ^2 statistic of 1.03 specifying the goodness-of-fit to the displayed data set.

would be an indication that a higher level of theory should be used, but their agreement here suggests that such methods are not warranted. The electronic structure calculations were performed by using the Gaussian 09 and Molpro 2012 program packages [FTS09, WKK12].

The calculated results predicted the Ca ($^1S_0$) + $BaOCH_3^+ \rightarrow BaOCa^+ + CH_3$ reaction to be exothermic by 5.3 kcal/mol at the CCSD(T)/cc-pVTZ level of theory. Most of the exothermicity resulted from a loss of vibrational zero-point energy between reactants and products. At the more expensive CCSD(T)/cc-pV5Z level of theory, the heat of reaction increased to 8.4 kcal/mol. In mixed hypermetallic oxides, the electronic degeneracy of the metal atom locations is removed, and our calculations predicted electron localization on the Ca atom because of its higher ionization potential (Figure 5.2a). This conclusion was supported by a natural bond order analysis assigning partial charges of +1.67 to barium and +0.91 to calcium in BaOCa. Calculations also indicated that the ion has a larger permanent dipole moment (2.80 D) than that of neutral BaOCa (1.32 D), again supporting principal removal of Ba-centered electron density upon ionization. The first strong electronic transition in $BaOCa^+$ corresponds to transfer of this electron density from Ca to Ba. Because this electron does not strongly participate in the molecular bonding, the associated Franck-Condon factors are moderately diagonal and may allow optical cycling and detection [BMN14].

Further, studies of neutral BaOCa also revealed an ionization energy of 4.18 eV, which is slightly higher than in BaOBa (experimentally reported as 3.87 eV [BLA98]) but closer to BaOBa than CaOCa, which is calculated to be 4.90 eV. Calculations for neutral BaOCa also predicted that, like BeOBe, it is a diradicaloid system with a similarly small singlet-triplet splitting of only 407 cm^{-1} but with very different energies for the radical centers. The small singlet-triplet splitting in neutral MOM′ molecules is a manifestation of the spin uncoupling on the metal centers. The reaction experimentally studied in this work produces the $BaOCa^+$ cation and a CH_3 coproduct, two doublets whose spins are uncorrelated, and thus, the singlet-triplet splitting vanishes, and the potential energy surfaces are degenerate.

A calculation of the intrinsic reaction coordinate (IRC) leading from the transition state

to reactants and products was performed (B3LYP/cc-pVTZ) along the Ca ground-state singlet surface (Figure 5.2c) and revealed the existence of two bound $BaOCH_3Ca^+$ complexes, one in the entrance channel and one in the exit channel. These structures and their relative energies were further investigated at the more sophisticated CCSD(T)/cc-pVTZ level of theory (Figure 5.2a), indicating the existence of a 10.2 kcal/mol barrier to the reaction.

Last, multiconfigurational self-consistent field calculations were performed on all stationary points presented in Figure 5.2a and verified that multireference effects do not play a substantial role in the system, except possibly in the singlet transition state. To this end, natural orbital analysis and a coupled cluster theory calculation, by using the singlet wave function with the two most relevant configurations included, was performed and indicated a 3.4 kcal/mol increase in the singlet barrier height. This barrier still precludes reaction along the singlet surface, and the calculation further verifies that multireference effects would not substantially alter the conclusions of our computational study.

5.4 Experimental Search for Reaction Pathway

Given that the predicted barrier is insurmountable at experimentally realized collision energies and that the tunneling probability through the barrier is negligible, we hypothesized that the observed synthesis occurred through an electronically excited state of the Ca reactant. To test this explanation, we varied the Ca electronic state populations via control of the Ca MOT lasers and measured the resultant changes in $BaOCa^+$ production. The excited-state populations of the Ca atoms were determined from a rate equation model spanning 75 electronic states that incorporated the intensities and detunings of all near-resonant laser fields present in the MOT trapping volume [MPY17]. The chemical reaction rate for the Ca + $BaOCH_3^+3 \rightarrow BaOCa^+ + CH3$ reaction is given by $\Gamma = n_a k_t$, where n_a is the Ca atom number density and k_t the total reaction rate constant, which is found as $k_t = \sum_i p_i k_i$, where p_i and k_i are the population and reaction rate constant of the i^{th} electronic state, respectively.

The total reaction rate constant was experimentally measured by monitoring the amount of both $BaOCH_3^+$ and $BaOCa^+$ present in the LQT as a function of interaction time with a Ca MOT of known density. The solution of a differential equation incorporating all measured loss and production rates for each molecular ion due to photodissociation, chemical reactions, and background loss was then fit to the reaction kinetics data in order to determine k_t.

The experimentally measured reaction rate exhibited no statistically significant dependence on the population of the singlet Ca electronic states involved in the laser cooling process, the $4s^2\ ^1S_0$, $4s4p\ ^1P_1$, $4s5p\ ^1P_1$, and $3d4s\ ^1D_2$ states. This observation is consistent with preliminary theoretical calculations, which suggested that a reaction barrier, similar to that of the Ca ($^1S_0$) + $BaOCH_3^+$ channel, exists on all of these singlet channels.

Studies have shown spin-forbidden optical transitions lead to the production of a small number of Ca atoms in the $4s4p\ ^3P_J$ states (Figure 5.3c) in Ca MOTs [MPY17, OBF99]. Although atoms in these metastable states are not trapped by the MOT force, they are continually produced, leading to a steady-state population in the trapping volume. Further, controlling the MOT lasers can vary the electronic populations in these states and reveal how they affect the reaction rate in a manner similar to studies of the singlet state. The observed reaction rate as a function of total population in the $4s4p\ ^3P_J$ states is shown in Figure 5.2d, with a characteristic kinetics data set and the corresponding fitted solutions shown in the inset. Here, the linear dependence of the reaction rate constant on the $4s4p\ ^3P_J$ population was shown to be consistent with zero vertical intercept, suggesting that the observed formation of $BaOCa^+$ initiates predominantly along the triplet Ca (^3P_J) + $BaOCH_3^+$ surface.

Although nonadiabatic interactions from the excited singlet surfaces coupling to other electronic states could permit reaction despite the calculated barriers, the experimental observations indicate that these effects, if present, do not play a substantial role. Additionally, because the collected data are sensitive to reaction entrance channel, but not necessarily to the surface along which the reaction completed, events in which coupling from the triplet

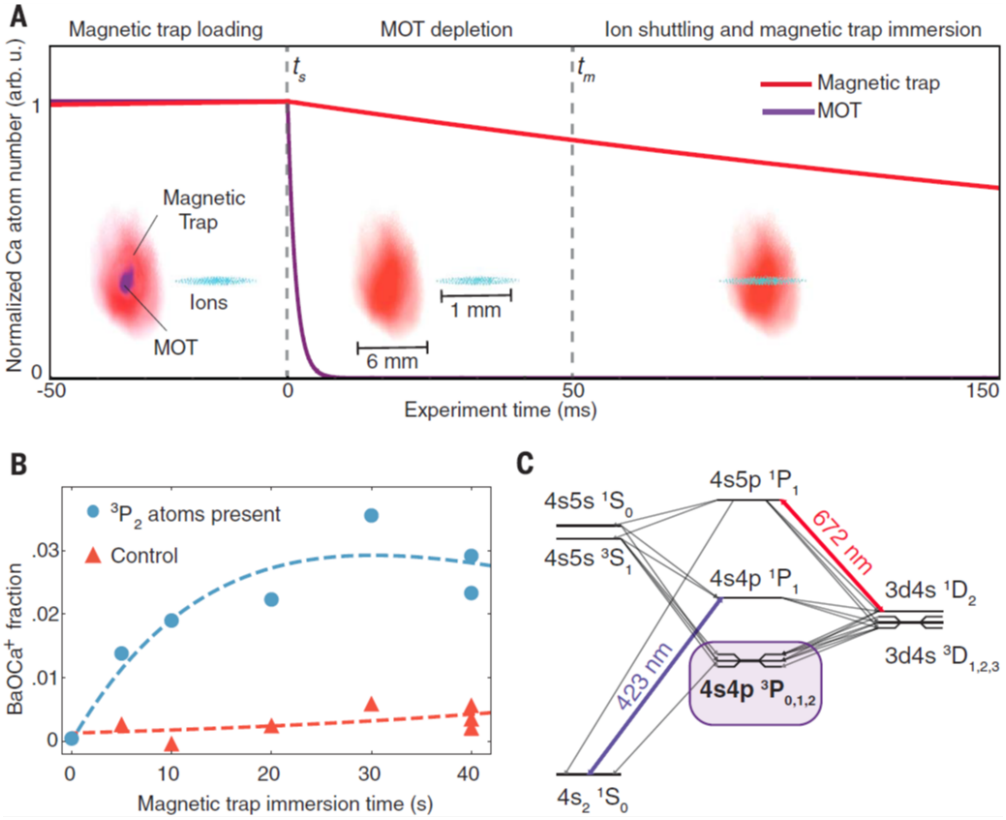

Figure 5.3: **Production of BaOCa+ through reaction with metastable magnetically trapped calcium.** (a) The number of atoms (normalized by the initial atom amount in each trap) in both the magnetic trap and the MOT probed as a function of experiment time by monitoring the amount of fluorescence produced from each when illuminated with a near-resonant laser. A typical experimental time sequence is also presented, along with scaled false-color fluorescence images of both the atoms and ions for illustration. Approximate spatial scales, provided separately for the atom and ion images, are also displayed for reference. Ions are initially displaced from the MOT as the magnetic trap is loaded. At t_s, the atom cooling beams are extinguished to deplete MOT atoms from the magnetic trap region, and the LQT endcaps are subsequently adjusted at t_m to overlap the ions with the center of the magnetic trap for roughly 500 ms, enabling $BaOCH_3^+$ reactions with Ca ($^3P_2$) atoms. (b) $BaOCa^+$ accumulation, expressed as a fraction of initial Ba^+ amount, plotted as a function of interaction time with the magnetic trap. A control case in which a laser is used to depopulate the $^3P_2$ Ca level during magnetic trap loading is also presented. Fitted solutions to differential equations, obtained in the same manner as those in Figure 5.2d, are presented alongside the data, and after estimating the magnetic trap density, they yield reaction rate constants of $8(3)\times10^{-9}$ cm^3/s and $0(3)\times10^{-9}$ cm^3/s for the experimental case and the control, respectively. (c) A level scheme for Ca including the relevant electronic states involved in the laser cooling process, with the reactive $^3P_{0,1,2}$ states highlighted.

surface to the singlet surface occurred and resulted into reaction would not be experimentally distinguishable from reactions evolving exclusively along the triplet surface.

5.5 Experimental Verification of Triplet Reaction Pathway

In order to verify the Ca ^3P_J pathway of the reaction, we performed two additional experiments. First, we measured the reaction rate of Ca atoms in a single internal quantum state, the $|^3P_2, m_J = +2\rangle$ state, by loading MOT atoms in this state into a magnetic trap and overlapping them with the ions. This experiment showed unequivocally that the reaction occurs between a Ca atom in the ^3P_J state and a $BaOCH_3^+$ ion. In the second experiment, we used additional optical pumping lasers to populate only a single ^3P_J state during Ca MOT operation, enabling the extraction of fine-structure-resolved reaction rate constants for the ^3P_J states.

Under normal MOT operation, multiple energy levels in the laser cooling cycle are populated simultaneously. Although the triplet population data in Figure 5.2d suggests the ^3P_J pathway of the reaction, it is possible that other electronic states may be contributing to the observed reaction through nonadiabatic processes. The magnetic trap, mentioned above, provides a means to isolate a sample of triplet Ca atoms and ensure that reaction initiates on the triplet surface. The magnetic trap, a separate atom trap from the MOT whose non-optical trapping force is produced by the MOT field gradients, serves as a nearly pure reservoir of Ca triplet atoms because only atoms in the $|^3P_2, m_J = +2\rangle$ state have large enough magnetic moments to produce substantial atomic trap densities.

In the magnetic trapping experiment, ions were first initialized as described earlier. To ensure that reaction only occurred between the magnetically trapped Ca atoms and $BaOCH_3^+$ molecules, the voltages of the LQT were adjusted so that $BaOCH_3^+$ ions were first displaced from the center position of the MOT by ∼3 mm, corresponding to a displacement of ∼5 MOT radii, precluding background reactions from direct MOT-$BaOCH_3^+$ overlap. After

the magnetic trap was loaded to capacity, the MOT was depleted by extinguishing the atom-cooling beams, removing any background Ca MOT atoms from the magnetic trap region within ∼5 ms. The endcap voltages were then adjusted to shuttle the ion crystal to the center of the magnetic trap, allowing it to react directly with a nearly pure sample of $|^3P_2, m_J = +2\rangle$ atoms for the duration of the magnetic trap lifetime (∼500 ms), and this process was repeated up to 100 times for each ion crystal. Here, m_J is defined with respect to the trap magnetic field direction, whereas the relative velocity vector defining the reaction is isotropically distributed, meaning that the Ca m_J sublevel is not controlled along the reaction quantization axis.

$BaOCa^+$ accumulation in the LQT was observed to increase with $BaOCH_3^+$ magnetic trap immersion time, whereas the chemical reaction rate for a control case, in which an optical pumping laser was used to depopulate $^3P_2$ atoms throughout the experiment and thus deplete the magnetic trap, was consistent with zero (Figure 5.3b). When $|^3P_2, m_J = +2\rangle$ atoms were present in the magnetic trap, a reaction rate constant of $\sim 10^{-9}$ cm^3/s was measured, which is consistent with the reaction rate measurement described earlier. Here, fluorescence imaging and spatial estimates of the magnetic trap derived from the magnetic field gradients of the MOT were used to estimate the $^3P_2$ atom number density needed for the rate constant calculation. The uncertainty of this estimate prevents a more precise measurement of the reaction rate constant.

Therefore, to find more accurate reaction rate constants and to resolve the rate constant for each of the ^3P_J fine-structure states, optical pumping lasers were used to deplete population from two ^3P_J levels simultaneously, isolating population in a single triplet state while reaction kinetics data were measured. All three measured fine-structure-resolved reaction rate constants (Figure 5.4d) were of order 10^{-9} cm^3/s, with the $^3P_1$ state exhibiting the largest rate constant value of $5.4(9)\times10^{-9}$ cm^3/s. These results are in reasonable agreement with predictions from a long-range capture theory (discussed below).

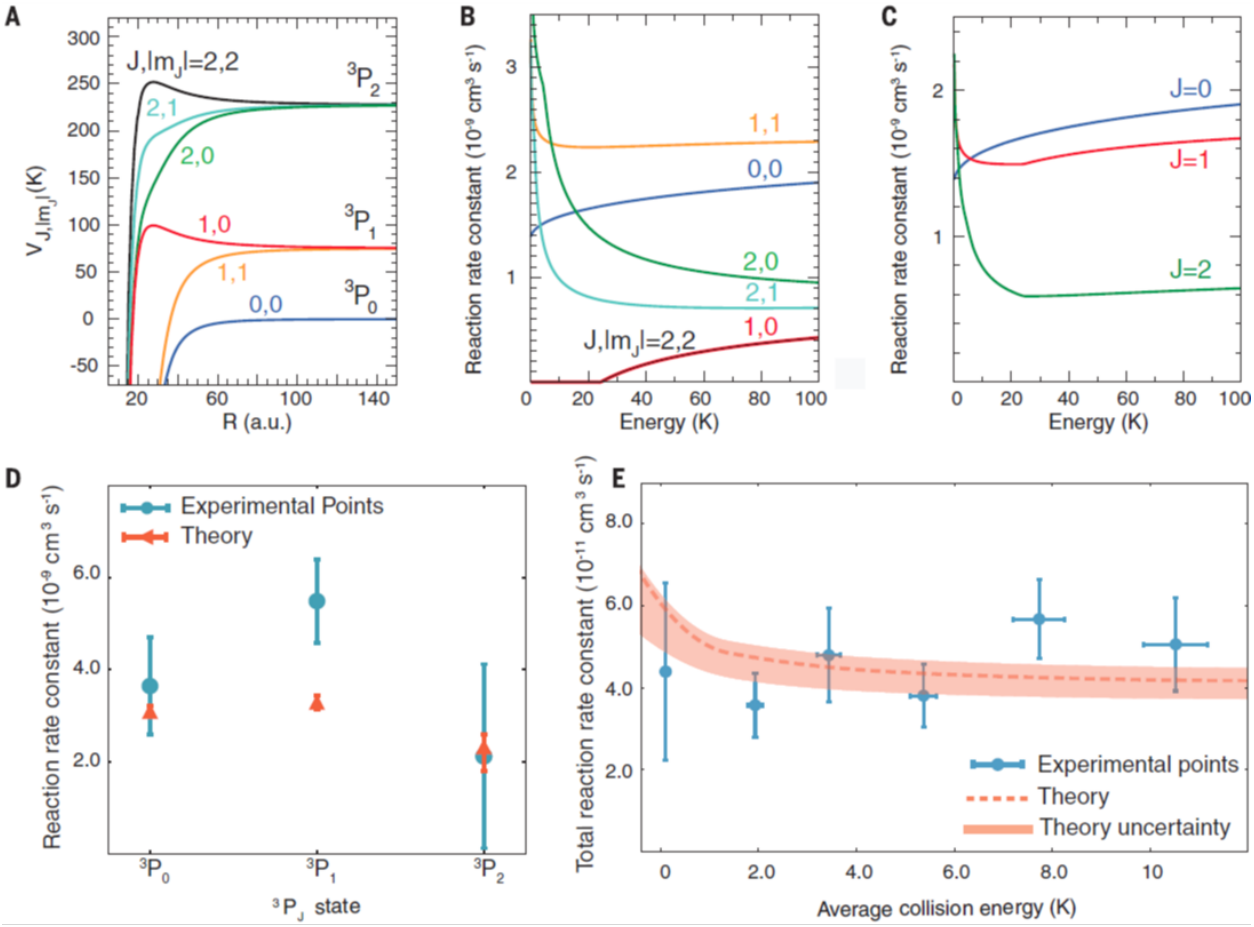

Figure 5.4: **Individual triplet-level molecular potentials and reaction rate constants.** (a) The molecular potential for each triplet sublevel. (b) The subsequent energy-dependent rate constants obtained from capture theory. (c) The m_J averaged rate constants assuming equal population of each m_J level for each J level. (d) The rate constant of each individual triplet state, measured by depopulating the other triplet states through optical pumping and acquiring reaction kinetics data. Solutions of differential equations were fitted to ∼250 kinetic data points to obtain reaction rate constants at each triplet setting, with experimental uncertainties expressed at the 1-σ level. Theoretical estimates, along with uncertainty bands associated with the polarizability and quadrupole moment values used to construct the molecular potentials in (a), are presented alongside the data. (e) The temperature dependence of the total reaction rate compared with theory by varying the micromotion energy of ions in the LQT and recording reaction kinetics data at each temperature, with the theoretical uncertainty denoted by the thickness of the theory band. Roughly 250 data points were collected at each collision energy, and experimental uncertainties are presented at the 1-σ level.

5.6 Triplet Surface Electronic Structure Calculations and Long-Range Capture Model

Having concluded experimentally that the synthesis of $BaOCa^+$ occurs via the triplet channel, electronic structure calculations, as described earlier, were performed in order to characterize the Ca (^3P) + $BaOCH_3^+ \rightarrow BaOCa^+ + CH_3$ reaction. Although the general features of the triplet potential-energy surface leading to the two product doublet molecules were similar to those discussed above for the ground state, the transition state for reaction on the triplet surface (Figure 5.2c) was calculated to be 25.4 kcal/mol (CCSD(T)/cc-pVTZ) below the energy of the reactants (Figure 5.2a and b), meaning that the reaction proceeds without barrier for each ^3P_J fine-structure state. The ground-state and triplet potential surfaces both have entrance channel complexes that feature a strongly bent Ba-O-Ca backbone, with the methyl attached to the oxygen while retaining the pyramidal *sp*3 configuration. The ground-state exit channel shows a strongly bound complex with the methyl chemically bound to Ca, whereas the triplet exit channel minimum may be characterized as a van der Waals-type interaction between a planar methyl radical and the incipient BaOCa+ molecule. This reaction shows very different dynamics on the singlet and triplet surfaces, but in contrast to the commonly seen case of a singlet atom inserting into a covalent bond [GLS03], here the triplet is more reactive because the singlet-triplet splitting is substantial in the calcium atom but small at the transition state and in the product.

The predicted absence of a barrier suggested that the observed reaction rate could be estimated from long-range capture theory. To this end, we evaluated molecular potential curves (Figure 5.4a) for Ca (^3P_J) in states (J, m_J) by considering both the long-range R^{-3} interaction associated with the quadrupole moment of the ^3P_J states and the usual R^{-4} polarization potential [MZ08, Mie73, SC85]. The curves for $\pm m_J$ are identical, resulting in three distinct curves for $J = 2$, two curves for $J = 1$, and a single curve for $J = 0$. The effect of the quadrupole moment is nontrivial, leading to barriers that reduce reaction rates

for some channels or more attractive curves that increase the reaction rates for others.

To compute theoretical energy-dependent reaction rates, we used a simple Langevin capture model [Lan05, DMW58]. The results for each (J, $|m_J|$) state as a function of the collision energy are shown in Figure 5.4b. An energy-dependent rate constant for each fine structure component J (Figure 5.4c) was calculated by summing over the m_J components. Whereas at collision energies greater than ∼10 K the rate constants decrease with J, this trend shifts drastically at lower temperatures and even reverses for collision energies below ∼1 K. To compare with experimental rate coefficients, these rates were averaged over the velocity distribution of the ions in the LQT. The results, which demonstrate reasonable agreement with experiment, are shown in Figure 5.4d, in which an uncertainty band based on a 10% range in published theoretical values for the quadrupole moments and polarizabilities used in the molecular potential calculations is also included [Der01, SCG04, MTR01].

Last, to directly probe for the existence of a barrier on the triplet surface, we monitored the collision energy evolution of the reaction rate constant. Because the micromotion energy in an ion trap scales with the spatial radial width of the ion crystal, average collision energies can be controlled by simply changing the size of ion crystals initially loaded into the LQT. Using this method, we probed reaction rates at average collision energies ranging from 0.1 to 30 K and compared the results (Figure 5.4e) with the capture theory prediction weighted by the spatially dependent energy distribution of the ions. As seen here, the measured reaction rate constant does not have a strong collision energy dependence over these temperatures and agrees with the capture theory calculation, indicating a barrierless reaction.

Further, in experiments with linear ion chains, $BaOCa^+$ formation was still observed at the lowest collision energies reached of ∼0.005 K, confirming the absence of potential barriers to the reaction at temperatures near the ultracold regime. However, at these temperatures the ion crystals used in the LQT are extremely small, and because of the large accumulation time needed for $BaOCH_3^+$ buildup and ToF measurement shot noise, accurate reaction rate data were experimentally inaccessible. Consequently, such temperatures were excluded from

the kinetics data shown in Figure 5.4e.

5.7 Summary

Through precise control of entrance channels and fine-tuning of reaction energetics, from high temperature to the ultracold regime, techniques used here and elsewhere [CDK13, KWS12, HW12, ONW10] offer promising platforms for extending the tools of ultracold physics to the study of high-precision quantum chemical dynamics. Therefore, they are expected to enable a next generation of chemical studies in the quantum regime, providing opportunities to look more deeply into chemical bonding and to anticipate and predict new chemical species and structures that may have exotic or useful properties.

CHAPTER 6

Ion Shuttling as a Method to Vary Ion–Neutral Collision Energy with High Energy Resolution

One critical parameter for these ion–neutral reactions is the collision temperature. For our experiments, the ions often have a higher velocity than the atoms due to excess micromotion. As such, the collision energy or collision temperature, is typically dominated by the ion energy or temperature. Thus, to study a cold atom–ion reaction as a function of the collision temperature, it is typical to vary the temperature of the ions. One can do this either by varying the crystal size—larger crystals will have more ions farther from the trap center, causing a large excess micromotion amplitude, increasing the average energy or temperature—or by applying a static electric field to push all the ion off the trap axis by a similar amount.

We find that either of these techniques works well for varying the average energy, but the *energy resolution* is not very high, meaning that the spread of collision energy is similar in size to its average value. To more precisely study the energy-dependence of these reactions, or to see narrow features such as shape resonances [CDK87], a higher collision energy resolution is desired. To this end, we develop and characterize such a method in this chapter, by shuttling a small crystal of ions through a stationary MOT at a roughly constant velocity. This chapter is a version of our group's publication "High-resolution collision energy control through ion position Modulation in Atom–Ion Hybrid Systems."

We demonstrate an ion shuttling technique for high-resolution control of atom–ion collision energy by translating an ion held within a radio-frequency trap through a magneto-optical atom trap. The technique is demonstrated both experimentally and through nu-

merical simulations, with the experimental results indicating control of ion kinetic energies from 0.05 to 1 K with a fractional resolution of ∼10 and the simulations demonstrating that kinetic energy control up to 120 K with a maximum predicted resolution of ∼100 is possible, offering order-of-magnitude improvements over most alternative techniques. Finally, we perform a proof-of-principle chemistry experiment using this technique and outline how the method may be refined in the future and applied to the study of molecular ion chemistry.

6.1 Introduction

Reactant collision energy can strongly influence the kinetics and product outcomes of a reaction, revealing fundamental properties about the underlying chemical system [BON15, KSS17, GMG12]. Consequently, there has been much work on creating methods capable of precisely controlling this parameter. Lee, Herschbach, and co-workers developed the crossed molecular beam apparatus to explore the effect of collision energy on the angular distributions of products in neutral–neutral reactions, revolutionizing the field of gas-phase chemistry [LML69]. Other groups [SKS15, HGS12, AS17] have since extended the technique to the millikelvin regime with improved energy resolution, enabling observations of quantum scattering resonances in reaction rates [KSS17, VOC15, KWS15, DXW10]. In this work, we take a step toward enabling similar high-resolution studies of ion–neutral reactions, which have been observed to play an important role in the formation of the interstellar medium and other astrophysical processes [IOG10, SB08, MSA99, RGM10], by developing a novel technique for controlling collision energy in these systems.

Early efforts to control collision energies in ion–neutral systems, such as the SIFT [SS96, Arm04] and CRESU [RDM84, RP95] techniques, combined gas-discharge ion sources with neutral beams of tunable temperature. Current implementations of these experiments are typically restricted to collision energies of ∼10–500 K with fractional energy resolutions of ∼10–100 [SR00], depending on neutral beam parameters. We define the fractional resolution

of a distribution X as $R_X = \overline{X}/\sigma_X$, where $\overline{X}$ and σ_X are the average and standard deviation of X, respectively.

Ion–neutral reaction experiments have recently been extended to laser-cooled hybrid systems (Figure 6.1a) capable of accessing millikelvin temperatures [LWY17, ZRP11, HH14], where they have been used to explore reaction rate dependencies on conformational and electronic states [CDK13, SRK12, HW12, RSK11, RZS12] and to produce novel chemical species [PMS17]. The majority of these hybrid systems contain radiofrequency (rf) ion traps, and typically the atom–ion collision energy is controlled by manipulating the ion excess micromotion energy, either by using electric fields to displace the ions from the rf trap null [HW12, ZPS10, ZPR10] or by changing the size of the ion sample [PMS17, HHF13, GCO09].

Upon displacing an ion from the rf trap null, the ion excess micromotion energy distribution approximately follows that of a simple harmonic oscillator (Figure 6.1b). The distribution stretches from 0 K to twice its average value, with the average energy varying quadratically with radial displacement (all energies in this work are expressed in units J/k_B = K). Similarly, when using crystal size to tune the collision energy, each ion at a distinct radial position within the crystal has a unique harmonic distribution, and upon averaging over all radial positions, the resultant energy distribution is peaked at low energies with a high-energy tail. While the average kinetic energy of an ion sample can be precisely controlled using both of these techniques, their energy resolution is $\sim$1, making it difficult to measure energetically narrow features. Furthermore, micromotion interruption collisions [CSH14] and calculations of the atom–ion spatial overlap [RSS13] may provide further complications for these micromotion-based techniques as collision energy is scanned. In particular, ions held within rf traps integrated into atom–ion hybrid systems are known to settle into Tsallis law energy distributions characterized by power-law tails after undergoing several collisions with an atomic sample [CSH14, RW17] thereby leading to extreme high energy collision events that can jeopardize controlled collision energy studies. While active laser-cooling can mitigate many of these concerns, in certain cases they can still be nontrivial; however, the

intricacies of such considerations will be omitted for simplicity in the following discussion.

Thus, other techniques have been developed to avoid these drawbacks and achieve higher energy resolutions. For example, Zeeman [CCJ17, DTS15] and Stark decelerators[OBH12] have been coupled to ion traps to probe atom–ion collision energies in the ∼10–100 K range with an energy resolution of ∼50 [PFL09]. In other work, Eberle [EDP16] and co-workers recently demonstrated a novel method that uses optical "push" beams to precisely control the motion of atom clouds for kinetic energies ranging from ≈10 to 500 mK with a resolution of ≈10.

Here, inspired by Eberle et al. [EDP16], we describe a simple alternative that can be immediately used in most existing hybrid systems. In this technique, ions are translated at fixed velocities across a neutral sample by adjusting their axial trapping potential, maintaining the ions on the rf trap null throughout the process. At constant translational ion velocity, R_E is primarily limited by the micromotion energy of the ion crystal (Figure 6.1b) and can exceed values of 100. In what follows, we describe the experimental system, investigate the shuttling technique through both experiment and simulation, and identify parameters where constant velocity ion motion can be approximately realized.

6.2 Experimental System

The MOTion trap system employed in this study (Figure 6.1a), consists of a Ca magneto-optical trap (MOT) with a co-located linear quadrupole rf trap (LQT), which is in turn radially coupled to a time-of-flight mass spectrometer (ToF-MS) [SCR12, SSY16]. An electron-multiplying charged-coupled device (EMCCD) camera and a photomultiplier tube (PMT) capture fluorescence from the ions through a reentrant flange imaging system (NA=0.2), while the MOT atoms are imaged using two separate EMCCD cameras equipped with laser-line optical filters.

An arbitrary waveform generator produces the endcap voltage waveforms that modulate

the ion axial position. Output from the generator is amplified and low-pass filtered to remove any electrical noise near secular resonances of the trapped ions.

6.3 Shuttling Principles

For small displacements from the ion trap center, the electrostatic potential in the axial dimension z at time t is given as $U_{\mathrm{ax}}(z,t) \approx \frac{\kappa V_{\mathrm{end}}}{z_{\mathrm{A}}^2}(z - z_0(t))^2$, where κ is a factor associated with the ion trap geometry, V_{end} is the endcap voltage, z_{A} is the endcap electrode spacing of the LQT, and $z_0(t)$ is the time-dependent axial equilibrium position of the trap. In our system, $\kappa \approx 0.02$ and $z_{\mathrm{A}} \approx 10.2$ mm. By adding a time-dependent voltage waveform between right and left endcap electrodes (Figure 6.1c), $z_0(t)$, and hence the ion crystal position, can be modulated at a speed proportional to the time derivative of the applied waveform. By changing the ramping speed of the waveform while keeping the peak-to-peak voltage constant, the translational velocity of the ion, and thus the ion kinetic energy E, can be conveniently controlled.

When the modulation technique is used in conjunction with laser cooling, the motion of the resulting system can be described as a damped harmonic oscillator (DHO),

$$m\ddot{z} = -k_{\mathrm{eff}}(z,t)(z - z_0(t)) + F_\beta(\dot{z}) \tag{6.1}$$

where m is the mass of the ion of interest, $k_{\mathrm{eff}}(z,t)$ is the effective spring constant of the moving endcap potential, approximated as $q\frac{\mathrm{d}^2}{\mathrm{d}z^2}U_{\mathrm{ax}}(z,t)$ where q is the charge of the ion of interest, and $F_\beta(\dot{z})$ is a velocity-dependent damping force with an e^{-1} motional damping time constant β (units s^{-1}) determined by the laser parameters of a given Doppler-cooled system. Higher order terms are neglected.

In order to achieve well-controlled energy resolution, the ion position should adiabatically follow the moving equilibrium position of the axial potential. However, if the Fourier

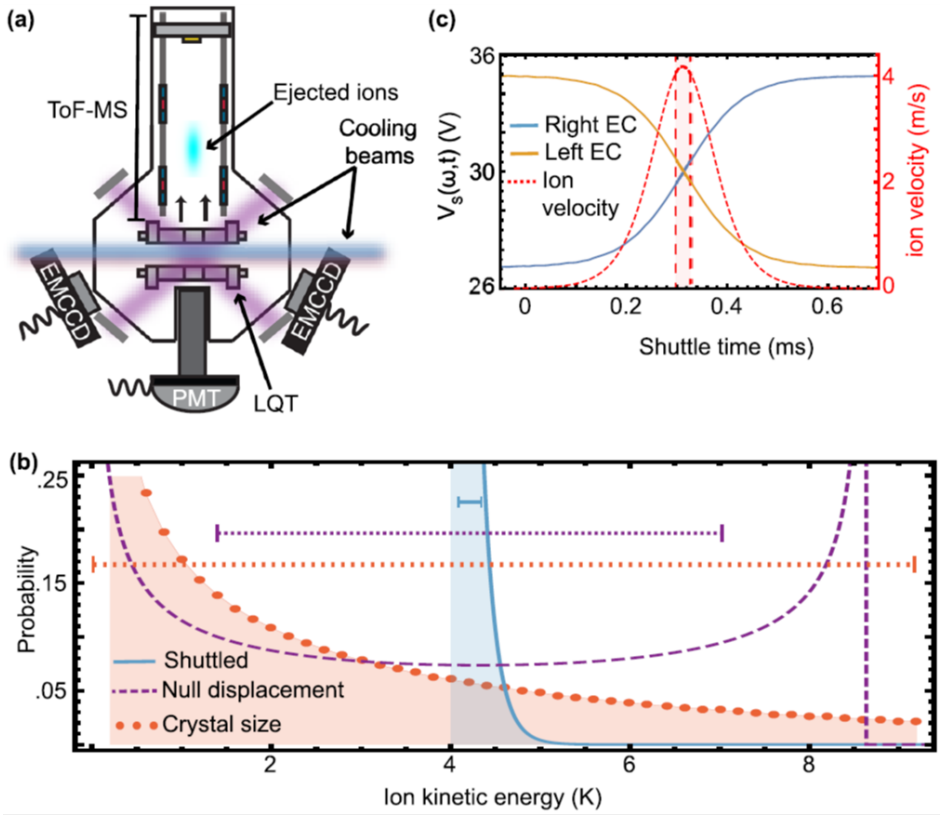

Figure 6.1: **Shuttling procedure and energy resolution.** (a) Schematic of the MOTion trap apparatus displaying an ion cloud being ejected from the 12-segment LQT (3 segments per rod) into the ToF-MS, with arrows denoting the direction of ejection. (b) Energy distributions, derived from approximate Mathieu equation solutions, of a Yb^+ sample tuned to an average kinetic energy of ∼4 K through ion chain displacement from the trap null, crystal size tuning, and idealized shuttling at a constant velocity of a crystal with an initial micromotion energy of ∼100 mK. The standard deviations for each distribution are denoted by horizontal scale bars. (c) Voltage waveforms measured on the right and left endcap (EC) electrodes of the LQT, as well as the corresponding predicted ion velocities, expressed as a function of shuttle time. The waveforms follow the $V_S(\omega, t)$ profile, presented in Equation 6.3, with $V_{DC} = 30$ V, $V_{amp} = 5$ V, $\gamma = 0.18$, and $\omega = 2\pi \cdot 95$ Hz. The portions of the waveform where the ions are stationary are omitted for clarity. The shaded region denotes the approximate period of overlap between the shuttled ions and the MOT.

transform of $z_0(t)$ possesses frequency components near secular resonances of the ion, the shuttling motion may excite secular oscillations and heat the ion. To avoid this, we raise the trap axial confinement, thereby increasing the ion secular frequency above these frequency components, and strategically choose a ramping waveform less prone to ion heating.

Waveform optimization is a well-studied problem in the quantum information community [HYH08, BOV09, BOV11, RLB06]. In this work, when transporting an ion from one shuttling endpoint to another, we implement a hyperbolic tangent profile similar to that presented in Ref. [HYH08] given by

$$f_{\tanh}(\tau) = \frac{\tanh(2\alpha\tau - \alpha)}{\tanh\alpha} \tag{6.2}$$

where τ s the shuttle time as a fraction of total shuttle duration and α is a parameter that characterizes the slope of the function, chosen to have a value of 4 in the work presented here. While a linear profile would seem to produce a flatter velocity profile at the trajectory midpoint, such a profile, once Fourier-decomposed, may possess frequency terms near secular resonances of the ion that could lead to secular heating, especially at high shuttle energies. The hyperbolic profile, while exhibiting a larger velocity spatial dependency, avoids these effects while still allowing for sufficient velocity control over the narrow region of MOT interaction such that other effects, such as excess micromotion compensation, are generally the limiting factor to energy resolution (see Section 6.5).

To meet the demands of our experiment, additional modifications were made to the applied shuttling waveform. First, the waveform was chosen to be periodic in time to allow for waveform frequency, and thus ion velocity, to be varied while not affecting other experimental parameters, such as the time-averaged spatial overlap between the atom and ion sample. Second, the waveform was constructed such that the ions remain at the stationary endpoints for a majority of the shuttling period, allowing sufficient laser cooling time to dampen any excitations that may occur during the transport process. A natural choice of waveform that

satisfies the above criteria, shown in Figure 6.1c, is given by the following piecewise function:

$$V_{\mathrm{S}}(\omega,t)=\begin{cases} V_{\mathrm{DC}}-V_{\mathrm{amp}} & 0\le t<\frac{T}{2}(1-\gamma) \\ V_{\mathrm{DC}}+f_{\tanh}\left(\frac{t-\frac{T}{2}(1-\gamma)}{\frac{T}{2}\gamma}\right) & \frac{T}{2}(1-\gamma)\le t<\frac{T}{2} \\ V_{\mathrm{DC}}+V_{\mathrm{amp}} & \frac{T}{2}\le t<\frac{T}{2}(2-\gamma) \\ V_{\mathrm{DC}}-f_{\tanh}\left(\frac{t-\frac{T}{2}(2-\gamma)}{\frac{T}{2}\gamma}\right) & \frac{T}{2}(2-\gamma)\le t<T \end{cases} \tag{6.3}$$

where ω is the angular shuttle frequency, V_{DC} is the base endcap voltage, V_{amp} is the amplitude of the shuttle waveform, $T=\frac{2\pi}{\omega}$ is the shuttle period, and γ is a factor that determines the ratio of stationary time to shuttled time during the ion trajectory. For a standard shuttle with an endpoint-to-endpoint distance of ∼1 mm, parameters are chosen as follows: $V_{\mathrm{DC}}\sim 30$ V, V_{amp} ∼2 V, γ ∼0.1, and ω can be tuned as desired from $\sim 2\pi\cdot$(0–500) Hz, providing control of the ion kinetic energy from ≈0.01 to 10 K. For reference, the axial secular frequency of our trap is typically chosen to be $\approx 2\pi\cdot$30–150 kHz for the range of axial confinements explored in this work.

Fluorescence from the laser-cooled Yb^+ ions was collected with an EMCCD while shuttling. Shuttling images are presented in Figure 6.2 for a single ion, a five-ion chain, and a two-dimensional Coulomb crystal, the last two of which are embedded with a non-laser-cooled Yb^+ isotope, indicating that this technique may also be used with sympathetically cooled species, such as molecular ions.

6.4 Experimental Investigation of Technique

6.4.1 Fluorescence Detection While Shuttling

Understanding the energy dynamics of the shuttled ions requires knowledge of their velocity distribution. In order to experimentally characterize this distribution, a $^{174}Yb^+$ crystal was shuttled over a ≈1 mm distance by applying $V_{\mathrm{S}}(\omega t)$ to the endcap electrodes of the ion trap.

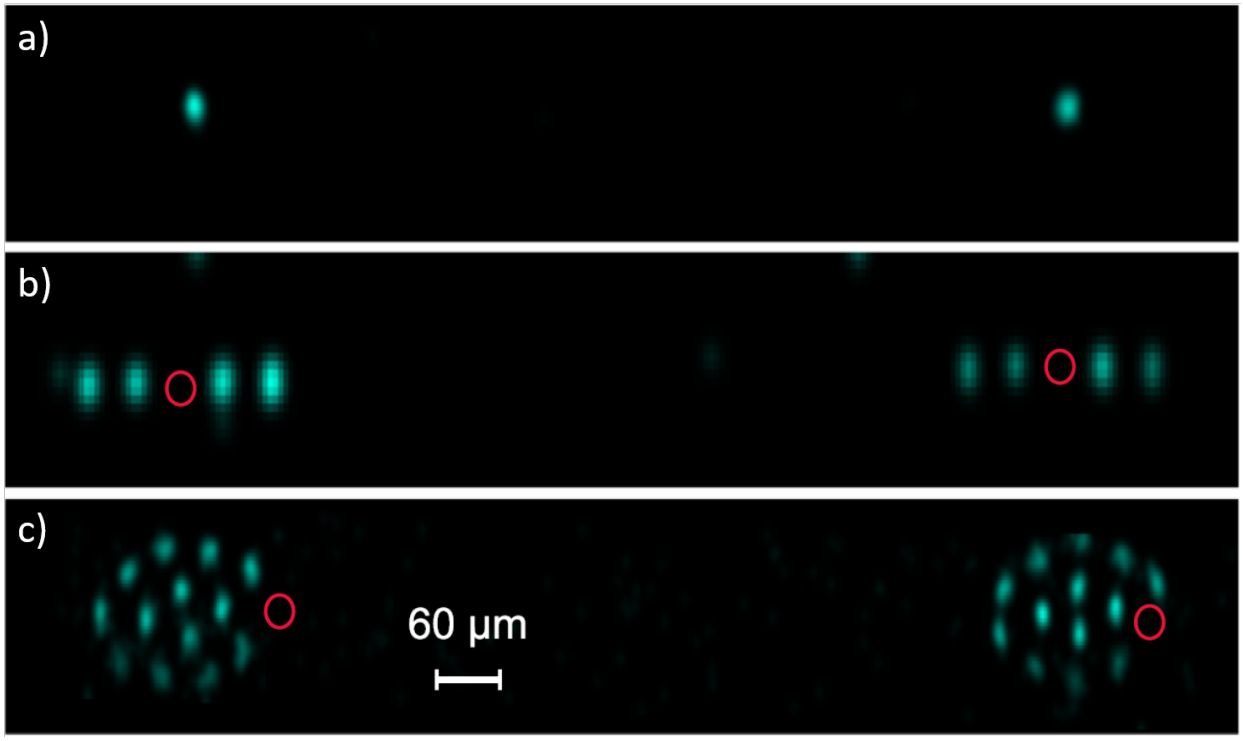

Figure 6.2: **Ion shuttling imaging.** False-color experimental fluorescence images of Yb^+ ions undergoing shuttling presented for the following cases: (a) a single ion, (b) a five-ion chain with one non-laser-cooled dark isotope, and (c) a two-dimensional Coulomb crystal with one embedded dark isotope. As the ions spend ∼90% of the time at the trajectory endpoints, their fluorescence is only evident in these locations.

The EMCCD in our imaging system was replaced with a PMT to record the ion photon scattering rate throughout the shuttling process.

The photon scattering rate of laser-cooled Yb^+ can be approximated [MS07] as

$$\Gamma_{\text{scat}}(v_z) = \frac{\Gamma}{2}\frac{s}{1+s+4\frac{(\delta-k_z v_z)^2}{\Gamma^2}} \tag{6.4}$$

where Γ is the transition linewidth, s is the saturation parameter of the cooling laser, given as I/I_{s} where I is the intensity of the laser beam and I_{s} is the saturation intensity of the transition, δ is the detuning of the laser from resonance, k_z is the magnitude of the k-vector of the axially aligned cooling laser, and v_z is the z-component of the ion velocity. The

scattering rate is insensitive to micromotion or secular motion in the radial dimension.

6.4.2 Ensemble and Spatial Averaging of Velocity Distributions

For a single shuttled ion, the velocity-dependent scattering rate (see Equation 6.4) during each PMT time acquisition bin (∼10 ns width) can be used to measure $v_z(t)$. In order to enhance the PMT signal in the experiment, we interrogate an ensemble of ∼100 ions, and consequently, the velocities extracted in each time bin are ensemble averages of the total axial velocity distribution, defined as $\langle v_z \rangle$. Here, we define the ensemble average of a data set X as $\langle X \rangle$.

Furthermore, the shuttled ions are only overlapped with the neutral sample at the center of the ion trap for a small portion of their trajectory. Therefore, the relevant resolution to consider is the resolution of $[\langle v_z \rangle]_{\mathrm{S}}$, the velocity distribution with weighting factors determined by the spatial overlap of the ions at each shuttle time with an atom sample of characteristic length scale w_{A}. Here, we define the spatially weighted distribution of a data set X as $[S]_{\mathrm{S}}$ [HBC14]. For optimal resolution, the neutral sample should be placed at the center of the ion trajectory where the ion velocity is most constant.

6.4.3 Simulation Parameters

The experimental results are compared to predictions of molecular dynamics (MD) simulations conducted with the SIMION 8.1 software package [Dah00], as shown in Figure 6.3a and b. The simulation software employs finite difference methods to numerically solve Laplace's equation for a given set of electrodes and point charges, allowing for determination of ion trajectories and energy distributions. Time-dependent trapping potentials were incorporated into the simulation to properly include the effects of micromotion, and ion–ion repulsion was treated by superimposing the Coulomb interaction from co-trapped ions with the potential produced by the quadrupole trap electrodes. The simulations were performed using 100 ions,

approximately equivalent to the number used during the experiment, and also employed a laser-cooling damping force whose velocity profile was derived from a simple four-level rate equation model.

In order to optimize the accuracy of the simulated laser cooling force, both in experiment and simulation, the ions were initialized in the LQT, non-adiabatically transported between trajectory endpoints through a square-wave-like voltage ramp, and subsequently observed as the laser cooling force damped the motion of the excitation (Figure 6.3c). The saturation parameter of the simulated laser cooling force was adjusted until the e^{-1} decay constant β matched that observed in experiment. We also investigated how this damping time scale varied with laser cooling intensity by repeating the above measurement at various laser powers (Figure 6.3d). The results are comparable with those expected from our rate equation cooling model and are instructive when considering what laser cooling parameters to implement while shuttling. Namely, one should operate in a laser cooling regime such that the time spent at the shuttle endpoints during each cycle is much longer than the damping time, ensuring the ions are sufficiently cooled before the next shuttle cycle begins. Furthermore, the simulations confirm that at experimental conditions, the laser cooling damping force does not significantly influence the trajectory of the ions while shuttling.

6.4.4 Analysis of Results

The experimental and simulated results for $\overline{[\langle v_z \rangle]}_{\mathrm{S}}$ are in reasonable agreement (Figure 6.3a). Both exhibit a linear relationship with waveform frequency, affirming that ω_{A} can be varied to predictably control the velocity, and thus collision energy, of the ions. The trajectory for the ions assuming a damped harmonic oscillator model, shown in Figure 6.3b, also appears to describe the ion motion well, confirming that the model may be used to gain intuition about the shuttling procedure. We attribute minor discrepancies between the simulation and experiment, such as differing damping time scales and amplitudes of secular oscillation while shuttling, to imperfect voltage matching due to unmeasured electrode charging and rf

pickup, minor discrepancies in laser cooling velocity profiles, and effects not considered in the simulation such as micromotion interruption collisions with background gas particles.

The experimental energy resolution can also be compared to predictions from simulation. $\overline{[\langle \hat{E}_z \rangle]_S}$, defined as $\frac{1}{2}m\overline{[\langle v_z \rangle^2]_S}$, was scanned over ≈0.01–1 K over the velocities explored in Figure 6.3a, with probing of higher kinetic energies precluded by difficulty in discriminating between scattering rates at large v_z. Shown in the inset of Figure 6.3a, the measured ensemble-averaged axial energy resolutions, $R_{[\langle \hat{E}_z \rangle]_S}$, were determined to be ≈10, in agreement with simulations.

However, the resolution of the non-ensemble-averaged kinetic energy distribution, $[E_z]_S = \frac{1}{2}m[v_z^2]_S$, is the more relevant quantity to consider when characterizing collision energy control since it is sensitive to center-of-mass frame velocity dispersions. Measuring $R_{[E_z]_S}$ involves knowing the velocities of each individual ion, information unavailable with our velocimetry technique. Therefore, we utilize the simulations to estimate this quantity and obtain $R_{[E_z]_S}$ ≈6.

Experimental average velocity distributions were also obtained at various levels of axial confinement, and, as expected, higher axial confinement offered superior resolution. To exaggerate this effect, we performed a shuttle using a linear ramping profile prone to ion heating and observed that increased confinement more effectively suppressed secular oscillations (Figure 6.3e). Probing of even higher axial confinements was prohibited in our system by technical considerations.

6.5 Single Ion and Molecular Ion Simulation Results

While Section 6.4 demonstrates large ion samples can be successfully shuttled, the resolution is maximized when used with a single ion, where ion heating effects are minimal and the ion shuttling energy can dominate over its micromotion energy. In this section, kinetic energy will refer to the total kinetic energy of the ion, including both axial and radial motion.

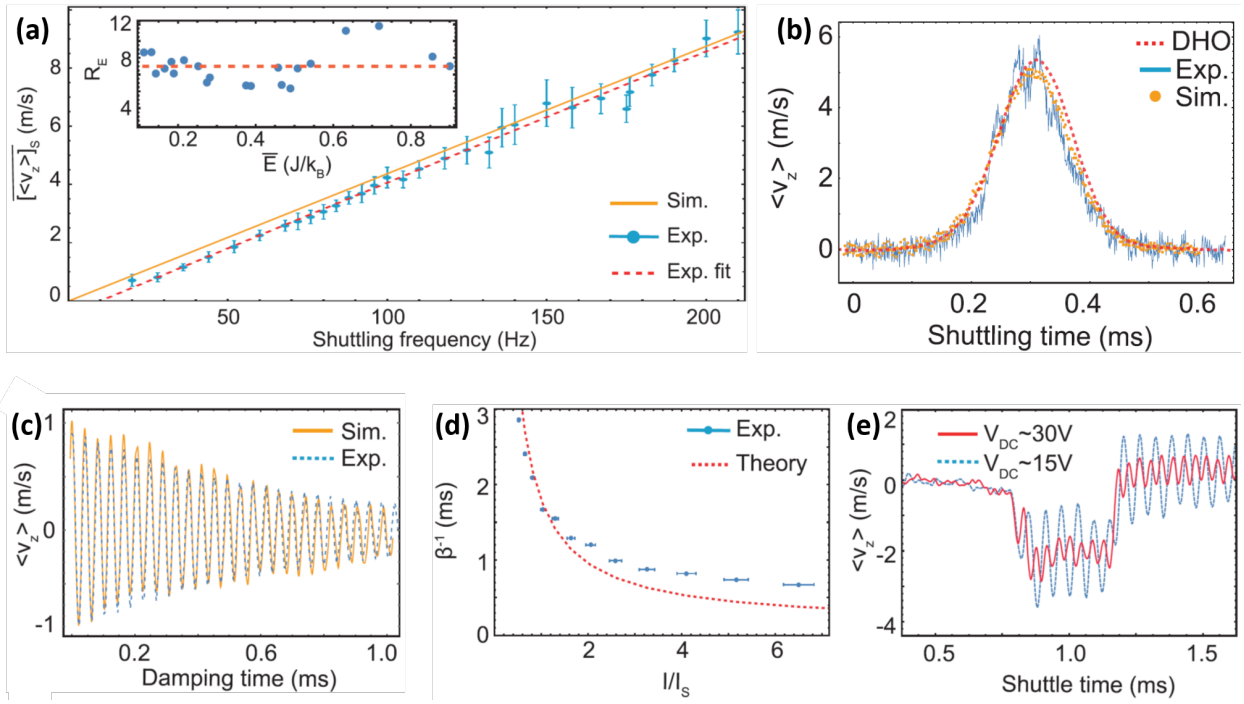

Figure 6.3: **Doppler velocimetry and large crystal simulation results.** (a) Experimentally measured $\overline{[\langle v_z \rangle]_S}$ of a ∼100 ion crystal obtained through Doppler velocimetry at different shuttling frequencies, where the error bars are displayed at the 1-σ level. The experimental results show reasonable agreement with MD simulations. A linear fit applied to the experimental data shows that varying the shuttle frequency modifies the axial velocity of the trapped ions in the expected way. The inset shows the corresponding mean kinetic energies and energy resolutions obtained at the various shuttling frequencies, with the dotted line referring to the average resolution. Note here that the plot refers to averages and resolutions of the distribution $[\langle \hat{E}_z \rangle]_S$, but the subscript was omitted in the plot for clarity. (b) Experimental $\langle v_z \rangle$ values, obtained as a function of shuttle time at a shuttle frequency of 120 Hz, are compared to results of a MD simulation and the predictions of a 1D damped harmonic oscillator model. (c) The effects of laser cooling on damping secular motion from both simulation and experiment. The saturation parameter used to construct the laser cooling force in the simulations was tuned until β matched well with experiment. (d) Experimental damping time scales are obtained as a function of laser cooling saturation parameter and are compared with predictions from a rate equation model. Horizontal and vertical error bars are expressed at the 1σ level, with the latter being smaller than the data points. (e) Measured $\langle v_z \rangle$ as a function of shuttle time for two different axial confinement strengths. The shuttle was performed with a linear ramping profile more prone to ion heating than $f_{\tanh}(t)$ in order to accentuate the increase in energy resolution that is possible with greater axial confinement.

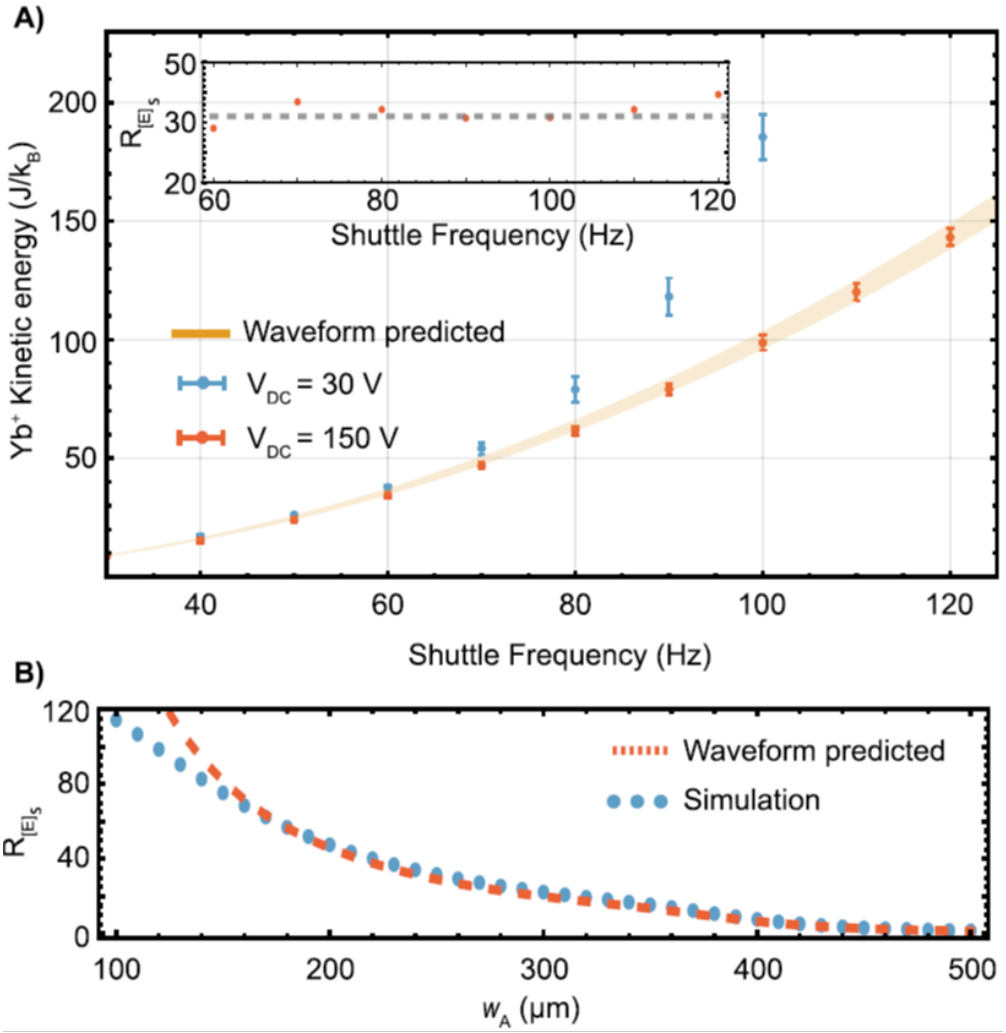

Figure 6.4: **Single ion simulation results.** (a) Total kinetic energy for a simulated single ion shuttled at various waveform frequencies using two separate axial confinements. The simulations performed at the higher axial confinement display higher energy resolutions and exhibit less significant secular oscillations, as evidenced by their adherence to the waveform-predicted energy, shown in bands. Error bars are expressed at the 1-σ level. The inset in the figure shows $R_{[E]_S}$, the total kinetic energy resolution including both axial and radial motion, for the high axial confinement simulations, with the average resolution of ≈35 denoted by the dotted line. Low axial confinement simulations produced average energy resolutions of ≈20. (b) $R_{[E]_S}$ of a simulated ion shuttled at ≈100 K of kinetic energy as a function of neutral cloud spatial dimension. The results are compared to the resolutions that would be expected if the ions perfectly followed the motion of the equilibrium position without any micromotion or secular excitation.

While our experimental optical detection efficiency prevents extensive single ion measurements, reasonable best-case- scenario simulations are performed with a single Yb^+ ion utilizing the electrode geometry of the MOTion trap and the laser cooling profile described in Section 6.4. Furthermore, laser cooling while shuttling was necessary in the work discussed in Subsection 6.4.1 for Doppler velocimetry purposes, but in general laser cooling may be switched off during transport if, for example, finer control of ion electronic state populations is desired. However, we choose to maintain laser cooling throughout the shuttling process in the following simulations for consistency with the simulations performed in Subsection 6.4.4. The end-to-end shuttle distance, experimentally limited to ≈1 mm by the field of view of our imaging system, is increased to ≈2 mm to enhance energy resolution. Furthermore, idealized waveforms were implemented in the simulation instead of the waveforms measured in the experiment, where unintended filtering due to trap electronics and rf pickup caused slight waveform distortion.

These simulations, presented in Figure 6.4a, were performed at two different axial confinements ($V_{\mathrm{DC}} = 150$ V and 35 V) and once again indicate that confinement plays a pivotal role in determining energy resolution. When the endcap voltages were raised to 150 V in the simulation, the rf voltage amplitude was also increased by a factor of 2 relative to the low-confinement case to prevent radial defocusing caused by the increased axial confinement. At high enough axial confinements, further resolution improvement is eventually limited by the need to operate at increasingly large rf voltages to avoid this defocusing effect, forcing the trap toward high Mathieu q-parameter regimes where the ions become unstable.

At higher energy, in particular, the results presented in Figure 6.4a indicate that low axial confinement can facilitate secular excitation of the ion motion. The excitation can cause the ion to either lag or lead the equilibrium position of the moving potential during MOT interaction, increasing the ion kinetic energy spread. At high enough energies, the shuttling process is no longer adiabatic, leading to large-scale secular oscillations that significantly broaden the ion kinetic energy distribution, as evidenced in the increasing energy spreads

for the low axial confinement points in Figure 6.4a. However, increasing the axial confinement postpones this behavior until higher energies. For $V_{\mathrm{DC}} = 150$ V, the ion position follows $z_0(t)$ closely for kinetic energies up to 120 K while the kinetic energy resolution, $R_{[E]_{\mathrm{S}}}$, approaches 35 for $E \gtrsim 2$ K. Here the resolution is limited by a combination of increased micromotion energy at the large axial confinement, minor secular excitation during transport, and non-uniformities in the velocity profile of the shuttling waveform.

On the other hand, for $E \lesssim 2$ K where secular oscillations play less of a role, the resolution is ultimately limited by excess micromotion compensation techniques, which are typically accurate to within ∼10 mK in quadrupole traps with dimensions similar to that used in this work. In this low-energy regime, $V_{\mathrm{DC}} \approx 5$ V is optimal since the reduced confinement limits micromotion from radial defocusing, permitting $R_{[E]_{\mathrm{S}}} \approx 20$.

While a 250 μm neutral cloud size was assumed when computing the energy resolutions in Figure 6.4a, further resolution increases can be realized by reducing the size of the neutral atom sample, thereby also reducing the sampled velocity spread of the ion trajectory. Often the spatial dimensions of neutral atom traps can be conveniently tuned using optical or magnetic fields, with some atom systems, such as dipole traps, approaching 5 μm in size [ZFT09]. In Figure 6.4b, R_E is shown as a function of w_{A}, with resolutions in excess of 100 predicted for atom traps nearing the 100 μm regime. Conversely, resolution may also be improved by increasing the distance between shuttling endpoints for a fixed atom cloud size. Increases in shuttle distance would also have the added benefit of mitigating secular oscillations as a lower frequency waveform with Fourier components further spaced from ion secular resonances could be used to obtain a given shuttle velocity. However, this improvement would come at the expense of more difficult micromotion compensation, as to be discussed below.

The simulations do not consider the effect of atom–ion collisions on the ion trajectory; however, at experimental atomic densities ($\approx 10^{10}$ cm^{-3}), over the range of energies explored in the simulations, there is a $\approx 10^{-3}$ probability of a collision occurring with the MOT atoms in a given shuttle cycle. Therefore, any deviations from the expected ion motion

caused by collision events are not expected to influence the energy of subsequent collisions, as there is only a $\approx 10^{-6}$ probability of a second collision occurring before the ion motion is reinitialized through laser cooling at the trajectory endpoints. Additionally, to reduce the effect of background gas collisions on the ion trajectory, the technique may be used under ultra-high vacuum conditions.

Furthermore, the technique may ultimately be limited by effects unconsidered in the simulations, such as patch potentials and electrode charging, that make it difficult to optimally micromotion compensate at each trajectory position, especially given the comparatively large size of the utilized ion trap and the limited number of compensation electrodes.

For example, in our system, if excess micromotion compensation is performed at the center of the shuttling trajectory, we experimentally observe ~ 100 mK of uncompensated excess micromotion at the trajectory endpoints displaced 2 mm from the center point. While proper compensation throughout the trajectory may be a challenge in certain applications, we note that proper compensation in the narrow region of MOT interaction is most important for determining collision energy resolution, as the micromotion amplitude of the ion motion generally adiabatically follows any local uncompensated electric field. Furthermore, axial micromotion may provide additional complications, although radial micromotion will likely dominate this effect. Through simulations performed using our system, we observe < 2 mK difference in ion energy due to axial micromotion between the center of our shuttling trajectory and a point displaced 2 mm from the center; however, experimental imperfections may further increase this value.

To minimize these effects, the appropriate electrode shim voltages can first be identified for the ions at each trajectory position while the ions are stationary. Subsequently, the shim voltages can be updated while shuttling to ensure uniform micromotion compensation as the ion transits from one endpoint to the other. Additionally, excess micromotion compensation techniques, such as photon cross-correlation spectroscopy [BMB98] or parametric excitation [KPB15], may be used to compensate micromotion with greater precision and maintain ions

with excess micromotion energies nearing $\lesssim$5 mK.

While the precise kinetic energy control of laser cooled species is beneficial, ultimately this technique may be most useful when applied to molecular ion chemistry, where it can be used to detect nuances in long range capture models [SLG16] and possibly illuminate rotational and vibrational resonance features that have thus far evaded current techniques. To explore this possibility, simulations are performed while shuttling two laser cooled Ba^+ ions and a sympathetically cooled $BaCl^+$ molecular ion, with the resulting energy distributions of the molecular ion depicted as a function of shuttle frequency and trajectory position in Figure 6.5a and b, respectively. In contrast to Yb^+, Ba^+ possesses a Λ level-structure system, and thus, the three-level optical Bloch equations are solved to account for coherent-population-trapping effects in the simulated laser cooling force.

The results from the simulation demonstrate that, similar to the Yb^+ single-ion case, energy resolutions for $BaCl^+$ approaching 40 are achievable assuming a neutral atom cloud size of 250 μm, a value over an order-of-magnitude greater than that offered by alternative micromotion-based techniques in this energy range and one that can be further improved by changing the axial confinement and employing a smaller atom cloud size, as discussed earlier in this section. At kinetic energies below 1 K and when combined with a light mass atomic partner that would yield a low reduced mass, this resolution may be sufficient to resolve reaction resonance features, which have been predicted to have collision energy widths of order $\sim$ 1–10 mK [SRA15], although the particulars of the resonance of interest and control of the systematics alluded to above will ultimately determine if this is feasible. Here, the collision energy is proportional to the reduced mass of the atom–ion system, and in most current hybrid systems, the average and the width of its distribution are typically a factor of $\approx$1–10 smaller than the corresponding kinetic energy values.

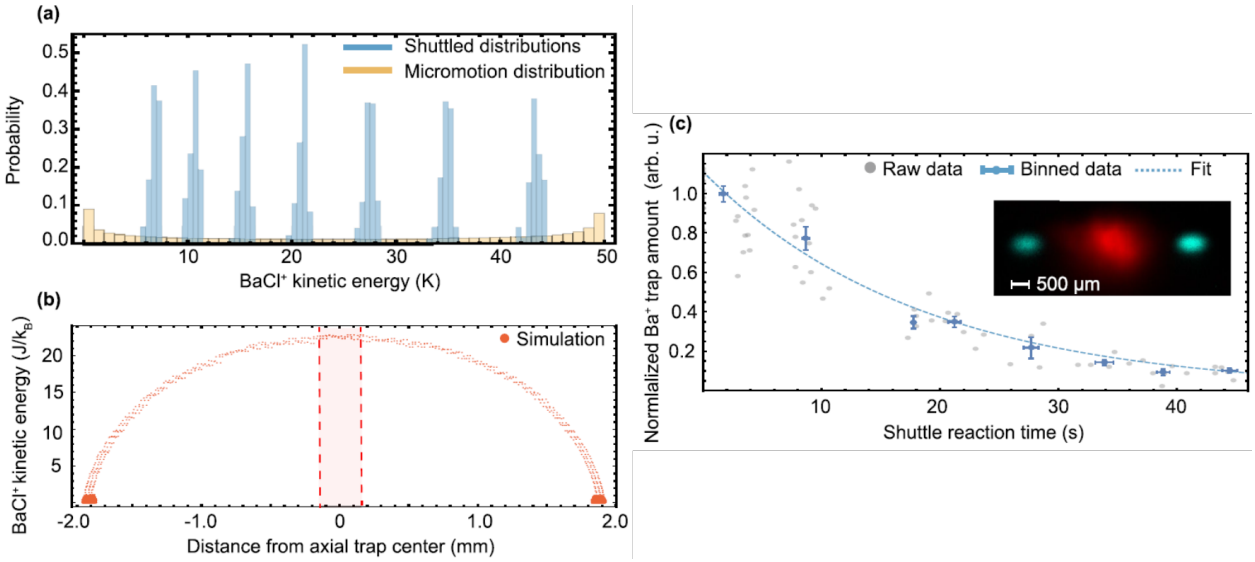

Figure 6.5: **Controlled chemistry implemented with ion shuttling.** (a) Simulated energy distributions for a single shuttled $BaCl^+$ molecular ion sympathetically cooled by two laser-cooled Ba^+ ions. The shuttled distributions are presented for a variety of shuttle frequencies and are compared to the theoretical distribution obtained from using the excess micromotion of a single ion to access an average kinetic energy of ≈ 25 K. (b) Simulated $BaCl^+$ kinetic energy as a function of axial ion position while shuttling. The dashed lines enclose the 250 μm effective region of MOT interaction where the ion velocity is approximately constant. (c) Decay of Ba^+ amount from the LQT as a function of shuttling time when a Ca MOT is placed at the center of the trajectory. The inset displays superimposed experimental fluorescence images of a $\sim$ 500 ion Ba^+ sample and a Ca MOT containing roughly one million atoms taken while performing a shuttling reaction rate measurement. The large ion sample utilized in the experiment was initially liquid upon loading into the LQT and remained so while shuttling.

6.6 Demonstration of Technique for Charge-Exchange Reaction Investigation

As a proof-of-principle experiment, a cloud of $\approx$ 500 Ba^+ ions was loaded into the LQT and shuttled through a Ca MOT located at the center of the ion trajectory at an average kinetic energy of 14(4) K. Here the resolution was limited by the inherent excess micromotion energy of the three-dimensional crystal. Figure 6.5c shows the decay of Ba^+ ion amount in the LQT, measured by the ToF, as a function of shuttling duration due to charge-exchange

collisions with ground-state Ca. The inset in Figure 6.5c presents superimposed images of the atoms and ions obtained during shuttling, with each image taken using separate laser line optical filters. The geometric overlap between the atoms and ions was measured by phase-triggering the EMCCD cameras on the shuttling waveform to acquire ion images, and hence ion positions, at various points along their trajectory. This technique allowed for the effective imaging of ions with velocities $\lesssim$ 50 m/s, bounded by effects related to the minimum camera exposure time of 10 μs. For velocities in this range, the ions are seen to follow the expected shuttling trajectory and numerical simulations are used to verify this trend at higher collision energies. After the overlap factor was verified, measured atomic densities were used, in a manner similar to Ref. [PMS17], to calculate a total reaction rate of $2.4(4)\times10^{-11}$ cm^3/s, a value consistent with a previously measured result [SRK12] after ion excited state fraction normalization.

This proof-of-principle experiment demonstrates that this technique can be used to measure accurate rate constants for reactions between laser-cooled species and neutrals, paving the way for similar studies incorporating sympathetically cooled molecular ions.

6.7 Conclusion

Blending techniques from the quantum information and hybrid trapping communities, we have demonstrated a method for controlling ion–neutral collision energy based on ion axial position modulation that is capable of offering energy resolutions, $\overline{E}/\sigma_E$, from $\sim$ 10 to 100 over kinetic energies ranging from $\approx$0.05 to 120 K. This combination of both range and resolution improves on alternative techniques that typically compromise one for the other. In addition to investigating the technique through experiment and simulation, we also performed a reaction rate measurement by shuttling laser-cooled atomic ions, and we suggested how the shuttling method may be implemented in future experiments to study molecular ion chemistry.

Furthermore, the technique can be immediately implemented in currently existing hybrid traps with little experimental overhead. The shuttling procedure is also quite adaptable, and properties such as axial confinement, neutral atom size, and endpoint-to-endpoint shuttle distance can be custom-tailored to a variety of experimental conditions to obtain desired energy resolutions while obeying most experiment-specific constraints.

Additional improvements may further increase the effectiveness of the technique. Ion traps with multiple-segmented endcap electrodes that can more reliably compensate micromotion and produce more pure harmonic potentials throughout the trap may be utilized, allowing the ions to be shuttled over longer axial distances and while minimizing their acceleration in the MOT region. Furthermore, if laser cooling during transport is necessary for a particular application, Doppler shifting of the ions while shuttling may be problematic if constant electronic state populations are desired. To this end, one may choose to appropriately adjust the frequency of the Doppler cooling laser while shuttling in order to produce a constant effective laser detuning. In addition, an imaging system with higher capture efficiency and a radial probe beam may be used to apply the Doppler velocimetry technique toward detecting the radial micromotion of single ions while shuttling and thus set more realistic bounds on excess micromotion compensation.

Finally, the waveforms utilized in this proof-of-principle study were largely chosen out of convenience and speed of implementation. While sufficient for the purposes of this work, they are by no means optimal. More sophisticated waveforms [Osw15, FGP14, CLM16] that maintain flatter velocity profiles while not inducing secular heating may be used if even finer energy resolution is required.

CHAPTER 7

Reaction Blockading: Suppression of Low-Temperature Excited-State Reactions of $BaCl^+$ with Ca

One reason we choose to use Ca atoms to sympathetically cool $BaCl^+$ is that reactions of $BaCl^+$ with ground-state Ca are energetically forbidden, so collisions can sympathetically cool the $BaCl^+$ without destructive reactions. As Ca is laser-cooled, there is a steady-state population fraction in excited states, labeled Ca*, that can be reactive. While these reactions can be interesting to study, for sympathetic cooling they are a nuisance and should be minimized. An effect known as reaction blockading occurs in these reactions at low temperature, suppressing these excited-state reactions. Reaction blockading occurs because the electric field due to the presence of a nearby ion shifts the atomic energy levels, causing the Ca cooling lasers to become off-resonant when the atom and ion are in close proximity. At low temperature, when the atom and ion are slowly approaching each other, the shift increases the likelihood of a ground-state collision, suppressing the probability of a potentially destructive excited-state collision. While this effect is expected in such low-temperature, excited-state reactions, it had not been observed prior to this work. In this chapter, we present evidence of reaction blockading for low-temperature reactions with $BaCl^+$ and Ca* and report the branching fractions of different possible reaction products. This chapter is a version of our group's publication "Reaction blockading in a reaction between an excited atom and a charged molecule at low collision energy."

Recent advances have enabled studies of atom–ion chemistry at unprecedentedly low temperatures, allowing precision observation of chemical reactions and novel chemical dynamics.

So far, these studies have primarily involved reactions between atoms and atomic ions or non-polar molecular ions, often in their electronic ground state. Here, we extend this work by studying an excited atom–polar-molecular-ion chemical reaction ($Ca^* + BaCl^+$) at low temperature in a hybrid atom–ion trapping system. The reaction rate and product branching fractions are measured and compared to model calculations as a function of both atomic quantum state and collision energy. At the lowest collision energy we find that the chemical dynamics differ dramatically from capture theory predictions and are primarily dictated by the radiative lifetime of the atomic quantum state instead of the underlying excited-state interaction potential. This reaction blockading effect, which greatly suppresses the reactivity of short-lived excited states, provides a means for directly probing the reaction range and also naturally suppresses unwanted chemical reactions in hybrid trapping experiments.

7.1 Introduction

Over the past decade, techniques from ultracold physics have been adapted to the study of chemical systems, bringing unique capabilities including precise control of the reagent quantum states and energy [KSS17, CDK09, DFN16, TSC13]. While early work focused on all-neutral chemistry, more recently there has been a shift to the study of charged–neutral reactions [HAR13, RSK11, LWY17, RZS12, SMB18], as available techniques allow the probing of a wider range of energy [BM18] and species, as well as trapping and the study of reaction products [SCR12, SSY16, SGM17]. These so-called hybrid systems have already been used to study the reactions of several atom–ion combinations [TJG19, YLC18, HW12, ZPS10, ZPR10], showing a dependence of reactivity on molecular conformation [CDK13] and the production of novel molecules [PMS17]. Despite this work, there has yet to be a study of atom–polar molecular ion chemistry in these systems. Given that such reactions play a central role in the chemistry of the interstellar medium [SZ96, Smi92, RGM10], which provides the raw materials from which stars, planets and potentially even life developed,

understanding these reactions at low temperature is a fundamental goal for chemistry and physics. Moreover, these same reactions could severely limit experiments aiming to produce quantum-state-selected polar molecular ions [CB18, SHD13, WWH16] via sympathetic cooling [RSS13, Hud16, HLC15] for quantum logic applications [HC18].

Here, we advance these fronts by using a hybrid trap to study the reaction between electronically excited Ca atoms and $BaCl^+$ molecules. Using the capabilities of the hybrid trap, we measure the reaction rates and product branching fractions of these reactions at collision energies from 15 K down to 0.2 K (all temperatures in this work refer to collision energies in units of J/k_B =K, where k_B is the Boltzmann constant). At the lowest energies in our study, which are among the lowest ever studied in a molecular ion–atom system [HLC15, MRJ15, ADS17, HS91], we find a chemical regime where the chemical dynamics are primarily dictated by the radiative lifetime of the reagent quantum state instead of the underlying excited-state interaction potential. Additionally, we provide a simple rule for calculating at what temperature this regime (where the collision time is longer than the radiative lifetime of the quantum state) is reached.

This result parallels previous work in excited-state ultracold neutral–neutral systems where reduced reaction rate constants have been observed and explained as a consequence of spontaneous emission suppressing a short-range excited-state population [JM89, GP89]. Subsequent studies also demonstrated that external optical fields could be used to modify radiative dynamics and directly control the reaction outcome [WBZ99, GG98].

The work presented here extends these techniques to the rapidly developing field of cold molecular-ion chemistry. Specifically, the phenomenon observed here should be universal to atom–ion chemical systems and, through its dependence on the reactive trajectory, provides a means to probe the range of a chemical reaction. It also greatly suppresses the reactivity of short-lived excited states. Therefore, this work implies that care must be taken when interpreting low-temperature atom–ion reaction data and that certain unwanted chemical reactions in hybrid trapping experiments can be mitigated by simply moving to low temper-

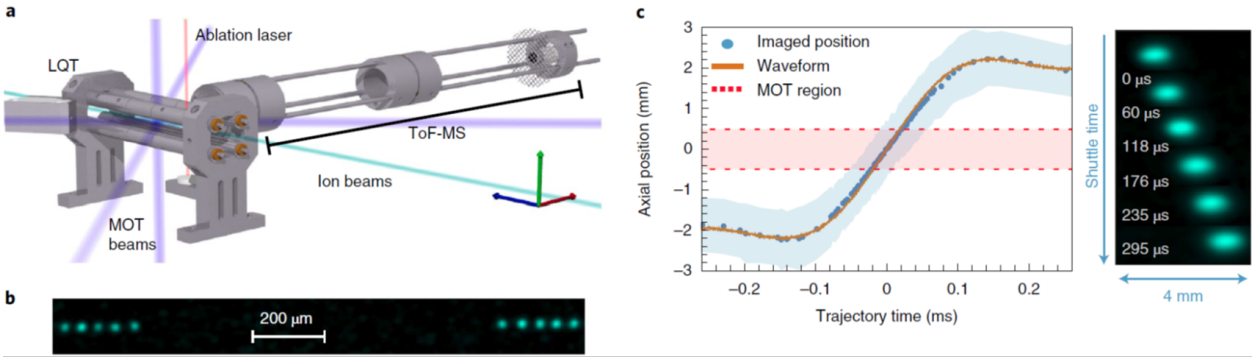

Figure 7.1: **Experimental apparatus and techniques.** (a) A 3D rendering of the MOTion trap apparatus. (b) Image of an ion chain being shuttled over a distance of ∼1 mm at a collision energy of ∼750 mK. To reduce secular heating, the ions spend over 90% of the time at the trajectory endpoints, and thus ion fluorescence is only visible at these locations. (c) The trajectory of a shuttled ion sample, as determined by fluorescence images acquired by triggering on the phase of the shuttling waveform. Also presented is the location of the potential minimum of the axial potential as predicted from the endcap waveform voltages at particular instances of time. For reference, the blue shaded region represents the $1/e$ spatial density width of the 3D Coulomb crystal used in the measurement. The horizontal red shaded region represents the $1/e$ spatial distance of the MOT cloud. Right, experimental false-colour fluorescence images of the shuttled ions at various times along the shuttling trajectory.

atures and thereby allowing longer molecular ion coherence and interrogation times.

In the remainder of this chapter, we first describe the experimental system and technique for energy control and then present the observed total reaction rates and branching fractions of the Ca $^1P_1$ and $^3P_2$ states, which show very different behaviours. We then describe a qualitative model for the observed effect that provides a simple means to calculate the temperature at which this radiative regime is reached. Finally, we compare our experimental results to a more rigorous model of the observed effect that is integrated into a modified long-range capture theory.

7.2 Results

7.2.1 Experimental System

The atom–ion apparatus utilized in this experiment (Figure 7.1a), dubbed the MOTion trap, is a hybrid system consisting of a co-located magneto-optical trap (MOT) and a linear quadrupole trap (LQT) that is radially coupled into a time-of-flight mass spectrometer (ToF). Ba^+ ions are co-loaded into the trap and can be laser-cooled to temperatures of $\sim$100 mK to provide sympathetic cooling for the reactant $BaCl^+$ molecules. To tune the reactant collision energy, we employ both the ion-shuttling technique described in Chapter 6 and Ref. [PMW18] as well as the traditional method of micromotion energy tuning through crystal sample size modulation [GCO09, HHF13]. The former technique, which may be used with both three-dimensional (3D) structures and linear ion chains (Figure 7.1b), utilizes precise control of the endcap electrode voltages within the ion trap to modulate the position of the ion at a fixed velocity (Figure 7.1c). This allows for collision energy scanning without problematic effects associated with micromotion, such as micromotion interruption collisions and poor energy resolution [CSH14, RW17]. For the reaction rate data discussed in the following, we implement the technique with 3D structures to increase the data acquisition throughput. Additionally, while not measured directly, we expect that the internal degrees of freedom of the reactant $BaCl^+$ molecules are cooled via sympathetic cooling collisions [RSS13] with the Ca MOT.

7.2.2 Observation of Reaction Blockading

The studied reaction is energetically forbidden in the ground state; however, by using previously established methods involving optical pumping and magnetic trapping, the reaction is shown to proceed via the Ca $^1P_1$ and Ca $^3P_2$ electronic states.

After identifying the reaction pathways of the system, the dependence of reaction rate

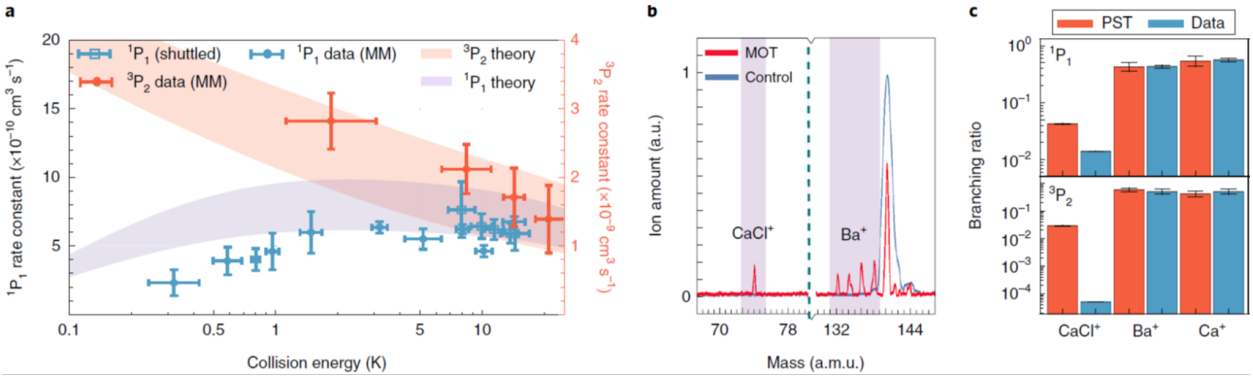

Figure 7.2: **Reaction blockading in excited neutral–ion systems.** (a) Experimental dependence of reaction rate constant on collision energy, as measured through both micromotion (MM) tuning (circles) and shuttling (squares) for both the singlet and triplet reaction surfaces. Note that the y-axis scale is different for the two reactions. Both data sets are in reasonable agreement with a modified capture theory incorporating reaction blockading, with the reaction rate of the short-lived Ca $^1P_1$ state significantly suppressed at low temperatures as compared to its standard capture theory prediction. For the triplet data, an absolute rate constant is measured at 10 K and all subsequent data points are normalized with respect to this value due to technical difficulties associated with frequent magnetic trap density measurements. Each data point consists of approximately 100 measurements, and error bars are expressed at the one-standard-error level. (b) Mass spectra, obtained from ToF-MS, of the identified product ions of the reaction. Shaded areas identify the masses corresponding to the product ions, and a control spectrum is included where the ions were ejected into the ToF-MS without MOT exposure. (c) A comparison of the measured branching fractions and the predictions of the statistical phase space theory (PST) for both Ca singlet (top) and triplet (bottom) reactions. Experimental error bars are expressed at the one standard error level and, in the case of the $CaCl^+$ values, may be smaller than the marker size.

on the collision energy was explored. Atom–ion chemical reaction cross-sections are typically estimated using a Langevin capture model [DMW58, Lan05] as $\sigma(E_{\text{col}}) = \pi b(E_{\text{col}})^2$, where the impact parameter $b(E_{\text{col}}) = (\ell+1/2)/(\mu v)$ is determined by the maximum angular momentum ℓ that allows the reaction pair to reach short range at a given collision energy E_{col} where μ is the reduced mass of the system and v is the collision velocity. The energy-dependent rate constant $k(E_{\text{col}})$ is subsequently calculated by integrating $\sigma(E_{\text{col}})$ over the relative velocity probability distribution of the reaction pair, as $k(E_{\text{col}}) = \langle\sigma(E_{\text{col}})v\rangle$. Ultimately, the long-range form of the studied molecular potential determines how the chemical reaction rate scales with E_{col}. For the excited-state systems studied in this work, standard

capture theory predicts a reaction rate that increases with decreasing collision energy due to the quadrupole–ion interaction.

To assess this trend in the $^3P_2$ state, a $BaCl^+$ sample was overlapped with a magnetic trap of pure triplet atoms [PMS17] while micromotion energy tuning was used to change the reactant collision energy from ∼1 K to 20 K. The measured reaction rate appears to increase at low energy as expected for an ion–quadrupole reaction, as shown in Figure 7.2a.

Two methods, excess micromotion energy tuning through crystal size manipulation and ion shuttling, were used to measure the collision energy dependence of the Ca ($^1P_1$) + $BaCl^+$ reaction. Over their common range (4–20 K), the two methods agree and reveal an essentially energy-independent reaction rate constant. However, interestingly, unlike the Ca ($^3P_2$) state, the measured rate constant decreases at low temperature instead of increasing as predicted by standard quadrupole–ion capture theory (Figure 7.2a). All presented theory curves are averaged over the energy distribution of the ions before comparison with the data, and the theory error bands are determined by uncertainties in the polarizability and quadrupole moment values used to construct the molecular potentials utilized in the calculation (see Subsection 7.2.5 for a description of the modified capture theory presented in Figure 7.2a).

7.2.3 Branching Fraction Analysis

Given this departure from standard capture theory, we then measured the product branching fractions to gain a fuller understanding of the chemical dynamics. For experimental convenience, reactions between Ca and non-shuttled $BaCl^+$ ions were studied at an average energy of ∼5 K. For reactions with the Ca $^1P_1$ and Ca $^3P_2$ states, there are three energetically

allowed pathways:

$$\begin{aligned} \mathrm{BaCl^+ + Ca} &\rightarrow \mathrm{CaCl^+ + Ba} \\ &\rightarrow \mathrm{Ba^+ + CaCl} \\ &\rightarrow \mathrm{Ca^+ + BaCl} \end{aligned} \tag{7.1}$$

Products from the first two reactions are experimentally identified by the appearance of reaction products in ToF-MS spectra (Figure 7.2b). While the reaction products are created with $\lesssim$1 eV of energy, the radial (axial) trap depth of the LQT is $\sim$4 (0.5) eV and thus $\geq$95% of charged products are expected to be recaptured in the LQT, assuming isotropic scattering of ions after the reaction. Products from the direct charge exchange reaction cannot be inferred directly due to a background Ca^+ influx from MOT atom photoionization; thus, Ca^+ product branching ratios are inferred indirectly through the presence of the other two products. Additionally, Ba^+ products are distinguished via their mass from the isotopically pure $^{138}Ba^+$ coolant ions because the initial $BaCl^+$ reactant sample is present in natural abundance.

By monitoring the appearance of Ba^+ and $CaCl^+$ ions in the ToF spectra, branching fractions γ_i, defined as the number of product ions in the i^{th} exit channel formed per $BaCl^+$ loss event, are measured. For the $4s4p\ ^1P_1$ entrance channel, $[\gamma_{CaCl^+}, \gamma_{Ba^+}, \gamma_{Ca^+}] = [0.014(4), 0.43(6), 0.57(6)]$, while $[\gamma_{CaCl^+}, \gamma_{Ba^+}, \gamma_{Ca^+}] = [0.0001(8), 0.5(2), 0.5(2)]$ is measured for the $4s4p\ ^3P_2$ state. Notably, the $CaCl^+$ molecule is only definitively detected in $^1P_1$ reactions, providing a means for quantum state control of the reaction products.

Also shown in Figure 7.2c are the branching fractions predicted by a phase space theory calculation [PLR66]. This calculation assumes that all product states that are accessible via energy and angular momentum conservation are equally probable. Thus, product branching fractions are calculated by counting the total number of states available to each reaction product (see Subsection 7.4.3). The model predicts branching fractions of $[\gamma_{CaCl^+}, \gamma_{Ba^+}, \gamma_{Ca^+}] =$

[0.04(2), 0.42(17), 0.53(19)] for the singlet and $[\gamma_{CaCl^+}, \gamma_{Ba^+}, \gamma_{Ca^+}]$ = [0.018(14)), 0.56(21), 0.41(23)] for the triplet, which are in reasonable agreement with the experimental values (Figure 7.2c). The error bars are primarily determined by energetic uncertainties in the exothermicity of each reaction channel. The relative ordering of the branching fractions can be attributed to two main factors. First, the $CaCl^+$ exit channel has the lowest product exothermicity and therefore the fewest accessible rovibronic states. Second, the ground state of the $CaCl^+$ + Ba asymptote is composed of two singlets, whereas the other asymptotes are composed of two doublets, reducing the number of states accessible to $CaCl^+$ by a factor of approximately four.

The relatively good agreement of this model with the data suggests that the reaction proceeds via a long-lived collision complex, which facilitates the realization of ergodicity and therefore the statistical assumption of the model.

7.2.4 Modeling of Reaction Blockading

Given the evidence for a long-lived collision complex from the product branching data and the dramatic difference in reactivity as a function of temperature for quantum states with a long ($^3P_2$, $\tau \approx$118 min) and short ($^1P_1$, $\tau \approx$4 ns) radiative lifetime, the observations suggest that spontaneous emission modifies the chemical dynamics. Because any reaction on an excited surface starts in the separated atom limit, the reagents must propagate inward to short-range separation ($\sim$10 a_0) before a chemical reaction can occur. If the time it takes to propagate inward to form a collision complex and pass through the transition state to products is similar to the radiative lifetime of the excited reagent, it is likely that spontaneous emission will occur during the chemical event. In this limit, which is more likely at extremely low temperatures, the reactivity of excited reagents will be given by the reactivity of the potential surface reached through spontaneous emission, which in the present case is the endoergic ground-state surface.

To estimate the temperature at which this effect becomes important, it is necessary to

calculate the dependence of the total collision time on temperature. Normally, this would be estimated by calculating the lifetime of the three-body collision complex from Rice–Ramsperger–Kassel–Marcus theory [RR27, Dag77]; however, this lifetime, which is typically a few vibrational periods, severely underestimates the total collision time at low temperature as it neglects the time it takes for the reagents to fall into the collision complex.

Following similar approaches in neutral–neutral systems [WBZ99], to account for this effect we consider the collision trajectory of the reactants as they spiral inward along their ground-state and excited-state surfaces. Because these surfaces have different long-range forms due to their differing polarizabilities and quadrupole moments, they diverge from one another as the atom–ion separation distance decreases. This causes any lasers resonant with the system in the dissociation limit to become far-detuned in the region where chemical dynamics occur. At cold temperatures, this effect, dubbed reaction blockading, makes it unlikely that the Ca atom will remain in the excited state long enough to react before spontaneously emitting; however, at higher collision velocities, such events are less likely to occur before the atom reaches short range.

This effect is particularly sensitive to the atomic lifetime of the reactive state, as longer excited-state lifetimes allow the reaction complex to reach short range more easily before being interrupted by a spontaneous emission event. As a result, once reaction blockading is integrated into the capture theory predictions, we observe good agreement with the Ca $^1P_1$ data, whereas for the long-lived triplet state the effect of reaction blockading is negligible, as expected (Figure 7.2a).

A more quantitatively rigorous model of the blockading effect is presented in the next section, but we first develop a simple model to estimate when radiative effects become significant. The collision energy E_B at which the blockading effect reduces the total reaction rate by half can be approximated by considering the amount of time, $t_\mathrm{B} = \tau \ln(2)$, it takes to deplete the excited-state population by the same amount, where τ is the excited-state lifetime.

From conservation of energy, $E_{\mathrm{tot}} = E_{\mathrm{col}}(r) + V_{\mathrm{ex}}(r)$, where E_{tot} is the total energy of the system and $V_{\mathrm{ex}}(r)$ is the excited-state potential of the system and thus t_{B} can be expressed in terms of the collision energy as

$$t_{\mathrm{B}} = \tau \ln(2) = \int_{r_{\mathrm{c}}}^{r_{\mathrm{s}}} \left(\frac{\mu}{2[E_{\mathrm{tot}} - V_{\mathrm{ex}}(r)]} \right)^{1/2} \mathrm{d}r \tag{7.2}$$

where r_{s} is the short-range distance at which the chemical event occurs ($\sim 50\ a_0$ in our system) and r_{c} is the critical internuclear separation distance where the addressing laser becomes detuned by one linewidth from its associated atomic transition ($\sim 1200\ a_0$ in our system). We obtain r_{c} by solving $V_{\mathrm{ex}}(r_{\mathrm{c}}) = V_{\mathrm{gs}}(r_{\mathrm{c}}) + \Delta E - \hbar\Gamma$ where $V_{\mathrm{ex}}(r)$ and $V_{\mathrm{gs}}(r)$ are the excited-state and ground-state molecular potentials of the system, ΔE is the separation-limited energetic difference between the ground and excited states and Γ is the linewidth of the neutral cooling transition.

Furthermore, if we approximate the velocity, and thus the kinetic energy, of the system as being constant during the latter portion of the trajectory, then $E_{\mathrm{tot}} - V_{\mathrm{ex}} \approx E_{\mathrm{B}}$ and Equation 7.2 can be inverted to yield the final result

$$\begin{aligned} E_{\mathrm{B}} &= \frac{1}{\ln(2)^2} \frac{(r_{\mathrm{c}} - r_{\mathrm{s}})^2}{\tau^2} \frac{\mu}{2} \\ &\approx \frac{1}{\ln(2)^2} \frac{r_{\mathrm{c}}^2}{\tau^2} \frac{\mu}{2} \end{aligned} \tag{7.3}$$

where $r_{\mathrm{s}} \ll r_{\mathrm{c}}$ in this approximation. Applying Equation 7.3 to the Ca* + $BaCl^+$ system, we calculate E_{B} to be 560 mK for the $^1P_1$ state and $\ll 1\ \mu$K for the $^3P_2$ state.

7.2.5 Modified Capture Theory

For quantitative comparison to the measured rate constant, we require a more rigorous model of the blockading effect than the one presented in the previous section. To this end, we modify standard long-range capture theory to include a probability of reaching short

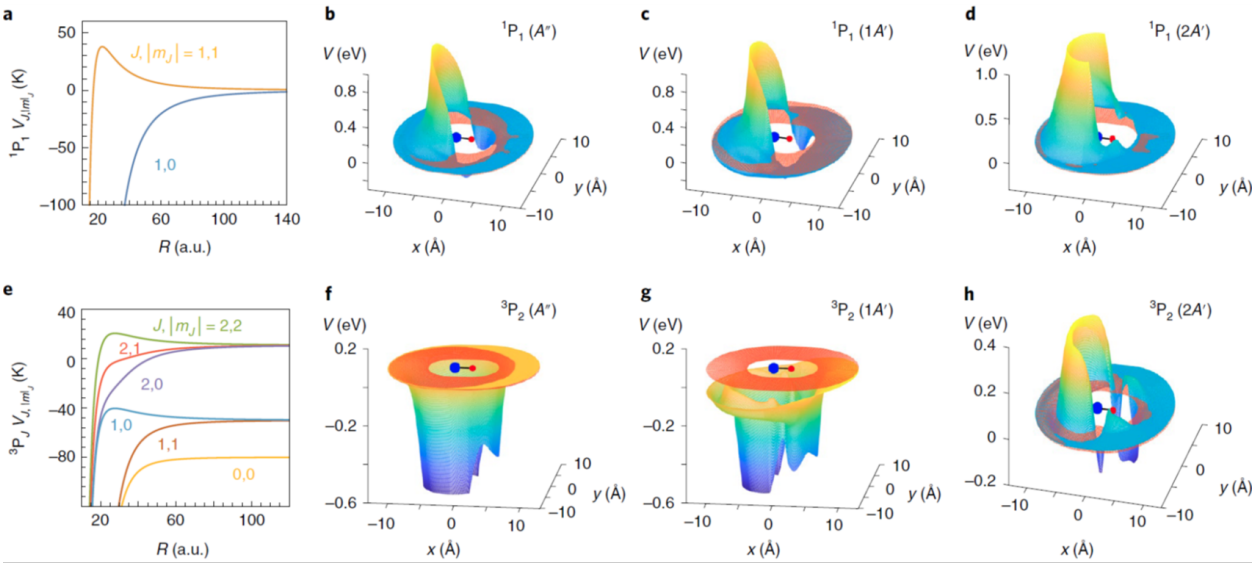

Figure 7.3: **Potential energy curves and surfaces.** (a) Potential energy curves for each $(J, |m_J|)$ level expressed as a function of internuclear separation coordinates for $BaCl^+ + Ca(^1P_1)$, where the molecular ion is considered as a point charge placed at the origin (Ba^+ in blue, Cl in orange). (b–d) Potential energy surfaces corresponding to the A'' symmetry (b) and the two A' symmetries (c,d) for the $BaCl^+ + Ca(^1P_1)$ complex. The x and y axes are in Å and the z axis is in eV. The orange plane is the asymptotic value of 3.08 eV above the global ground state of $BaCl^+ + Ca$, computed with the same level of theory at $R = 50$ Å. Short-range energetic barriers along the A'' (b) and $2A'$ (d) surfaces prevent the reactants in these surfaces from reaching the reaction region at short range, resulting in a reduction in the overall Ca $^1P_1$ reaction rate by a factor of 1/3 (see Equation 7.4). (e–h) Similarly, for the $BaCl^+ + Ca(^3P_2)$ complex, potential energy curves (e) and surfaces are displayed corresponding to the A'' (f) and two A' symmetries (g,h), with axes consistent with those of the singlet. The orange plane is the asymptotic value 1.88 eV above the global ground state of $BaCl^+ + Ca$ (singlet) computed with the same level of theory at $R = 30$ Å. Unlike the Ca $^1P_1$ surfaces, no short-range energetic barriers prevent reaching the reaction region for the triplet surfaces and thus there is no additional reduction in triplet reaction rate.

range before spontaneous emission for each partial wave, $P_\ell(E_{\rm col}, m_J)$:

$$\sigma(E_{\rm col}) \approx \frac{\pi\hbar^2}{2\mu E_{\rm col}} \sum_{m_J} \frac{\eta_{m_J}\chi_{\rm S}}{2J+1} \sum_{\ell=0}^{\ell_{\rm max}(E_{\rm col},m_J)} (2\ell+1) P_\ell(E_{\rm col}, m_J) \tag{7.4}$$

where η_{m_J} is the probability that the m_J Zeeman level reacts if it reaches short range, $\chi_{\rm S}$ is the probability that the reaction does not produce an excited $BaCl^+$ molecule, and $\ell_{\rm max}(E_{\rm col}, m_J)$ is the maximum orbital angular momentum that the entrance system can possess at energy $E_{\rm col}$ while still being able to reach short range. $P_\ell(E_{\rm col}, m_J)$ is calculated by simultaneously finding the trajectory of the colliding pair on their interaction potential and solving a two-level Einstein rate equation model to account for electronic population dynamics in the presence of changing electronic energy levels.

The long-range potentials, assuming the ion to be a positive point charge, are dominated by the ion–dipole polarizability and ion–quadrupole terms, as shown in Figure 7.3a and e. As can be seen, for the $^3P_2$ and $^1P_1$ levels the (J, m_J)=(2, 2) and (1, 0) and (J, m_J)=(1, 1) states, respectively, have large barriers. Reactants on these potentials cannot reach short range on any partial wave. While the other potentials are attractive at long range, it is necessary to match the long-range potential to the short-range potential energy surface for a complete reaction rate calculation.

To this end, electronic structure calculations were performed using the Gaussian 09 [FTS09] and Molpro 2012 [WKK12] program packages to calculate the reaction surface for each excited-state reagent, using equation-of-motion coupled cluster theory including single and double excitations (EOM–CCSD). The resulting potential surfaces for separation between $BaCl^+$ and Ca ranging from 4 Å and 10 Å are shown in Figure 7.3 for the three excited singlet and triplet symmetries, $1A'$, $2A'$ and A''. The orange mesh in each panel indicates the asymptotic energy of $BaCl^+$ + Ca*—3.08 eV for the singlet and 1.88 eV for the triplet, neglecting spin–orbit couplings. Most notably, in the case of the singlet, the surfaces corresponding to the $2A'$ and A'' geometries contain energetic barriers above their respective

asymptotic energies at all angles of approach, preventing the reactants from accessing the reaction region at short range. Since only the surface corresponding to the $1A'$ geometry allows approach to the reaction region, $\eta_{m_J} = 1/3$ for reactions originating in the Ca ($^1P_1$) state. In the case of the triplet, all three surfaces possess a pathway to reach the reaction region. Therefore, given the low temperatures probed here, we take $\eta_{m_J} = 1$ for all reactions originating in the Ca ($^3P_2$) state.

Finally, for the present system there are many inelastic channels that lead to a loss of the initial reagent population, but result in excited states of [$BaCl^+$ + Ca] that ultimately radiatively decay back into the [$BaCl^+$ + Ca] ground state, making such reactions indistinguishable from non-reaction events. To estimate the probability of such events, we apply the phase space theory model described earlier to the exit channel product [$BaCl^+$ + Ca]. After including all energetically accessible excited states, we obtain $\chi_S = 0.76(13)$ and 0.72(17) for the singlet and triplet channels, respectively, with the errors again determined by uncertainties in the exit channel exothermicities.

The results of this modified long-range capture model, after thermal averaging, are shown in Figure 7.2a and are in reasonable agreement with the data. Our model, while capturing the key features of the blockading effect, does not consider non-adiabatic processes that could also play a role in the system. For example, relaxation of the excited-state complex during the collision through internal conversion processes could lead to ground-state reactions and thus a global increase in reaction rate at all studied collision energies. Additionally, the radiative lifetime of the collision complex may change as the system transitions to short range; however, in our model, we assume this lifetime to be constant, fixed by its value in the separated-atom limit.

7.3 Discussion

The observed reaction blockading is expected to be a general effect in low-temperature ion–neutral chemistry, as the monopole field of the ion significantly alters the electronic structure of the neutral at relatively long range. Although the modified capture theory developed here can quantitatively treat the suppression effect, the simple expression presented in Equation 7.3 can be used to estimate if reaction blockading will be important for a given system. For example, in the (Rb + N_2^+) [HW12] and (Rb + Ba^+)[HAR13] systems studied by the group at the University of Basel, Equation 7.3 predicts that reaction blockading is important at $E \leq 10$ mK, significantly below the temperatures of their studies.

In addition to the role reaction blockading may play in the study of low-temperature excited-state reactions, it has an important consequence for the field of quantum-state-selected molecular ions. The reactions studied here represent the dominant loss mechanism for preparing cold molecular ions with laser-cooled neutral atoms [Hud16], and the described suppression effect may be critical for enhancing sample overlap times in next-generation hybrid trapping experiments [HC18, SHS10].

In summary, we have presented an investigation of polar molecular ion–neutral chemistry at cold temperature. A recently developed ion-shuttling technique, along with micromotion-energy tuning, was employed to measure the dependence of the reaction rate on collision energy. Branching fractions for the reaction were measured and advanced electronic structure calculations, complemented by a long-range capture theory analysis, were performed to understand the collision dynamics of the system, revealing a strong dependence of the reaction on the approach angle of the incoming Ca atom. We have also demonstrated that spontaneous emission during the collision strongly affects the reaction rate of the system, resulting in a reaction blockading phenomenon. This effect was incorporated into a modified capture theory model and compared to the experimental data, demonstrating reasonable agreement. A rule of thumb was developed to estimate at what temperature the reaction

blockading effect becomes important for a given chemical system. This work builds on previous studies exploring radiative effects in neutral–neutral reactions [GP89, WBZ99, GG98] and represents an important step towards understanding quantum chemical dynamics in hybrid systems as well as controlling such dynamics with optical and electromagnetic fields.

7.4 Methods

7.4.1 Reaction Rate Measurements

To extract the reaction rate constants, depletion of $BaCl^+$ from the LQT, caused by reactive collisions with the ultracold Ca sample, was monitored as a function of reaction time. In general, the $BaCl^+$ sample may react with several Ca electronic levels that are simultaneously populated, each of which may have differing spatial density distributions and chemical reactivities. Consequently, the reaction kinetics data were fit to a simple rate equation model incorporating the populations and densities of the different electronic states in order to determine a total reaction rate Γ_{T} (units of s^{-1}) as

$$\Gamma_{\mathrm{T}} = \sum_i \int \hat{\rho}_{\mathrm{ion}}(\vec{r})\hat{\rho}_i(\vec{r})k_i(E_{\mathrm{col}}(\vec{r}))\mathrm{d}^3r \tag{7.5}$$

where $\hat{\rho}_i(\vec{r})$ is the peak-normalized atom number density of the i^{th} Ca electronic state at position $\vec{r}$, $\hat{\rho}_{\mathrm{ion}}(\vec{r})$ is the integral-normalized ion-number density evaluated at position $\vec{r}$, and $k_i(E_{\mathrm{col}}(\vec{r}))$ is the reaction rate constant of the i^{th} electronic state at the spatially dependent collision energy $E_{\mathrm{col}}(\vec{r})$. In the case of shuttled ion samples, the ion positions included in the above integral are time-dependent, and thus Γ_{T} is time-averaged over the experimental duty cycle. Additionally, fluorescence from the laser-cooled Ba^+ ions and Ca atoms can be imaged with three separate electron-multiplying charge-coupled device (EMCCD) cameras, allowing for accurate determination of the spatial distributions and densities needed for the rate constant extraction.

7.4.2 Collision Energy Control

We used a recently developed [PMW18] ion-shuttling technique to measure how the reaction rate varied with reactant collision energy. Collision energy in hybrid trap experiments is typically controlled by tuning the excess micromotion energy of an ion sample within the LQT; however, while this method allows precise control of the average collision energy, it suffers from poor energy resolution and is susceptible to problematic effects such as micromotion interruption heating. The shuttling method improves on this technique by offering comparatively higher energy resolution while maintaining the ions on the trap null. The essentials of the method are briefly reviewed in the following.

For small displacements around the ion trap centre, the potential in the axial dimension can be approximated as a harmonic oscillator, where offsets in voltages applied to opposing endcap electrodes serve to shift the equilibrium position of the harmonic potential. A time-dependent voltage offset between the endcaps provides precise control of the velocity of the ion, and thus the collision energy, as a function of time. Additionally, the endcap voltage waveforms must be selected carefully to ensure that the ions respond adiabatically to the translating axial potential and experience minimal secular heating.

The position of the ions while shuttling can be tracked for ions with velocities of ≤ 50 m/s by phase triggering an EMCCD camera on the shuttling waveform and obtaining fluorescence images at various positions along the shuttling trajectory, as shown in Figure 7.1b. In this range, the ions follow the waveform predicted trajectory and experience roughly linear motion in the region of intersection with the MOT. Control measurements were taken by monitoring the quantity of ions in the LQT while shuttling for several hundred seconds with no MOT present; these measurements demonstrated that ion loss due to secular heating is negligible.

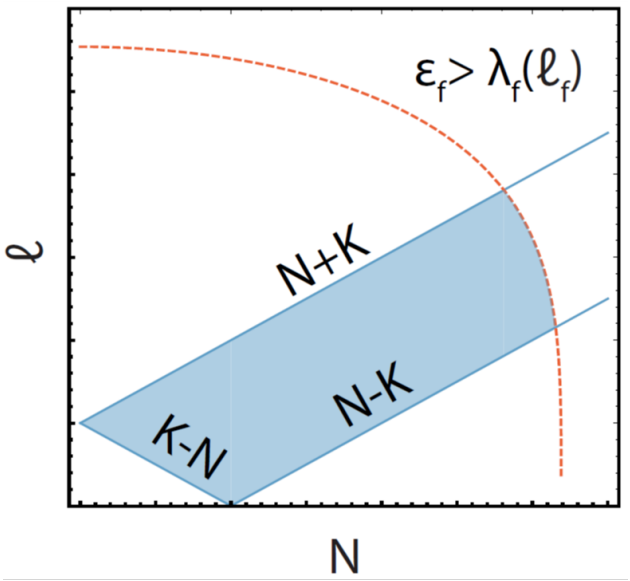

Figure 7.4: **Phase space diagram for branching fraction calculation.** A phase space diagram showing the range of rotational (N) and orbital (ℓ) angular momentum product states accessible at a given reactant total angular momentum (K). The shaded region of the curve denotes the final states that both obey angular momentum conservation and possess enough product kinetic energy, ϵ_f , to clear the product state centrifugal energy barrier, $\lambda_f(\ell_f)$, and dissociate from the three body reaction complex into the final product atom and diatomic molecule.

7.4.3 Branching Fraction Phase Space Theory Calculation

Under the assumption of strong coupling, all electronic, orbital, and angular momenta are expected to mix. Thus, while each individual angular momentum is not a conserved quantity throughout the reaction, the total angular momentum, K, along with its cylindrical axis projection, K_z, are conserved [WT72], with K being the magnitude of the vector sum

$$\vec{K} = \vec{\ell} + \vec{N} + \vec{L} + \vec{S} \tag{7.6}$$

where $\vec{\ell}$, $\vec{N}$, $\vec{L}$, and $\vec{S}$ are the vectors for the orbital, rotational, electronic orbital, and electronic spin angular momenta of the reaction complex. For the reactions studied in this work, $|\vec{L}|$ and $|\vec{S}|$ are ≤ 1, while generally $|\vec{\ell}|$ and $|\vec{N}|$ can often exceed ≈ 10, meaning the former can be neglected in the following calculation for simplicity.

In both the reactant (i) and product (f) states, K is bounded as

$$|\ell_{i(f)} - N_{i(f)}| \leq K \leq |\ell_{i(f)} + N_{i(f)}|. \tag{7.7}$$

Additionally, the final product must possess enough kinetic energy to escape the angular momentum barrier of the exit channel, permitting the three-body complex to dissociate into its molecular and atomic constituents. The later restriction is satisfied by enforcing

$$\epsilon_f \geq \lambda_f(\ell) \tag{7.8}$$

where ϵ_f is the final kinetic energy of a given product state and $\lambda_f(\ell_f)$ is the height of the centrifugal barrier in each product exit channel at orbital angular momentum ℓ_f. ϵ_f can be calculated as

$$\epsilon_f(\epsilon_i, v_i, N_i, v_f, N_f, Q_{i,f}) = \epsilon_i + E_{\text{int}}(v_i, N_i) - E_{\text{int}}(v_f, N_f) + Q_{i,f} \tag{7.9}$$

where ϵ_i is the initial collision energy of the reaction complex, $Q_{i,f}$ is the exothermicity of the reaction for exit channel f and

$$E_{\text{int}}(v_{i(f)}, N_{i(f)}) = \omega_{i(f)}(v_{i(f)} + 1/2) + 2\beta_{i(f)}N_{i(f)}(N_{i(f)} + 1) - \omega_{i(f)}\chi_{i(f)}(v_{i(f)} + 1/2)^2 \tag{7.10}$$

is the internal energy in the reactant (product) state associated with the $v_{i(f)}$ and $N_{i(f)}$ vibrational and rotational level, respectively, which is characterized by the spectroscopic constants $\omega_{i(f)}$, $\beta_{i(f)}$, and $\omega_{i(f)}\chi_{i(f)}$.

Equation 7.7 and Equation 7.8 restrict the number of ℓ_f and N_f states accessible to each exit channel (see Figure 7.4) at a given total angular momentum K and exit-channel kinetic energy ϵ_f. By counting the number of states accessible to each possible exit channel at given

K and ϵ_f, one can define the probability of accessing each exit channel as

$$P_f(K, \epsilon_f(\epsilon_i, v_i, N_i, v_f, N_f, Q_{i,f})) = \frac{\sum_{v_f, N_f} d_f \overline{n}_f(K, \epsilon_f(\epsilon_i, v_i, N_i, v_f, N_f, Q_{i,f}))}{\sum_b \sum_{v_b, N_b} d_b \overline{n}_b(K, \epsilon_b(\epsilon_i, v_i, N_i, v_b, N_b, Q_{i,b}))} \tag{7.11}$$

where $\overline{n}_b(K, \epsilon_b(\epsilon_i, v_i, N_i, v_b, N_b, Q_{i,b}))$ is the total number of states accessible for exit channel b at a given K and ϵ_b, and d_b is a degeneracy factor that accounts for spin multiplicity of each product state. We note that $\overline{n}_b(K, \epsilon_b(\epsilon_i, v_i, N_i, v_b, N_b, Q_{i,b}))$ is proportional to the area bounded by the curves presented in Figure 7.4.

Therefore, following Ref. [PL65], the total reaction cross section for a given exit channel f, given an initial reactant rotational quantum number N_i (assuming the reactant is in the ground vibrational state), and summed over all accessible product rotational and vibrational states is given as

$$\begin{aligned} \sigma_f(N_i, \epsilon_i) &= \sum_{\ell_i=0}^{\ell_{\max}(\epsilon_i)} \frac{2(\ell_i+1)\pi\hbar^2}{2\mu_f \epsilon_i} P_f(\ell_i) \\ &= \sum_{\ell_i=0}^{\ell_{\max}(\epsilon_i)} \frac{\pi\hbar^2}{2\mu_f \epsilon_i (2N_i+1)} \sum_{|\ell_i - N_i| \le K \le |\ell_i + N_i|} (2K+1) P_f(K, \epsilon_f(\epsilon_i, v_i, N_i, v_f, N_f, Q_{i,f})) \end{aligned} \tag{7.12}$$

where μ_f is the reduced mass of the product complex.

Lastly, to calculate the final branching fractions, we must average each cross section across the rotational temperature of the sample as

$$\overline{\sigma}_f = \sum_{N_i} \frac{1}{Z} (2N_i+1) e^{-2\beta_i N_i(N_i+1)/(k_{\mathrm{B}}T)} \sigma_f(N_i, \epsilon_i) \tag{7.13}$$

where $T \approx 2\epsilon_i / k_{\mathrm{B}}$ is the effective rotational temperature of the initial reactant molecular ion and Z is the rotational partition function.

Finally, after the relevant cross sections have been computed, the branching fraction into

each exit channel γ_f is given by

$$\gamma_f = \frac{\overline{\sigma}_f}{\sum_f \overline{\sigma}_f}. \tag{7.14}$$

Equation 7.14 is applied to the Ca* + $BaCl^+$ system, and the results are compared directly to experimental branching fractions in Figure 7.2c. In addition to the product branching fractions, Equation 7.14 is also applied to estimate the percentage of collisions that occur and result in excited states of [$BaCl^+$ + Ca] that ultimately radiatively decay back into the [$BaCl^+$ + Ca] ground state. This factor is included as χ_S and adjusts our rate constant calculation to account for experimentally indistinguishable events where inelastic collisions occur but no new molecular products are formed. Errors in the calculated branching ratios can be primarily attributed to uncertainties in the exit channel exothermicities, nonergodicity in the system, and uncertainties in the molecular constants used in the state counting process.

CHAPTER 8

Optical Control of Low-Temperature Excited-State Ion–Neutral Interactions

As shown in the previous chapter, reaction blockading acts to suppress excited-state reactions at low temperature. In essence, reaction blockading describes the fact that the presence of a nearby ion shifts the energy levels of a Ca atom, resulting the MOT lasers to be off-resonant, precluding excited-state collisions for slowly approaching, cold collisions. In this chapter, we use $Yb^+(^2S_{1/2})$ as a proxy for $BaCl^+$—$Yb^+(^2S_{1/2})$ is similar to $BaCl^+$ in that they react only with excited-state Ca atoms—to again measure the effects of reaction blockading. Further, we reverse the effect of reaction blockading with the addition of a "catalyst laser," which is resonant with the shifted Ca $4s4p\ ^1P_1 \leftarrow 4s^2\ ^1S_0$ transition at short atom–ion separation. This catalyst laser increases the rate of excited-state reactions, allowing us to effectively turn these reactions on or off with the addition or omission of the catalyst laser. This chapter is a version of our group's publication "Engineering excited-state interactions at ultracold temperatures."

Using a recently developed method for precisely controlling collision energy, we observe a dramatic suppression of inelastic collisions between an atom and ion (Ca + Yb^+) at low collision energy. This suppression, which is expected to be a universal phenomenon, arises when the spontaneous emission lifetime of the excited state is comparable to or shorter than the collision complex lifetime. We develop a technique to remove this suppression and engineer excited-state interactions. By dressing the system with a strong catalyst laser, a significant fraction of the collision complexes can be excited at a specified atom–ion separation. This

technique allows excited-state collisions to be studied, even at ultracold temperature, and provides a general method for engineering ultracold excited-state interactions.

8.1 Introduction

In the last quarter century, the development of techniques for producing ultracold matter led to the ability to observe few and even single partial wave collision events, enabling the observation of quantum threshold behavior and unitarity-limited processes [TKJ04, ONW10, NOW10]. It also revealed the impact chemical binding forces, quantum statistics, internal structure, and dimensionality have on collisions, as well as provided the potential for control of chemical reactions [DBB99, JTL06, LWS08, HTS06, RZS12, YLC18, CXY19].

The overwhelming majority of these studies were performed with collision partners in their ground electronic state. This is at least partially due to the fact that interactions at ultracold temperatures tend to naturally suppress electronically excited collisions, as pointed out in [JM89] and demonstrated in [WSD95, PMS18]. This suppression arises as the long-range interactions between collision partners tend to shift any laser that would electronically excite one of the collision partners out of resonance at very long range. This effect, known as reaction blockading [PMS18], is especially strong in systems with long-range interactions such as atom–ion or molecule–molecule pairs.

Collisions involving electronically excited atoms and molecules play an important role in processes such as combustion [SSF08], explosives, atmospheric chemistry [Wie82], stellar evolution [MBH06], interactions in the interstellar medium [AGC10], and the formation of new molecules [PMS17], yet many studies of these reactions have been limited to high temperature, where quantum effects are often obscured. Here, we demonstrate a general technique to enable the study of such collisions at ultracold temperatures in a prototypical atom–ion system. Building from work on hyperfine-changing collisions in laser-cooled systems [SWM89, WSD95, SGT95], we apply a strong laser field that dresses the system and

promotes the molecular collision complex to a specified excited state at a specified range. In this way, we engineer the electronic excitation of collision partners at short range and extract the excited channel rate constants. Additionally, by controlling the range at which this laser addresses the reactants, this technique is sensitive to the features of molecular potentials, enabling a new class of experiments to probe molecular potentials at controlled atom–ion separations. Excitingly, the technique appears to be completely general and can be applied at higher temperatures.

In what follows, we use a recently developed method [PMW18] for precisely controlling collision energy to study the charge-exchange collision between $Ca(4s4p\ ^1P_1) + Yb^+(6s\ ^2S_{1/2})$ as a function of collision energy from 0.05 K to 0.65 K. From this data, we observe reaction blockading of the charge-exchange rate and measure the dependence of this suppression on collision energy. Finally, we introduce a strong laser to dress the system and observe an increased charge-exchange rate for the $Ca(4s4p\ ^1P_1) + Yb^+(6s\ ^2S_{1/2})$ channel, effectively eliminating the suppression. A quantum coupled-channels calculation based on ground- and excited-state diabatic potentials, their couplings, and the infinite-order sudden approximation is presented and shows good agreement with the data. The technique is qualitatively explained using a simple semi-classical model based on dressed molecular potentials and a Landau–Zener type transition.

8.2 Suppression of Reactions due to Reaction Blockading

The experiment is performed in the second-generation MOTion trap, sketched in Figure 8.1 and described in detail in Refs. [RSS13, SDC16]. Coulomb crystals of Yb^+ ions are confined in a segmented radio-frequency linear quadrupole trap, while a small Ca oven provides atomic Ca vapor which is loaded into a magneto-optical trap (MOT). By smoothly ramping the voltages of the ion trap end caps, we can shuttle an ion chain through the MOT at a controlled velocity, illustrated in Figure 8.1a, b, and c and described in detail in [PMW18],

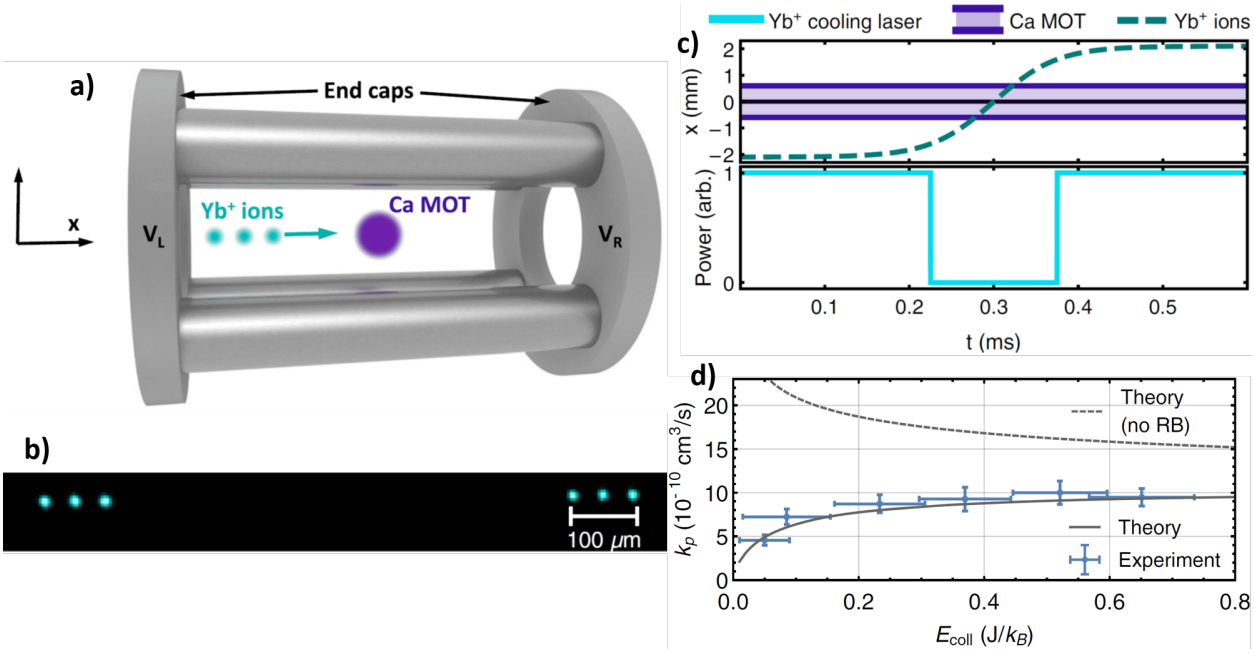

Figure 8.1: **Shuttling in the hybrid atom–ion MOTion trap.** (a) Schematic of the MOTion trap. (b) False-color fluorescence image of 3 shuttled Yb^+ ions. As the exposure time is greater than the shuttling period, fluorescence from the 3 ions is concentrated at the positions of the two end points, where the ions spend the most time. (c) Experimental sequence illustrating the shuttling technique. As the Yb^+ ions are shuttled through the Ca MOT, the 369 nm Yb^+ cooling beams are extinguished to prepare the ions in the 6s $^2S_{1/2}$ state. (d) Measured charge-exchange rate coefficient (with standard errors) for $Ca(^1P_1)$ + $Yb^+(^2S_{1/2})$ as a function of collision energy using the shuttling technique. Also shown are rate coefficients from coupled-channels calculations, one with (solid line) and one without (dashed line) the effect of reaction blockading (RB).

allowing precise control of the reactant collision energy. By extinguishing the 369 nm Yb^+ cooling laser when the Yb^+ ions are shuttled through the Ca MOT, the ions are prepared in the ground 6s $^2S_{1/2}$ state. Using this shuttling method, we measure the charge-exchange rate of Ca(4s4p $^1P_1$) + Yb^+(6s $^2S_{1/2}$) as a function of collision energy and observe reaction blockading of the rate, shown in Figure 8.1d. Specifically, for an ion chain with 50 mK collision energy (defined as $\langle E_{col}\rangle/k_B$, where $\langle E_{col}\rangle$ is the average kinetic energy in the center of mass frame and k_B is the Boltzmann constant), we measure a rate constant of $k_p = (4.6 \pm 0.6) \times 10^{-10}$ cm^3/s, compared to the no-suppression theoretical prediction of $k_p = 23 \times 10^{-10}$ cm^3/s, an observed suppression factor of ~ 5.

This reaction blockading can be understood by considering the long-range atom–ion interaction [JM89, PMS18]. At long range the atom and ion interact primarily through the charge-induced dipole and charge–quadrupole potentials of the forms $-\frac{\alpha}{2}R^{-4}$ and $-\frac{Q}{2}(3\cos^2(\theta)-1)R^{-3}$, respectively, where R is the atom–ion separation, α is the neutral atom polarizability, Q is the neutral atom quadrupole moment, and θ is the angle between the quadrupole moment and the internuclear axis. Thus, a laser resonant with two atomic states at long range, which have different polarizabilities and quadrupole moments, is no longer resonant when the atom and ion are in close proximity. For the Ca $^1\mathrm{P}_1 \leftarrow {}^1\mathrm{S}_0$ transition with linewidth Γ and a laser detuning $\delta = -\Gamma = 2\pi\times(-34.6\text{ MHz})$, the laser becomes resonant at $R \approx 1300$ a_0 and becomes detuned by 10Γ at ~ 600 a_0. Therefore, for a charge-exchange event to occur, the atom–ion pair must propagate inward without the Ca atom decaying from this distance to distances of ~ 40 a_0, where couplings to other states become significant. For collision temperatures greater than $\gtrsim 10$ K, the atom–ion pair approaches quickly enough such that the Ca $^1P_1$ state is unlikely to decay before reaching short range, affecting the rate coefficient by $\lesssim 1\%$. For a collision temperature of 1 mK, however, this effect leads to a suppression by a factor of $\sim$100.

To understand this behavior, we first consider charge exchange at low temperatures with no measures taken to overcome reaction blockading. Figure 8.2 shows the relevant CaYb^+ long-range diabatic potentials, labeled by the projection Ω of the total angular momentum onto the intermolecular axis, as a function of atom–ion separation R. These potentials are the diagonal matrix elements in our diabatic electronic basis, which changes only slowly with R. Asymptotically, these basis states correspond to atomic eigenstates so that non-adiabatic coupling among the potentials are negligible. The variable R describes the separation between the center of mass of the atom and ion. Moreover, the center of mass changes in charge transfer. The couplings originating from these changes are negligibly small for our purposes, justifying our definition for R. The entrance channel to the studied charge-exchange process, $\mathrm{Ca}(4s4p\ {}^1\mathrm{P}_1) + \mathrm{Yb}^+(6s\ {}^2\mathrm{S}_{1/2})$, has both a four-fold-degenerate

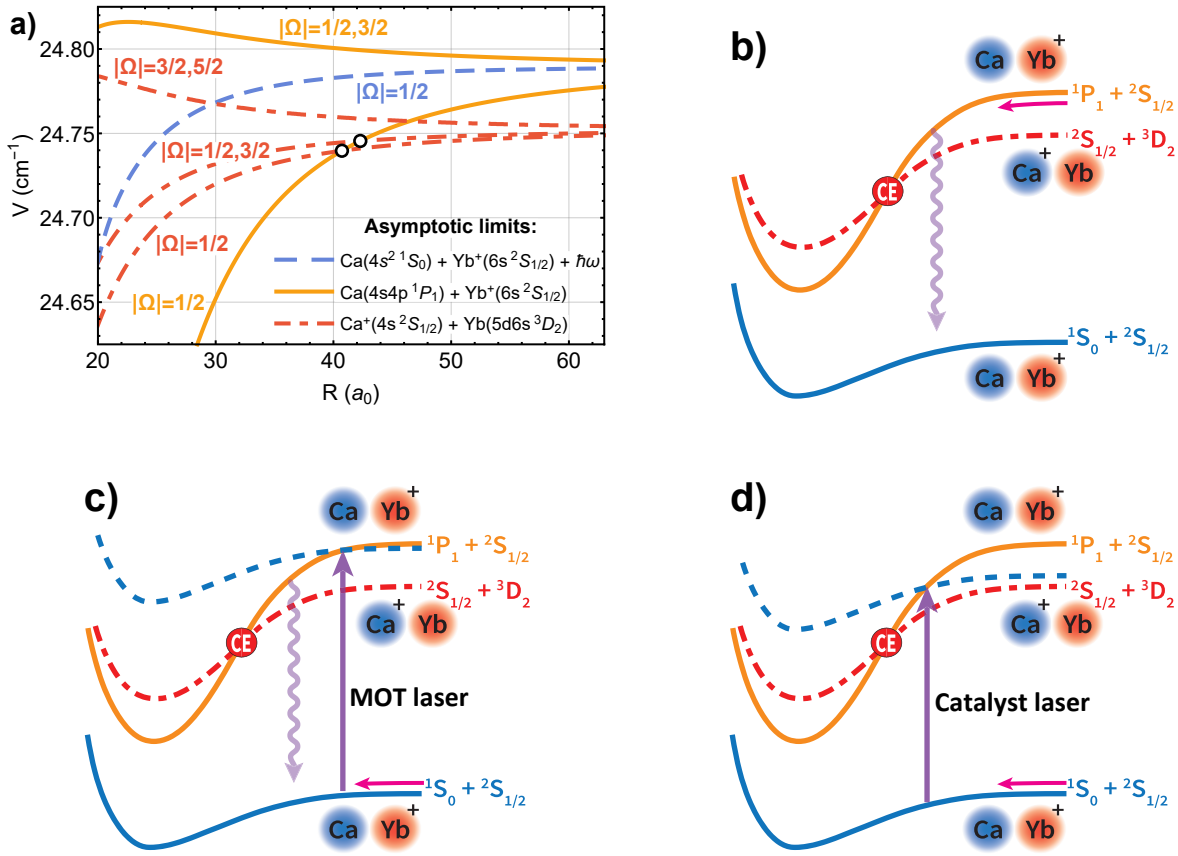

Figure 8.2: **Long-range diabatic potential energy curves.** (a) Relevant long-range molecular potentials. The two crossings between potentials relevant for charge exchange are indicated with black circular markers. The potential energy zero is located at the $\mathrm{Ca}(4s^2\ {}^1S_0)$ + $\mathrm{Yb}^+(6s\ {}^2S_{1/2})$ dissociation limit. (b) The first pathway corresponds to a collision between an excited $4s4p\ {}^1P_1$ Ca atom with a ground-state $6s\ {}^2S_{1/2}$ Yb^+ ion. The charge-exchange (CE) crossing is shown by a red circle. The vertical wavy line represents spontaneous emission to the ground $\mathrm{Ca}(4s^2\ {}^1S_0)$ + $\mathrm{Yb}^+(6s\ {}^2S_{1/2})$ channel. (c) The second pathway corresponds to a collision between a ground-state $4s^2\ {}^1S_0$ Ca atom with a $6s\ {}^2S_{1/2}$ Yb^+ ion in the presence of a photon of the MOT laser. The dashed blue curve corresponds to the dressed-state potential for this entrance channel. It has an avoided crossing with the excited $\mathrm{Ca}(4s4p\ {}^1P_1)$ + $\mathrm{Yb}^+(6s\ {}^2S_{1/2})$ potential. (d) In the presence of a catalyst laser, the incoming $\mathrm{Ca}(4s^2\ {}^1S_0)$ + $\mathrm{Yb}^+(6s\ {}^2S_{1/2})$ state is coupled to the reactive $\mathrm{Ca}(4s4p\ {}^1P_1)$ + $\mathrm{Yb}^+(6s\ {}^2S_{1/2})$ state at short range, where spontaneous emission is unlikely before reaction.

($|\Omega| = 1/2, 3/2$) repulsive potential and two-fold-degenerate ($|\Omega| = 1/2$) attractive potential. Substantial non-radiative charge transfer only occurs to the $Ca^+(4s\ ^2S_{1/2})$ + $Yb(5d6s\ ^3D_2)$ exit channel. The $Ca^+(4s\ ^2S_{1/2})$ + $Yb(5d6s\ ^3D_3)$ channel is energetically inaccessible to this entrance channel, and the $Ca^+(4s\ ^2S_{1/2})$ + $Yb(5d6s\ ^3D_1)$ channel is only crossed at short range $R \approx 25\ a_0$, where the the estimated couplings between these diabatic potentials, using the Heitler–London method [TTY98], are too large to significantly contribute to the rate coefficient. More details about the potentials, the diabatic couplings, and the calculation are given in our accompanying paper of Ref. [LMP19].

Therefore, the non-radiative charge transfer is primarily driven by coupling of the $|\Omega| = 1/2$ entrance channel diabats at their crossings with the exit channels. In the diabatic representation, this coupling arises from the molecular electrostatic interaction and therefore conserves Ω, implying that only charge transfer to the $|\Omega| = 1/2$ exit channel diabats, at crossing points $R_c = 40.7\ a_0$ and $42.3\ a_0$, is relevant. Since the electronic basis functions are very different for the two channels, the non-adiabatic coupling is localized and approximated by identical Lorentzians centered at each R_c. The half width of this Lorentzian, R_0, is chosen to match the experimentally determined charge transfer rates. In the absence of any additional means to overcome reaction blockading, the atom–ion pair can reach these crossing points and undergo a charge-exchange reaction via two pathways. The first pathway is directly on the $Ca(4s4p\ ^1P_1)$ + $Yb^+(6s\ ^2S_{1/2})$ entrance channel, where we determine the population of Ca atoms in the $^1P_1$ state by solving a rate equation derived from the optical Bloch equations, which includes the distance-dependent detuning of the MOT beams [MPY17]. The second pathway describes a collision on the photon-dressed $Ca(4s^2\ ^1S_0)$ + $Yb^+(6s\ ^2S_{1/2})$ state, which is coupled to the $Ca(4s4p\ ^1P_1)$ + $Yb^+(6s\ ^2S_{1/2})$ state via the MOT laser. Because the MOT laser is tuned $2\pi \times 34.6$ MHz below the asymptotic transition energy, as the atom and ion collide the laser is shifted into resonance. At this point, there is a resonant amplification of the coupling to the $Ca(4s4p\ ^1P_1)$ + $Yb^+(6s\ ^2S_{1/2})$ state by the molecular interaction due to the large density of states near the threshold.

Using the infinite-order sudden approximation (IOSA) [Pac74, Sec75, Hun75, Kou79], a coupled-channels calculation is performed on these potentials to determine the charge transfer cross-section, $\sigma(E, \ell)$. The effect of spontaneous emission is included by classically computing the collision time on the entrance channel and determining the probability, $p(E, \ell)$, for a colliding pair to survive to R_c without spontaneously emitting. The charge transfer rate constant is then determined as

$$k = \sum_{\ell=0}^{\infty} (2\ell + 1) p(E, \ell) \sigma(E, \ell) \tag{8.1}$$

where ℓ is the average orbital angular momentum quantum number used in the IOSA and E is the collision energy. The resulting rate constant is displayed alongside the data in Figure 8.1d for $R_0 = 0.39\ a_0$, with and without the inclusion of $p(E, \ell)$. A detailed description of the excited-state potentials and charge transfer can be found in [LMP19].

8.3 Introduction of Catalyst Laser

Given that this reaction blockading is expected to occur in all low-temperature excited-state collisions, it is desirable to develop a method to remove it. Here, we demonstrate one such means. Building on ideas developed for control of hyperfine-changing collisions [WSD95, SGT95, ZMM96], we apply a strong laser, dubbed the catalyst laser, that couples the ground-state with an excited state at short range. This allows selection of the excited-state reaction channel and may, in principle, be used to select a desired reaction product in polyatomic systems.

The operation of the technique is sketched in Figure 8.2d, where the $CaYb^+$ molecular potentials dressed by the photon energy of the applied laser are shown. Near the catalyst laser avoided crossing distance R_{CL}, the catalyst beam couples the upper and lower states, promoting the complex to the $Ca(^1P_1)$ + $Yb^+(^2S_{1/2})$ state at short range.

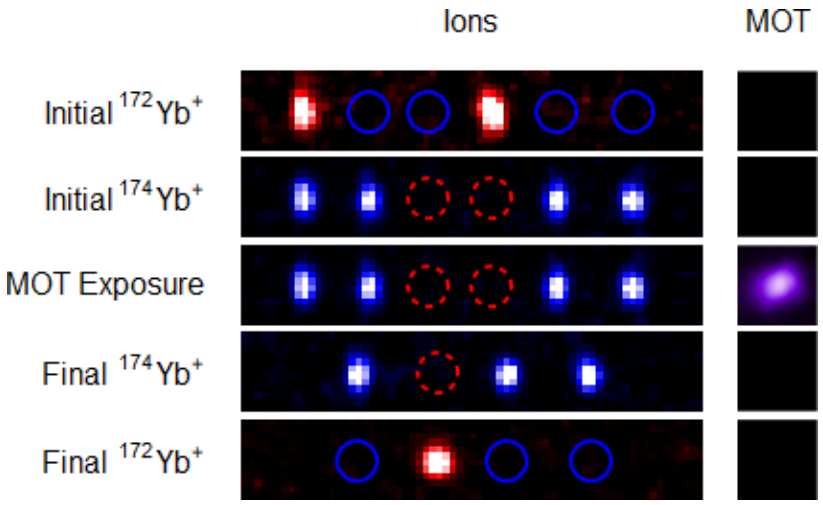

Figure 8.3: **Dual-isotope technique.** False-color fluorescence images of the Yb^+ ions and the Ca MOT (not to scale), illustrating the dual-isotope method used to measure the low decay rate of $^{172}Yb^+(^2S_{1/2})$. We first trap $^{172}Yb^+$ and $^{174}Yb^+$, while laser-cooling only $^{172}Yb^+$ ions (shown in red), while the $^{174}Yb^+$ ions (shown as blue circles) remain dark. We then switch the 369 nm cooling laser frequency to cool $^{174}Yb^+$ ions (shown in blue), while the $^{172}Yb^+$ ions (shown as red dashed circles) remain dark. We then overlap the MOT with the laser-cooled $^{174}Yb^+$ ions as well as the ground-state $^{172}Yb^+(^2S_{1/2})$ ions for a variable amount of time. Finally, we cool and measure the final number of $^{172}Yb^+$ ions.

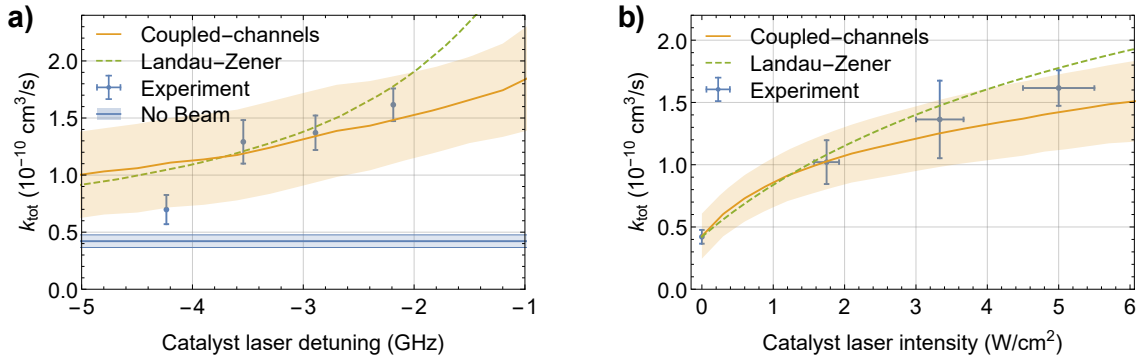

Figure 8.4: **Removing suppression with addition of a catalyst laser.** Total CEX rate coefficient as a function of catalyst laser (a) detuning from the $4s4p\ ^1P_1 \leftarrow 4s^2\ ^1S_0$ transition and (b) intensity. Plotted alongside experimental data are the results of a coupled-channels calculation and an estimate using the Landau–Zener approximation. For reference, the experimental rate with no catalyst beam is shown. Error bars correspond to the standard error in experimental measurements and error bands include uncertainties from the theoretical simulations and experimental parameters. Horizontal error bars in (a) are smaller than the plot marker. Details are found in Subsection 8.5.3.

The probability of promotion can be estimated from Landau–Zener transition theory as $P(\Omega_R) = 1 - \mathrm{Exp}\left[-\pi(\hbar\Omega_R)^2/\left(2\hbar v\frac{\partial}{\partial R}\Delta E\right)\right]$, where Ω_R is the Rabi frequency of the catalyst beam, v is the radial velocity, and ΔE is the energy difference between the diabatic potentials [Wit05]. Thus, for a scattering event with rate constant, k, this technique yields an experimentally observable rate $k_o = kP(\Omega_R)e^{-\Delta t(R_{CL})/\tau_{\mathrm{P}}}$, where $\Delta t(R_{CL})$ is the time required for the atom–ion pair to propagate from R_{CL} to short range and τ_{P} is the lifetime of the excited state.

In order to test the catalyst laser technique at the lowest possible collision energy, where the suppression is strongest, the ions cannot be shuttled but must be arranged in a stationary linear ion chain overlapped with the MOT. Due to collisional heating effects [CSR13, CSH14, SDC16], the linear ion chain cannot be maintained during MOT exposure without active laser cooling. However, if the ions are laser cooled, the charge-exchange rates include collisions originating in the $\mathrm{Yb}^+(^2\mathrm{P}_{1/2})$ and $\mathrm{Yb}^+(^2\mathrm{D}_{3/2})$ states [RSK11]. Therefore, in order to isolate the $\mathrm{Ca}(^1\mathrm{P}_1)$ + $\mathrm{Yb}^+(^2\mathrm{S}_{1/2})$ charge-exchange rate without the shuttling method, we develop and implement a dual-isotope technique (see Figure 8.3) for collision rate measurement. Specifically, we simultaneously trap both $^{172}\mathrm{Yb}^+$ and $^{174}\mathrm{Yb}^+$ ions, while laser-cooling only the $^{174}\mathrm{Yb}^+$ ions, which, in turn, sympathetically cool the $^{172}\mathrm{Yb}^+$ ions. As the $^{172}\mathrm{Yb}^+$ ions are only sympathetically cooled, they remain in the 6s $^2\mathrm{S}_{1/2}$ state. Due to off-resonant scattering of the cooling laser for the $^{174}\mathrm{Yb}^+$ ions, it is necessary to apply a repumping laser for the $^{172}\mathrm{Yb}^+$ ions to prevent population from accumulating in the 5d $^2\mathrm{D}_{3/2}$ state. Therefore, by monitoring the number of $^{172}\mathrm{Yb}^+$ ions with time, we isolate and measure the charge exchange of $\mathrm{Ca}(^1\mathrm{P}_1)$ + $\mathrm{Yb}^+(^2\mathrm{S}_{1/2})$.

Figure 8.4a and b show the results of using this dual-isotope technique to monitor $\mathrm{Ca}(^1\mathrm{P}_1)$ + $\mathrm{Yb}^+(^2\mathrm{S}_{1/2})$ charge-exchange reactions as a function of the detuning and intensity of the catalyst laser, respectively, at a collision temperature of ∼50 mK. For large detunings, although the atom–ion pair is promoted at a small value of R_{CL}, increasing the likelihood of reaching short range before spontaneous emission, the large value of $\frac{\partial}{\partial R}\Delta E$ and the high

velocity of the reactants leads to a lower probability of promotion to the reactive state from Landau–Zener transition theory. For the given experimental intensity of 5 W/cm^2, the catalyst beam cannot be closer to resonance than ~ -2 GHz due to adverse effects on the MOT.

The dependence of the measured rate on the catalyst laser intensity can be understood by the increased probability of promotion to the reactive state given by Landau–Zener transition theory for increasing Rabi frequencies Ω_R. Also shown are the results of a coupled-channels calculation. Here, the rates are calculated by allowing for, in addition to the two previously discussed pathways from the MOT laser, a catalyst-laser-enhanced charge-exchange pathway, coupling the Ca(^{1}S$_0$) + Yb$^+$(^{2}S$_{1/2}$) entrance channel to the Ca$^+$(^{2}S$_{1/2}$) + Yb(^{3}D$_2$) exit channel via the intermediate Ca(^{1}P$_1$) + Yb$^+$(^{2}S$_{1/2}$) channel. The experimental data shows good agreement with both the coupled-channels calculations and the simple Landau–Zener model, supporting this interpretation of the results.

8.4 Conclusion

In summary, we have investigated and engineered electronically excited-state collisions of Ca with Yb$^+$ at low collision energy. Using a method for precise control of collision energy, we find that the interaction of the atom with the ion leads to a strong shift between the ground and excited atomic states, causing any laser addressing the bare atomic transition frequency to be shifted from resonance, even at long range. Thus, at low collision energy, an atomic excited state is likely to undergo spontaneous emission before reaching short range. This leads to a strong suppression of scattering events that occur via molecular states corresponding to an atomic excited state. These features are expected to be universal at low temperature for systems with short-lived electronic excitations and long-ranged interactions. To overcome this suppression, we demonstrate a technique using a catalyst laser, which selectively excites colliding molecular complexes at short range. This technique removes

the observed reaction blockading, allowing excited-state collisions to be studied even at ultracold temperatures. As low-temperature techniques provide precise information about the underlying dynamics, this technique should find use as a general tool for studying excited-state collisions. Further, because the technique selectively excites the colliding pair to a chosen state it may be used as a means to select a desired product outcome in polyatomic chemical reactions.

Finally, the reaction blockading effect observed and controlled here is extremely important for the growing field of hybrid atom–ion trapping, where sympathetic cooling of ions with laser-cooled atoms is being pursued [RSS13, Hud16, HC18]. The existence of this reaction blockading effect means that detrimental chemical reactions from excited atomic states, which are energetically unavoidable, will not occur during the sympathetic cooling process. Thus, a large variety of molecular ions can be cooled by laser-cooled atoms without loss to unwanted chemical reactions.

8.5 Supplementary Information

In this section, we provide additional details about experimental techniques and theoretical calculations performed for this experiment.

8.5.1 Determination of State-Specific Rate Constants

Experimental data is recorded by initializing an ion chain and loading the Ca MOT, which is overlapped with the Yb^+ ions. After a variable amount of exposure time, some ions undergo charge exchange (CEX), leading to a loss of ion fluorescence, shown in Figure 8.5. Also apparent from Figure 8.5, the presence of Ca does result in the blurring of the Yb^+ ions, due to collisional heating effects [SDC16], but does not result in a statistically significant change in the fraction of time the Yb^+ ion spends in the 6p $^2P_{1/2}$ state, ρ_{pp}. By fitting the fluorescence decay to an exponential loss, we can determine the reaction rate and calculate

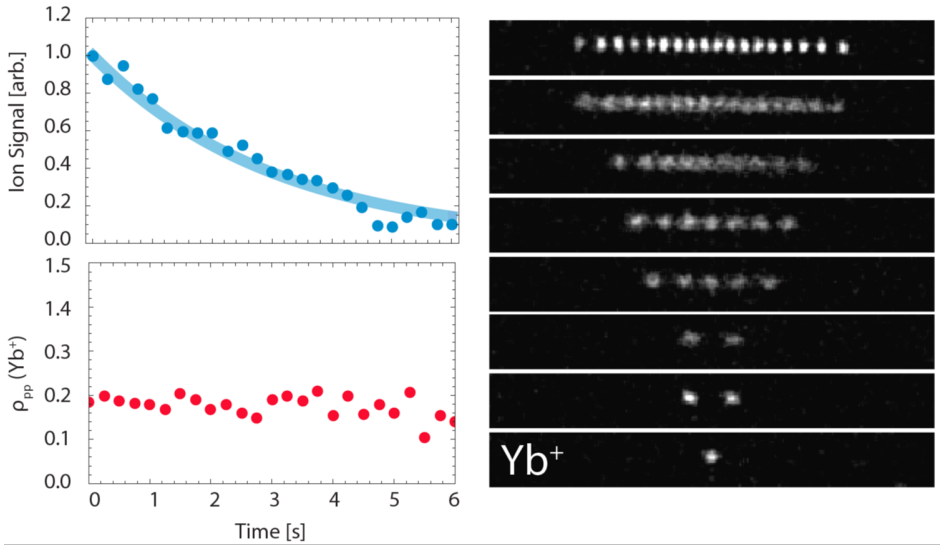

Figure 8.5: **Fluorescence during a CEX reaction.** Exponential decay (upper left) of $^{174}Yb^+$ fluorescence during immersion in the Ca MOT due to CEX as indicated by the EMCCD images (right). The excited-state fraction ρ_{PP} (bottom left), as determined by the fluorescence per ion, is shown to be constant.

the rate coefficient using the density of the Ca atom cloud, measured by absorption imaging.

Repeating this measurement for a variety of Yb^+ laser cooling parameters with constant MOT parameters, the rate constant is measured with various sets of Yb^+ excitation values, $\vec{\rho}_i = \{\rho^i_{\rm ss}, \rho^i_{\rm pp}, \rho^i_{\rm dd}\}$. These values are inferred from the fluorescence measurement of $\rho^i_{\rm pp}$ along with a rate equation model using known experimental parameters. The experimental results using this method of fluorescence detection are shown by blue data points in Figure 8.6 as a function of $\vec{\rho}_i$. Vertical error bars represent standard errors in the reaction rate, and horizontal error bars are estimated uncertainties in parameters for the rate equation model.

The positive correlation between rate constant and the populations in the 6p $^2P_{1/2}$ and 5d $^2D_{3/2}$ states suggests that these channels exhibit a larger charge exchange rate with Ca than the 6s $^2S_{1/2}$ state. However, because $|\vec{\rho}_i| \equiv 1$, it is necessary to perform a multidimensional fit of the experimental rate constant, $k_{\rm tot}$, as a function of $^{174}Yb^+$ excited fraction to the model: $k_{\rm tot} = \rho_{\rm ss}k_{\rm s} + \rho_{\rm pp}k_{\rm p} + \rho_{\rm dd}k_{\rm d}$. Here the k_i are the channel specific rate constants for the three Yb^+ states occupied in the system. From this fit, we find the state-specific

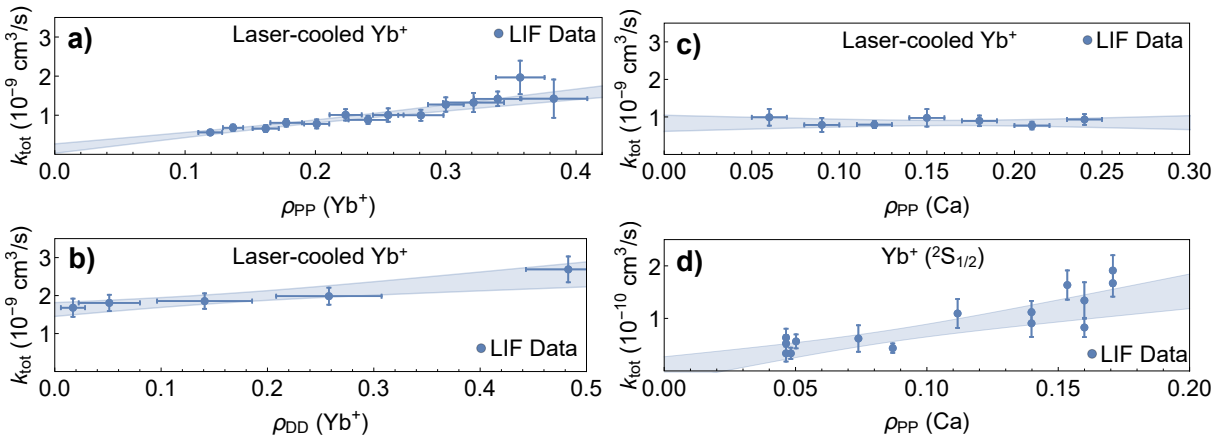

Figure 8.6: **Measured CEX rate constants.** Measured CEX rate constants for laser–cooled Yb^+ (a–c) are shown as a function of state population in (a) $^{174}Yb^+(^2P_{1/2})$, (b) $^{174}Yb^+(^2D_{3/2})$, and (c) $Ca(^1P_1)$. With laser-cooled Yb^+, the CEX rate constant appears to be independent of the excited-state fraction of $Ca(^1P_1)$. This, however, *actually* reflects the experimental inability of measuring the reactivity of the $Ca(^1P_1)$ state due to the high rate of other reactions. (d) The measured CEX rate constant for $^{172}Yb^+(^2S_{1/2})$ is shown as a function of $Ca(^1P_1)$ state population fraction ρ_{PP}. Using the dual isotope method shown in Figure 8.3, we are able to detect the $Ca(^1P_1)$ + $Yb^+(^2S_{1/2})$ rate constant which was previously overshadowed by CEX involving the $Yb^+(^2P_{1/2})$ state.

reaction rate constants given in Table 8.1. The reaction rate constant k_s cannot be resolved with this method, due to the inability of the system to maintain a resolved ion chain at low cooling power, *i.e.* low ρ^i_{pp}.

Similarly, we also measure the charge exchange rate constant as a function of the state populations, $\vec{\rho}_a = \{\rho^a_{ss}, \rho^a_{pp}, \rho^a_{dd}\}$, of the Ca atoms in MOT, while holding the ion cooling parameters constant. This is accomplished by modulating the presence of the MOT lasers

Yb^+ state	Ca state	k_i (cm^3/s)
6p,$^2P_{1/2}$	4s,$^1S_0$	$3.3(3) \times 10^{-9}$
5d,$^2D_{3/2}$	4s,$^1S_0$	$4.2(2) \times 10^{-9}$
6s,$^2S_{1/2}$	4s,$^1S_0$	$< 3 \times 10^{-11}$
6s,$^2S_{1/2}$	4p,$^1P_1$	$7.5(1.5) \times 10^{-10}$

Table 8.1: **Measured state-resolved charge exchange rate coefficients for the Yb^+ + Ca system.** The inferred state-dependent CEX rate coefficients based on fits to experimental data are shown for several combinations of Yb^+ and Ca states.

with an acousto-optic switch, which effectively reduces their intensity and changes the values of $\vec{\rho}_a$. The measured rate constant along one of the populations, ρ^a_{pp} is shown in Figure 8.6c.

Naively, the lack of dependence on ρ^a_{pp} might be interpreted to suggest that the internal state of the Ca atom does not affect the charge exchange rate. However, as discussed in [RSK11, JM89] the relatively short lifetime of the Ca 4p $^1\mathrm{P}_1$-state ($\tau_{\mathrm{p}} \approx 4.5$ ns) and the energy shift of the $^1\mathrm{P}_1 \leftarrow {}^1\mathrm{S}_0$ transition as the Yb^+ ion approaches the atom combine to create a dramatic suppression of any collisions on the excited neutral atom channel. Thus, the reactions we observe here are dominated by the reactive excited states of Yb^+ with the ground state of Ca. To observe the suppressed reactions with the Ca($^1\mathrm{P}_1$) state, we use the dual isotope technique discussed in the main text to isolate Yb^+ in its $^2\mathrm{S}_{1/2}$ ground state, removing the large charge exchange rate from the excited Yb^+ states and allowing greater sensitivity to reactions from excited states of Ca.

8.5.2 Details of Landau–Zener Calculation

A simple theoretical model was shown using the Landau–Zener formula (LZF) to estimate the effect of the catalyst laser. In this model, the long-range attractive potentials are used to determine which partial waves contribute to the reaction, and what the relative speed of the atom–ion pair is as it crosses the distance when the catalyst laser is near-resonant, which is important for the LZF. As the atoms are laser-cooled and are not on a single attractive potential, the force the atom–ion pair feels varies depending on which potential it is on. This fact can complicate both the cross sections predicted by long-range capture theory as well as the probability of the catalyst laser exciting the complex according to the LZF. Outlined below are details of the calculation presented as the "Landau–Zener" predictions in Figure 8.4. We are specifically interested in calculating what the probability is that an atom that would otherwise collide along the ground state would be excited by the catalyst laser and reach short range along the potential corresponding to the Ca($4s4p\ ^1P_1$) state.

- Assume collision energy E with velocity $v = \sqrt{\frac{2E}{\mu}}$ where μ is the reduced mass of the atom–ion pair.

- For each partial wave of orbital angular momentum ℓ, we determine the trajectory in order to know the velocity when the catalyst laser is resonant (which occurs at distance R_{cross})

  - We choose a piecewise force depending on the potential:

    * $R > 800\ a_0$: A time-averaged force is used, with $\sim 92\%$ of the force due to a Ca($4s^2\ ^1S_0$) atom and $\sim 8\%$ of the force due to a Ca($4s4p\ ^1P_1$) atom, matching experimental conditions.

    * $R_{\text{cross}} < R < 800\ a_0$: Once the atom–ion pair has a separation of $\sim 800\ a_0$, the MOT cooling lasers are detuned by 10 linewidths, and are ignored. The force of a Ca($4s^2\ ^1S_0$) atom is used (as we are interested in atoms that approach on the ground channel and get excited by the catalyst laser).

    * $R_{\text{CEX}} < R < R_{\text{cross}}$: The force of a Ca($4s4p\ ^1P_1$) atom is used as the atom–ion pair approaches the distance at which CEX can occur (R_{CEX}).

  - We only accept partial waves with ℓ such that the atom–ion pair will reach R_{cross} and not get turned around at a farther distance. (The atom–ion pair must also reach $\sim 40\ a_0$ along the excited potential after being excited by the catalyst laser after crossing R_{cross})

- Using these calculated trajectories, we now know the velocities at $R = R_{\text{cross}}$ for all partial waves that will contribute to the reaction. Now we use the LZF to calculate the probability of the catalyst laser exciting the collision complex to the state corresponding to the Ca($4s4p\ ^1P_1$) state.

- For the atom–ion pairs that are excited by the catalyst laser, the trajectory is now calculated according to the force from a Ca($4s4p\ ^1P_1$) atom. We use this trajectory to

determine the probability that the Ca atom will spontaneously decay before traversing the distance from R_{cross} to R_{CEX} for each partial wave.

- Combining these probabilities, we now have the probability that the catalyst laser will cause an excited-state, short-range collision (that would otherwise be a ground-state collision) for each partial wave of orbital angular momentum ℓ.

- According to the coupled-channels calculation, $\sim$11% of all excited-state collisions lead to a reaction, so we include this probability in the calculation of the added reaction rate from the catalyst laser.

- We determine ℓ_{max}, the maximum value of ℓ that allows the atom–ion pair to reach short range. From this, the maximum impact parameter b_{max} can also be determined, allowing one to calculate the cross section and rate constant k for this reaction (for a specific collision energy E).

- Each partial wave has its own probability of leading to an excited-state reaction, so we average all contributing partial waves, weighting the values by the partial wave degeneracy factor $(2\ell + 1)$.

- By thermally averaging over the collision energy distribution, we determine a thermally averaged rate constant, which is reported in Figure 8.4.

8.5.3 CEX Rate Coefficient Uncertainty Bands

We estimate uncertainties in the CEX rate coefficients that are caused by uncertainties in both experimental measurements and theoretical calculations. The vertical error bars in Figure 8.1 and Figure 8.4 show the standard error of the rate coefficient measurements. The horizontal error bars in Figure 8.1 come from the uncertainty in the experimental determination of the ion temperature. In Figure 8.4, other uncertainties in the experiment, including the ion temperature and the intensity of the catalyst laser, are incorporated in the

uncertainty bands of the coupled-channels calculations along with theoretical uncertainties as described in more detail in the following.

We account for the uncertainty in the relative temperature of the data, which is measured to lie between 20 mK and 100 mK. As the rate coefficient is not linear over this temperature range we compute it every 10 mK within this entire range.

The experimental uncertainty of the intensity of the catalyst laser is due to the uncertainty of its spatial alignment relative to the location of atom and ion clouds. In Figure 8.4a, the intensity is estimated to be $I = 5(1)$ W/cm^2. We compute rate coefficients for $I = 4$ W/cm^2 and 6 W/cm^2 and rely on its monotonic dependence on I in this range for other values. The intensity of the experimental data in Figure 8.4b is assumed to be 5/6 of the peak intensity of the given laser power and beam waist with a 20% uncertainty.

A major theoretical uncertainty is due to the uncertainty of the scattering length of the ground state potential and the bound state structure in the excited attractive $|\Omega| = 1/2$ Ca(4s4p ^{1}P$_1$) + Yb$^+$(6s ^{2}S$_{1/2}$) potential. There is no spectroscopic data available from literature about these potentials. We account for such uncertainty by varying the scattering length of the ground-state Ca(4s^2 ^{1}S$_0$) + Yb$^+$(6s ^{2}S$_{1/2}$) potential. We slightly modify the depth of this potential and create three potentials with vastly different scattering lengths, $a \approx 0$, β_4, and ∞, but with the same number of $l = 0$ bound states, where $\beta_4 = \sqrt{2\mu|C_4|/\hbar^2} = 3.05\times10^3\ a_0$ is the characteristic length scale for the C_4/R^4 potential. The range of scattering lengths modifies the thermalized rate coefficients of the catalyst pathway and increase the width of the uncertainty band to up to 15%.

Another theoretical uncertainty is related to the width of the non-adiabatic coupling between the excited potentials at their crossings that lead to charge exchange. The area of the crossings is schematically marked by "CE" in a circle in Figure 8.2b, c, and d. Assuming to be a Lorentzian function, the non-adiabatic coupling matrix element has a half width $R_0 = 0.37\ a_0$ with an uncertainty $\sim 0.02\ a_0$. The values are determined by fitting the coupled-channel calculations to the experimentally measured CEX rate coefficients without

the catalyst laser. Details can be found in [LMP19]. To incorporate this uncertainty, we compute rate coefficients for $R_0 = 0.35\ a_0$ and $0.39\ a_0$ and rely on its monotonic behavior with R_0 for other values.

All these uncertainties are added in quadrature to find the final uncertainty bands in both Figure 8.4a and b.

CHAPTER 9

Rotational State Thermometry of $BaCl^+$

To demonstrate the effectiveness of the sympathetic rotational cooling of $BaCl^+$ molecular ions by the cold Ca atoms in the MOT, one must have a method to measure the rotational temperature. This can be done by measuring the population in each rotational state and comparing to a thermal distribution with some rotational temperature T_{rot}. As molecules do not tend to have optical cycling transitions to make state readout simple, we utilize photodissociation spectroscopy. Specifically, we use a UV laser that dissociates some excited vibrational level $v' > 0$ in $BaCl^+$ that does not strongly dissociate $v = 0$. We drive an overtone vibrational transition $v' \leftarrow v = 0$ transition in a manner that will only address a specific rotational state J in the $v = 0$ manifold, labeled $|0, J\rangle$. For example, by using the rotational R-branch, the $|v', J' = J + 1\rangle \leftarrow |v, J\rangle$ transition is driven. The dissociation laser can then be introduced. If the $BaCl^+$ molecular ion was excited to the v' vibrational state, it will be dissociated, indicating that the molecule was initially in the $|v, J\rangle$ state. By repeating this process while sweeping the overtone-driving laser frequency, the relative populations of the different rotational levels in the $v = 0$ state can be determined. By comparing the number and relative strengths of the peaks for different rotational levels, the rotational temperature can be inferred. This process is illustrated in Figure 9.1 for $v' = 8$.

The signal shown in Figure 9.1c and d consists of peaks spaced by ~ 6 GHz, each with a linewidth limited by by linewidth of the laser driving the vibrational overtone transition, which may be on the order of $\sim$ 1MHz. As such, one must know the precise frequency of the vibrational overtone transition. The energies relative to the $v = 0$ state of levels $v = 1$–$v = 7$

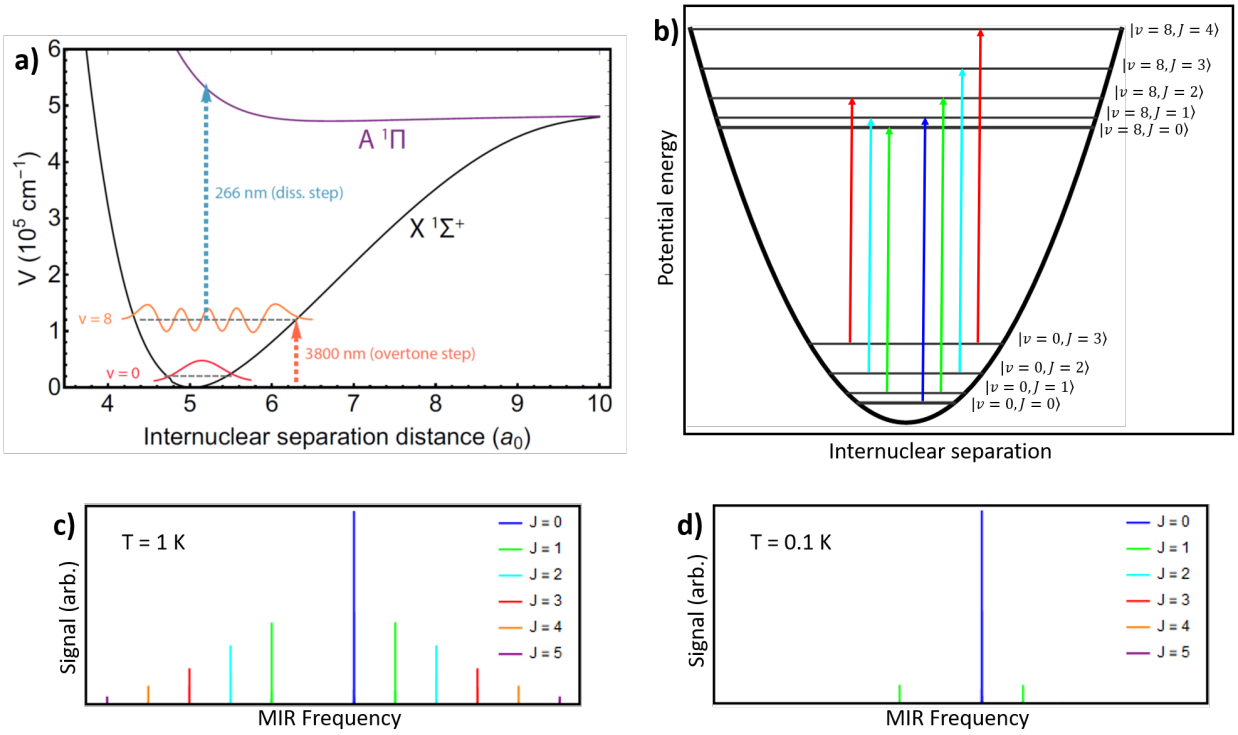

Figure 9.1: **Rotational thermometry with vibrational overtone transition and vibration-state-selective dissociation.** An overview of the technique described in this chapter is presented for $v' = 8$. (a) The electronic X $^1\Sigma^+$ and A $^1\Pi$ states of $BaCl^+$ are shown, with the $v = 0$ and $v = 8$ states depicted for the ground state. The $v' = 8 \leftarrow v = 0$ transition is driven by a MIR laser with wavelength ~ 3800 nm. Then, a 266 nm dissociation laser dissociates the $v = 8$ population, but not the $v = 0$ population. (b) Within the $v = 0$ and $v = 8$ manifolds, several low-lying rotational states are shown (not to scale). R-branch transitions are shown to the right of the center of the potential well, and P-branch transitions are shown to the left. (c) Simulated results are shown for a rotational temperature of 1 K as a function of the MIR frequency scanned. R-branch transitions are shown to the right of center, and P-branch transitions are shown to the left. (d) Simulated results are shown for a rotational temperature of 0.1 K. By measuring an experimental spectrum, the rotational temperature can be inferred by the number and relative strength of measured peaks.

have been measured experimentally in Ref. [VPH19], with 2-σ error bar ranges of ~ 300 GHz. These data can be extrapolated to approximate the energies of higher vibrational states. To more precisely locate the transition frequency, a scan of the vibrational overtone laser frequency must be performed. We aim to perform such a scan, by scanning a laser near the $v' \leftarrow v$ transition frequency while the photodissociation laser is present. If the laser drives the vibrational transition, the trapped $BaCl^+$ will be dissociated and a signal will be detected. We expect long experiment times to scan over a large range while looking for the transition. To achieve such long experiment times, we operate without the MOT present, as reactions with the MOT would cause the $BaCl^+$ to react and disappear, making the real dissociation signal difficult to detect. As a result, the internal temperature of the $BaCl^+$ ions will be ~ 300 K.

To detect the dissociation of $BaCl^+$, there are a few options. First, since the dissociation of $BaCl^+$ produces a Ba^+ ion, an increase in the fluorescence of Ba^+ can be measured to detect dissociation. Second, after a search is complete, the ions can be ejected into the ToF and their amounts measured. The ToF method has a few disadvantages in that it does not resolve *when* during an experiment the $BaCl^+$ was dissociated, and that the initial amount of $BaCl^+$ must be known. Using the controlled gas leak system, a consistent fraction of $BaCl^+$ ions compared to the total number of ions can be loaded, minimizing the second drawback. Even so, one might think that the fluorescence measurement is even more useful because it gives not only the amount of $BaCl^+$ dissociated, but information on when it was dissociated. We have found that in reality, certain experimental drawbacks limit its usefulness. We find that the Ba^+ fluorescence decreases over time due to reactions with background gases in the vacuum chamber. Noticeably, $BaOH^+$ and $BaOCH_3^+$ build in over time. $BaOCH_3^+$ we have found can be dissociated by UV wavelengths as high as 280 nm, resulting in a Ba^+ ion from what we have observed, limiting losses due to that reaction. Still, we find that over time, $BaOH^+$ loads in over time ($\sim 10\%$ of ions are $BaOH^+$ after ~ 1 hour), and these molecules are not dissociated by a UV laser that would not also dissociate $BaCl^+$. Additionally, we

have found that the Ba^+ fluorescence per ion depends on the ion crystal size, dark ion fraction, and may drift over time due to drifting parameters such as cooling laser overlap. For this reason, we typically rely on ToF data to yield a more reliable measure of the $BaCl^+$ dissociation rate.

Several considerations must be taken when selecting an appropriate excited vibrational level v'. It is advantageous to select a vibrational level that is not significantly populated at 300 K. For this reason, we limit the choice to $v' \geq 4$. Additionally, the vibrational overtone must be driven with a finite laser power, so the strength of the transition must be considered. There can be significant uncertainties in calculated transition strengths of high overtones, but in general, higher overtones will be harder to drive. Additionally, the UV photodissociation laser must dissociate the v' state relatively efficiently (before the v' state can spontaneously decay to a lower vibrational state) while not dissociating the states thermally populated at 300 K. There will be some trade-off between these last two criteria. Higher values of v' will be more difficult to drive, but the wavelength of the dissociation laser will be well-separated from the wavelength that dissociates the thermally populated vibrational states. Combined, this will result in a weak dissociation signal due to the weak overtone transition strength, but also a weak dissociation background due to the well-separated dissociation wavelengths. Conversely, lower values of v' will result in a faster signal dissociation and a faster background dissociation of a 300 K sample. The combination that will provide the highest signal-to-background dissociation rate is unknown due to the uncertainty in the vibrational overtone transition rates.

With no vibrational overtone being driven, the background dissociation rate for $BaCl^+$ with various photodissociation wavelengths was measured and the results are plotted in Figure 9.2. The data point at 266 nm was taken using the fourth harmonic of the Spectra Physics Nd:YAG laser, and the other data points were taken using the Sirah PDL. The repetition rate of each of these pulsed lasers was the same at 10 Hz, and an effort was made to keep the beam waist the same. We normalize the photodissociation rates by the UV

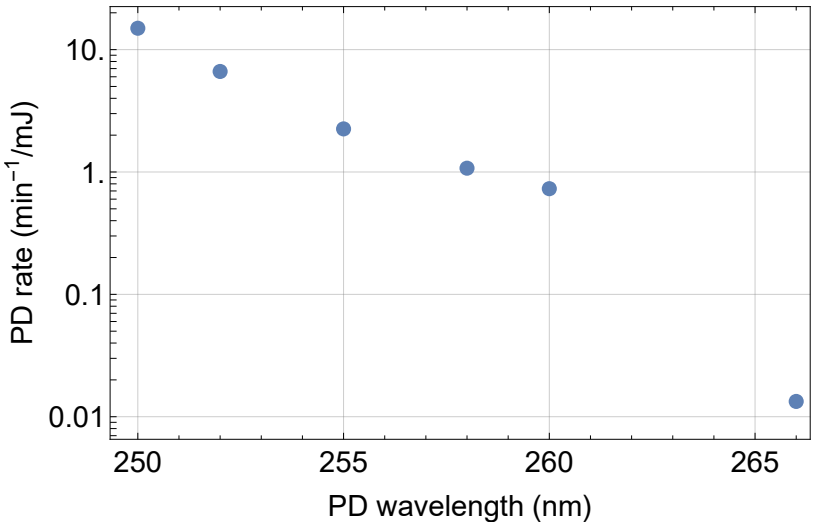

Figure 9.2: **$BaCl^+$ photodissociation rate as a function of wavelength.** The photodissociation rate of $BaCl^+$ was measured for various photodissociation wavelengths. For each data point, the repetition rate is the same at 10 Hz and an effort was made to maintain the same UV beam waist. For each data point, the dissociation rate was measured in min^{-1} as a function of the UV pulse energy. The slope of this curve is plotted, giving a pulse-energy-normalized dissociation rate.

energy per pulse, which can easily be measured and monitored using a Gentec laser energy meter. For each data point, the loss rate of $BaCl^+$ was measured for a variety of different pulse energies. These measured loss rates were fitted with a linear function to determine the pulse-energy-normalized loss rate in units min^{-1}/mJ. This experiment was repeated for various photodissociation wavelengths, yielding the results shown in Figure 9.2. As expected, the background loss rate, which is the rate at which $BaCl^+$ with an internal temperature of 300 K is lost, decreases for larger wavelengths. This information can help inform the decision of which excited vibrational state v' to use. This data does not, however, give information on how efficiently the UV laser will dissociate the v' state. Additionally, it should be noted that even in the absence of any photodissociation laser, a small loss rate of the $BaCl^+$ is observed over long time periods. This UV-laser-free background loss was measured to be 0.013 min^{-1}, or 0.8 hr^{-1}, meaning that over an hour, only a fraction of $e^{-0.8} = 0.45$ of the initial $BaCl^+$ remains. This loss also implies that there will be diminishing returns to the

advantage of using much longer wavelengths than 266 nm, as the combined background loss rate (including UV losses and UV-free losses) will not significantly decrease.

To help to quantify these effects in an attempt to optimize the choice of v' and experimental parameters, we simulate the system including transition rates between different rovibrational states and state-dependent photodissociation cross sections. To allow us to calculate these transition rates and cross sections, Professor Hua Guo calculated the molecular potentials and dipole moment functions for $BaCl^+$. These potentials and dipole moment functions were input in to the LEVEL and BCONT program packages to obtain photodissociation cross sections and transition strengths.

Several experiments have been performed to detect a $BaCl^+$ dissociation signal from this scheme, without luck so far, using various values of v'. The following sections describe each of these experiments, including motivations or calculations for each technique, what has been done, what was learned, and what can still be done. The ordering of these sections follows the chronological order of the experiments attempted, which also range from the cheapest implementation to the most expensive implementation.

9.1 Ti:sapph, $v' \approx 40$

One simple experimental implementation of this technique, requiring no new lasers, is to use the M2 Ti:sapph laser at ∼800 nm to attempt to drive the $v' \approx 40 \leftarrow v = 0$ transition. While driving such a high overtone seems unlikely, the Ti:sapph outputs > 1 W at 800 nm and can be focused to high intensity at the ions. Additionally, the third harmonic of the Nd:YAG laser at 355 nm can act as the photodissociation laser, allowing pulse energies of 50 mJ to be used in experiment with virtually no background $BaCl^+$ dissociation due to this laser. Also, most importantly, this scan can be easily performed without purchasing new equipment. As such, we were able to perform this experiment while determining the best path forward for a future experiment and purchasing the necessary equipment, minimizing

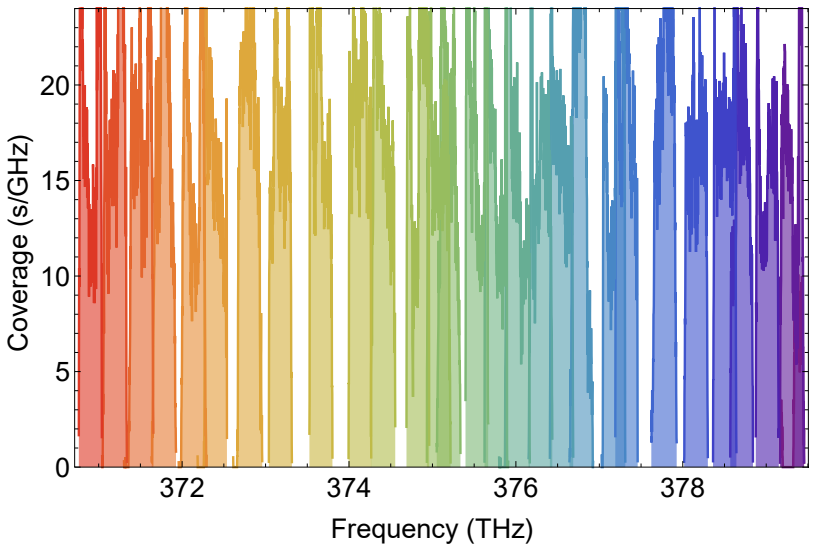

Figure 9.3: **Frequency covered during Ti:sapph scan.** The coverage, defined as the amount of time spent in a given frequency bin, is plotted as a function of Ti:sapph frequency, showing the range of frequencies scanned in this experiment.

any potential down time.

While performing this experiment, we noticed that the formation of $BaOH^+$ and $BaOCH_3^+$ limited the experiment time due to the loss of Ba^+ ions. To partially remedy this, we found that by adding a 280 nm UV pulsed laser from the PDL, we could dissociate the $BaOCH_3^+$ and increase the lifetime of the Ba^+. Additionally, this laser may help dissociate any vibrationally excited Ba^+ molecules.

As one might have expected, we were not able to produce any $BaCl^+$ dissociation noticeable above a control experiment with no Ti:sapph present. The full range of Ti:sapph frequencies covered is shown in Figure 9.3, where the coverage is defined as the amount of time spent in a frequency bin. Each experimental sequence is shown as a shaded area, corresponding to approximately 1 hour each over a typical range of $\sim$ 250 GHz. I had a little bit of fun with the colors, with the reddest frequencies of the scan shaded in red and the bluest shaded in violet, with intermediate shading for intermediate frequencies.

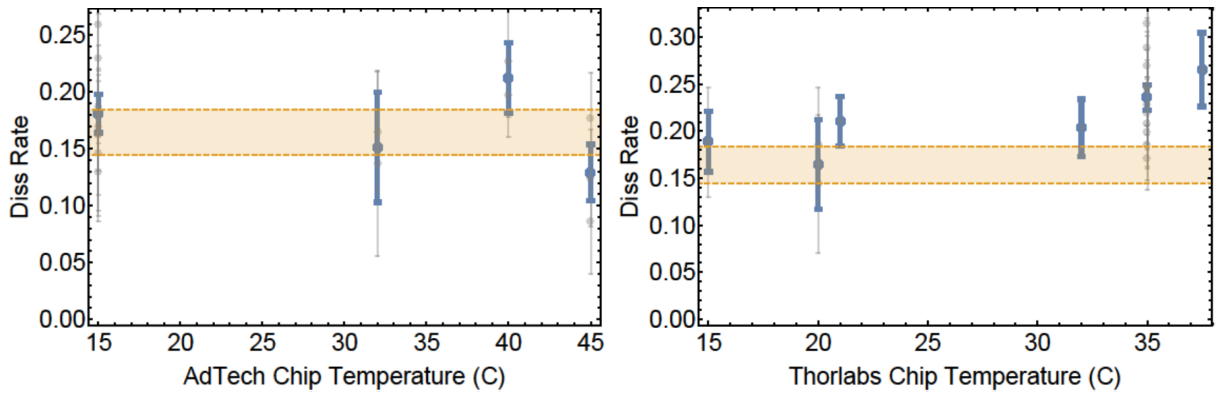

Figure 9.4: **Broadband QCL dissociation rates.** The dissociation rate of $BaCl^+$ is measured using either the AdTech or Thorlabs QCL to attempt to drive the $v' = 7 \leftarrow v = 0$ transition followed by 266 nm dissociation. The 1-σ statistical error range of the dissociation rate with no MIR is shown as a yellow band for comparison. The dissociation rate with one of the QCLs at various operating temperatures are shown as blue dots with 1-σ statistical error bars. For data points that are the average of multiple data sets, the individual experimental results comprising the average are shown as gray dots with 1-σ statistical error bars.

9.2 Broadband QCLs, $v' = 7$

To drive a vibrational overtone much lower in energy than the previous experiment, a mid-infrared (MIR) source is needed. To achieve high power in this wavelength range, a quantum cascade laser (QCL) can be utilized. A QCL, first demonstrated in 1994 [FCS94], rely on many alternating layers of semiconductor material to form quantum energy wells. As an electron traverses these wells, it can transition from one valence band energy state to a lower one, emitting a photon. As traditional diode lasers generate photons by transitions between the conduction band and the valence band, the output wavelength is limited by the bandgap to ~ 2.5 μm. QCLs rely on transitions from one valence band energy state to another, so they are not limited by this effect and can achieve wavelengths in the mid- to far-infrared.

Without an external cavity, the output of such a QCL can be quite broad, of order THz. This output can be narrowed to ~ 1 MHz using an external cavity, similar to a traditional diode laser. Instead of constructing an external cavity for one of these broadband QCLs, we elect to use the broad output. While the spectral density is not high at a single rovibrational

transition, this broad output can address many rotational states at once. Example spectra of these lasers are shown in Figure 2.45. By changing the QCL operating temperature and current, the output spectrum can by varied. The typical power of these QCLs is 200–300 mW with a beam waist of ~ 1 mm. To dissociate the $BaCl^+$ in the $v' = 7$ state, a 266 nm UV laser is used with a pulse energy of ~ 1 mJ.

The results of such an experiment are shown in Figure 9.4. Shown are the measured $BaCl^+$ dissociation rates for various QCL operating temperatures. Average rates are shown as blue dots with 1-σ statistical error bars. For rates consisting of the average of multiple measurements, the values comprising the average are shown as gray dots with 1-σ statistical error bars. For comparison, the measured $BaCl^+$ dissociation rage with no QCL present is shown as a yellow band indicating the 1-σ statistical error bounds. Based on this data, there is no clear dissociation signal above a control $BaCl^+$ dissociation rate. Between the two steps critical to this experiment—MIR vibrational overtone excitation and UV photodissociation of the excited molecules—it is difficult to determine which step was the limiting factor. For example, the UV dissociation spectrum has peaks and troughs, and it's possible that the selection of 266 nm is unlucky. If this effect is not significantly limiting the overall signal dissociation, we estimate that based on the MIR intensity and spectral density over the range of the expected transition frequency, that the Einstein A-coefficient between a typical $|v = 0, J\rangle$ and $|v' = 7, J' = J \pm 1\rangle$ state must be $A_{07} < 1 \times 10^{-3}$ s^{-1}.

9.3 Daylight Laser, $v' = 8$

To achieve a higher spectral density, a Daylight Laser system was purchased (M1038-PC-QCL-J0162). This laser has an output power of ~ 50 mW at the wavelength we operate it, a tuning range of 3650–3850 nm, and a linewidth of ~ 1 MHz (although measuring the frequency on a Bristol 671A-MIR wavelength meter, we found the frequency oscillating by ~ 10 MHz on the time scale of seconds). Additionally, we selected to purchase this laser

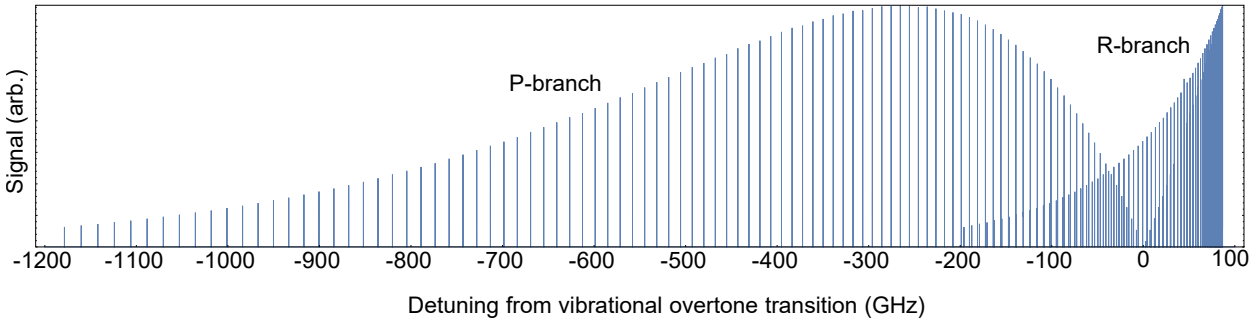

Figure 9.5: **Simulated signal versus frequency for the $v' = 8 \leftarrow v = 0$ transition.** Based on the rotational state population at 300 K and assuming perfect UV dissociation of the $v' = 8$ state, the expected $BaCl^+$ dissociation signal for a MIR laser with a linewidth of 10 MHz is plotted as a function of the MIR detuning from the energy difference between the $v' = 8$ and $v = 0$ states.

to drive the $v' = 8 \leftarrow v = 0$ transition instead of using the $v' = 7$ transition as previously attempted. This decision was made in case the transition rate for the $v' = 7$ transition was lower than expected or in case the 266 nm dissociation of $v' = 7$ was inefficient. If the $v' = 7$ dissociation was actually efficient and the $v' = 8$ dissociation *is* inefficient, this would still not be catastrophic, as the vibrational relaxation is most likely to occur by a $\Delta v = 1$ transition, meaning that if the $v' = 8$ $BaCl^+$ was not dissociated, it would likely decay to the $v' = 7$ state and hopefully be dissociated.

With an effective MIR linewidth of 10 MHz, the expected $BaCl^+$ dissociation signal as a function of the MIR frequency is plotted in Figure 9.5, assuming the UV photodissociation is efficient. The individual lines correspond to the P- and R-branch transitions for various rotational states in the $v = 0$ state that are populated at 300 K. The width of each of these peaks is limited by the MIR linewidth of 10 MHz. Compared to the linewidth of the broad QCL ($\sim$ 1 THz), even though the power for this laser is lower by a factor of a few, the narrow linewidth gives this laser $\sim 10^4\times$ more spectral intensity at a specific rovibrational transition.

One may expect, then, that scanning this MIR laser on one of these peaks will yield a strong dissociation signal. Unfortunately, even if the laser frequency is tuned exactly at

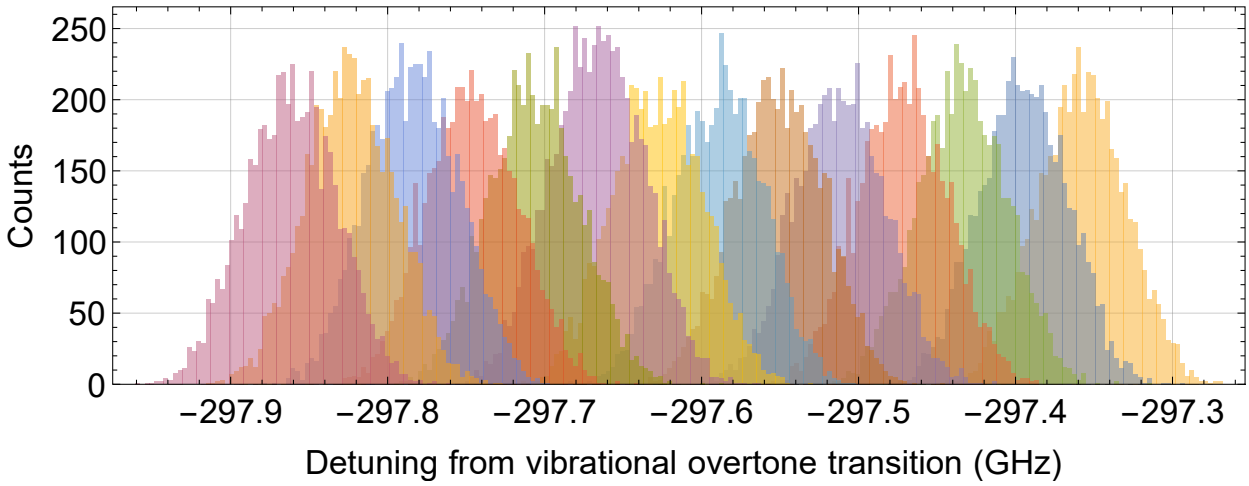

Figure 9.6: **Example MIR scan spectra.** Example data of the MIR frequency distribution for 14 data points are shown. The frequency step is chosen such that the gaps between data points are minimal.

the highest peak, only one rotational state ($\sim 1\%$ of the $BaCl^+$ population) will be driven to the $v' = 7$ state. It is possible, however, for the rotational states to redistribute over time. This happens through a few mechanisms. One such way is that blackbody radiation (BBR) can drive the $|v' = 1, J' = J \pm 1\rangle \leftarrow |v = 0, J\rangle$ transition, which will decay to either the $|v = 0, J + 2\rangle$, $|v = 0, J - 2\rangle$, or $|v = 0, J\rangle$ state. The vibrational excitation due to BBR happens roughly every 5 s, and the relaxation takes roughly 1 s. Another possibility is a collision with a background gas can alter the rotational state of the $BaCl^+$. Given the experimental vacuum pressure ($< 10^{-9}$ mbar), these collisions are not very frequent. To attempt to increase this rotational redistribution rate, we leak in argon gas at a pressure of 2×10^{-8} mbar. Based on the Langevin rate constant, we expect the $BaCl^+$ to collide with an Ar atom roughly once every 4 s. While this redistribution time is not significantly faster than the BBR redistribution rate, every improvement possible is valuable. Because of the relatively slow timescale of the rotational state redistribution, long experiment times must be used. The desired experiment time depends on certain experimental parameters, but a typical value is 30 minutes.

Because of the long experiment times, scanning over a large frequency range with each

experiment covering 10 MHz would take a long time, even if only one data point per frequency were taken. As one can see in the simulated signal in Figure 9.5, the highest density of rovibrational spectrum peaks occurs near the band head of the R-branch. Additionally, the rotational states corresponding to these peaks are near the maximum state population. To minimize the scan range required to hit one of these large peaks, it seems natural to aim for this feature. One issue is that the frequencies shown have a 2-σ uncertainty of roughly $\pm$150 GHz. As the band head feature is only $\sim$ 40 GHz wide, one would have to do multiple searches to hope to achieve the correct frequency. Instead, we elect to use a frequency in the P-branch, at a detuning of roughly -300 GHz. This way, even if the frequency is off by 150 GHz in either direction, we are still near a relatively large peak. Then, by scanning a range of 13 GHz, more than enough frequency space has been covered that we can be essentially certain that we have addressed one of the rotational states (The spacing between lines should be $\lesssim$ 10 GHz). (In fact, we also attempted to look for the band head feature in an attempt to get lucky.) We have found that to ensure a frequency range coverage with no gaps, a frequency step of roughly 2/3 of the linewidth should be used. To cover 13 GHz with a linewidth of 10 MHz, a step size of 6.7 MHz, and 90% experimental up time to allow for loading and initialization, this scan would take 68 days with a 16-hour work day. To make this scan more manageable, we instead artificially broaden the MIR laser to 60 MHz by dithering the voltage on a piezo that controls the laser frequency. We then use a step size of 40 MHz to ensure a gap-free coverage. An example of the measured MIR frequency histograms for 14 data points is shown in Figure 9.6.

A typical experimental sequence for a data point is as follows. Before starting to take data, argon gas is introduced at a pressure of 2×10^{-8} mbar to accelerate rotational state redistribution. First, a crystal of pure laser-cooled $^{138}Ba^{+}$ is loaded using the techniques described in Subsection 2.2.8. The ion number is on the order of a few 1000 ions. The precise number is not important, but the ion crystal size is kept as constant as possible to minimize any systematic errors due to crystal size. Then, using the controlled gas leak system, a

controlled and measured amount of CH_3Cl gas is leaked in to the chamber, producing a known fraction of $BaCl^+$ ions compared to the total number of trapped ions. By calibrating this fraction with some dedicated measurements each day, this gives us the initial fraction of $BaCl^+$ during an experiment. Again, to minimize systematic errors, the same amount of $BaCl^+$ is loaded for each data point. Once the ion crystal has been initialized with the desired $BaCl^+$ fraction, the MIR and UV lasers are introduced for 30 minutes. During this time, the MIR laser frequency is monitored, recorded, and locked to the desired frequency, and the UV laser pulse energy is monitored and recorded. After this time, the MIR and UV lasers are blocked, and the trapped ions are ejected into the ToF for measurement. The final fraction of $BaCl^+$ is measured and compared to the expected initial fraction based on the amount of CH_3Cl leaked in. Based on the experiment time, a loss rate k (typically of order 1.5 hr^{-1}) can be calculated by $k = -\log\left[\frac{\text{final BaCl}^+\text{ fraction}}{\text{initial BaCl}^+\text{ fraction}}\right]/t_{\text{exp}}$ where $t_{\text{exp}} = 30$ minutes is the experiment time. This rate k can be compared to the expected loss rate k_{exp} due to the expected decay with no lasers in that time plus the expected decay due to the presence of the 266 nm laser at the average measured pulse energy. By looking at the difference in those rates $k_{\text{diff}} = k - k_{\text{exp}}$, one can correct for any changes in the 266 nm laser pulse energy. Additionally, we limit the analysis to the $BaCl^+$ including the ^{35}Cl isotope, as that is the only isotopologue we expect to address with the MIR laser.

The results of this experiment are plotted in Figure 9.7. For a total of 375 data points covering 13 GHz, k_{diff} is plotted with estimated 1-σ experimental error bars as a function of detuning from the vibrational overtone transition frequency. While some points appear to be outliers with a higher-than-expected $BaCl^+$ decay rate, any of these promising-looking points was repeated multiple times, and none of them produced repeatably high $BaCl^+$ decay rates. Based on the spread of values for k_{diff} and our tendency to repeat any data points that had a higher-than-typical value of k_{diff}, we estimate our sensitivity to be approximately 0.75 hr^{-1}. That is to say we expect that if the actual increased rate due to the presence of the MIR was 0.75 hr^{-1} or greater, we would have noticed it and been able to detect it as a

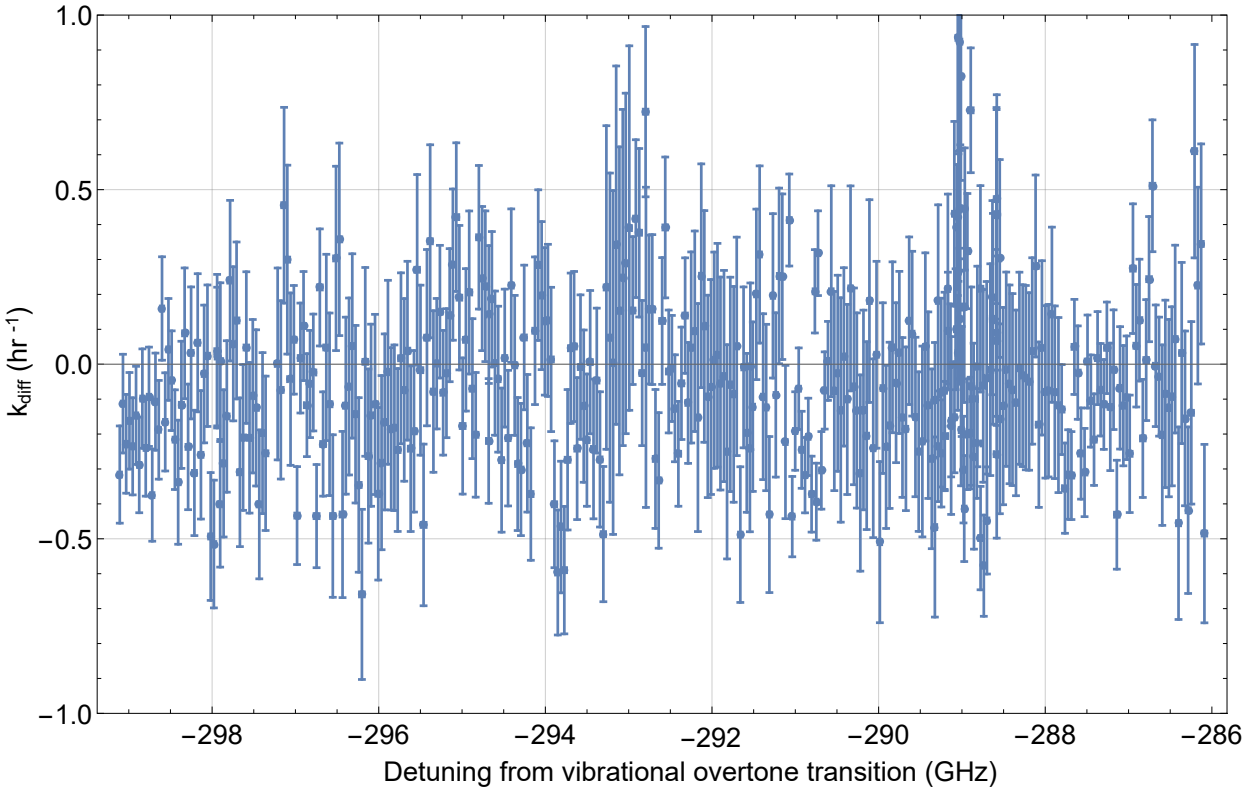

Figure 9.7: **Daylight laser $v' = 8$ scan results.** The measured difference in $BaCl^+$ decay rate from the expected decay rate $k_{\text{diff}} = k - k_{\text{exp}}$ is plotted with estimated 1-σ experimental error bars as a function of detuning from the vibrational overtone transition frequency. Any data point appearing to be an outlier was repeated multiple times, and no frequencies resulted in a repeatably higher-than-expected rate.

signal. Based on this value and a conservative estimate of our experimental parameters, we estimate that the Einstein A-coefficient between a typical $|v = 0, J\rangle$ and $|v' = 8, J' = J \pm 1\rangle$ state must be $A_{08} < 1 \times 10^{-5}$ s^{-1}. This limit corresponds to a factor of 5 smaller than the expected A-coefficient from the theoretical calculations, meaning that the transition strength is measured to be lower than expected.

In addition to the scan presented in this section, we also performed experiments with varying MIR linewidths and varying detunings from the vibrational overtone transition. For example, it is possible that using a broad MIR laser (on the order of 50 GHz) that can address multiple rotational states at once is beneficial, especially if the laser is near the R-branch

band head. We of course played around with these settings in simulation and attempted such experiments, but none of them yielded any significant $BaCl^+$ decay rate above the expected background decay rate.

As this search was unsuccessful, it appears that it is possible that the theoretical rates overestimate the strength of high vibrational overtone transitions. To this end, we sent the MIR laser back to Daylight Solutions to replace the QCL chip with one that can operate near the $v' = 4 \leftarrow v = 0$ transition, near 7530 nm. This experiment is in progress and is discussed further in Chapter 11.

CHAPTER 10

Dipole–Phonon Quantum Logic with Alkaline-Earth Monoxide and Monosulfide Cations

Once control of molecular ions has been attained, there are several promising applications towards quantum information science. One such recently proposed application is dipole–phonon quantum logic (DPQL) [CH20]. DPQL is a toolkit of quantum logic operations that utilizes the interaction between the oscillating dipole of a molecular ion with the phonon modes in an ion trap. One key requirement of DPQL is that the molecular ion must have a pair of electric-dipole-connected states with a transition frequency near the secular frequency of a normal mode of motion in the ion trap, typically on the order of MHz. These states could be the $|0\rangle$ and $|1\rangle$ states in a molecular ion qubit. To take advantage of DPQL, it is necessary to find a suitable molecular ion.

As rotational states are typically separated by GHz or more, these states are not suitable for DPQL. There are linear polyatomic and symmetric-top molecules that have ℓ- and K-doublets that could be suitable, but compared to diatomic molecules, the rovibrational structure of polyatomic molecules is more complicated and may lead to additional experimental difficulties. Restricting the consideration to diatomic molecules, Ω-doublets seem to be a promising structure. We find that alkaline-earth monoxides and monosulfides have the structure necessary for DPQL and have the added advantage of easily being produced in existing atomic ion experiments. This chapter outlines our study of this class of molecules towards the application of DPQL as a version of our group's publication "Dipole–phonon quantum logic with alkaline-earth monoxide and monosulfide cations."

Dipole–phonon quantum logic (DPQL) leverages the interaction between polar molecular ions and the motional modes of a trapped-ion Coulomb crystal to provide a potentially scalable route to quantum information science. Here, we study a class of candidate molecular ions for DPQL, the cationic alkaline-earth monoxides and monosulfides, which possess suitable structure for DPQL and can be produced in existing atomic ion experiments with little additional complexity. We present calculations of DPQL operations for one of these molecules, CaO^+, and discuss progress towards experimental realization. We also further develop the theory of DPQL to include state preparation and measurement and entanglement of multiple molecular ions.

10.1 Introduction

Trapped-ion qubits have demonstrated the highest-fidelity quantum operations of all quantum systems [BHL16, HAB14, GTL16, CHC20]. As such, they are promising candidates for a scalable quantum information platform if the challenge of integrating and scaling the associated technology can be met. Chief among these challenges is this integration of the lasers required not only for cooling of the ions, but typically for manipulation of the qubits. Currently, two main approaches to this problem are being pursued. First, integrated photonics could provide a scalable means to deliver the requisite lasers [BMS19, MZM20] if the capabilities demonstrated in silicon photonics can be extended to materials compatible with the visible and ultraviolet wavelengths necessary for atomic ion qubits [MBM16]. Second, several schemes for laser-less manipulation of atomic ion qubits are being explored, which involve microwave fields paired with either a strong static magnetic field gradient [MW01, JBT09, KPS12], a microwave magnetic field gradient [OLA08, OWC11, BWC11], microwave dressed states [TBJ11], or a magnetic field gradient oscillating near a motional mode frequency [SBS19, SSB19]. Both integrated optics and microwave control require advances in ion trap fabrication to be truly scalable.

A recent proposal [CH20] outlined a third potential avenue to scaling by using the interaction between polar molecular ions and the phonon modes of a multi-ion Coulomb crystal for quantum logic. Broadly speaking, this dipole–phonon quantum logic (DPQL) provides a means to initialize, process, and read out quantum information encoded in molecular ion qubits without the need to optically illuminate the molecules (and in some cases without the need for ground-state cooling). Together with the use of the direct, electromagnetic dipole–dipole interaction between trapped molecular ions [HC18], this could provide a route to a robust and scalable platform for quantum computation, sensing, and communication, including the possibility of microwave–optical transduction [CH20].

Though the simplicity of DPQL makes it an attractive approach, it is not without requirements for practical implementation. Chief among these is the prerequisite that the qubit molecule possess two opposite-parity states that are energetically spaced by an interval similar to the energy of the trapped-ion phonon modes, i.e. $\lesssim 20$ MHz. While the ℓ- and K-doublets of many linear polyatomic and symmetric top molecules satisfy this requirement [KH17], this criterion is more restrictive for diatomic molecules, where typically only certain Ω-doublets have the necessary structure. As the low density of populated rovibrational states found in diatomic molecules makes them attractive candidates for DPQL, identifying molecules with the requisite properties for and understanding their application to DPQL is necessary before experimental implementation.

Here, we discuss the theory of DPQL and present a case study of using DPQL to observe a phonon-mediated interaction between two trapped CaO^+ ions. We follow this discussion with a survey of likely DPQL candidate molecules, the cationic alkaline-earth monoxides and monosulfides (MO^+ and MS^+). Through *ab initio* calculations, we find that these molecules possess a large electric dipole moment ($\geq$ 7 D) and exhibit Λ-doublets with $\sim$ 1 kHz to $\sim$ 10 MHz spacing, making them particularly amenable to DPQL. Further, since the trapped *atomic* ions used in quantum information experiments are predominantly alkaline-earth atoms, these molecules can be formed *in situ* by simply 'leaking' e.g. oxygen

into the vacuum chamber [GCV13]. As DPQL requires no additional lasers, this means many current experimental platforms could easily be extended to this work. We conclude with considerations for practical implementation of this scheme, as well as report on recent progress towards an experimental demonstration of this technique.

10.2 Dipole–Phonon Quantum Logic

At its core, DPQL utilizes the coupling between the motional mode of a Coulomb crystal and the dipole moment of a polar molecular ion to transfer information between a qubit encoded within the internal states of the molecule and a shared phonon mode of the trapped ions. Essentially, an oscillating ion experiences an electric field due to the combination of the trapping electric field and repulsion from the other ions. If the energy interval between the two opposite parity states within the molecule, here assumed to be the two components of a Λ-doublet, is similar to the energy of the phonon mode, a Jaynes–Cummings type Hamiltonian is realized and the molecule may emit and absorb phonons. This interaction provides a complete set of quantum logic operations, including state preparation and measurement of the molecular qubit and atom–molecule and molecule–molecule entanglement. In this section we develop the basic building blocks of DQPL and show how they can be used to observe phonon-mediated molecule–molecule interactions.

The dipole–phonon interaction derives from the interaction $H_{dp} = -\mathbf{d}^{(i)} \cdot \mathbf{E}^{(i)}$, where $\mathbf{d}^{(i)} = d\sigma_x^{(i)}\hat{\mathbf{z}}$ is the dipole moment of molecular ion (i), $\mathbf{E}^{(i)}$ is the total electric field at the position of ion (i), $\sigma_x^{(i)} = \left|\mathrm{e}^{(i)}\right\rangle\left\langle\mathrm{f}^{(i)}\right| + \left|\mathrm{f}^{(i)}\right\rangle\left\langle\mathrm{e}^{(i)}\right|$ where $\left|\mathrm{f}^{(i)}\right\rangle$ and $\left|\mathrm{e}^{(i)}\right\rangle$ are the upper and lower Λ-doublet states of molecule (i), respectively, and $\hat{\mathbf{z}}$ is the quantization axis, taken to be along the axial direction of a linear Paul trap. Assuming only one phonon mode is near the Λ-doublet splitting $\omega_{\mathrm{mol}}^{(i)}$ of molecule (i) and following the treatment in Ref. [CH20], the interaction between the molecular qubit state of ion (i) and the axial motion of normal mode

q can be described by a spin–boson Hamiltonian:

$$H_q^{(i)} = \frac{\omega_{\text{mol}}^{(i)}}{2}\sigma_z^{(i)} + \omega_q\left(a_q^\dagger a_q + \frac{1}{2}\right) + \frac{g_q^{(i)}}{2}\sigma_x^{(i)}\left(a_q^\dagger + a_q\right), \tag{10.1}$$

where $\hbar = 1$, ω_q is the secular frequency of the normal mode q along the trap axis, $a_q^\dagger$ and a_q are the creation and annihilation operators for normal mode q, and $\sigma_z^{(i)} = \left|\mathrm{f}^{(i)}\right\rangle\left\langle\mathrm{f}^{(i)}\right| - \left|\mathrm{e}^{(i)}\right\rangle\left\langle\mathrm{e}^{(i)}\right|$. Here, $g_q^{(i)} \equiv d\mathcal{E}_{0,q}^{(i)} = \frac{d}{e}\sqrt{2m^{(i)}\omega_q^3}b_q^{(i)}$ is the vacuum Rabi frequency of the interaction where $\mathcal{E}_{0,q}^{(i)}$ is the electric field amplitude at the position of ion (i) due to a single phonon in normal mode q, $m^{(i)}$ is the mass of ion (i), e is the elementary charge, and $b_q^{(i)}$ is the component of the eigenvector of normal mode q at ion (i). Due to weak coupling, when the normal mode frequency ω_q is near the resonant frequency of the molecular qubit ω_{mol}, the rotating wave approximation is justified and Equation 10.1 simplifies to

$$H_q^{(i)} \approx \frac{\omega_{\text{mol}}^{(i)}}{2}\sigma_z^{(i)} + \omega_q\left(a_q^\dagger a_q + \frac{1}{2}\right) + \frac{g_q^{(i)}}{2}\left(\sigma_+^{(i)}a_q + \sigma_-^{(i)}a_q^\dagger\right), \tag{10.2}$$

which, except for the dependence of $g_q^{(i)}$ on ω_q, is the well-known Jaynes–Cummings model.

10.2.1 DPQL with One Molecule and One Atom

The dipole–phonon interaction couples the states $|\mathrm{f}, n_q\rangle$ and $|\mathrm{e}, n_q + 1\rangle$, where $|\mathrm{f}\rangle$ and $|\mathrm{e}\rangle$ are the upper and lower Λ-doublet states, respectively, and $|n_q\rangle$ is the Fock state labeled by the number of phonons n_q in motional mode q. This coupling leads to an avoided crossing when the normal mode frequency ω_q is near ω_{mol}, as shown in Figure 10.1 for the case of $|\mathrm{f}, 0\rangle$ and $|\mathrm{e}, 1\rangle$. We define $\delta_q \equiv \omega_q - \omega_{\text{mol}}$ and $g_{\text{mol}} \equiv |g_q|\Big|_{\omega_q=\omega_{\text{mol}}} = 2\pi \cdot 58$ kHz for the center-of-mass (COM) mode of an ion chain with a Ca^+ ion and a CaO^+ molecular ion in the $J = 7/2$ state. We define the eigenvectors of Equation 10.2 as $|\pm, n_q\rangle$. As shown in Figure 10.1, for $\delta_q/g_{\text{mol}} \ll -1$, $|+, 1\rangle$ and $|-, 1\rangle$ asymptote to $|\mathrm{f}, 0\rangle$ and $|\mathrm{e}, 1\rangle$, respectively. In the limit $\delta_q/g_{\text{mol}} \gg 1$, the situation is reversed with $|+, 1\rangle$ converging to $|\mathrm{e}, 1\rangle$ and $|-, 1\rangle$ to $|\mathrm{f}, 0\rangle$.

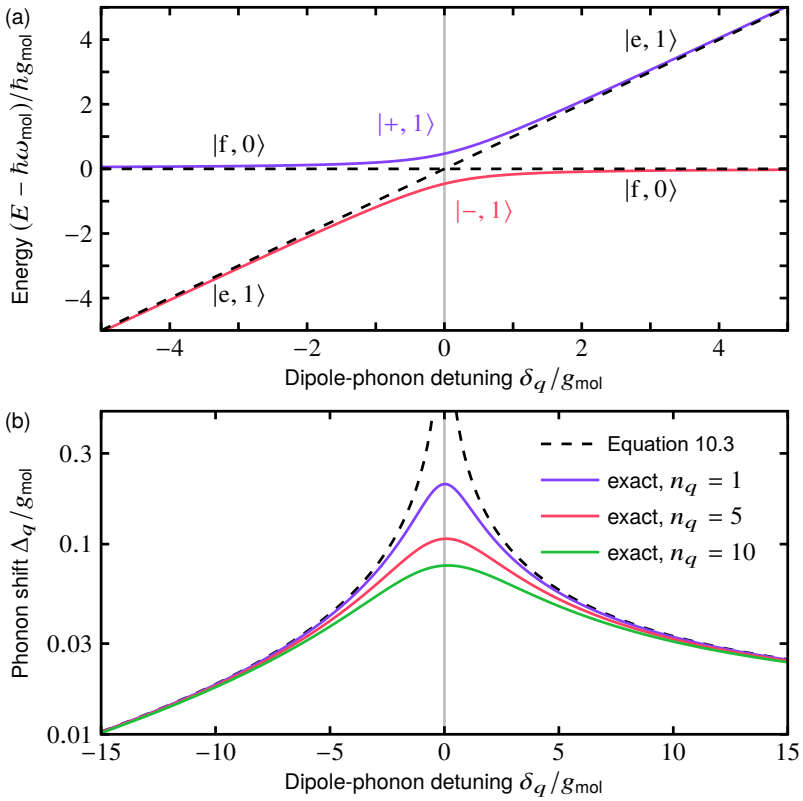

Figure 10.1: **DPQL with one molecule and one atom.** For the eigenvectors $|+, 1\rangle$ and $|-, 1\rangle$ of Equation 10.2, the normalized eigenvalues of the energy are plotted in (a) as a function of normalized detuning $\delta_q = \omega_q - \omega_{\text{mol}}$. Far away from resonance, these eigenvectors asymptote to the uncoupled eigenvectors $|\text{f}, 0\rangle$ and $|\text{e}, 1\rangle$. If one starts with normal mode frequency ω_q far below ω_{mol} in the $|\text{f}, 0\rangle$ state and sweeps ω_q adiabatically through resonance until it is much larger than ω_{mol}, the population will adiabatically transfer to the $|\text{e}, 1\rangle$ state. Energies and detunings are normalized by g_{mol}, defined as $|g_q|$ evaluated at $\omega_q = \omega_{\text{mol}}$. (b) We calculate the normalized quantum AC Stark shift [JJ07] Δ_q of normal mode q as a function of normalized detuning from resonance for several values of n_q by numerically solving Equation 10.1 and compare to Equation 10.3. In the far-detuned limit, the shift is independent of n_q and Equation 10.3 is valid. The shift is asymmetric about $\delta_q = 0$ due to the ω_q-dependence of g_q.

Therefore, by adiabatically sweeping the trap potential, ω_q passes through ω_{mol} and induces an adiabatic exchange of energy from the qubit to the motion, with the probability of transition from e.g. $|\mathrm{f}, 0\rangle$ to $|\mathrm{e}, 1\rangle$ given as $P \approx 1 - \exp(-2\pi(g_{\mathrm{mol}}/2)^2/\dot{\omega}_q)$ [Zen32]. The desire for high-fidelity transfer, therefore, constrains the rate of the frequency sweep to $\dot{\omega}_q \ll g_{\mathrm{mol}}^2$. There is an additional constraint on the rate of the frequency sweep, $\dot{\omega}_q \ll \omega_q^2$, in order to retain adiabaticity with respect to normal mode q [SUP07]. It has been shown that under this constraint, one can significantly vary the normal mode frequency without significantly changing the Fock state [PD12]. This constraint is generally much less stringent than $\dot{\omega}_q \ll g_{\mathrm{mol}}^2$.

This coupling also leads to an effective shift in the normal mode frequency ω_q, which can be understood by examining the energies of states $|+, n_q\rangle$ and $|-, n_q\rangle$. In the limit $|\delta_q| \gg |g_q|\sqrt{n_q}$, the rotating wave approximation used to write eqn (10.2) is not necessarily valid (if the limit $|\delta_q| \ll \omega_{mol}$ is not maintained) and Equation 10.1 must be used. Defining the normal mode frequency as the energy required to add a phonon $E_{\pm}(n_q + 1) - E_{\pm}(n_q)$, the dipole–phonon interaction leads to a shift of the normal frequency by [CH20]

$$\Delta_q = E_{\pm}(n_q + 1) - E_{\pm}(n_q) - \omega_q = \pm \left(\frac{g_q}{2}\right)^2 \frac{2\omega_{\mathrm{mol}}}{\omega_{\mathrm{mol}}^2 - \omega_q^2}. \tag{10.3}$$

As the $|+, n_q\rangle$ and $|-, n_q\rangle$ states shift the normal mode frequency away from ω_q in opposite directions, one can determine the molecular state by measuring this frequency shift. For instance, given a molecule in an unknown internal state in the far-detuned limit, the trap frequency can be brought closer to resonance. For a molecule initially in the $|\mathrm{f}\rangle$ state, the normal mode frequency will increase, while a molecule initially in the $|\mathrm{e}\rangle$ state will lower the motional frequency. As a quantitative example, for an ion chain with one Ca^+ ion and one CaO^+ molecular ion in the $J=7/2$ state ($\omega_{\mathrm{mol}} = 2\pi \cdot 5$ MHz), a center-of-mass (COM) mode frequency 100 kHz below $\omega_{\mathrm{mol}}/2\pi$ results in a shift of the COM mode frequency of ± 7 kHz, which is easily measured with standard techniques [SK11, GCV13].

10.2.2 DPQL with Two Molecules and One Atom

When a second molecule is added to the chain, the molecular dipoles interact directly and via the normal modes of motion. The direct interaction has been considered in Ref. [HC18] and when ω_{mol} and ω_q are comparable it is typically weaker than the phonon-mediated interaction, which we focus on here. As an illustrative example, we consider a three-ion chain composed of two molecular ions co-trapped with a single atomic ion. For molecules (1) and (2), the interaction with normal mode q is described by

$$H_q^{(1,2)} = \frac{1}{2}\left(g_q^{(1)}\sigma_x^{(1)} + g_q^{(2)}\sigma_x^{(2)}\right)\left(a_q^\dagger + a_q\right). \tag{10.4}$$

This mutual coupling to mode q leads to a coupling of the two dipoles mediated by virtual excitations of the mode.

This virtual-phonon-mediated dipole–dipole (VDD) interaction is similar to a Raman transition, as illustrated in Figure 10.2, where one path is shown connecting molecular states $|\mathrm{fe}\rangle \equiv \left|\mathrm{f}^{(1)},\mathrm{e}^{(2)}\right\rangle$ and $|\mathrm{ef}\rangle \equiv \left|\mathrm{e}^{(1)},\mathrm{f}^{(2)}\right\rangle$. In general for normal mode q, there are four paths connecting $|\mathrm{fe},n_q\rangle$ and $|\mathrm{ef},n_q\rangle$, via intermediate states $|\mathrm{ee},n_q+1\rangle$, $|\mathrm{ee},n_q-1\rangle$, $|\mathrm{ff},n_q-1\rangle$, and $|\mathrm{ff},n_q+1\rangle$. The effective Hamiltonian [JJ07] for this interaction is then

$$\begin{aligned} H_{\mathrm{eff}} = \sum_{i=1,q}^{2} \frac{2\omega_{\mathrm{mol}}^{(i)}}{\left(\omega_{\mathrm{mol}}^{(i)}\right)^2 - \omega_q^2}\left(\frac{g_q^{(i)}}{2}\right)^2\left(a_q^\dagger a_q + \frac{1}{2}\right)\sigma_z^{(i)} \\ + J_{12}\left(\sigma_+^{(1)}\sigma_-^{(2)}e^{i\left(\omega_{\mathrm{mol}}^{(1)}-\omega_{\mathrm{mol}}^{(2)}\right)t} + \sigma_-^{(1)}\sigma_+^{(2)}e^{-i\left(\omega_{\mathrm{mol}}^{(1)}-\omega_{\mathrm{mol}}^{(2)}\right)t}\right) \end{aligned} \tag{10.5}$$

where the first term represents the quantum AC Stark shift [JJ07] and the VDD interaction strength is given by

$$J_{12} = \sum_q \frac{g_q^{(1)}g_q^{(2)}}{4}\left(\frac{\omega_q}{\left(\omega_{\mathrm{mol}}^{(1)}\right)^2 - \omega_q^2} + \frac{\omega_q}{\left(\omega_{\mathrm{mol}}^{(2)}\right)^2 - \omega_q^2}\right). \tag{10.6}$$

This VDD coupling facilitates an exchange interaction, similar to the direct dipole–dipole interaction [HC18], and has been shown to be significantly stronger than the direct dipole–dipole interaction at long distances [CH20]. This interaction is also insensitive to phonon number n_q. If the initial state $|\text{fe}\rangle$ is prepared and allowed to evolve under this interaction, the population will coherently oscillate between $|\text{fe}\rangle$ and $|\text{ef}\rangle$. If $\left|g_q^{(1)}\right| \neq \left|g_q^{(2)}\right|$ for any mode q, it can lead to a differential quantum AC Stark shift $\Delta_{\text{diff}} = \Delta_{\text{fe}} - \Delta_{\text{ef}}$ between the $|\text{fe}\rangle$ and $|\text{ef}\rangle$ states of the form

$$\Delta_{\text{diff}} = \sum_q 2\left(n_q + \frac{1}{2}\right)\left[\left(\frac{g_q^{(1)}}{2}\right)^2 \frac{2\omega_{\text{mol}}^{(1)}}{\left(\omega_{\text{mol}}^{(1)}\right)^2 - \omega_q^2} - \left(\frac{g_q^{(2)}}{2}\right)^2 \frac{2\omega_{\text{mol}}^{(2)}}{\left(\omega_{\text{mol}}^{(2)}\right)^2 - \omega_q^2}\right]. \tag{10.7}$$

and the effective Hamiltonian is

$$H_{\text{eff}} = J_{12}\left(\sigma_+^{(1)}\sigma_-^{(2)} e^{i(\Delta_{\text{mol}}+\Delta_{\text{diff}})t} + \sigma_-^{(1)}\sigma_+^{(2)} e^{-i(\Delta_{\text{mol}}+\Delta_{\text{diff}})t}\right) \tag{10.8}$$

where $\Delta_{\text{mol}} = \omega_{\text{mol}}^{(1)} - \omega_{\text{mol}}^{(2)}$. For an initial molecular state $|\psi_{\text{mol}}(0)\rangle = |\text{fe}\rangle$, the time-dependent probability of flipping to the $|\text{ef}\rangle$ state $p_{\text{ef}}(t)$ is

$$p_{\text{ef}}(t) = |\langle \text{ef}|\psi(t)\rangle|^2 = \frac{4J_{12}^2}{4J_{12}^2 + \Delta_{\text{tot}}^2} \sin^2\left[\frac{\sqrt{4J_{12}^2 + \Delta_{\text{tot}}^2}}{2}\, t\right] \tag{10.9}$$

where $\Delta_{\text{tot}} = \Delta_{\text{mol}} + \Delta_{\text{diff}}$.

In what follows, we are specifically interested in two cases. In the first case, depicted in Figure 10.2a, $\Delta_{\text{tot}} = 0$ and the population transfers between $|\text{fe}\rangle$ and $|\text{ef}\rangle$ with unit amplitude and frequency $2J_{12}$. The second case, illustrated in Figure 10.2b, is when $|\Delta_{\text{tot}}| \gg |J_{12}|$. In this limit, the amplitude of the population transfer is effectively 0, meaning that the effect of the VDD interaction can largely be ignored.

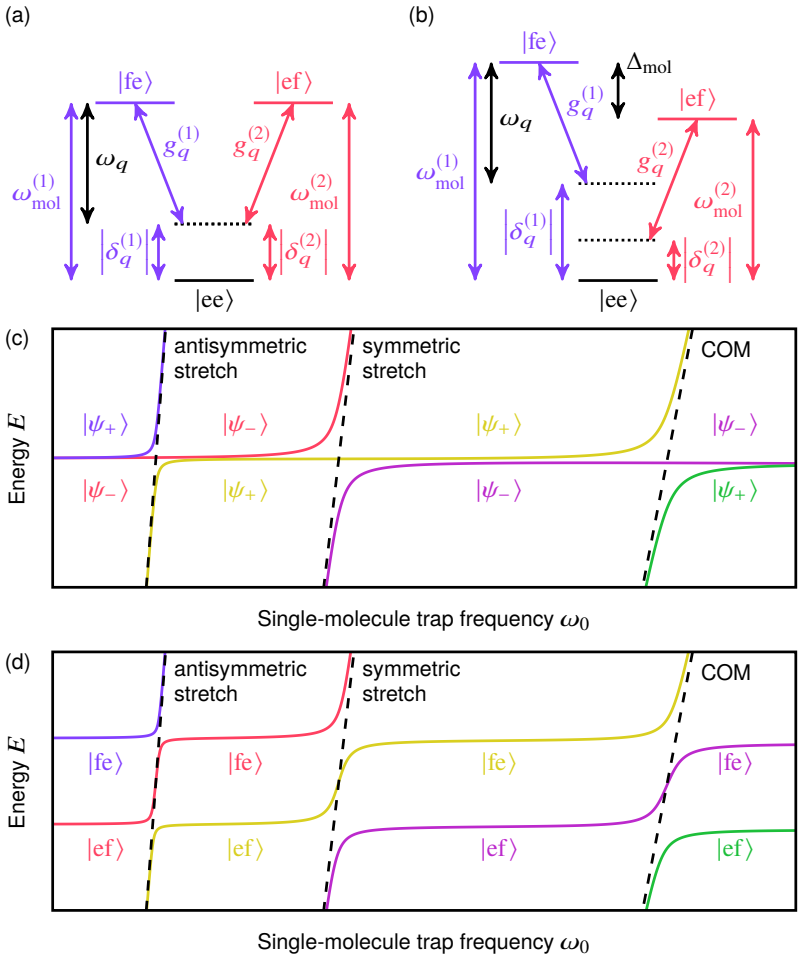

Figure 10.2: **DPQL with two molecules and one atom.** (a) Energy levels of several molecular states, illustrating one path in which the mutual coupling of two molecules to the same intermediate state can lead to an indirect coupling of the two molecules via virtual phonons. (b) If the molecular splittings are different, such a two-phonon transition will be off-resonant and the molecules will not be strongly coupled. Also shown are adiabatic potentials for a 3-ion chain with molecular ions at the outer edges for (c) $\omega_{\rm mol}^{(1)} = \omega_{\rm mol}^{(2)}$ and (d) $\omega_{\rm mol}^{(1)} \neq \omega_{\rm mol}^{(2)}$ as a function of the secular frequency of a single molecular ion. The single-molecular-excitation eigenstates are labeled. These states are of particular importance because they have a one-to-one mapping to phonon states after an adiabatic sweep through resonance. In (c), these states are the Bell states $|\psi^{\pm}\rangle = (|{\rm fe}\rangle \pm |{\rm ef}\rangle)/\sqrt{2}$

10.2.2.1 State Preparation

Often the first step in any operation is to prepare a known state. To this end, in this section we explore the preparation of $|\mathrm{ee}\rangle$, a Bell state, and $|\mathrm{fe}\rangle$ (or $|\mathrm{ef}\rangle$) in the case that a single Ca^+ ion is in the center of the chain and surrounded by CaO^+ molecular ions. A numerical simulation of these techniques is presented in Subsection 10.6.2.

Preparation of $|\mathrm{ee}\rangle$ – To prepare the molecular ions in the $|\mathrm{ee}\rangle$ state, regardless of whether the molecular splittings are identical or not, one can start with all normal mode frequencies below ω_{mol}. After ground-state cooling, the combined molecular state $|\psi_{\mathrm{mol}}\rangle$ will be unknown. By adiabatically increasing the axial confining potential such that the frequency of the two highest-energy modes—in this case the antisymmetric and symmetric stretch modes—sweep through ω_{mol}, any molecular excitation will be converted to motional excitation of these modes. By ground-state cooling once again, one prepares the ground molecular state in the ground motional state, $|\mathrm{ee}, 0_q\rangle$. To verify the state preparation, one can sweep the mode frequencies below ω_{mol}, apply a global molecular π pulse to generate the $|\mathrm{ff}, 0_q\rangle$ state, and sweep the frequencies back. If the state preparation in $|\mathrm{ee}\rangle$ was successful, this sequence will yield two phonons in the antisymmetric stretch mode. If detected, these phonons herald preparation in the $|\mathrm{ee}\rangle$ state. Alternatively, one can measure the quantum AC Stark shift of one of the normal modes to verify the molecular state.

Preparation of a Bell State – Due to the spatial symmetry of the molecules in the ion chain, $\left|g_q^{(1)}\right| = \left|g_q^{(2)}\right|$ for all modes q and $\Delta_{\mathrm{tot}} = \Delta_{\mathrm{diff}} = 0$. Equation 10.8 then simplifies to $H_{\mathrm{VDD}} = J_{1,2}\sigma_+^{(1)}\sigma_-^{(2)} + \mathrm{H.c.}$ and the eigenstates are then the Bell states $|\psi^{\pm}\rangle = (|\mathrm{fe}\rangle \pm |\mathrm{ef}\rangle)/\sqrt{2}$. As shown in Figure 10.2c, each normal mode couples to only one of these eigenstates. It is then straightforward to produce the Bell states $|\psi^{\pm}\rangle$ for this case. Starting with $|\mathrm{ee}\rangle$ in the ground motional state, one can add a single phonon to the antisymmetric or symmetric stretch mode followed by an adiabatic sweep of both of these mode frequencies across ω_{mol} to prepare the $|\psi^+\rangle$ or $|\psi^-\rangle$ state, respectively.

Preparation of $|\mathrm{fe}\rangle$ *or* $|\mathrm{ef}\rangle$ – It is also possible to use the scheme detailed above to produce $|\mathrm{fe}\rangle$ or $|\mathrm{ef}\rangle$ by adding a single phonon in a superposition of the antisymmetric and symmetric stretch modes before the sweep of the normal mode frequencies. In practice, this may be difficult, since the two components of the motional superposition will oscillate at different rates, causing a relative phase difference. This relative phase must be at a specific value to produce the desired final state, requiring precise timing of the ramping sequence.

An alternative method to produce the $|\mathrm{fe}\rangle$ or $|\mathrm{ef}\rangle$ state is to generate a difference in the molecular splittings of the two molecules, depicted in Figure 10.2b. Specifically, if $|\Delta_{\mathrm{tot}}| \gg |J_{12}|$, the effect of the VDD interaction can be ignored. The eigenstates of Equation 10.8 for this case are simply the basis states $|\mathrm{fe}\rangle$ and $|\mathrm{ef}\rangle$. By starting with $|\mathrm{ee}\rangle$ in the ground motional state, one can add a single phonon to the antisymmetric or symmetric stretch mode followed by an adiabatic sweep of both of these mode frequencies across ω_{mol} to prepare either $|\mathrm{fe}\rangle$ or $|\mathrm{ef}\rangle$ in the motional ground state.

One way to generate such a difference ($\omega_{\mathrm{mol}}^{(1)} \neq \omega_{\mathrm{mol}}^{(2)}$) in the molecular splittings of two different molecules (CaO^+, in the $X\,^2\Pi_{3/2}$ state, with $J = 7/2$) is by taking advantage of the small differential g-factor between $|\mathrm{e}, J = 7/2, m_J = 7/2\rangle$ and $|\mathrm{f}, J = 7/2, m_J = 7/2\rangle$, which arises through the differing nuclear rotational-electronic orbit interactions of the Λ-doublet states with the $A^2\Sigma^+$ states. Since there is a lack of spectroscopic data for CaO^+, we estimate the differential g-factor between $|\mathrm{e}, J = 7/2, m_J\rangle$ and $|\mathrm{f}, J = 7/2, m_J\rangle$ of CaO^+ $X^2\Pi$ as $\delta g \approx 0.8$ kHz/Gauss by applying Equation 8 in Ref. [Rad61]. For two molecular ions separated by 3 μm, a magnetic field gradient of 1.3 T/cm is required to produce a difference of 20 kHz in the molecular splittings. This value of magnetic gradient can be realized by placing a straight wire 30 μm away from the molecular ions and driving 1 A through the wire, similar to conditions discussed in Ref. [OLA08].

10.2.2.2 Observing a Phonon-Mediated Dipole–Dipole Interaction

The VDD interaction can be observed by preparing $|\psi_{\text{mol}}(0)\rangle = |\text{fe}\rangle$, allowing the molecules to interact via the exchange interaction, and then reading out the final molecular state $|\psi_{\text{mol}}(t)\rangle$. As detailed previously, the $|\text{fe}\rangle$ state can be prepared by generating a difference in molecular splittings Δ_{mol} and ramping the trap frequency. By suppressing the field used to break the degeneracy for state preparation, Δ_{mol} can then be set to 0, effectively turning on the VDD interaction. After a wait time of $t_\pi = \frac{\pi}{2J_{12}}$, $|\psi_{\text{mol}}(t)\rangle = -i\,|\text{ef}\rangle$ and the degeneracy can again be broken by the control field to turn off the VDD interaction and the state measured as discussed in the next section. As the $|\text{ee}\rangle$ and $|\text{ff}\rangle$ states are unaffected, this interaction facilitates an iSWAP gate. A numerical simulation of this method is presented in Figure 10.9a.

Performing the same experiment with $\Delta_{\text{diff}} \neq 0$, as is generally true if the two molecules do not have spatial symmetry about the center of the ion chain, will cause the population to partially (but not fully) transfer to $|\text{ef}\rangle$. Using the control field, complete transfer can be recovered by setting $\Delta_{\text{mol}} = -\Delta_{\text{diff}}$ instead of $\Delta_{\text{mol}} = 0$, cancelling out the differential quantum AC Stark shift and allowing a complete transfer from $|\text{fe}\rangle$ to $|\text{ef}\rangle$.

An alternative method to transfer the population from $|\text{fe}\rangle$ to $|\text{ef}\rangle$ using the VDD interaction is to perform an adiabatic sweep of Δ_{mol}. One can start again with $|\Delta_{\text{mol}}| \gg |J_{12}|$ to prepare the $|\text{fe}\rangle$ state. By slowly ramping the differential splitting from Δ_{mol} to $-\Delta_{\text{mol}}$ at speed $\dot{\Delta}$, the population will adiabatically transfer from $|\text{fe}\rangle$ to $|\text{ef}\rangle$ with probability of $P = 1 - \exp\left(-2\pi J_{12}^2/\dot{\Delta}\right)$. This method is simulated in Figure 10.9c. While this method is slower than the first method described, it has the advantage of being insensitive to the differential quantum AC Stark shift Δ_{diff} as long as $|\Delta_{\text{diff}}| < |\Delta_{\text{mol}}|$, and does not require precise timing. Thus, it is not necessary to know the values of Δ_{diff} and J_{12} to achieve complete state transfer. As such, this method may be useful in general cases where the two molecules do not have spatial symmetry in the ion chain or are otherwise nonidentical.

10.2.2.3 State Detection

After applying the VDD interaction, a method is needed for reading out the final molecular state $|\psi_{\text{mol}}(t_{\text{final}})\rangle = \alpha\,|\text{fe}\rangle + \beta\,|\text{ef}\rangle$. Before beginning the readout procedure, ground-state cooling can remove any potential motional heating that occurred during the sequence. Following ground-state cooling, the single-molecule trap frequency can be adiabatically increased such that the antisymmetric and symmetric stretch modes sweep through $\omega_{\text{mol}}^{(1)}$ and $\omega_{\text{mol}}^{(2)}$. For $|\Delta_{\text{mol}}| \gg |J_{12}|$ there is a one-to-one mapping of molecular excitations onto motional excitations and there will be a single phonon in the state

$$|\psi_{\text{phonon}}\rangle = \beta\,|1,0\rangle + e^{i\phi}\alpha\,|0,1\rangle \tag{10.10}$$

where $|n_{\text{as}}, n_{\text{ss}}\rangle$ denotes the number of phonons in the antisymmetric and symmetric stretch mode and ϕ is a relative phase difference that depends on the timing of the ramping sequence. Red motional sideband transitions of the atomic ion (repeated over many experiments) can be used to probe the phonon occupations ($|\alpha|^2$ and $|\beta|^2$) in each mode. To keep the phase information, one can utilize simultaneous, phase-coherent sideband operations on the atomic ion in conjunction with precise timing of the sequence. For the specific case described here with a single atomic ion at the center of the chain, one cannot efficiently use atomic sideband operations on the symmetric stretch mode, since the atomic ion does not participate in this mode. This shortcoming can be overcome by e.g. chain reordering operations [SHB09] or adding a second atomic ion to the chain.

10.2.2.4 Single Qubit Rotations

Since the VDD interaction is a tunable exchange interaction, it can be utilized to perform an iSWAP gate. Thus, with the ability to perform qubit-specific, single-qubit rotations DPQL is sufficient for a universal gate set [SS03]. To perform such single-qubit rotations, one can generate a difference in the molecular splittings and apply a direct microwave pulse

to the ion chain; the trap electrodes themselves provide a convenient structure to deliver the microwave radiation. Although this pulse will not be spatially selective, it can select only the frequency of the target molecule. Control of the Rabi frequency of such a pulse and, if needed, composite pulse sequences can be used to prevent off-resonant excitation of non-target qubits and heating of the motional modes.

10.2.3 DPQL with N Molecules and N Atoms

Extending this technique to a general number of molecules N may be of particular interest for applications such as quantum simulation and the transduction of quantum information from microwave to optical frequencies [CH20]. To allow for efficient state preparation and measurement of these molecular ions, it may be useful to also have N atomic ions in the ion chain. With N atoms and N molecules, one can perform state mirroring [KS05] to create a one-to-one mapping of atomic qubit states to molecular qubit states or vice versa. By utilizing atomic sideband operations, one can map the state of each atomic qubit to the excitation of corresponding normal modes. A precisely timed adiabatic sweep of these normal mode frequencies through all the molecular qubit resonance frequencies then maps these phonon states onto the molecular qubit states.

10.3 Survey of the Alkaline-Earth Monoxides and Monosulfides for DPQL

Cationic alkaline-earth monoxides (see Table 10.1) play important roles in combustion, atmospheric chemistry, and astrochemistry. They have been the subject of several theoretical studies. Electronic structure models predict that the bonding is predominantly ionic, with a lowest-energy electronic configuration that can be formally represented as $M^{2+}O^{-}(2p^5)$. The M^{2+} ion is closed shell and the $O^{-}(2p^5)$ anion may approach with the half-filled orbital pointing towards M^{2+} ($2p\sigma$, resulting in a $^2\Sigma^+$ state) or perpendicular to the internuclear

	A_{SO} (cm^{-1})	B_e (cm^{-1})	ω_e (cm^{-1})	D_e (eV)	R_e (Å)	PDM (Debye)	$10^{-3} \cdot T_e$ (cm^{-1})	Λ-doublet splitting (MHz)				4 K/300 K Population (%)			
								J=3/2	5/2	7/2	9/2	J=3/2	5/2	7/2	9/2
BeO^+	-117	1.44	1242	3.8	1.42	7.5	9.4	3.8	16	42	84	89/2.1	10/3.1	1/3.9	0/4.6
MgO^+	-130	0.53	718	2.3	1.83	8.9	7.3	0.19	0.84	2.1	4.3	54/0.8	32/1.1	11/1.5	3/1.8
CaO^+	-130	0.37	634	3.3	1.99	8.7	0.7	0.45	1.9	5.0	10	42/0.5	32/0.8	17/1.0	6/1.3
SrO^+	-147	0.31	659	4.2	2.10	7.5	0.4	0.16	0.67	1.7	3.5	0/0.1	0/0.1	0/0.1	0/0.1
BaO^+	-214	0.24	506	2.2	2.24	7.9	1.5	0.089	0.39	0.98	2.0	0/0	0/0	0/0	0/0
YbO^+	-132	0.28	601	2.2	2.03	7.0	1.0	0.14	0.59	1.5	3.0	33/0.4	30/0.6	20/0.8	10/1.0
RaO^+	-228	0.20	451	3.3	2.40	7.7	0.3	0.081	0.35	0.89	1.8	25/0.3	26/0.5	21/0.6	14/0.8
BeS^+	-310	0.71	875	3.4	1.84	7.6	15.7	0.11	0.45	1.2	2.3	66/1.2	27/1.8	6/2.3	1/2.8
MgS^+	-303	0.25	469	2.0	2.26	9.2	12.9	0.0051	0.022	0.056	0.11	30/0.4	29/0.6	21/0.8	12/1.0
CaS^+	-299	0.15	390	4.0	2.52	11.3	5.0	0.0028	0.012	0.031	0.062	19/0.3	22/0.4	20/0.5	16/0.6
SrS^+	-316	0.12	423	3.1	2.42	8.7	0.3	0.0086	0.036	0.094	0.19	16/0.1	20/0.2	19/0.3	16/0.4
BaS^+	-273	0.08	291	3.3	2.81	9.1	2.5	0.00093	0.0040	0.010	0.021	11/0.1	14/0.2	15/0.2	15/0.3
YbS^+	-254	0.10	345	2.2	2.48	7.8	4.6	0.0013	0.0056	0.014	0.029	13/0.1	17/0.2	18/0.3	16/0.3
RaS^+	-405	0.07	266	4.5	2.91	9.4	2.7	0.00043	0.0018	0.0047	0.0094	10/0.1	13/0.1	14/0.2	14/0.2

Table 10.1: **A list of dipole–phonon quantum logic (DPQL) candidates in electronic state $^2\Pi_{3/2}$.** This table includes the spin–orbital coupling constant (A_{SO}), rotational constant (B_e), vibrational constant (ω_e), dissociation energy (D_e), equilibrium distance (R_e), permanent dipole moment (PDM), energy interval between two lowest electronic states (T_e), Λ-doublet splitting and population of several low-lying rotational states. The ground electronic state of all the species in this table is $X^2\Pi_{3/2}$, except for SrO^+ and BaO^+, whose ground state is $X^2\Sigma^+$ and the first excited state is $A^2\Pi_{3/2}$.

axis ($2p\pi$, resulting in a $^2\Pi$ state). For the lighter alkaline-earth ions Be^{2+}, Mg^{2+}, and Ca^{2+}, the electrostatic attraction favors a filled $2p\sigma$ orbital so that the vacancy resides in $2p\pi$, yielding an $X^2\Pi$ ground state. The configuration with the vacancy in the $2p\sigma$ orbital produces a low-lying $A^2\Sigma^+$ electronically excited state. This state ordering is reversed for Sr^{2+} and Ba^{2+} because the interatomic electron-electron repulsion terms become more significant, favoring the approach of the half-filled $2p\sigma$ orbital, resulting in an $X^2\Sigma^+$ ground state. Surprisingly, *ab initio* calculations for RaO^+ suggest that the state ordering reverts to $X^2\Pi$ due to relativistic effects.

There are several notable systematic trends for the low-energy states arising from the $M^{2+}O^-(2p^5)$ configuration. First, as the $^2\Sigma^+$ state involves the direct approach of the half-filled $2p\sigma$ orbital, the equilibrium distance for the $^2\Sigma^+$ state is smaller than that of the $^2\Pi$ state, regardless of the state energy ordering. Second, except for RaO^+ where relativistic effects are important, the spin–orbit coupling constant (A_{SO}) for the $^2\Pi$ state predominantly reflects the spin–orbit interaction of $O^-(2p^5)$ where ζ_{2p}=−118.1 cm^{-1} [NLA85].

This term is negative (E(Ω=3/2)¡E(Ω=1/2)) as the $^2\Pi$ state is derived from the more than half-filled $2p\pi^3$ configuration. Third, because these low-lying states are derived from the same $2p^5$ configuration, the interactions between them can be adequately treated using the pure precession model of Van Vleck [Van29]. The most important interaction, from the perspective of the present model, is the coupling of the $^2\Pi$ and $^2\Sigma^+$ states that gives rise to the energy splitting of the $^2\Pi$ state Λ-doublets. As described below, calculation of the Λ-doublet splitting requires knowledge of the potential energy curves and molecular constants for both the $^2\Pi$ and $^2\Sigma^+$ states. The Λ-doublet components of the $^2\Pi$ state are conventionally labeled as e for the levels with parity $(-1)^{J-1/2}$ and f for levels with parity $-(-1)^{J-1/2}$. When the $^2\Sigma^+$ state is above the $^2\Pi$ state the perturbation pushes the e component below the f component for a given value of J. In the present work we are focused on the Λ-doublet splitting of the $^2\Pi$, v=0 level. If the $^2\Sigma^+$ state is somewhat below the $^2\Pi$, v=0 level, the vibrationally-excited levels of the $^2\Sigma^+$ state that are above $^2\Pi$, v=0 can still result in the e component being pushed below the f component (see Equation 10.11 and 10.12 below).

This overall description of the properties of $M^{2+}O^-(2p^5)$ species is also valid for $Yb^{2+}(4f^{14})O^-(2p^5)$ and the alkaline-earth monosulfide ions $M^{2+}S^-(3p^5)$, which we also include in Table 10.1. For the latter the $^2\Pi$ spin–orbit splitting is stronger, reflecting the larger $S^-(3p^5)$ spin–orbit coupling constant of ζ_{3p}=−321 cm^{-1} [LW70].

For the present purpose we focus on species that have a $^2\Pi$ ground state and are primarily concerned with their permanent electric dipole moment (PDM) and the magnitude of the Λ-doublet splittings of the low-energy rotational levels. These parameters have not been measured previously and the spectroscopic data needed for theoretical predictions are mostly unavailable (limited spectroscopic data have been reported for CaO^+ [VBH18] and BaO^+ [BVH15]). Consequently, we use *ab initio* electronic structure models to calculate the relevant molecular parameters. The results reported here were obtained using the Molpro suite of programs [WKK12]. The low-energy states were predicted using a standard sequence of methods. First, a state-averaged complete active space – self-consistent field

calculation (SA-CASSCF) was carried out to provide the orbital input for a multi-reference singles and doubles configuration interaction (MRSDCI) calculation. The spin–orbit interaction was then included by evaluating the matrix elements of the Breit-Pauli Hamiltonian in the CASSCF eigenbasis. Note that Molpro does not support calculation of the spin–orbit matrix elements using the full MRCI eigenbasis. The program documentation indicates that the errors introduced by using the CASSCF wavefunctions to evaluate the spin–orbit matrix elements are usually smaller than 1 cm^{-1}. All-electron basis sets of augmented valence quadruple zeta quality were used for all of the ions with the exception of RaO^+ and YbO^+. Relativistic effective core potentials for 78 (ECP78MDF) and 28 (ECP28MWB) electrons were used for these metals, respectively.

Potential energy curves were constructed from single point energies obtained from *ab initio* calculations, with a typical grid spacing of 0.04 Å. Morse potential energy functions were fitted to these data, providing direct values for the equilibrium distances (R_e) and term energies (T_e). The spin–orbit coupling constants were obtained from the energy difference between the T_e values for the $^2\Pi_{3/2}$ and $^2\Pi_{1/2}$ potential energy curves. Harmonic vibrational frequencies (ω_e) were obtained from the fitted Morse parameters using a standard algebraic expression [Her50]. The results from these calculations are collected in Table 10.1. The body-fixed permanent electric dipole moments and other calculated values determined for the equilibrium bond lengths are also provided in Table 10.1. Electronic structure calculations have been reported previously for BeO^+ [PLB86, GLB08], MgO^+ [PLB86, BLP94, MHY11], CaO^+ [PLB86, KLL13, VBH18], SrO^+ [PLB86, DFG87], BaO^+ [DFG87, BVH15], BeS^+ [LKG10], and MgS^+ [CWL17] (and references therein). Overall, the present results are in reasonable agreement with calculations performed at a similar level of theory. For example, in their MRSDCI study of CaO^+, Khalil et al. [KLL13] reported ground state constants of A_{SO}=−127 cm^{-1}, ω_e=639 cm^{-1}, B_e=0.37 cm^{-1} and D_e=3.4 eV. The term energy for the $A^2\Sigma^+$ state was $T_e(A)$=570 cm^{-1}. The corresponding experimental data [VBH18] for CaO^+ are A_{SO}=−130.5 cm^{-1}, ω_e=646.9 cm^{-1}, B_e=0.37 cm^{-1} and $T_e(A)$=685.2 cm^{-1}. Note that

the sign of the spin–orbit coupling constant given for $BeO^+(X^2\Pi)$ in Ref. [GLB08] is in error.

$$p_v = 2\sum_{n',v'} \frac{\langle n^2\Pi v|A_{SO}(R)\hat{\mathbf{L}}^+|n'^2\Sigma^+v'\rangle \ \langle n'^2\Sigma^+v'|B(R)\hat{\mathbf{L}}^-|n^2\Pi v\rangle}{E_{nv} - E_{n'v'}}, \tag{10.11}$$

$$q_v = 2\sum_{n',v'} \frac{\left|\ \langle n^2\Pi v|B(R)\hat{\mathbf{L}}^+|n'^2\Sigma^+v'\rangle\right|^2}{E_{nv} - E_{n'v'}}, \tag{10.12}$$

where $A_{SO}(R)$ is the spin–orbit coupling constant, $B(R)$ is the rotational constant and $\hat{\mathbf{L}}^+/\hat{\mathbf{L}}^-$ are the raising and lowering operators for the electronic orbital angular momentum. Evaluation of the matrix elements is simplified by the fact that, near the equilibrium distance both $A_{SO}(R)$ and $B(R)$ are slowly varying functions of R that can be approximated by their values at R_e. These 'constants' can then be taken outside of the vibrational overlap integrals which then, when squared, are the Franck-Condon factors (FCF). Finally, with the application of the pure precession model, the matrix elements of the raising and lowering operators are given by $\langle^2\Pi|\hat{\mathbf{L}}^+|^2\Sigma^+\rangle = \langle^2\Sigma^+|\hat{\mathbf{L}}^-|^2\Pi\rangle = \sqrt{2}\hbar$. The FCFs needed for calculations of the p_v and q_v parameters were obtained for the fitted Morse potentials using the computer code LEVEL 8.0 [Le]. Algebraic expressions for the rotational energies of a $^2\Pi$ state, with inclusion of the Λ-doublet splitting terms, were reported by Mulliken and Christy [MC31]. Equation 14 of Ref. [MC31] was used to calculate the Λ-doublet splittings listed in Table 10.1. Figure 10.3 illustrates the energy level schemes of CaO^+ within different energy scales.

Among these candidate ions, BeO^+, BeS^+, MgO^+, CaO^+, YbO^+, and RaO^+ appear particularly promising. These ions have large PDMs, suitable Λ-doublet splittings, and are easily produced from and co-trapped with commonly laser-cooled atomic ions. However, the dissociation energies of BeO^+, BeS^+, MgO^+, and YbO^+ are less than the energy of the lasers used for Doppler cooling their parent ions: Be^+ (3.96 eV), Mg^+ (4.42 eV), and Yb^+ (3.36 eV). Therefore, photodissociation from the atomic ion cooling laser could be problematic for

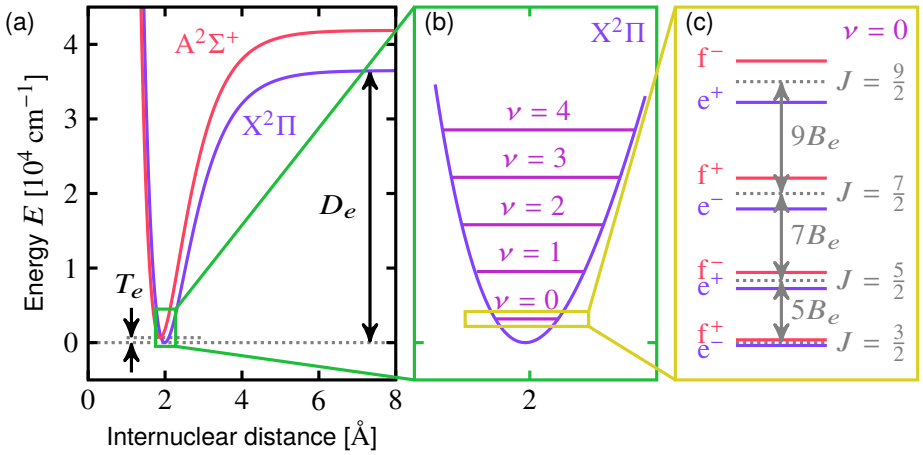

Figure 10.3: **Energy level scheme of CaO^+.** (a) Potential energy surfaces of the two lowest electronic states. (b) The low-lying vibrational states of $X^2\Pi_{3/2}$. (c) The low-lying rotational states in $X^2\Pi_{3/2}$, $v = 0$. The Λ-doublet splittings are not to scale—they are exaggerated for better visibility.

these species—although BeO^+, for example, could be used with Ca^+ (3.12 eV) with added complexity for the trap loading process. Furthermore, the recent progress on laser cooling of Ra^+ [FHW19] makes RaO^+ a promising candidate for exploring physics beyond the Standard Model [CGG17, AAD18], since relativistic effects are clearly important in this molecule and it has very small Λ-doublet splittings. Similar to cationic alkaline-earth monoxides, multiply-charged ions such as BO^{2+} also possess Λ-doublet splittings close to 5 MHz in the ground rotational state and can also be candidates for DPQL study [Hea].

In this work, we focus on using CaO^+ since it is easily produced from and sympathetically cooled by co-trapped Ca^+ [GCV13] and its main isotopologue does not possess hyperfine structure. Unless otherwise noted, we work in the $J = 7/2$ rotational state, which we have calculated to have a blackbody-limited lifetime of $\tau \approx 4$ s at room temperature; this lifetime increases to $\tau \approx 5000$ s at 4 K.

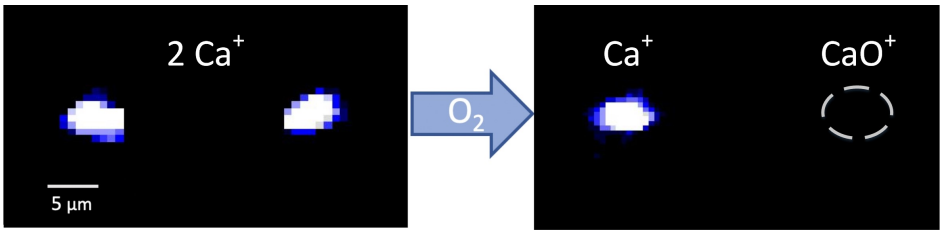

Figure 10.4: **CaO^+ loading protocol.** Two Ca^+ ions are produced in the trap via resistive heating of a Ca sample and subsequent photo-ionization. O_2 gas is introduced into the chamber via a manual leak valve converting one of the Ca^+ to CaO^+ presumably via the reaction $Ca^+(^2P_{1/2}) + O_2 \rightarrow CaO^+ + O$.

10.4 Practical Considerations

In this section we describe progress towards an experimental demonstration of DPQL and examine the effects of motional heating and electric field noise on DPQL fidelity. Furthermore, we present a method to prepare the molecular qubit in a single m_J sublevel.

10.4.1 Experiment

To demonstrate these ideas, our colleagues at Duke University have re-purposed an apparatus available to us that was previously used in other trapped molecular ion experiments and is described in Refs. [GCV13], [Goe13], and [Rug16]. This system can achieve a stable axial secular frequency (COM mode) in the range $2\pi \cdot 180$ kHz $\leq \omega_q \leq 2\pi \cdot 700$ kHz for Ca^+. Therefore, we leverage the flexibility of molecular systems and choose the Λ-doublet states of the $J=3/2$ manifold, which are separated by $\omega_{\text{mol}} = 2\pi \cdot 450$ kHz, as our qubit.

To begin, two Ca^+ are trapped and laser-cooled, see Figure 10.4. Oxygen is introduced into the vacuum chamber via a leak valve at a pressure of 5×10^{-10} Torr until one of the Ca^+ reacts to form CaO^+. Since this reaction is endoergic by ≈ 1.7 eV, it presumably proceeds as $Ca^+(^2P_{1/2}) + O_2 \rightarrow CaO^+ + O$.

The experiment is now working to demonstrate state preparation and measurement capabilities for the molecular qubit. For this, the ions are cooled to the motional ground state via

Doppler cooling of Ca^+ along the $^2P_{1/2} \leftarrow {}^2S_{1/2}$ electric dipole transition and sideband cooling along $^2D_{5/2} \leftarrow {}^2S_{1/2}$ electric quadrupole transition [GCV13]. Next, the the DC voltage applied to the trap end caps to form the axial trapping potential will be smoothly increased such that the stretch mode frequency of the ions is scanned from 300 kHz to 600 kHz and passes through ω_{mol}. If the molecule was initially in $|\text{f}, 0\rangle$ it will transfer to $|\text{e}, 1\rangle$, and the state can be detected by the presence of a phonon in the symmetric stretch mode. This phonon is detected by driving a red sideband on the Ca^+ $^2D_{5/2} \leftarrow {}^2S_{1/2}$ transition and then detecting if the Ca^+ ion is in the $^2D_{5/2}$ or $^2S_{1/2}$. If the molecule was initially in $|\text{e}, 0\rangle$ no phonon will be detected and a microwave pulse can be applied to produce $|\text{f}, 0\rangle$ and the process repeated.

The fidelity of the transition from $|\text{f}, 0\rangle$ to $|\text{e}, 1\rangle$ depends heavily on the sweep rate of the stretch mode frequency, which has upper and lower bounds governed by the requirement for adiabaticity, $\dot{\omega}_q \ll g_q^2$, and the heating rate of the motional mode, respectively. To determine the optimum sweep rate, we simulate the evolution of the system with the master equation:

$$\begin{aligned}\dot{\rho} = &- i[H_s^{(i)}, \rho] + \frac{\gamma_s}{2}\left(a_s^\dagger a_s \rho - 2a_s \rho a_s^\dagger + \rho a_s^\dagger a_s\right) \\ &- \frac{\gamma_s}{2}\left(a_s a_s^\dagger \rho - 2a_s^\dagger \rho a_s + \rho a_s a_s^\dagger\right),\end{aligned} \tag{10.13}$$

where ρ is the molecule-phonon density matrix, $H_s^{(i)}$ is the evolution described in Equation 10.2, and γ_s is the stretch mode motional heating rate. The heating rates of the current trap has been previously measured for the COM mode to be 100 phonons/s for a single ion and 300 phonons/s for two ions [Rug16]. The stretch mode heating rate has not been measured, but is expected to be significantly less than this [KWM98]. This simulation omits contributions of electric field noise heating of the internal states of the molecule. As the molecular dipole is of order ea_o, this heating rate is much smaller than the motional heating rate (detailed calculation in Subsection 10.6.1), which is characterized by a transition dipole moment of order 10 $e$nm.

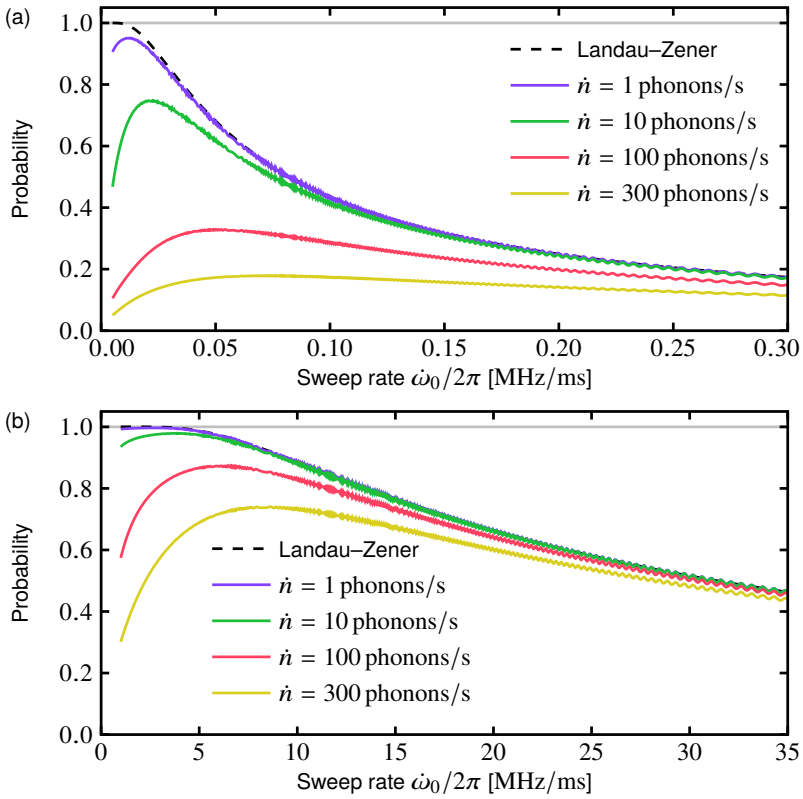

Figure 10.5: **DPQL state-flip probability simulations.** These plots show the probability of successful state flip from $|\mathrm{f},0\rangle$ to $|\mathrm{e},1\rangle$ after a sweep of the stretch mode frequency for (a) the $X^2\Pi_{3/2}$ $J = 3/2$ and (b) the $J = 7/2$ states of CaO^+ as a function of the sweep rate of the stretch mode frequency for various rates of motional heating. For the $J = 3/2$ state the simulated stretch mode frequency was swept from 0.3 MHz to 0.6 MHz, while for the $J = 7/2$ state it was swept from 3.0 MHz to 7.0 MHz. We compare the simulation results to the probability expected from the Landau–Zener formula.

The results of this simulation are shown in Figure 10.5 for both the $J=3/2$ state, which will be used in the current experiment, and the $J=7/2$ state explored above. The state-flip probability is larger and can be performed with faster sweep rates for the $J=7/2$ state due to its larger g_{mol}, which scales as $\omega_{\mathrm{mol}}^{3/2}$. The sweeping time for the high-fidelity transfer using a linear sweep is on the order of a millisecond, which is small compared to the blackbody-limited lifetime of the rotational states. The time required for an adiabatic sweep can be significantly reduced by performing an idealized nonlinear ramp, further reducing the effects of motional heating.

10.4.2 Qubit State Preparation

While the process described above can detect the adiabatic transfer of a molecular excitation to a phonon, without additional operations, it does not resolve the m_J state of the molecule prepared in $|\mathrm{e}\rangle$. A magnetic field could be used to spectrally resolve the different m_J states through their differential g-factor. However, this slows the process considerably. Further, as indicated in Table 10.1, the energy of Λ-doublet splitting (and the rotational splitting) of CaO^+, X $^2\Pi_{3/2}$ are much smaller than $k_\mathrm{B}T$ at room temperature, where k_B is the Boltzmann constant. Therefore, all the parities and m_J sublevels are equally populated and the probability of success—defined as the observation of the adiabatic transfer—is small for a single attempt. It is therefore desirable, both for efficiency and for use of a qubit, to devise a method to 'pump' the molecule into a given m_J using DPQL techniques.

In this section, we present a method of preparing CaO^+, $^2\Pi_{3/2}$, $J = 3/2$ into its upper stretched state ($m_J = 3/2$) of e parity[1]. Figure 10.6a shows the Zeeman shift of CaO^+, $^2\Pi_{3/2}$, J=3/2. The right panel of Figure 10.6a shows the Zeeman shift for smaller magnetic field values, where the Λ-doublet is noticeable. The e and f parities are represented by blue and red solid lines, respectively. Figure 10.6b introduces our procedure of state preparation with the assumption that CaO^+ has been cooled to its motional ground state of e parity—f parity can be addressed by using a microwave pulse. (1) A uniform magnetic field is applied along the axial direction to break the degeneracy of the sublevels. With a circularly polarized microwave π-pulse, the populations swap from $|\mathrm{e}, m_J - 1, 0\rangle$ to $|\mathrm{f}, m_J, 0\rangle$. The three notations in the kets represent parity, projection of total angular momentum along quantization axis and number of phonons, respectively. (2) By adiabatically sweeping the normal mode frequency across the Λ-doublet splitting, all the populations in $|\mathrm{f}, m_J, 0\rangle$ can be transferred to $|\mathrm{e}, m_J, 1\rangle$. (3) The quantum state of CaO^+ ends in $|\mathrm{e}, m_J, 0\rangle$ via applying sideband cooling. The process is repeated until CaO^+ is in the upper stretched state ($m_J =$

[1] $J = 3/2$ is used in this example due to its simpler energy structure compared with higher rotational states. However, this method can also be applied to other higher rotational states.

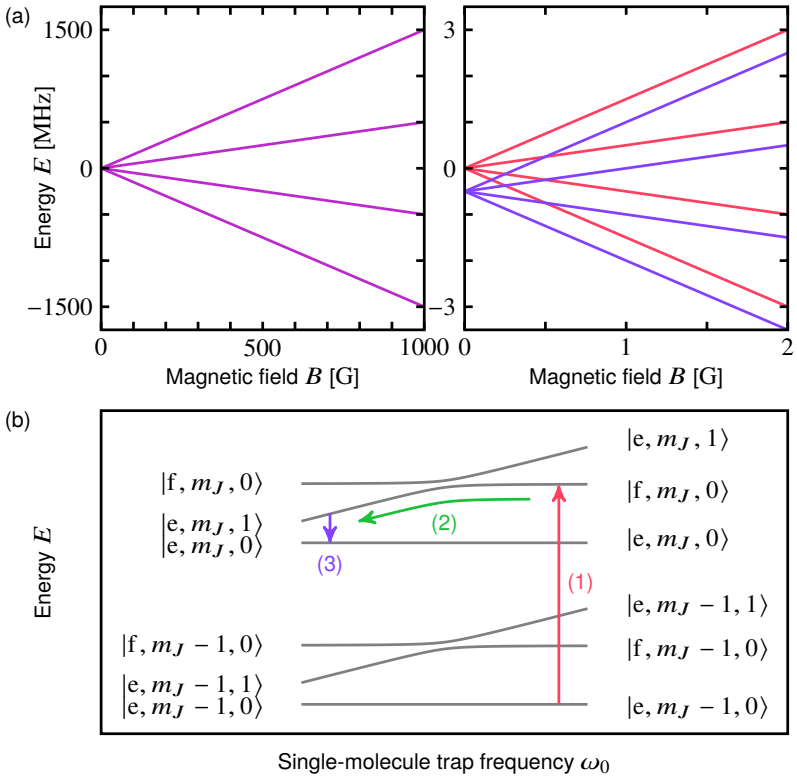

Figure 10.6: **Qubit state preparation.** (a) Zeeman shift of CaO^+, $X^2\Pi_{3/2}$, J=3/2 (left panel). The right panel shows a zoomed part of the left panel with a visible Λ-doublet splitting. In the right panel, f and e parities are indicated by red and blue colors, respectively. (b) The procedure of qubit state preparation. Assume the initial population is cooled to motional ground state of e parity. (1) Utilize a σ^+ microwave pulse to move the population from $|\mathrm{e}, m_J - 1, 0\rangle$ to $|\mathrm{f}, m_J, 0\rangle$. In the ket, there are three notations, which correspond to parity, projection of total angular momentum, and number of phonons, respectively. (2) Adiabatically sweep the normal mode frequency across the Λ-doublet splitting to transfer all the CaO^+ populated in $|\mathrm{f}, m_J, 0\rangle$ to $|\mathrm{e}, m_J, 1\rangle$. (3) Apply sideband cooling to cool CaO^+ back to motional ground state. By repeating these steps, CaO^+ can be accumulated in stretched state of e parity ($|\mathrm{e}, m_J = 3/2, 0\rangle$). For this procedure, 800 G uniform bias magnetic field can be applied to break the degeneracy of sublevels.

3/2) of e parity, which does not participate in this process. Due to the fact that the upper stretched state of e parity is a dark state, the nonequivalent Clebsch-Gordan coefficients of σ^+ transitions for different m_J does not set any fundamental limit for population transfer.

For the sake of practicality, is is useful to set the microwave frequency within the range from 500 MHz to a few GHz, so that it can be applied through the trap electrodes. As shown in Figure 10.6a, a magnetic field with amplitude of 800 Gauss will cause a differential Zeeman shift between nearby m_J states up to 800 MHz.

10.5 Summary

In summary, we have detailed a path towards an experimental demonstration of the basic interactions in dipole–phonon quantum logic (DPQL) for atom–molecule and molecule–molecule systems. We present and discuss the results of *ab initio* calculations for alkaline-earth monoxide and monosulfide cations. We find that they appear to be excellent candidates for DPQL as they have nearly ideal rovibronic structure, often do not possess hyperfine structure, and are easily produced in existing trapped ion systems. Using a candidate from among these molecules, CaO^+, we present early experimental progress and guiding calculations of the expected rates and fidelities for basic DPQL operations with attention to experimental realities, including motional heating and Zeeman substructure. We also show, for a chain including two molecules, a scheme to utilize the virtual-phonon-mediated dipole–dipole interaction to perform an iSWAP gate and therefore outline a path to universal quantum computation via DPQL.

10.6 Supplemental Calculations

In this section, several supplemental calculations are presented that were not included in the main text, but are of interest towards the application of DPQL.

10.6.1 Effect of Electric-Field Noise on Internal States of Molecular Ions

There are many sources of electric-field noise in ion traps [TKK00]: fluctuating electrical fields from injected circuits, varying patch potentials from the trap surface, Johnson noise from the resistance of trap electrodes, and so on. In the DPQL procedure, these noise sources could directly couple to the dipole moments of molecular ions and thus cause transitions between Λ-doublet splittings and rotational states as well as via ion motion. Here we consider two major forms of electric-field noise [SM99]: one is a fluctuating, uniform electrical field $\zeta(t)$; the other is a fluctuating quadrupole field, which perturbs the spring constant of the trap by $\Delta K = \epsilon(t) M\omega_z^2$, where M is ion mass and ω_z is the axial secular frequency. The Hamiltonian under the above noise model can then be written as:

$$H = \frac{P^2}{2M} + \frac{1}{2}M(1+\epsilon(t))\omega_z^2 z^2 + \zeta(t)qz. \tag{10.14}$$

Here P is the ion momentum and q is the charge of ion. Using first-order time-dependent perturbation theory, we can derive the heating rate near the motional ground state [SOT97, GYN00]:

$$\frac{d}{dt}\langle n\rangle = \frac{\pi\omega_z^2}{4}S_\epsilon(2\omega_z) + \frac{q^2}{2M\hbar\omega_z}S_\zeta(\omega_z) \tag{10.15}$$

where $S_j(\omega) = \int_{-\infty}^{\infty} d\tau \langle j(t)j(t+\tau)\rangle e^{i\omega\tau}$ (with $j = \epsilon, \zeta$) is the power spectral density of the fluctuating $\epsilon(t)$ and $\zeta(t)$ respectively and $|n\rangle$ is the motional state. Here, we neglect the higher order term $\langle \epsilon^2(t)\zeta^2(t)\rangle$. The first term in Equation 10.15 is from the quadrupole field fluctuation. For a molecular ion that is sympathetically cooled and well compensated from excess micromotion, the coupling between the quadrupole field fluctuation and the molecular ion dipole is small since the electric field noise is close to zero at the RF null. The second term couples the molecular ion dipole through $S_\zeta(\omega)$, which results in a spectral energy

density $\rho_H(\omega)$

$$\rho_H(\omega) = \epsilon_0 S_\zeta(\omega) = \frac{2M\hbar\epsilon_0\omega_z\Gamma^*}{q^2} \tag{10.16}$$

where ϵ_0 is the permittivity of free space and Γ^* is the heating rate caused by $\zeta(t)$. We model the frequency dependence of the electric field noise as a single power law [BSC15], $S_\zeta(\omega) \propto f^{-0.6}$ over the Λ-doublet splitting range ($\omega < 2\pi \times 100$ MHz) and broadband noise for higher frequencies. Here we consider the co-trapped Ca^+ and CaO^+ to have an axial COM frequency of $\omega_z = 2\pi \cdot 450$ kHz and the COM heating rate to be $\Gamma^* = 300$ quanta/s. For Λ-doublet of $J=7/2$, electric-field noise results in a transition rate $B_{ef}\rho_H(\omega) \sim 0.001$ s^{-1}, where B_{ef} is the Einstein B coefficient for the transition. This transition rate is negligible compared to the thermalization process from blackbody radiation, in which the blackbody-limited life time is 4 s. This result indicates that electric-field noise could affect the DPQL process via motional heating with effective dipole moment of order 10 e·nm, but not via directly coupling with dipole moment of molecular ion which is on the order of 0.1 e·nm. We also calculate the effect of electric-field noise on the rotation state distribution under room temperature using the rate equation model. The results shows that the blackbody-limited lifetime of the states is not affected.

10.6.2 Numerical Simulation

To demonstrate some two-molecule techniques, we present the results of a numerical simulation of the Hamiltonian

$$H = \sum_{q,i} \left(\frac{\omega_{\text{mol}}^{(i)}}{2}\sigma_z^{(i)} + \omega_q \left(a_q^\dagger a_q + \frac{1}{2} \right) + \frac{g_q^{(i)}}{2}\sigma_x^{(i)} \left(a_q^\dagger + a_q \right) \right) \tag{10.17}$$

where $\hbar = 1$, $\omega_{\text{mol}}^{(i)}$ is the energy splitting of molecule (i), ω_q is the secular frequency of the normal mode q along the trap axis, $\sigma_x^{(i)} = \left|\mathrm{e}^{(i)}\right\rangle\left\langle\mathrm{f}^{(i)}\right| + \left|\mathrm{f}^{(i)}\right\rangle\left\langle\mathrm{e}^{(i)}\right|$, and $\sigma_z^{(i)} =$

$\left|\mathrm{f}^{(i)}\right\rangle\left\langle\mathrm{f}^{(i)}\right| - \left|\mathrm{e}^{(i)}\right\rangle\left\langle\mathrm{e}^{(i)}\right|$. Here, $g_q^{(i)} \equiv d\mathcal{E}_{0,q}^{(i)} = \frac{d}{e}\sqrt{2m^{(i)}\omega_q^3}b_q^{(i)}$ is the vacuum Rabi frequency of the interaction where $\mathcal{E}_{0,q}^{(i)}$ is the electric field amplitude at the position of ion (i) due to a single phonon in normal mode q, $m^{(i)}$ is the mass of ion (i), e is the elementary charge, and $b_q^{(i)}$ is the component of the eigenvector of normal mode q at ion (i). For simplicity, the effect of motional heating is not included in these simulations.

We present the results of numerical simulations of a three-ion chain with two CaO^+ molecular ions in the $X\,^2\Pi_{3/2}$ state, with $J = 7/2$ on the outside ends of the chain and a single Ca^+ atomic ion at the center of the chain. We present simulations of various techniques for state preparation and for demonstrating the virtual-phonon-mediated dipole–dipole interaction. To demonstrate the results, we plot the "average excitation" of each molecule (i) and each normal mode q. We define the "average excitation" of molecule (i) to be the probability of measuring the molecule in the $\left|f^{(i)}\right\rangle$ state $\left|\left\langle f^{(i)}\middle|\psi(t)\right\rangle\right|^2$. We define the "average excitation" of normal mode q to be the average phonon number $\langle n_q\rangle = \langle\psi(t)|\, a_q^\dagger a_q\, |\psi(t)\rangle$.

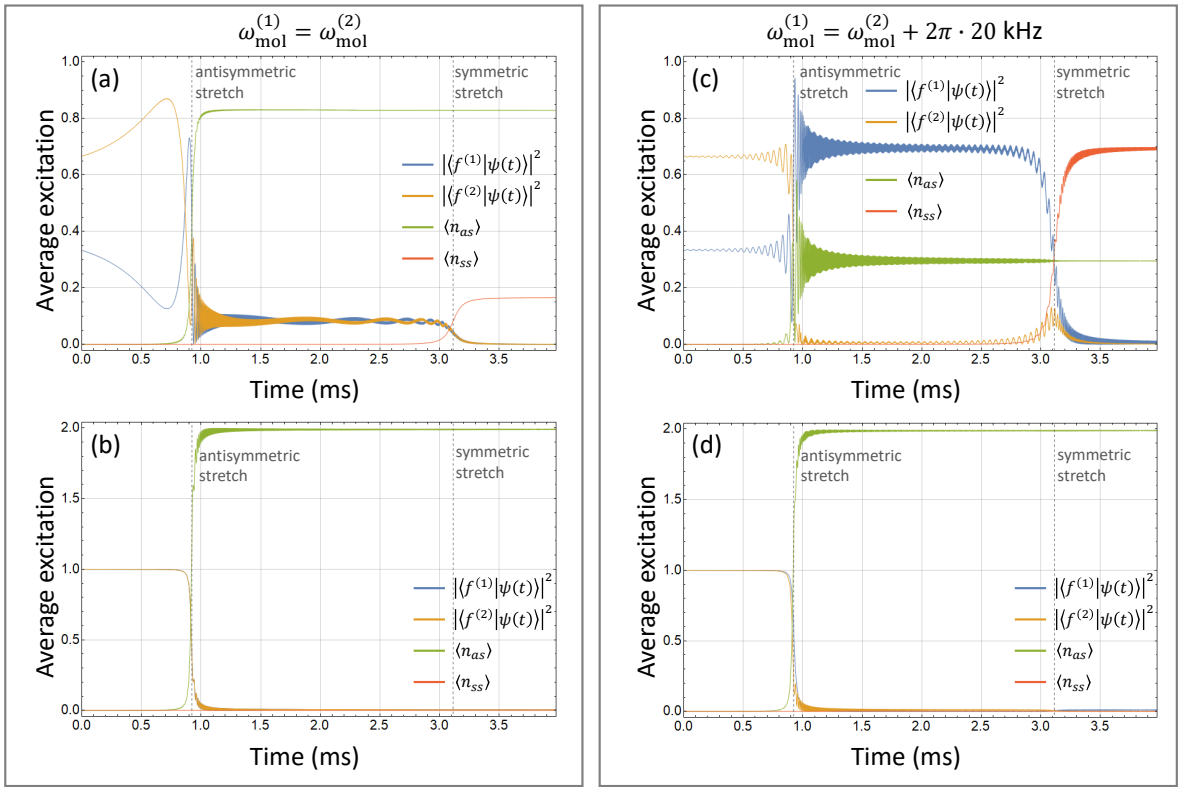

Figure 10.7: **Simulation of a frequency sweep to prepare the $|\text{ee}\rangle$ state.** We begin with all normal mode frequencies below $\omega_{\text{mol}}^{(1)}$ and $\omega_{\text{mol}}^{(2)}$ in the motional ground state for all normal modes. We then increase the single-molecule trap frequency ω_0 linearly at a rate of $\dot{\omega}_0 = 3.0 \times 10^9$ rad/s^2 until both the antisymmetric and symmetric stretch mode frequencies pass through $\omega_{\text{mol}}^{(1)}$ and $\omega_{\text{mol}}^{(2)}$. (a) With equal splittings ($\omega_{\text{mol}}^{(1)} = \omega_{\text{mol}}^{(2)}$), we select an arbitrary single-molecular-excitation initial state $|\psi_{\text{mol}}(0)\rangle = \sqrt{\frac{2}{3}}\,|\text{ef}\rangle + \sqrt{\frac{1}{3}}\,e^{i\pi/4}\,|\text{fe}\rangle$. (b) With equal splittings, we start with $|\psi_{\text{mol}}(0)\rangle = |\text{ff}\rangle$. In this plot, the average excitations for molecules (1) and (2) are overlapping within the thickness of the line. (c) $\omega_{\text{mol}}^{(1)} = \omega_{\text{mol}}^{(2)} + 2\pi \cdot 20$ kHz and $|\psi_{\text{mol}}(0)\rangle = \sqrt{\frac{2}{3}}\,|\text{ef}\rangle + \sqrt{\frac{1}{3}}\,e^{i\pi/4}\,|\text{fe}\rangle$. Far away from resonance, $\left|\omega_{\text{mol}}^{(1)} - \omega_{\text{mol}}^{(2)}\right| \gg |J_{12}|$, and the amplitude of oscillation between $|\text{fe}\rangle$ and $|\text{ef}\rangle$ is small. As one of the normal mode frequencies approaches resonance, the coupling strength J_{12} increases, and the previously stated limit is no longer valid. In this regime, there are nontrivial oscillations between $|\text{fe}\rangle$ and $|\text{ef}\rangle$. (d) $\omega_{\text{mol}}^{(1)} = \omega_{\text{mol}}^{(2)} + 2\pi \cdot 20$ kHz and $|\psi_{\text{mol}}(0)\rangle = |\text{ff}\rangle$. Again, the average excitations for molecules (1) and (2) are overlapping within the thickness of the line. In every case shown, sweeping the frequency such that the antisymmetric and symmetric stretch mode frequencies pass through $\omega_{\text{mol}}^{(1)}$ and $\omega_{\text{mol}}^{(2)}$ removes any molecular excitation and prepares the molecular state in $|\text{ee}\rangle$. Additionally, if the initial molecular state is $|\psi_{\text{mol}}(0)\rangle = |\text{ff}\rangle$, such a sweep will yield two phonons in the antisymmetric stretch mode—as this is the first mode to sweep through resonance—regardless of the difference in molecular splittings.

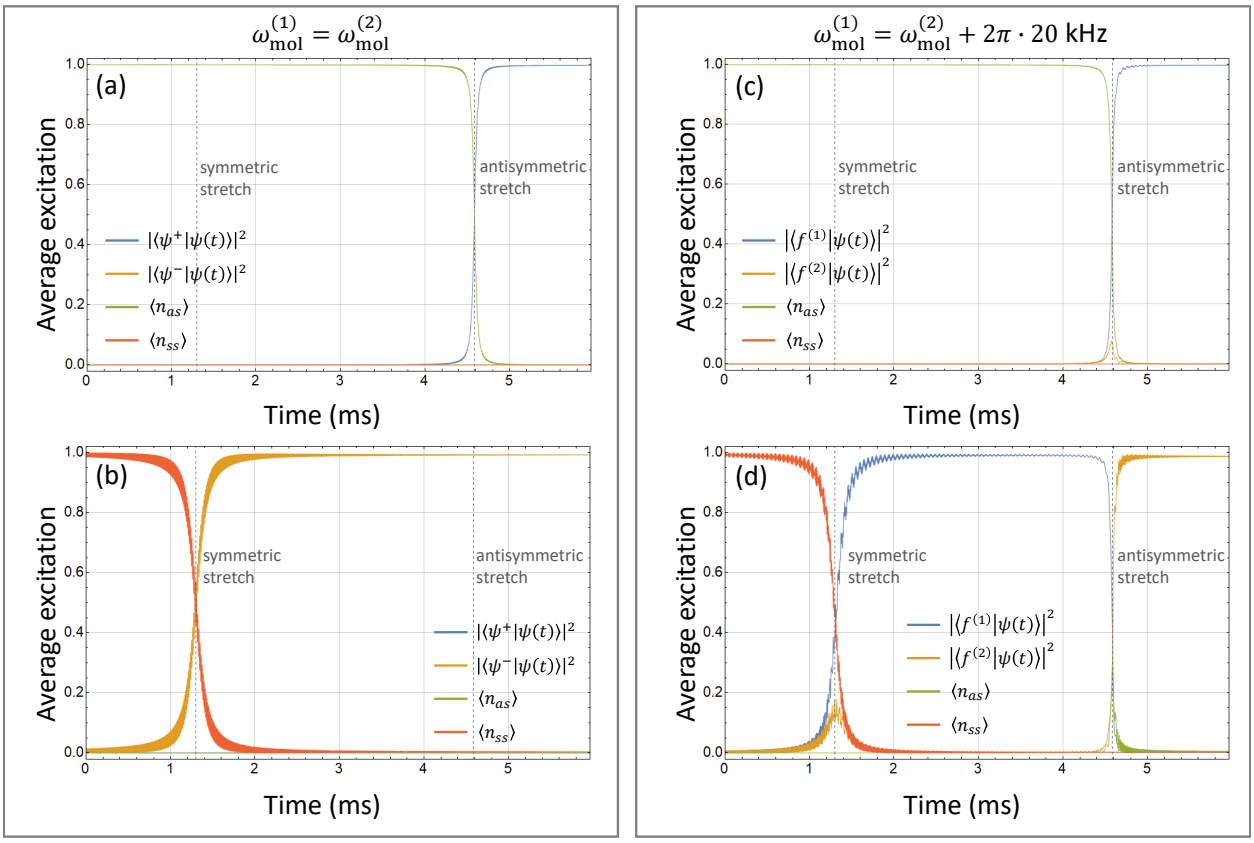

Figure 10.8: **Simulation of molecular state preparation techniques.** For each simulation, the initial molecular state is $|\text{ee}\rangle$ with a single phonon in either the symmetric or antisymmetric stretch mode, and the initial single-molecule trap frequency is tuned such that the symmetric and antisymmetric stretch mode frequencies are above $\omega_{\text{mol}}^{(1)}$ and $\omega_{\text{mol}}^{(2)}$. The single-molecule trap frequency is decreased at a rate of $\dot{\omega}_0 = -2.0 \times 10^9$ rad/s^2 until the antisymmetric and symmetric stretch mode frequencies are below $\omega_{\text{mol}}^{(1)}$ and $\omega_{\text{mol}}^{(2)}$. (a) With $\omega_{\text{mol}}^{(1)} = \omega_{\text{mol}}^{(2)}$, starting with a single phonon in the antisymmetric stretch mode yields the Bell state $|\psi^+\rangle = (|\text{fe}\rangle + |\text{ef}\rangle)/\sqrt{2}$. (b) With $\omega_{\text{mol}}^{(1)} = \omega_{\text{mol}}^{(2)}$, starting with a single phonon in the symmetric stretch mode yields the Bell state $|\psi^-\rangle = (|\text{fe}\rangle - |\text{ef}\rangle)/\sqrt{2}$. (c) With $\omega_{\text{mol}}^{(1)} = \omega_{\text{mol}}^{(2)} + 2\pi \cdot 20$ kHz, starting with a single phonon in the antisymmetric stretch mode yields $|\text{fe}\rangle$. (d) With $\omega_{\text{mol}}^{(1)} = \omega_{\text{mol}}^{(2)} + 2\pi \cdot 20$ kHz, starting with a single phonon in the symmetric stretch mode yields $|\text{ef}\rangle$.

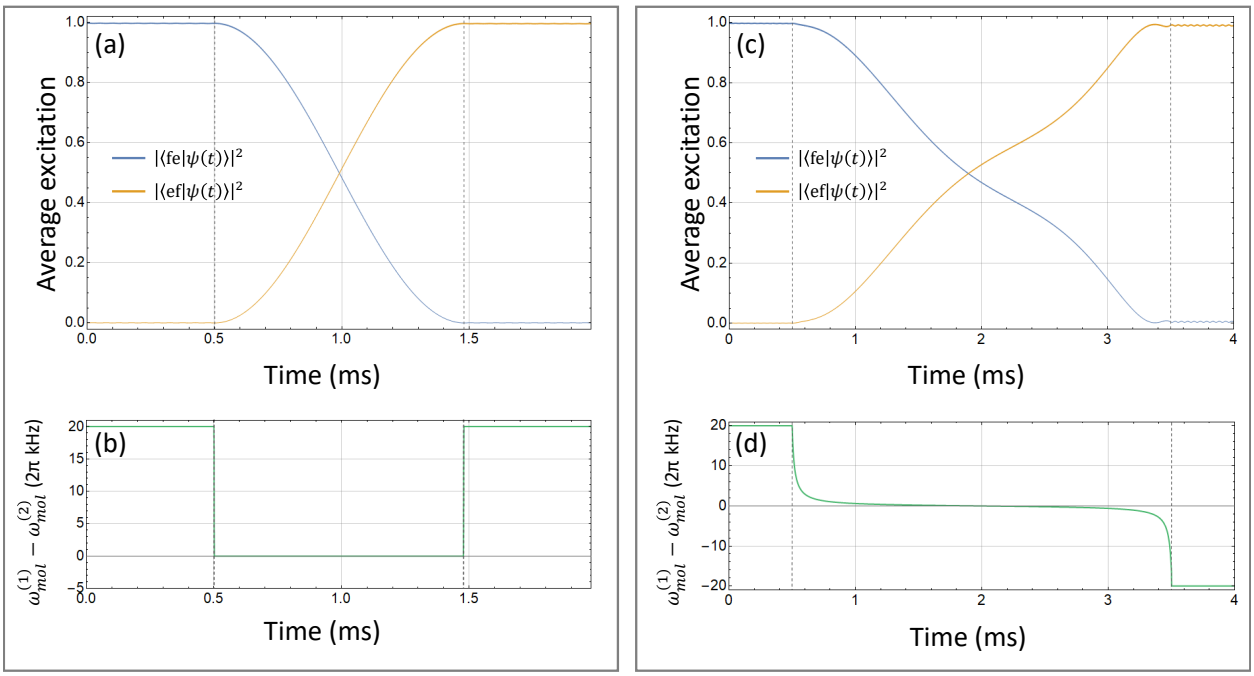

Figure 10.9: **Two different methods to transfer the population from** $|\text{fe}\rangle$ **to** $|\text{ef}\rangle$**.** In the first method, depicted in (a) and (b), we start with the molecular splittings different by $2\pi \cdot 20$ kHz. To begin the transfer, we quickly set this difference to zero, allowing the population to coherently oscillate between $|\text{fe}\rangle$ and $|\text{ef}\rangle$. After waiting $t_\pi = \frac{\pi}{2J_{12}}$, where J_{12} is the virtual-phonon-mediated dipole–dipole interaction strength, we restore the difference in molecular splittings to stop this oscillation. The average molecular excitation of molecules (1) and (2) are shown in (a) and the difference in molecular splittings as a function of time is shown in (b). For the second method, shown in (c) and (d), we adiabatically vary the difference in molecular splitting. To achieve a high probability transfer with a linear sweep of the molecular splitting difference, it is necessary for the sweep of the molecular splitting difference $\left|\dot{\Delta}\right| \ll J_{12}^2$. To dramatically decrease the time needed to perform an adiabatic sweep, we change the molecular splitting difference in a nonlinear fashion, with ramping speed $\dot{\Delta}(t)$. The ramp is faster for larger differences in molecular splittings. For all times, we maintain the limit $\left|\dot{\Delta}(t)\right| \ll J_{12}^2 + \left(\frac{1}{2}(\omega_{\text{mol}}^{(1)} - \omega_{\text{mol}}^{(2)})\right)^2$.

CHAPTER 11

Future Work

In this chapter, future work to be done in the MOTion trap is discussed. Specifically, a path towards performing rotational thermometry is provided, giving a method by which to measure the rotational cooling effects of the MOT. Once this is accomplished, it is then possible to demonstrate the dipolar quantum logic methods proposed in Ref. [HC18]. In order to demonstrate the techniques of DPQL and EGGs, it is beneficial to design and build a new apparatus, dedicated to the design parameters required by DPQL and EGGs. To this end, I briefly discuss these techniques and considerations for building an ion trap suitable for these studies.

11.1 Rotational State Thermometry

To demonstrate the sympathetic cooling of the rotational degrees of freedom of $BaCl^+$ by the Ca MOT, it is first necessary to measure the rotational temperature. Our efforts to achieve a method for this rotational thermometry is outlined in Chapter 9. Simply, we aim to drive a vibrational transition $v' \leftarrow v = 0$ in $BaCl^+$ in a manner that is dependent on the initial rotational state. Then, by UV photodissociation, we dissociate only molecules in the v' state, but not in the $v = 0$ state. We have attempted to demonstrate such a scheme in several ways, detailed in Chapter 9. In this section, I describe the next iteration of this experiment, which is currently in progress. We aim to drive the $v' = 4 \leftarrow v = 0$ transition at ~ 7530 nm using a Daylight Solutions QCL with ~ 80 mW power.

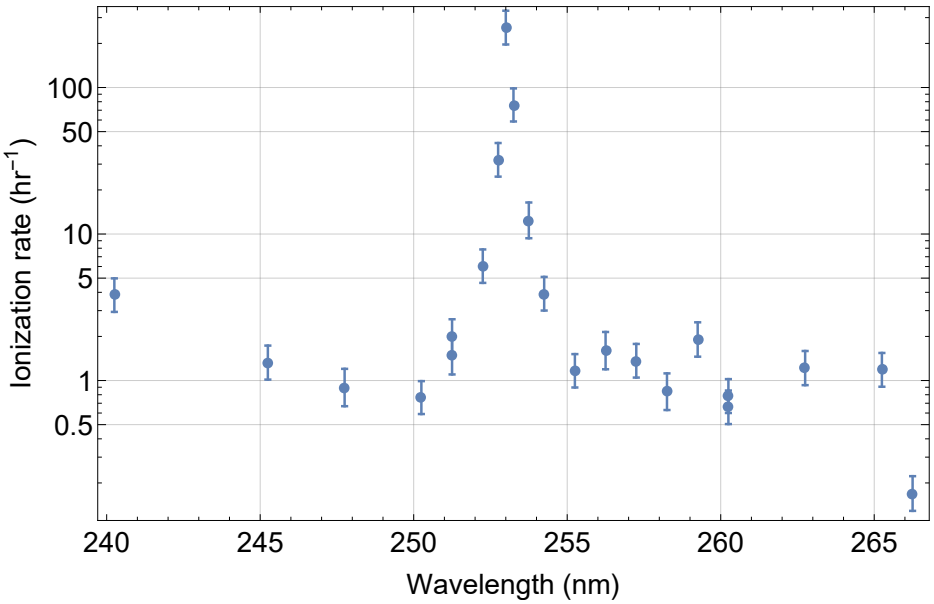

Figure 11.1: **Measured Ba^+ ionization rate as a function of UV wavelength.** We observe the ionization of Ba^+, producing Ba^{2+}, by a two-photon process from the UV laser. The large peak is due to resonance-enhanced multi-photon ionization (REMPI), where $Ba^+(6p\ ^2P_{1/2})$ ions are ionized by two $\sim$ 252.75 nm photons coupling to the intermediate $7d\ ^2D_{3/2}$ state. The increase in ionization rate at wavelengths $\lesssim$ 265 nm is presumed to be due to the fact that below this wavelength, two photons have enough energy to ionize the $Ba^+(5d\ ^2D_{3/2})$ ions. To prevent this ionization, the 493 nm Ba^+ cooling laser is quickly turned off during a UV pulse, so the Ba^+ is in its ground state.

To dissociate the $v' = 4$ state, we utilize the PDL operating at 255 nm. With this UV wavelength, there will be an increased background $BaCl^+$ dissociation rate due to the UV laser (see Figure 9.2), so the transition strength of the $v' = 4 \leftarrow v = 0$ transition must be much larger than the $v' = 8 \leftarrow v = 0$ transition in order to detect a signal. Alternatively, we can use only a very low UV pulse energy. In this case, however, it may become unlikely to dissociate the $v' = 4$ population before it spontaneously decays. As before, many parameters must be considered to try and produce the highest signal-to-background dissociation rate ratio. In addition to the pulse energy, the UV wavelength can be tuned. If the wavelength is too blue, the background dissociation rate of $BaCl^+$ will be too large; with a wavelength that is too red, the background dissociation rate will decrease, but the signal dissociation rate will decrease by an even larger factor.

An additional complexity with the UV required for dissociation is the ionization of Ba^+, forming Ba^{2+}. This ionization is a source of loss of our Ba^+ ions and must be minimized in experiment to maintain sufficient sympathetic translational cooling of the $BaCl^+$. We measure this ionization rate as a function of the UV wavelength and present the results in Figure 11.1. This ionization is only significant at wavelengths $\lesssim 265$ nm, where two UV photons possess enough energy to ionize the $Ba^+(5d\ ^2D_{3/2})$ ions. Additionally, we observe a large peak in the ionization spectrum at ~ 252.75 nm, attributed to resonance-enhanced multi-photon ionization (REMPI), where $Ba^+(6p\ ^2P_{1/2})$ ions are ionized by two UV photons, coupling to the intermediate $7d\ ^2D_{3/2}$ state. In order to minimize this ionization loss of Ba^+, we shelve the ions in the ground $Ba^+(^2S_{1/2})$ state during a UV pulse. We accomplish this by passing the 493 nm cooling beam through an AOM, which we can quickly switch on and off, triggered by the UV laser pulse.

For the $v' = 8 \leftarrow v = 0$ transition attempted in Chapter 9, the background UV dissociation was small, leading to long interrogation times of order 30 minutes being plausible. Such long timescales allowed us to attempt to drive a single rovibrational transition, allowing rotational state redistribution to slowly re-populate the state we hoped to drive. With the $v' = 4 \leftarrow v = 0$, the background dissociation will be faster due to the UV wavelength needed, and we cannot rely on rotational state redistribution, which takes minutes. Instead, we aim to broaden the MIR laser to cover the vibrational transitions for multiple rotational levels. Again, there is a trade-off between driving more transitions weakly with a broader laser and driving fewer transitions more strongly with a narrower laser. Based on simulations, we expect the optimal signal-to-background ratio for a linewidth of ~ 10 GHz.

Such experiments are currently in progress. If we are able to successfully observe a signal, we will then be able to precisely map out the rotational structure by scanning the MIR laser over range of the vibrational transition. Using the precise location of each rovibrational transition, we can measure the population in each rotational state by strongly driving each transition with a narrow MIR laser. Then, we can introduce the Ca MOT, and measure

the rotational temperature before and after immersion in the Ca MOT, demonstrating the sympathetic cooling of the rotational degrees of freedom of the $BaCl^+$ molecular ions.

11.2 Experimentally Demonstrate Dipolar Quantum Logic

With confirmation of the ability of the MOT to rotationally cool the $BaCl^+$ molecular ions, it is then possible to use this sympathetic cooling to produce $BaCl^+$ molecules in their rovibrational ground state, enabling demonstration of the dipolar quantum logic methods outlined in Ref. [HC18].

To understand this effect, we consider two identical molecular ions in an ion trap, both in the $J = 0$ rotational state. If one of these molecular ions is promoted to the $J = 1$ state by a spatially selective microwave π pulse, it then has a dipole moment oscillating at frequency Δ relative to the other molecule, where $\hbar\Delta$ is the energy difference between the $J = 1$ and $J = 0$ states. This oscillating dipole creates some oscillating electric field at the position of the other ion, which can resonantly drive the $J = 1 \leftarrow J = 0$ transition. An excitation of the other molecule must result in a de-excitation of the originally excited molecule, as energy is conserved. In this way, a dipole–dipole exchange interaction of the form [HC18]

$$V_{\mathrm{dd}}(\vec{r}) = \frac{J}{2}(\sigma_x^{(1)}\sigma_x^{(2)} + \sigma_y^{(1)}\sigma_y^{(2)}) \tag{11.1}$$

is realized, where $\sigma_x^{(i)}$ and $\sigma_y^{(i)}$ are Pauli operators for molecule i, and $J(\vec{r}) = d^2/(4\pi\epsilon_0 r^3)(1 - 3\cos^2\theta)$ is the dipole–dipole interaction strength, where d is the transition dipole moment and θ is the angle between the polarization axis and molecule–molecule separation $\vec{r}$.

While the previous example is useful for gaining an intuitive understanding of the technique, it is challenging to spatially address only one molecule with microwave radiation. Individual addressing is also not necessary to perform two-qubit entanglement. Defining $|0\rangle$ as the $J = 0$ state and $|1\rangle$ as the $J = 1$ state, we can begin an experiment with both

molecules in the $J = 0$ state, with $|\psi_1, \psi_2\rangle = |0, 0\rangle$. By applying a global, $\frac{\pi}{2}$ pulse, we prepare the $|^+X,^+X\rangle$ state, where $|^\pm X\rangle \equiv \frac{1}{\sqrt{2}}(|0\rangle \pm \mathrm{e}^{i\Delta t}|1\rangle)$ are the eigenstates of σ_x. As this state is not an eigenvalue of Equation 11.1, the state evolves with time. After evolution time $t_\mathrm{G} = \frac{\pi}{2J}$, the system evolves to the state $\frac{1}{\sqrt{2}}\mathrm{e}^{-i\pi/4}(|^+X,^+X\rangle + i\,|^-X,^-X\rangle)$. With another global $\frac{\pi}{2}$ pulse, the Bell state $\frac{1}{\sqrt{2}}\mathrm{e}^{-i\pi/4}(|1,1\rangle - |00\rangle)$ is prepared.

As these dipoles are rotating quickly, typically GHz or faster, the dipole moment averages to zero in the lab frame and is insensitive to slowly varying electric fields, such as those from the ion trap itself. Because of this, the dipole–dipole interaction is insensitive to phonon number and motional heating, meaning that this technique does not require ground-state cooling, meaning that this effect can be demonstrated in the MOTion trap without additional significant modifications other than the incorporation of a microwave source. By preparing $BaCl^+$ in the $v = 0$, $J = 0$ rovibrational ground state, we can demonstrate such an entangling interaction between two molecular ions, marking a major milestone for quantum logic with molecular ions.

11.3 Experimentally Demonstrate DPQL

As detailed in Chapter 10, DPQL opens up a wide suite of tools for quantum logic with molecular ions. This technique, however, requires a molecule with two states connected by an electric dipole transition with frequency near the motional secular frequency of the ion trap, which $BaCl^+$ does not have. Additionally, while some of the techniques of DPQL can be implemented without the need for ground-state cooling, some useful techniques do require ground-state cooling. Also, this dipole–phonon interaction strength g scales as $\Delta^{3/2}$, where $\hbar\Delta$ is the energy difference between the two molecular ion states, meaning that it is beneficial to have a molecule with large Δ and a trap with a high secular frequency to match it. The ion trap in the MOTion trap has a relatively low secular frequency (~ 60 kHz for Ba^+). For these reasons, it is advantageous to design a new ion trap dedicated to DPQL.

In designing this trap, there are a few key aspects to keep in mind. The first major choice is the choice of molecule. Among the molecules detailed in Table 10.1, CaO^+ appears especially promising. In its $J = 7/2$ rotational state, the Λ-doublet splitting is $2\pi \cdot 5.0$ MHz, which is a relatively high secular frequency for an ion trap, especially if DPQL is to be performed on the axial modes, which are typically lower in secular frequency than the radial modes. Additionally, there may be a large enough population in the $J = 7/2$ state at 4 K ($\sim 17\%$) to allow this experiment to operate at cryogenic temperatures without the need for sympathetic cooling of a MOT. This is especially true since DPQL provides a method to verify the state preparation, ensuring the molecule is in the desired rotational state. To summarize, an appropriate ion trap dedicated to demonstrating DPQL should be cryogenic at 4 K and be capable of ~ 5 MHz axial secular frequencies, with radial frequencies being likely at least twice as large.

11.4 Experimentally Demonstrate EGGs

The full description and derivation of electric-field gradient gates (EGGs) is provided in Ref. [HC20]. Simply put, these gates rely on the application of microwave radiation with an electric-field gradient on a molecular ion. This microwave radiation can be supplied directly to the ion trap rods, creating a quadrupolar microwave source. For an ion exactly at the trap center, this field can drive motional sidebands of a molecular electric dipole transition—such as a rotational transition—but cannot drive the "carrier" transition, where the internal state of the molecule is excited and the motion is not changed. To understand why this quadrupolar field cannot such a transition, we can think about the form of the oscillating electric field. The amplitude of such an oscillating electric field will be the same on either side of the trap center, but opposite in direction. We can an ion undergoing some radial motional oscillation in the x-axis about the trap center. When the ion has position $x > 0$, it will feel some oscillating electric field that can begin to drive a transition due to the $\vec{d} \cdot \vec{E}_+$

interaction, where $\vec{E}_+$ is the oscillating electric . When the ion position is on the opposite side of the trap with $x < 0$, however, the electric field flips direction, $E_- = -E_+$, and the resulting $\vec{d} \cdot \vec{E}_- = -\vec{d} \cdot \vec{E}_+$, and the oscillating electric field when $x < 0$ essentially coherently reverses the effect of the electric field when $x > 0$.

This effect allows one to drive motional sidebands in these molecules using only microwave sources that do not significantly drive the carrier transition. Additionally, such a technique could be used to drive what is essentially a Mølmer–Sørensen gate [MS99], by applying a two-tone microwave quadrupole field. In a standard Mølmer–Sørensen gate, the assumption must be made that $e^{-i\vec{k}\cdot\vec{x}} \approx (1 - i\vec{k} \cdot \vec{x})$, where $\vec{k}$ is the laser wavevector and $\vec{x}$ is the spatial extent of the motional wavefunction. This approximation is valid in the Lamb–Dicke regime, but breaks down if the phonon number is large and the motional wavefunction grows too large. For this similar gate using EGGs, the previous assumption is not necessary and the gate can be performed even for large phonon numbers, potentially easing requirements for scaling to larger systems. Beyond this, there are other exciting potential applications for EGGs, such as the possibility of performing "ultrafast" gates similar to those performed in atomic ion systems [GZC03, Dua04]. To take advantage of these EGGs, it is not necessary to reach such high secular frequencies as with DPQL, and may be easier to implement. Demonstrating these techniques would be a large step forward towards implementing molecular ions as a potentially scalable quantum logic candidate.

[AAB19] Frank Arute, Kunal Arya, Ryan Babbush, Dave Bacon, Joseph C Bardin, Rami Barends, Rupak Biswas, Sergio Boixo, Fernando GSL Brandao, David A Buell, et al. "Quantum supremacy using a programmable superconducting processor." *Nature*, **574**(7779):505–510, 2019.

[AAD18] V. Andreev, D. G. Ang, D. DeMille, J. M. Doyle, G. Gabrielse, J. Haefner, N. R. Hutzler, Z. Lasner, C. Meisenhelder, B. R. O'Leary, C. D. Panda, A. D. West, E. P. West, X. Wu, and Acme Collaboration. "Improved limit on the electric dipole moment of the electron." *Nature*, **562**(7727):355–360, 2018.

[Abe13] Manabu Abe. "Diradicals." *Chemical Reviews*, **113**(9):7011–7088, 2013.

[ABH11] Ivan O Antonov, Beau J Barker, and Michael C Heaven. "Pulsed-field ionization zero electron kinetic energy spectrum of the ground electronic state of BeOBe+." *The Journal of Chemical Physics*, **134**(4):044306, 2011.

[ACK19] K. J. Arnold, S. R. Chanu, R. Kaewuam, T. R. Tan, L. Yeo, Zhiqiang Zhang, M. S. Safronova, and M. D. Barrett. "Measurements of the branching ratios for $6P_{1/2}$ decays in $^{138}Ba^{+}$." *Phys. Rev. A*, **100**:032503, Sep 2019.

[ADS17] Pitt Allmendinger, Johannes Deiglmayr, Otto Schullian, Katharina Höveler, Josef A Agner, Hansjürg Schmutz, and Frédéric Merkt. "New method to study ion-molecule reactions at low temperatures and application to the $H_2^+ + H_2 \rightarrow H_3^+ + H$ reaction." *arXiv preprint arXiv:1705.00871*, 2017.

[AGC10] M Agúndez, JR Goicoechea, J Cernicharo, A Faure, and E Roueff. "The chemistry of vibrationally excited H2 in the interstellar medium." *Astrophys. J.*, **713**(1):662, 2010.

[ALB09] Aldenius, M., Lundberg, H., and Blackwell-Whitehead, R. "Experimental Ca I oscillator strengths for the 4p–5s triplet." *Astron. Astrophys.*, **502**(3):989–994, 2009.

[Arm04] PB Armentrout. "Fundamentals of ion–molecule chemistry." *Journal of analytical atomic spectrometry*, **19**(5):571–580, 2004.

[AS76] N.G. Adams and D. Smith. "The selected ion flow tube (SIFT); A technique for studying ion-neutral reactions." *International Journal of Mass Spectrometry and Ion Physics*, **21**(3):349 – 359, 1976.

[AS17] Chandika Amarasinghe and Arthur G Suits. "Intrabeam scattering for ultracold collisions." *The journal of physical chemistry letters*, **8**(20):5153–5159, 2017.

[BB84] Charles H. Bennett and Gilles Brassard. "Quantum cryptography: Public key distribution and coin tossing." In *Proceedings of IEEE International Conference on Computers, Systems and Signal Processing*, volume 175, p. 8, 1984.

[BB02] D. J. Berkeland and M. G. Boshier. "Destabilization of dark states and optical spectroscopy in Zeeman-degenerate atomic systems." *Phys. Rev. A*, **65**:033413, Feb 2002.

[BCM19] Colin D Bruzewicz, John Chiaverini, Robert McConnell, and Jeremy M Sage. "Trapped-ion quantum computing: Progress and challenges." *Applied Physics Reviews*, **6**(2):021314, 2019.

[Ben80] Paul Benioff. "The computer as a physical system: A microscopic quantum mechanical Hamiltonian model of computers as represented by Turing machines." *Journal of statistical physics*, **22**(5):563–591, 1980.

[BF94] T. Brage and C. F. Fischer. "Spline-Ggerkin methods ayylxed to Rydberg series between the 4S 'S and 3d 'D limits of calcium." *Phys. Rev. A*, **50**:2937, 1994.

[BHL16] C. J. Ballance, T. P. Harty, N. M. Linke, M. A. Sepiol, and D. M. Lucas. "High-Fidelity Quantum Logic Gates Using Trapped-Ion Hyperfine Qubits." *Phys. Rev. Lett.*, **117**:060504, Aug 2016.

[BLA98] V Boutou, MA Lebeault, Abdul-Rahman Allouche, C Bordas, F Paulig, J Viallon, and J Chevaleyre. "Structural transition in barium suboxide clusters." *Physical review letters*, **80**(13):2817, 1998.

[BLP94] Charles W. Bauschlicher, Stephen R. Langhoff, and Harry Partridge. "A redetermination of the dissociation energy of MgO+." *The Journal of Chemical Physics*, **101**(3):2644–2645, 1994.

[BM18] Maximilian Beyer and Frédéric Merkt. "Half-Collision Approach to Cold Chemistry: Shape Resonances, Elastic Scattering, and Radiative Association in the H++ H and D++ D Collision Systems." *Physical Review X*, **8**(3):031085, 2018.

[BMB98] D. J. Berkeland, J. D. Miller, J. C. Bergquist, W. M. Itano, and D. J. Wineland. "Minimization of ion micromotion in a Paul trap." *Journal of Applied Physics*, **83**(10):5025–5033, 1998.

[BMN14] J. F. Barry, D. J. McCarron, E. B. Norrgard, M. H. Steinecker, and D. DeMille. "Magneto-optical trapping of a diatomic molecule." *Nature*, **512**(7514):286–289, Aug 2014.

[BMS19] C. D. Bruzewicz, R. McConnell, J. Stuart, J. M. Sage, and J. Chiaverini. "Dual-species, multi-qubit logic primitives for Ca+/Sr+ trapped-ion crystals." *npj Quantum Information*, **5**(1):102, 2019.

[BO27] M. Born and R. Oppenheimer. "Zur Quantentheorie der Molekeln." *Annalen der Physik*, **389**(20):457–484, 1927.

[BON15] Astrid Bergeat, Jolijn Onvlee, Christian Naulin, Ad Van Der Avoird, and Michel Costes. "Quantum dynamical resonances in low-energy CO (j= 0)+ He inelastic collisions." *Nature chemistry*, **7**(4):349–353, 2015.

[BOV09] RB Blakestad, C Ospelkaus, AP VanDevender, JM Amini, J Britton, D Leibfried, and David J Wineland. "High-fidelity transport of trapped-ion qubits through an X-junction trap array." *Physical review letters*, **102**(15):153002, 2009.

[BOV11] RB Blakestad, C Ospelkaus, AP VanDevender, JH Wesenberg, MJ Biercuk, D Leibfried, and DJ Wineland. "Near-ground-state transport of trapped-ion qubits through a multidimensional array." *Physical Review A*, **84**(3):032314, 2011.

[BSC15] C. D. Bruzewicz, J. M. Sage, and J. Chiaverini. "Measurement of ion motional heating rates over a range of trap frequencies and temperatures." *Phys. Rev. A*, **91**:041402, Apr 2015.

[BVH15] Joshua H. Bartlett, Robert A. VanGundy, and Michael C. Heaven. "Spectroscopic and theoretical studies of the low-lying states of BaO+." *The Journal of Chemical Physics*, **143**(4):044302, 2015.

[BWC11] K. R. Brown, A. C. Wilson, Y. Colombe, C. Ospelkaus, A. M. Meier, E. Knill, D. Leibfried, and D. J. Wineland. "Single-qubit-gate error below 10^{-4} in a trapped ion." *Phys. Rev. A*, **84**(3):030303, September 2011.

[CB18] Aaron T Calvin and Kenneth R Brown. "Spectroscopy of molecular ions in Coulomb crystals." *The journal of physical chemistry letters*, **9**(19):5797–5804, 2018.

[CCJ17] Theo Cremers, Simon Chefdeville, Niek Janssen, Edwin Sweers, Sven Koot, Peter Claus, and Sebastiaan YT van de Meerakker. "Multistage Zeeman decelerator for molecular-scattering studies." *Physical Review A*, **95**(4):043415, 2017.

[CD00] R. Côté and A. Dalgarno. "Ultracold atom-ion collisions." *Phys. Rev. A*, **62**:012709, Jun 2000.

[CDK87] Jean-Michel Combes, Pierre Duclos, Markus Klein, and Ruedi Seiler. "The shape resonance." *Communications in mathematical physics*, **110**(2):215–236, 1987.

[CDK09] Lincoln D Carr, David DeMille, Roman V Krems, and Jun Ye. "Cold and ultracold molecules: science, technology and applications." *New Journal of Physics*, **11**(5):055049, 2009.

[CDK13] Yuan-Pin Chang, Karol Długołecki, Jochen Küpper, Daniel Rösch, Dieter Wild, and Stefan Willitsch. "Specific chemical reactivities of spatially separated 3-aminophenol conformers with cold Ca+ ions." *Science*, **342**(6154):98–101, 2013.

[CGG17] William B. Cairncross, Daniel N. Gresh, Matt Grau, Kevin C. Cossel, Tanya S. Roussy, Yiqi Ni, Yan Zhou, Jun Ye, and Eric A. Cornell. "Precision Measurement of the Electron's Electric Dipole Moment Using Trapped Molecular Ions." *Phys. Rev. Lett.*, **119**:153001, Oct 2017.

[CH20] Wesley C. Campbell and Eric R. Hudson. "Dipole-Phonon Quantum Logic with Trapped Polar Molecular Ions." *Phys. Rev. Lett.*, **125**:120501, Sep 2020.

[CHC20] Justin E. Christensen, David Hucul, Wesley C. Campbell, and Eric R. Hudson. "High-fidelity manipulation of a qubit enabled by a manufactured nucleus." *npj Quantum Information*, **6**(1):35, Apr 2020.

[CLM16] Ludwig E de Clercq, Hsiang-Yu Lo, Matteo Marinelli, David Nadlinger, Robin Oswald, Vlad Negnevitsky, Daniel Kienzler, Ben Keitch, and Jonathan P Home. "Parallel transport quantum logic gates with trapped ions." *Physical Review Letters*, **116**(8):080502, 2016.

[CMK05] Thierry Chanelière, Jean-Louis Meunier, Robin Kaiser, Christian Miniatura, and David Wilkowski. "Extra-heating mechanism in Doppler cooling experiments." *J. Opt. Soc. Am. B*, **22**(9):1819–1828, Sep 2005.

[CSH14] Kuang Chen, Scott T. Sullivan, and Eric R. Hudson. "Neutral Gas Sympathetic Cooling of an Ion in a Paul Trap." *Phys. Rev. Lett.*, **112**:143009, Apr 2014.

[CSR13] Kuang Chen, Scott T. Sullivan, Wade G. Rellergert, and Eric R. Hudson. "Measurement of the Coulomb Logarithm in a Radio-Frequency Paul Trap." *Phys. Rev. Lett.*, **110**:173003, Apr 2013.

[CWL17] Peng Chen, Ning Wang, Song Li, and Shan-Jun Chen. "Theoretical study of the low-lying electronic states of magnesium sulfide cation including spin–orbit interaction." *Journal of Quantitative Spectroscopy and Radiative Transfer*, **201**:104 – 114, 2017.

[CXY19] Gary K. Chen, Changjian Xie, Tiangang Yang, Anyang Li, Arthur G. Suits, Eric R. Hudson, Wesley C. Campbell, and Hua Guo. "Isotope-selective chemistry in the Be+(2S1/2) + HOD → BeOD+/BeOH+ + H/D reaction." *Phys. Chem. Chem. Phys.*, p. Advance Article, 2019.

[Dag77] Paul J Dagdigian. "Dependence of collision complex lifetime on product internal state: Laser fluorescence detection of the Ca+ NaCl crossed beam reaction." *chemical Physics*, **21**(3):453–466, 1977.

[Dah00] David A Dahl. "SIMION for the personal computer in reflection." *International Journal of Mass Spectrometry*, **200**(1-3):3–25, 2000.

[Dan20] Derek J. Daniel. "Exact solutions of Mathieu's equation." *Progress of Theoretical and Experimental Physics*, **2020**(4), 04 2020. 043A01.

[DB00] M. Drewsen and A. Brøner. "Harmonic linear Paul trap: Stability diagram and effective potentials." *Phys. Rev. A*, **62**:045401, Sep 2000.

[DBB99] B. DeMarco, J. L. Bohn, J. P. Burke, M. Holland, and D. S. Jin. "Measurement of p-Wave Threshold Law Using Evaporatively Cooled Fermionic Atoms." *Phys. Rev. Lett.*, **82**:4208–4211, May 1999.

[DeM02] D. DeMille. "Quantum Computation with Trapped Polar Molecules." *Phys. Rev. Lett.*, **88**:067901, Jan 2002.

[Der01] Andrei Derevianko. "Feasibility of Cooling and Trapping Metastable Alkaline-Earth Atoms." *Phys. Rev. Lett.*, **87**:023002, Jun 2001.

[DFG87] J. M. Dyke, M. Feher, B. W. J. Gravenor, and A. Morris. "High-temperature photoelectron spectroscopy: a study of the alkaline earth oxides strontium oxide and barium oxide." *The Journal of Physical Chemistry*, **91**(17):4476–4481, 1987.

[DFK96] Va A Dzuba, Vv V Flambaum, and Mg G Kozlov. "Combination of the many-body perturbation theory with the configuration-interaction method." *Phys. Rev. A*, **54**(5):3948–3959, nov 1996.

[DFN16] John M Doyle, Bretislav Friedrich, and Edvardas Narevicius. "Physics and chemistry with cold molecules." *ChemPhysChem*, **17**(22):3581–3582, 2016.

[DK11] Andrei Derevianko and Hidetoshi Katori. "Colloquium: Physics of optical lattice clocks." *Rev. Mod. Phys.*, **83**(2):331–348, may 2011.

[DKW11] Olivier Dulieu, Roman Krems, Matthias Weidemüller, and Stefan Willitsch. "Physics and chemistry of cold molecules." *Physical Chemistry Chemical Physics*, **13**(42):18703–18704, 2011.

[DMW58] Alexander Dalgarno, MR C McDowell, and Alan Williams. "The mobilities of ions in unlike gases." *Philosophical Transactions of the Royal Society of London. Series A, Mathematical and Physical Sciences*, **250**(982):411–425, 1958.

[DP11] Andrei Derevianko and Sergey G Porsev. "Accurate evaluation of parameters of optical lattice clocks." In Ennio Arimondo, Paul R Berman, and Chun C Lin, editors, *Advances in Atomic, Molecular, and Optical Physics*, volume 60, pp. 415–459. Academic Press, 2011.

[DPG15] E. A. Dijck, M. Nuñez Portela, A. T. Grier, K. Jungmann, A. Mohanty, N. Valappol, and L. Willmann. "Determination of transition frequencies in a single $^{138}Ba^{+}$ ion." *Phys. Rev. A*, **91**:060501, Jun 2015.

[DSL93] H Floyd Davis, Arthur G Suits, Yuan T Lee, Christian Alcaraz, and Jean-Michel Mestdagh. "State specific reactions of Ba (1 S 0) and Ba (1 D 2) with water and methanol." *The Journal of chemical physics*, **98**(12):9595–9609, 1993.

[DSL05] Carsten Degenhardt, Hardo Stoehr, Christian Lisdat, Guido Wilpers, Harald Schnatz, Burghard Lipphardt, Tatiana Nazarova, Paul-Eric Pottie, Uwe Sterr, Jürgen Helmcke, and Fritz Riehle. "Calcium optical frequency standard with ultracold atoms: Approaching 10^{-15} relative uncertainty." *Phys. Rev. A*, **72**:062111, Dec 2005.

[DTS15] Katrin Dulitz, Atreju Tauschinsky, and Timothy P Softley. "Zeeman deceleration of electron-impact-excited metastable helium atoms." *New Journal of Physics*, **17**(3):035005, 2015.

[Dua04] L-M Duan. "Scaling ion trap quantum computation through fast quantum gates." *Physical review letters*, **93**(10):100502, 2004.

[DXW10] Wenrui Dong, Chunlei Xiao, Tao Wang, Dongxu Dai, Xueming Yang, and Dong H Zhang. "Transition-state spectroscopy of partial wave resonances in the F+ HD reaction." *Science*, **327**(5972):1501–1502, 2010.

[Ear48] S. Earnshaw. "On the Nature of the Molecular Forces which Regulate the Constitution of the Luminiferous Ether." *Transactions of the Cambridge Philosophical Society*, **7**:97, January 1848.

[EDP16] Pascal Eberle, Alexander D Dörfler, Claudio von Planta, Krishnamurthy Ravi, and Stefan Willitsch. "A dynamic ion-atom hybrid trap for high-resolution cold-collision studies." *ChemPhysChem*, **17**(22):3769–3775, 2016.

[EDV15] Pascal Eberle, Alexander D Dörfler, Claudio Von Planta, Krishnamurthy Ravi, Dominik Haas, Dong Zhang, Sebastiaan YT van de Meerakker, and Stefan Willitsch. "Ion-atom and ion-molecule hybrid systems: Ion-neutral chemistry at ultralow energies." In *Journal of Physics: Conference Series*, volume 635, p. 012012. IOP Publishing, 2015.

[FCS94] Jerome Faist, Federico Capasso, Deborah L. Sivco, Carlo Sirtori, Albert L. Hutchinson, and Alfred Y. Cho. "Quantum Cascade Laser." *Science*, **264**(5158):553–556, 1994.

[FDH85] W. Federer, W. Dobler, F. Howorka, W. Lindinger, M. Durup-Ferguson, and E. E. Ferguson. "Collisional relaxation of vibrationally excited NO+(v) ions." *The Journal of Chemical Physics*, **83**(3):1032–1038, 1985.

[FFF05] C.J. Foot, D.P.C.J. Foot, and C.J.F. Foot. *Atomic Physics*. Oxford Master Series in Physics. OUP Oxford, 2005.

[FFS69] E.E. Ferguson, F.C. Fehsenfeld, and A.L. Schmeltekopf. "Flowing Afterglow Measurements of Ion-Neutral Reactions." *Advances in Atomic and Molecular Physics*, **5**:1 – 56, 1969.

[FGP14] HA Fürst, Michael H Goerz, UG Poschinger, M Murphy, Simone Montangero, Tommaso Calarco, F Schmidt-Kaler, K Singer, and Christiane P Koch. "Controlling the transport of an ion: classical and quantum mechanical solutions." *New Journal of Physics*, **16**(7):075007, 2014.

[FHW19] M. Fan, C. A. Holliman, A. L. Wang, and A. M. Jayich. "Laser Cooling of Radium Ions." *Phys. Rev. Lett.*, **122**:223001, Jun 2019.

[FKB99] R. C. Forrey, V. Kharchenko, N. Balakrishnan, and A. Dalgarno. "Vibrational relaxation of trapped molecules." *Phys. Rev. A*, **59**:2146–2152, Mar 1999.

[FT03] C. F. Fischer and G. Tachiev. "Allowed and spin-forbidden electric dipole transitions in Ca I." *Phys. Rev. A*, **68**:012507, 2003.

[FTS09] MJ Frisch, GW Trucks, HB Schlegel, GE Scuseria, MA Robb, JR Cheeseman, G Scalmani, V Barone, B Mennucci, GA Petersson, et al. "Gaussian 09, rev. D. 01." *Gaussian Inc., Wallingford CT*, 2009.

[GCO09] Andrew T Grier, Marko Cetina, Fedja Oručević, and Vladan Vuletić. "Observation of cold collisions between trapped ions and trapped atoms." *Physical review letters*, **102**(22):223201, 2009.

[GCV13] J. E. Goeders, C. R. Clark, G. Vittorini, K. Wright, C. R. Viteri, and K. R. Brown. "Identifying Single Molecular Ions by Resolved Sideband Measurements." *The Journal of Physical Chemistry*, **117**(39):9725–9731, 2013.

[GG98] SD Gensemer and PL Gould. "Ultracold collisions observed in real time." *Physical review letters*, **80**(5):936, 1998.

[GH01] J. Grünert and A. Hemmerich. "Optimizing the production of metastable calcium atoms in a magneto-optical trap." *Applied Physics B*, **73**(8):815–818, 2001.

[GJS07] Shaun P Green, Cameron Jones, and Andreas Stasch. "Stable magnesium (I) compounds with Mg-Mg bonds." *Science*, **318**(5857):1754–1757, 2007.

[GLB08] H. Ghalila, S. Lahmar, Z. Ben Lakhdar, and M. Hochlaf. "Spectroscopy and metastability of BeO^+." *J. Phys. B: At. Mol. Opt. Phys.*, **41**(20):205101, oct 2008.

[GLS03] Richard L Gross, Xianghong Liu, and Arthur G Suits. "O (3P) versus O (1D) reaction dynamics with n-pentane: a crossed-beam imaging study." *Chemical physics letters*, **376**(5-6):710–716, 2003.

[GMG12] Koos B Gubbels, Sebastiaan YT van de Meerakker, Gerrit C Groenenboom, Gerard Meijer, and Ad van der Avoird. "Scattering resonances in slow NH3–He collisions." *The Journal of Chemical Physics*, **136**(7):074301, 2012.

[Goe13] J. E. Goeders. *Resolved Sideband Spectroscopy for the Detection of Weak Optical Transitions*. PhD thesis, Georgia Institute of Technology, 2013. Unpublished PhD thesis.

[GP89] Alan Gallagher and David E Pritchard. "Exoergic collisions of cold Na*-Na." *Physical review letters*, **63**(9):957, 1989.

[GTL16] J. P. Gaebler, T. R. Tan, Y. Lin, Y. Wan, R. Bowler, A. C. Keith, S. Glancy, K. Coakley, E. Knill, D. Leibfried, and D. J. Wineland. "High-Fidelity Universal Gate Set for $^{9}Be^{+}$ Ion Qubits." *Phys. Rev. Lett.*, **117**:060505, Aug 2016.

[GYN00] C. W. Gardiner, J. Ye, H. C. Nagerl, and H. J. Kimble. "Evaluation of heating effects on atoms trapped in an optical trap." *Phys. Rev. A*, **61**:045801, Mar 2000.

[GZC03] Juan José García-Ripoll, Peter Zoller, and J Ignacio Cirac. "Speed optimized two-qubit gates with laser coherent control techniques for ion trap quantum computing." *Physical Review Letters*, **91**(15):157901, 2003.

[HAB14] T. P. Harty, D. T. C. Allcock, C. J. Ballance, L. Guidoni, H. A. Janacek, N. M. Linke, D. N. Stacey, and D. M. Lucas. "High-Fidelity Preparation, Gates, Memory, and Readout of a Trapped-Ion Quantum Bit." *Phys. Rev. Lett.*, **113**:220501, Nov 2014.

[HAR13] Felix HJ Hall, Mireille Aymar, Maurice Raoult, Olivier Dulieu, and Stefan Willitsch. "Light-assisted cold chemical reactions of barium ions with rubidium atoms." *Molecular Physics*, **111**(12-13):1683–1690, 2013.

[HBC14] Mounia Hocine, N Balakrishnan, Theodore Colton, Brian Everitt, Walter Piegorsch, Fabrizio Ruggeri, and Jozef Teugels. *Wiley statsref: Statistics reference online*. John Wiley & Sons, Ltd, 2014.

[HC18] Eric R. Hudson and Wesley C. Campbell. "Dipolar quantum logic for freely rotating trapped molecular ions." *Phys. Rev. A*, **98**:040302, Oct 2018.

[HC20] Eric R Hudson and Wesley C Campbell. "Laserless quantum gates for electric dipoles in thermal motion." *arXiv preprint arXiv:2011.08330*, 2020.

[Hea] M. Heaven. private communication.

[Her50] Gerhard Herzberg. *Molecular spectra and molecular structure. Vol.1: Spectra of diatomic molecules*. D. Van Nostrand Company, Inc., 1950.

[HGS12] Alon B Henson, Sasha Gersten, Yuval Shagam, Julia Narevicius, and Edvardas Narevicius. "Observation of resonances in Penning ionization reactions at sub-kelvin temperatures in merged beams." *Science*, **338**(6104):234–238, 2012.

[HH14] Arne Härter and J Hecker Denschlag. "Cold atom–ion experiments in hybrid traps." *Contemporary Physics*, **55**(1):33–45, 2014.

[HHF13] Shinsuke Haze, Sousuke Hata, Munekazu Fujinaga, and Takashi Mukaiyama. "Observation of elastic collisions between lithium atoms and calcium ions." *Physical Review A*, **87**(5):052715, 2013.

[HJH15] P. Hamilton, M. Jaffe, P. Haslinger, Q. Simmons, H. Müller, and J. Khoury. "Atom-interferometry constraints on dark energy." *Science*, **349**(6250):849–851, 2015.

[HLC15] Daniel Hauser, Seunghyun Lee, Fabio Carelli, Steffen Spieler, Olga Lakhmanskaya, Eric S. Endres, Sunil S. Kumar, Franco Gianturco, and Roland Wester. "Rotational state-changing cold collisions of hydroxyl ions with helium." *Nature Physics*, **11**(6):467–470, Jun 2015.

[HLH99] J. E. Hansen, C. Laughlin, H. W van der Hart, and G. Verbockhaven. "Energy levels, wavefunction compositions and electric dipole transitions in neutral Ca." *J. Phys. B: At. Mol. Opt. Phys.*, **32**:2099, 1999.

[Hol73] Alexander Semenovich Holevo. "Bounds for the quantity of information transmitted by a quantum communication channel." *Problemy Peredachi Informatsii*, **9**(3):3–11, 1973.

[HP86] L. R. Hunter and S. K. Peck. "Precision atomic lifetime measurements using collisionally induced coherence transfer." *Phys. Rev. A*, **33**:4452–4455, Jun 1986.

[HR86] David Husain and Gareth Roberts. "Energy pooling from Ca[4s4p(3P)] and Ca[4s3d(1D2)] studied by time-resolved atomic emission following pulsed dye-laser excitation." *J. Chem. Soc., Faraday Trans. 2*, **82**:1921–1933, 1986.

[HS91] M Hawley and MA Smith. "Gas phase collisional quenching of NO+ (v= 1) ions below 5 K." *The Journal of chemical physics*, **95**(11):8662–8664, 1991.

[HTS06] Eric R Hudson, Christopher Ticknor, Brian C Sawyer, Craig A Taatjes, Heather J Lewandowski, Jason R Bochinski, John L Bohn, and Jun Ye. "Production of cold formaldehyde molecules for study and control of chemical reaction dynamics with hydroxyl radicals." *Phys. Rev. A*, **73**(6):063404, 2006.

[Hud09] Eric R. Hudson. "Method for producing ultracold molecular ions." *Phys. Rev. A*, **79**:032716, Mar 2009.

[Hud16] Eric R Hudson. "Sympathetic cooling of molecular ions with ultracold atoms." *EPJ Techniques and Instrumentation*, **3**:1–21, 2016.

[Hun75] L. W. Hunter. "On infinite order sudden approximations for an arbitrary potential energy." *J. Chem. Phys.*, **62**(7):2855–2859, 1975.

[HVK14] A. K. Hansen, O. O. Versolato, Ł Kłosowski, S. B. Kristensen, A. Gingell, M. Schwarz, A. Windberger, J. Ullrich, J. R. Crespo López-Urrutia, and M. Drewsen. "Efficient rotational cooling of Coulomb-crystallized molecular ions by a helium buffer gas." *Nature*, **508**(7494):76–79, Apr 2014.

[HW12] Felix HJ Hall and Stefan Willitsch. "Millikelvin reactive collisions between sympathetically cooled molecular ions and laser-cooled atoms in an ion-atom hybrid trap." *Physical review letters*, **109**(23):233202, 2012.

[HWS01] C. J. Hawthorn, K. P. Weber, and R. E. Scholten. "Littrow configuration tunable external cavity diode laser with fixed direction output beam." *Review of Scientific Instruments*, **72**(12):4477–4479, 2001.

[HWW85] L. R. Hunter, G. M. Watson, D. S. Weiss, and A. G. Zajonc. "High-precision measurement of lifetimes and collisional decay parameters in Ca ^{1}D states using the two-photon Hanle effect." *Phys. Rev. A*, **31**:2268–2278, Apr 1985.

[HYH08] David Hucul, M Yeo, Winfried K. Hensinger, James Rabchuk, Steven Olmschenk, and Christopher Monroe. "On the transport of atomic ions in linear and multidimensional ion trap arrays." *Quantum Information and Computing*, **8**(6):0501–0578, 2008.

[Inc] Wolfram Research, Inc. "Mathematica, Version 12.1." Champaign, IL, 2020.

[IOG10] Nick Indriolo, Takeshi Oka, TR Geballe, and Benjamin J McCall. "Constraining the environment of CH+ formation with CH+ 3 observations." *The Astrophysical Journal*, **711**(2):1338, 2010.

[JBT09] M. Johanning, A. Braun, N. Timoney, V. Elman, W. Neuhauser, and Chr. Wunderlich. "Individual Addressing of Trapped Ions and Coupling of Motional and Spin States Using rf Radiation." *Phys. Rev. Lett.*, **102**(7):073004, February 2009.

[JJ07] D F James and J Jerke. "Effective Hamiltonian theory and its applications in quantum information." *Canadian Journal of Physics*, **85**(6):625–632, 2007.

[JM89] Paul S Julienne and Frederick H Mies. "Collisions of ultracold trapped atoms." *JOSA B*, **6**(11):2257–2269, 1989.

[JTL06] Kevin M. Jones, Eite Tiesinga, Paul D. Lett, and Paul S. Julienne. "Ultracold photoassociation spectroscopy: Long-range molecules and atomic scattering." *Rev. Mod. Phys.*, **78**:483–535, May 2006.

[KH17] Ivan Kozyryev and Nicholas R. Hutzler. "Precision Measurement of Time-Reversal Symmetry Violation with Laser-Cooled Polyatomic Molecules." *Phys. Rev. Lett.*, **119**:133002, Sep 2017.

[KLL13] H. Khalil, F. Le Quéré, C. Léonard, and V. Brites. "Theoretical Investigations on CaO Ions: Vibronic States and Photoelectron Spectroscopy." *The Journal of Physical Chemistry A*, **117**(44):11254–11260, 2013.

[Kos64] H. Köstlin. "Evidence for sympathetic vibrational cooling of translationally cold molecules." *Z. Phys.*, **178**:200, 1964.

[Kou79] Donald Jack Kouri. *Rotational Excitation II: Approximation Methods*, pp. 301–358. Springer US, Boston, MA, 1979.

[KPB15] J Keller, HL Partner, T Burgermeister, and TE Mehlstäubler. "Precise determination of micromotion for trapped-ion optical clocks." *Journal of Applied Physics*, **118**(10):104501, 2015.

[KPS12] A. Khromova, Ch. Piltz, B. Scharfenberger, T. F. Gloger, M. Johanning, A. F. Varón, and Ch. Wunderlich. "Designer Spin Pseudomolecule Implemented with Trapped Ions in a Magnetic Gradient." *Phys. Rev. Lett.*, **108**(22):220502, June 2012.

[KPS15] M G Kozlov, S G Porsev, M S Safronova, and I I Tupitsyn. "CI-MBPT: A package of programs for relativistic atomic calculations based on a method combining configuration interaction and many-body perturbation theory." *Comput. Phys. Commun.*, **195**:199–213, 2015.

[KRR16] A Kramida, Yu. Ralchenko, J Reader, and NIST ASD Team. "NIST Atomic Spectra Database (version 5.4).", 2016.

[KS92] T. Kurosu and F. Shimizu. "Laser cooling and trapping of alkaline earth atoms." *Jpn. J. Appl. Phys.*, **31**:908, 1992.

[KS05] Peter Karbach and Joachim Stolze. "Spin chains as perfect quantum state mirrors." *Phys. Rev. A*, **72**:030301, Sep 2005.

[KSS17] Ayelet Klein, Yuval Shagam, Wojciech Skomorowski, Piotr S Żuchowski, Mariusz Pawlak, Liesbeth MC Janssen, Nimrod Moiseyev, Sebastiaan YT van de Meerakker, Ad van der Avoird, Christiane P Koch, et al. "Directly probing anisotropy in atom–molecule collisions through quantum scattering resonances." *Nature Physics*, **13**(1):35–38, 2017.

[KTL16] Adam M. Kaufman, M. Eric Tai, Alexander Lukin, Matthew Rispoli, Robert Schittko, Philipp M. Preiss, and Markus Greiner. "Quantum thermalization through entanglement in an isolated many-body system." *Science*, **353**(6301):794–800, 2016.

[KWM98] B. E. King, C. S. Wood, C. J. Myatt, Q. A. Turchette, D. Leibfried, W. M. Itano, C. Monroe, and D. J. Wineland. "Cooling the Collective Motion of Trapped Ions to Initialize a Quantum Register." *Phys. Rev. Lett.*, **81**:1525–1528, Aug 1998.

[KWS12] Moritz Kirste, Xingan Wang, H Christian Schewe, Gerard Meijer, Kopin Liu, Ad van der Avoird, Liesbeth MC Janssen, Koos B Gubbels, Gerrit C Groenenboom, and Sebastiaan YT van de Meerakker. "Quantum-state resolved bimolecular collisions of velocity-controlled OH with NO radicals." *Science*, **338**(6110):1060–1063, 2012.

[KWS15] Jongjin B Kim, Marissa L Weichman, Tobias F Sjolander, Daniel M Neumark, Jacek Kłos, Millard H Alexander, and David E Manolopoulos. "Spectroscopic observation of resonances in the F+ H2 reaction." *Science*, **349**(6247):510–513, 2015.

[Lan05] MP Langevin. "A fundamental the kinetic formula." In *Annals of Chemistry and Physics, Series*, volume 5, pp. 245–288, 1905.

[LBS03] F Y Loo, A Brusch, S Sauge, M Allegrini, E Arimondo, N Andersen, and J W Thomsen. "Investigations of a two-level atom in a magneto-optical trap using magnesium." *Journal of Optics B: Quantum and Semiclassical Optics*, **6**(1):81–85, nov 2003.

[LBY15] Andrew D. Ludlow, Martin M. Boyd, Jun Ye, E. Peik, and P. O. Schmidt. "Optical atomic clocks." *Rev. Mod. Phys.*, **87**:637–701, Jun 2015.

[Le] R. J. Le Roy. Le Roy R J 2002 LEVEL 7.2, University of Waterloo, Chemical Physics Research Report CP-642.

[LH87] L. P. Lellouch and L. R. Hunter. "Measurement of the 4s4p 'P-4s3d 'D spontaneous emission rate in calcium by use of a Stark-electric-quadrupole interference." *Phys. Rev. A*, **36**:3490, 1987.

[LH96] C. Laughlin and J. E. Hansen. "An accurate model-potential description of the valence spectrum of Ca." *J. Phys. B: At. Mol. Opt. Phys.*, **29**:L441, 1996.

[LKG10] T. Larbi, F. Khadri, H. Ghalila, S. Lahmar, and M. Hochlaf. "Theoretical spectroscopy and metastability of BeS and its cation." *Chemical Physics*, **373**(3):193 – 202, 2010.

[LML69] YT Lee, JD McDonald, PR LeBreton, and DR Herschbach. "Molecular beam reactive scattering apparatus with electron bombardment detector." *Review of Scientific Instruments*, **40**(11):1402–1408, 1969.

[LMP19] Ming Li, Michael Mills, Prateek Puri, Alexander Petrov, Eric R Hudson, and Svetlana Kotochigova. "Excitation-assisted nonadiabatic charge-transfer reaction in a mixed atom-ion system." *Physical Review A*, **99**(6):062706, 2019.

[LW70] W. C. Lineberger and Benjamin W. Woodward. "High Resolution Photodetachment of S^- Near Threshold." *Phys. Rev. Lett.*, **25**:424–427, Aug 1970.

[LWS08] F. Lang, K. Winkler, C. Strauss, R. Grimm, and J. Hecker Denschlag. "Ultracold Triplet Molecules in the Rovibrational Ground State." *Phys. Rev. Lett.*, **101**:133005, Sep 2008.

[LWY17] Francois Lique, Stefan Willitsch, Jun Ye, Ian Sims, Astrid Bergeat, Andrey Vilesov, Maxence Lepers, Christiane Koch, Goulven Quemener, Timur Tscherbul, et al. *Cold chemistry: molecular scattering and reactivity near absolute zero*. Royal Society of Chemistry, 2017.

[MBH06] C Matei, L Buchmann, WR Hannes, DA Hutcheon, C Ruiz, CR Brune, J Caggiano, AA Chen, J D'Auria, A Laird, et al. "Measurement of the Cascade Transition via the First Excited State of O 16 in the C 12 (α, γ) O 16 Reaction, and Its S Factor in Stellar Helium Burning." *Phys. Rev. Lett.*, **97**(24):242503, 2006.

[MBH09] Jeremy M. Merritt, Vladimir E. Bondybey, and Michael C. Heaven. "Spectroscopy, Structure, and Ionization Energy of BeOBe." *The Journal of Physical Chemistry A*, **113**(47):13300–13309, 2009. PMID: 19921943.

[MBM16] Karan K. Mehta, Colin D. Bruzewicz, Robert McConnell, Rajeev J. Ram, Jeremy M. Sage, and John Chiaverini. "Integrated optical addressing of an ion qubit." *Nature Nanotechnology*, **11**(12):1066–1070, Dec 2016.

[MC31] Robert S. Mulliken and Andrew Christy. "Λ-Type Doubling and Electron Configurations in Diatomic Molecules." *Phys. Rev.*, **38**:87–119, Jul 1931.

[MHY11] A Maatouk, A Ben Houria, O Yazidi, N Jaidane, and M Hochlaf. "Theoretical investigations of the MgO^+ cation: spectroscopy, spin–orbit coupling and single ionization spectrum." *Journal of Physics B: Atomic, Molecular and Optical Physics*, **44**(22):225101, oct 2011.

[Mie73] FH Mies. "Molecular theory of atomic collisions: Fine-structure transitions." *Physical Review A*, **7**(3):942, 1973.

[Mit93] J. Mitroy. "Energy levels and oscillator strengths for neutral calcium." *J. Phys. B: At. Mol. Opt. Phys. 361*, **26**:3703, 1993.

[Mor04] Donald C. Morton. "Erratum: "Atomic Data for Resonance Absorption Lines. III. Wavelengths Longward of the Lyman Limit for the Elements Hydrogen to Gallium" (ApJS, 149, 205 [2003])." *Astrophys. J. Suppl. Ser.*, **151**(2):403, 2004.

[MPY17] Michael Mills, Prateek Puri, Yanmei Yu, Andrei Derevianko, Christian Schneider, and Eric R. Hudson. "Efficient repumping of a Ca magneto-optical trap." *Phys. Rev. A*, **96**:033402, Sep 2017.

[MRJ15] Dmytro Mulin, Štěpán Roučka, Pavol Jusko, Illia Zymak, Radek Plašil, Dieter Gerlich, Roland Wester, and Juraj Glosík. "H/D exchange in reactions of OH- with D 2 and of OD- with H 2 at low temperatures." *Physical Chemistry Chemical Physics*, **17**(14):8732–8739, 2015.

[MS99] Klaus Mølmer and Anders Sørensen. "Multiparticle Entanglement of Hot Trapped Ions." *Phys. Rev. Lett.*, **82**:1835–1838, Mar 1999.

[MS07] Harold J Metcalf and Peter Van der Straten. "Laser cooling and trapping of neutral atoms." *The Optics Encyclopedia: Basic Foundations and Practical Applications*, 2007.

[MSA99] Murray J McEwan, Graham BI Scott, Nigel G Adams, Lucia M Babcock, R Terzieva, and Eric Herbst. "New H and H2 reactions with small hydrocarbon ions and their roles in benzene synthesis in dense interstellar clouds." *The Astrophysical Journal*, **513**(1):287, 1999.

[MTR01] Mohammadou Mérawa, Claire Tendero, and Michel Rérat. "Excited states dipole polarizabilities of calcium atom and long-range dispersion coefficients for the low-lying electronic states of Ca2 and CaMg." *Chemical physics letters*, **343**(3-4):397–403, 2001.

[MW01] Florian Mintert and Christof Wunderlich. "Ion-Trap Quantum Logic Using Long-Wavelength Radiation." *Phys. Rev. Lett.*, **87**(25):257904, November 2001.

[MWR20] Michael Mills, Hao Wu, Evan C Reed, Lu Qi, Kenneth R Brown, Christian Schneider, Michael C Heaven, Wesley C Campbell, and Eric R Hudson. "Dipole–phonon quantum logic with alkaline-earth monoxide and monosulfide cations." *Physical Chemistry Chemical Physics*, **22**(43):24964–24973, 2020.

[MZ08] James Mitroy and J-Y Zhang. "Properties and long range interactions of the calcium atom." *The Journal of chemical physics*, **128**(13):134305, 2008.

[MZM20] Karan K. Mehta, Chi Zhang, Maciej Malinowski, Thanh-Long Nguyen, Martin Stadler, and Jonathan P. Home. "Integrated optical multi-ion quantum logic." *arXiv preprint arXiv:2002.02258*, 2020.

[NC15] Masayoshi Nakano and Benoît Champagne. "Theoretical design of open-shell singlet molecular systems for nonlinear optics." *The Journal of Physical Chemistry Letters*, **6**(16):3236–3256, 2015.

[NLA85] D. M. Neumark, K. R. Lykke, T. Andersen, and W. C. Lineberger. "Laser photodetachment measurement of the electron affinity of atomic oxygen." *Phys. Rev. A*, **32**:1890–1892, Sep 1985.

[NOW10] K-K Ni, S Ospelkaus, D Wang, G Quéméner, B Neyenhuis, MHG De Miranda, JL Bohn, J Ye, and DS Jin. "Dipolar collisions of polar molecules in the quantum regime." *Nature*, **464**(7293):1324, 2010.

[NSG02] Stéphane Noury, Bernard Silvi, and Ronald J. Gillespie. "Chemical Bonding in Hypervalent Molecules: Is the Octet Rule Relevant?" *Inorganic Chemistry*, **41**(8):2164–2172, 2002. PMID: 11952370.

[OBF99] C. W. Oates, F. Bondu, R. W. Fox, and L. Hollberg. "A diode-laser optical frequency standard based on laser-cooled Ca atoms: Sub-kilohertz spectroscopy by optical shelving detection." *The European Physical Journal D - Atomic, Molecular, Optical and Plasma Physics*, **7**(3):449–460, Oct 1999.

[OBH12] James M Oldham, Martin T Bell, Lee D Harper, and Timothy P Softley. "Cold Ion-Molecule Chemistry with a Stark Decelerator Beamline." *mss*, p. FD02, 2012.

[OBS11] Bojana Ostojić, PR Bunker, P Schwerdtfeger, B Assadollahzadeh, and Per Jensen. "The predicted spectrum of the hypermetallic molecule MgOMg." *Physical Chemistry Chemical Physics*, **13**(16):7546–7553, 2011.

[OBS12] Bojana Ostojić, PR Bunker, P Schwerdtfeger, Artur Gertych, and Per Jensen. "The predicted infrared spectrum of the hypermetallic molecule CaOCa in its lowest two electronic states X $1\Sigma g+$ and a $3\Sigma u+$." *Journal of molecular structure*, **1023**:101–107, 2012.

[OJS13] B Ostojic, Per Jensen, P Schwerdtfeger, and PR Bunker. "The predicted spectrum and singlet–triplet interaction of the hypermetallic molecule SrOSr." *The Journal of Physical Chemistry A*, **117**(39):9370–9379, 2013.

[OLA08] C. Ospelkaus, C. E. Langer, J. M. Amini, K. R. Brown, D. Leibfried, and D. J. Wineland. "Trapped-Ion Quantum Logic Gates Based on Oscillating Magnetic Fields." *Phys. Rev. Lett.*, **101**:090502, Aug 2008.

[ONW10] S Ospelkaus, K-K Ni, D Wang, MHG De Miranda, B Neyenhuis, G Quéméner, PS Julienne, JL Bohn, DS Jin, and J Ye. "Quantum-state controlled chemical reactions of ultracold potassium-rubidium molecules." *Science*, **327**(5967):853–857, 2010.

[Osw15] R Oswald. *Velocity control of trapped ions for transport quantum logic gates*. PhD thesis, M. Sc. thesis, Swiss Federal Institute of Technology Zurich, 2015.

[OWC11] C. Ospelkaus, U. Warring, Y. Colombe, K. R. Brown, J. M. Amini, D. Leibfried, and D. J. Wineland. "Microwave quantum logic gates for trapped ions." *Nature*, **476**(7359):181–184, August 2011.

[OYM07] S. Olmschenk, K. C. Younge, D. L. Moehring, D. N. Matsukevich, P. Maunz, and C. Monroe. "Manipulation and detection of a trapped Yb^+ hyperfine qubit." *Phys. Rev. A*, **76**:052314, Nov 2007.

[OZW06] A. Ostendorf, C. B. Zhang, M. A. Wilson, D. Offenberg, B. Roth, and S. Schiller. "Sympathetic Cooling of Complex Molecular Ions to Millikelvin Temperatures." *Phys. Rev. Lett.*, **97**:243005, Dec 2006.

[Pac74] Russell T Pack. "Space-fixed vs body-fixed axes in atom-diatomic molecule scattering. Sudden approximations." *J. Chem. Phys.*, **60**(2):633–639, 1974.

[Pau90] Wolfgang Paul. "Electromagnetic traps for charged and neutral particles." *Rev. Mod. Phys.*, **62**:531–540, Jul 1990.

[PD12] Gregers Poulsen and Michael Drewsen. "Adiabatic cooling of a single trapped ion." *arXiv preprint arXiv:1210.4309*, 2012.

[PDF20] JM Pino, JM Dreiling, C Figgatt, JP Gaebler, SA Moses, CH Baldwin, M Foss-Feig, D Hayes, K Mayer, C Ryan-Anderson, et al. "Demonstration of the QCCD trapped-ion quantum computer architecture." *arXiv preprint arXiv:2003.01293*, 2020.

[PFL09] LP Parazzoli, N Fitch, DS Lobser, and HJ Lewandowski. "High-energy-resolution molecular beams for cold collision studies." *New Journal of Physics*, **11**(5):055031, 2009.

[PKR01] S. G. Porsev, M. G. Kozlov, Yu. G. Rakhlina, and A. Derevianko. "Many-body calculations of electric-dipole amplitudes for transitions between low-lying levels of Mg, Ca, and Sr." *Phys. Rev. A*, **64**:012508, 2001.

[PL65] Philip Pechukas and John C Light. "On detailed balancing and statistical theories of chemical kinetics." *The Journal of Chemical Physics*, **42**(9):3281–3291, 1965.

[PLB86] Harry Partridge, Stephen R. Langhoff, and Charles W. Bauschlicher. "Ab initio calculations on the positive ions of the alkaline-earth oxides, fluorides, and hydroxides." *The Journal of Chemical Physics*, **84**(8):4489–4496, 1986.

[PLR66] Philip Pechukas, John C Light, and Charles Rankin. "Statistical Theory of Chemical Kinetics: Application to Neutral-Atom—Molecule Reactions." *The Journal of Chemical Physics*, **44**(2):794–805, 1966.

[PMS17] Prateek Puri, Michael Mills, Christian Schneider, Ionel Simbotin, John A Montgomery, Robin Côté, Arthur G Suits, and Eric R Hudson. "Synthesis of mixed hypermetallic oxide BaOCa+ from laser-cooled reagents in an atom-ion hybrid trap." *Science*, **357**(6358):1370–1375, 2017.

[PMS18] Prateek Puri, Michael Mills, Ionel Simbotin, John A. Montgomery, Robin Côté, Elizabeth P. West, Christian R. Schneider, Arthur G. Suits, and Eric R. Hudson. "Radiative suppression of charged-neutral photochemistry at low collision energy." *to be published*, 2018.

[PMW18] Prateek Puri, Michael Mills, Elizabeth P West, Christian Schneider, and Eric R Hudson. "High-resolution collision energy control through ion position modulation in atom-ion hybrid systems." *Review of Scientific Instruments*, **89**(8):083112, 2018.

[Pop75] RP Poplavskiĭ. "Thermodynamic models of information processes." *Soviet Physics Uspekhi*, **18**(3):222, 1975.

[PRT76] W. H. Parkinson, E. M. Reeves, and F. S. Tomkinst. "Neutral calcium. strontium and barium : determination of f values of the principal series by the hook method." *J. Phys. B: Atom. Molec. Phys.*, **9**:157, 1976.

[Pur19] Prateek Puri. *Sympathetically-cooled quantum chemical dynamics and progress towards a technique for internal state readout of a molecular ion.* PhD thesis, University of California, Los Angeles, 2019.

[Rad61] H. E. Radford. "Microwave Zeeman Effect of Free Hydroxyl Radicals." *Phys. Rev.*, **122**:114–130, Apr 1961.

[RDM84] B. R. Rowe, G. Dupeyrat, J. B. Marquette, and P. Gaucherel. "Study of the reactions N+2+2N2→N+4+N2 and O+2+2O2→O+4+O2 from 20 to 160 K by the CRESU technique." *The Journal of Chemical Physics*, **80**(10):4915–4921, 1984.

[RGM10] V Sivaranjana Reddy, S Ghanta, and S Mahapatra. "First principles quantum dynamical investigation provides evidence for the role of polycyclic aromatic hydrocarbon radical cations in interstellar physics." *Physical review letters*, **104**(11):111102, 2010.

[RLB06] Rainer Reichle, D Leibfried, RB Blakestad, J Britton, John D Jost, E Knill, Christopher Langer, R Ozeri, Signe Seidelin, and David J Wineland. "Transport dynamics of single ions in segmented microstructured Paul trap arrays." *Fortschritte der Physik: Progress of Physics*, **54**(8-10):666–685, 2006.

[RP95] BR Rowe and DC Parent. "Techniques for the study of reaction kinetics at low temperatures: application to the atmospheric chemistry of Titan." *Planetary and Space Science*, **43**(1-2):105–114, 1995.

[RPC87] E. L. Raab, M. Prentiss, Alex Cable, Steven Chu, and D. E. Pritchard. "Trapping of Neutral Sodium Atoms with Radiation Pressure." *Phys. Rev. Lett.*, **59**:2631–2634, Dec 1987.

[RR27] Oscar Knefler Rice and Herman C Ramsperger. "Theories of unimolecular gas reactions at low pressures." *Journal of the American Chemical Society*, **49**(7):1617–1629, 1927.

[RSK11] Wade G Rellergert, Scott T Sullivan, Svetlana Kotochigova, Alexander Petrov, Kuang Chen, Steven J Schowalter, and Eric R Hudson. "Measurement of a Large Chemical Reaction Rate between Ultracold Closed-Shell Ca 40 Atoms and Open-Shell Yb+ 174 Ions Held in a Hybrid Atom-Ion Trap." *Physical review letters*, **107**(24):243201, 2011.

[RSS13] Wade G. Rellergert, Scott T. Sullivan, Steven J. Schowalter, Svetlana Kotochigova, Kuang Chen, and Eric R. Hudson. "Evidence for sympathetic vibrational cooling of translationally cold molecules." *Nature*, **495**(7442):490–494, Mar 2013.

[Rug16] R. Rugango. *Spectroscopy of Molecular Ions in Coulomb Crystals*. PhD thesis, Georgia Institute of Technology, 2016. Unpublished PhD thesis.

[RW17] I Rouse and S Willitsch. "Superstatistical energy distributions of an ion in an ultracold buffer gas." *Physical review letters*, **118**(14):143401, 2017.

[RZS12] Lothar Ratschbacher, Christoph Zipkes, Carlo Sias, and Michael Köhl. "Controlling chemical reactions of a single particle." *Nature Physics*, **8**(9):649–652, 2012.

[SB08] Theodore P. Snow and Veronica M. Bierbaum. "Ion Chemistry in the Interstellar Medium." *Annual Review of Analytical Chemistry*, **1**(1):229–259, 2008. PMID: 20636080.

[SBH12] J. Shen, A. Borodin, M. Hansen, and S. Schiller. "Observation of a rotational transition of trapped and sympathetically cooled molecular ions." *Phys. Rev. A*, **85**:032519, Mar 2012.

[SBS19] R. Srinivas, S. C. Burd, R. T. Sutherland, A. C. Wilson, D. J. Wineland, D. Leibfried, D. T. C. Allcock, and D. H. Slichter. "Trapped-Ion Spin-Motion Coupling with Microwaves and a Near-Motional Oscillating Magnetic Field Gradient." *Phys. Rev. Lett.*, **122**(16):163201, April 2019.

[SC85] Jack Sugar and Charles Corliss. "Atomic energy levels of the iron-period elements: potassium through nickel." Technical report, American Chemical Society, 1985.

[SCG04] Robin Santra, Kevin V Christ, and Chris H Greene. "Properties of metastable alkaline-earth-metal atoms calculated using an accurate effective core potential." *Physical Review A*, **69**(4):042510, 2004.

[Sch16] Steven J. Schowalter. *Action Spectroscopy of Molecular Ions and Studies of Cold Collsions in a Hybrid Atom-Ion Trap.* PhD thesis, University of California, Los Angeles, 2016.

[SCR12] Steven J. Schowalter, Kuang Chen, Wade G. Rellergert, Scott T. Sullivan, and Eric R. Hudson. "An integrated ion trap and time-of-flight mass spectrometer for chemical and photo- reaction dynamics studies." *Review of Scientific Instruments*, **83**(4):043103, 2012.

[SDC16] Steven J. Schowalter, Alexander J. Dunning, Kuang Chen, Prateek Puri, Christian Schneider, and Eric R. Hudson. "Blue-sky bifurcation of ion energies and the limits of neutral-gas sympathetic cooling of trapped ions." *Nature Communications*, **7**(1):12448, Aug 2016.

[SDS04] U. Sterr, C. Degenhardt, H. Stoehr, Ch. Lisdat, H. Schnatz, J. Helmcke, F. Riehle, G. Wilpers, Ch. Oates, and L. Hollberg. "The optical calcium frequency standards of PTB and NIST." *Comptes Rendus Physique*, **5**(8):845 – 855, 2004.

[Sec75] Don Secrest. "Theory of angular momentum decoupling approximations for rotational transitions in scattering." *J. Chem. Phys.*, **62**(2):710–719, 1975.

[SGM17] Philipp C Schmid, J Greenberg, MI Miller, K Loeffler, and Heather J Lewandowski. "An ion trap time-of-flight mass spectrometer with high mass resolution for cold trapped ion experiments." *Review of Scientific Instruments*, **88**(12):123107, 2017.

[SGT95] V. Sanchez-Villicana, S. D. Gensemer, K. Y. N. Tan, A. Kumarakrishnan, T. P. Dinneen, W. Süptitz, and P. L. Gould. "Suppression of Ultracold Ground-State Hyperfine-Changing Collisions with Laser Light." *Phys. Rev. Lett.*, **74**:4619–4622, Jun 1995.

[SHB09] F Splatt, M Harlander, M Brownnutt, F Zähringer, R Blatt, and W Hänsel. "Deterministic reordering of40Ca^+ions in a linear segmented Paul trap." *New Journal of Physics*, **11**(10):103008, oct 2009.

[SHD13] Molu Shi, PF Herskind, Michael Drewsen, and IL Chuang. "Microwave quantum logic spectroscopy and control of molecular ions." *New Journal of Physics*, **15**(11):113019, 2013.

[SHG16] Thierry Stoecklin, Philippe Halvick, Mohamed Achref Gannouni, Majdi Hochlaf, Svetlana Kotochigova, and Eric R. Hudson. "Explanation of efficient quenching of molecular ion vibrational motion by ultracold atoms." *Nature Communications*, **7**(1):11234, Apr 2016.

[Sho95] Peter W Shor. "Scheme for reducing decoherence in quantum computer memory." *Physical review A*, **52**(4):R2493, 1995.

[SHS10] Peter F. Staanum, Klaus Højbjerre, Peter S. Skyt, Anders K. Hansen, and Michael Drewsen. "Rotational laser cooling of vibrationally and translationally cold molecular ions." *Nature Physics*, **6**(4):271–274, Apr 2010.

[SJ02] I. M. Savukov and W. R. Johnson. "Combined configuration-interaction and many-body-perturbation-theory calculations of energy levels and transition amplitudes in Be, Mg, Ca, and Sr." *Phys. Rev. A*, **65**:042503, 2002.

[SK11] Kevin Sheridan and Matthias Keller. "Weighing of trapped ion crystals and its applications." *New Journal of Physics*, **13**(12):123002, dec 2011.

[SKS15] Yuval Shagam, Ayelet Klein, Wojciech Skomorowski, Renjie Yun, Vitali Averbukh, Christiane P Koch, and Edvardas Narevicius. "Molecular hydrogen interacts more strongly when rotationally excited at low temperatures leading to faster reactions." *Nature chemistry*, **7**(11):921–926, 2015.

[SLG16] Hongwei Song, Anyang Li, and Hua Guo. "Rotational and isotopic effects in the H2+ OH+ $\rightarrow$ H+ H2O+ reaction." *The Journal of Physical Chemistry A*, **120**(27):4742–4748, 2016.

[SM99] S. Schneider and G. J. Milburn. "Decoherence and fidelity in ion traps with fluctuating trap parameters." *Phys. Rev. A*, **59**:3766–3774, May 1999.

[SMB18] Tomas Sikorsky, Ziv Meir, Ruti Ben-Shlomi, Nitzan Akerman, and Roee Ozeri. "Spin-controlled atom–ion chemistry." *Nature communications*, **9**(1):1–5, 2018.

[SMD11] E. J. Salumbides, V. Maslinskas, I. M. Dildar, A. L. Wolf, E.-J. van Duijn, K. S. E. Eikema, and W. Ubachs. "High-precision frequency measurement of the 423-nm Ca i line." *Phys. Rev. A*, **83**:012502, Jan 2011.

[Smi88] G Smith. "Oscillator strengths for neutral calcium lines of 2.9 eV excitation." *J. Phys. B: At. Mol. Opt. Phys.*, **21**:2827, 1988.

[Smi92] David Smith. "The ion chemistry of interstellar clouds." *Chemical reviews*, **92**(7):1473–1485, 1992.

[SO75] G. Smith and J. A. O'Neill. "Absolute transition probabilities for some lines of neutral calcium." *Astron. Astrophys.*, **38**:1–4, Jan 1975.

[SOT97] T. A. Savard, K. M. O'Hara, and J. E. Thomas. "Laser-noise-induced heating in far-off resonance optical traps." *Phys. Rev. A*, **56**:R1095–R1098, Aug 1997.

[SR81] G. Smith and D. St. J. Raggett. "Oscillator strengths and collisional damping parameters for lines of neutral calcium." *J. Phys. B: At. Mol. Phys.*, **14**:4015, 1981.

[SR00] Ian WM Smith and Bertrand R Rowe. "Reaction kinetics at very low temperatures: laboratory studies and interstellar chemistry." *Accounts of Chemical Research*, **33**(5):261–268, 2000.

[SRA15] Humberto da Silva Jr, Maurice Raoult, Mireille Aymar, and Olivier Dulieu. "Formation of molecular ions by radiative association of cold trapped atoms and ions." *New Journal of Physics*, **17**(4):045015, 2015.

[SRD10] T. Schneider, B. Roth, H. Duncker, I. Ernsting, and S. Schiller. "All-optical preparation of molecular ions in the rovibrational ground state." *Nature Physics*, **6**(4):275–278, Apr 2010.

[SRK11] Scott T. Sullivan, Wade G. Rellergert, Svetlana Kotochigova, Kuang Chen, Steven J. Schowalter, and Eric R. Hudson. "Trapping molecular ions formed via photo-associative ionization of ultracold atoms." *Phys. Chem. Chem. Phys.*, **13**:18859–18863, 2011.

[SRK12] Scott T Sullivan, Wade G Rellergert, Svetlana Kotochigova, and Eric R Hudson. "Role of electronic excitations in ground-state-forbidden inelastic collisions between ultracold atoms and ions." *Physical review letters*, **109**(22):223002, 2012.

[SS96] David Smith and Patrik Španěl. "Application of ion chemistry and the SIFT technique to the quantitative analysis of trace gases in air and on breath." *International Reviews in Physical Chemistry*, **15**(1):231–271, 1996.

[SS03] Norbert Schuch and Jens Siewert. "Natural two-qubit gate for quantum computation using the XY interaction." *Phys. Rev. A*, **67**:032301, Mar 2003.

[SSB19] R. T. Sutherland, R. Srinivas, S. C. Burd, D. Leibfried, A. C. Wilson, D. J. Wineland, D. T. C. Allcock, D. H. Slichter, and S. B. Libby. "Versatile laser-free trapped-ion entangling gates." *New J. Phys.*, **21**(3):033033, mar 2019.

[SSC14] Christian Schneider, Steven J. Schowalter, Kuang Chen, Scott T. Sullivan, and Eric R. Hudson. "Laser-Cooling-Assisted Mass Spectrometry." *Phys. Rev. Applied*, **2**:034013, Sep 2014.

[SSF08] V V Smirnov, O M Stelmakh, V I Fabelinsky, D N Kozlov, A M Starik, and N S Titova. "On the influence of electronically excited oxygen molecules on combustion of hydrogen–oxygen mixture." *J. Phys. D: Appl. Phys.*, **41**(19):192001, 2008.

[SSY16] Christian Schneider, Steven J. Schowalter, Peter Yu, and Eric R. Hudson. "Electronics of an ion trap with integrated time-of-flight mass spectrometer." *International Journal of Mass Spectrometry*, **394**:1 – 8, 2016.

[SUP07] Ralf Schützhold, Michael Uhlmann, Lutz Petersen, Hector Schmitz, Axel Friedenauer, and Tobias Schätz. "Analogue of Cosmological Particle Creation in an Ion Trap." *Phys. Rev. Lett.*, **99**(20):201301, November 2007.

[SWM89] D Sesko, T Walker, C Monroe, A Gallagher, and C Wieman. "Collisional losses from a light-force atom trap." *Phys. Rev. Lett.*, **63**(9):961, 1989.

[SZ96] PC Stancil and B Zygelman. "Radiative charge transfer in collisions of Li with H+." *The Astrophysical Journal*, **472**(1):102, 1996.

[TBJ11] N. Timoney, I. Baumgart, M. Johanning, A. F. Varón, M. B. Plenio, A. Retzker, and Ch. Wunderlich. "Quantum gates and memory using microwave-dressed states." *Nature*, **476**:185, August 2011.

[TJG19] Michał Tomza, Krzysztof Jachymski, Rene Gerritsma, Antonio Negretti, Tommaso Calarco, Zbigniew Idziaszek, and Paul S Julienne. "Cold hybrid ion-atom systems." *Reviews of Modern Physics*, **91**(3):035001, 2019.

[TKJ04] Nicholas R. Thomas, Niels Kjærgaard, Paul S. Julienne, and Andrew C. Wilson. "Imaging of s and d Partial-Wave Interference in Quantum Scattering of Identical Bosonic Atoms." *Phys. Rev. Lett.*, **93**:173201, Oct 2004.

[TKK00] Q. A. Turchette, Kielpinski, B. E. King, D. Leibfried, D. M. Meekhof, C. J. Myatt, M. A. Rowe, C. A. Sackett, C. S. Wood, W. M. Itano, C. Monroe, and D. J. Wineland. "Heating of trapped ions from the quantum ground state." *Phys. Rev. A*, **61**:063418, May 2000.

[TSC13] Sebastian Trippel, M Stei, JA Cox, and R Wester. "Differential Scattering Cross-Sections for the Different Product Vibrational States in the Ion-Molecule Reaction Ar++ N 2." *Physical review letters*, **110**(16):163201, 2013.

[TTY98] K.T. Tang, J. P. Toennies, and C. L. Yiu. "The generalized Heitler-London theory for interatomic interaction and surface integral method for exchange energy." *Int. Rev. Phys. Chem.*, **17**(3):363–406, 1998.

[UHF82] Kiyoshi Ueda, Yoshihiro Hamaguchi, and Kuniya Fukuda. "Measurements of Oscillator Strengths for the Transitions from the Metastable 3P Levels of Alkaline-Earth Atoms. III. Calcium–Low-n Members." *J. Phys. Soc. Jpn.*, **51**(9):2973–2976, 1982.

[UHF83] Kiyoshi Ueda, Yoshihiro Hamaguchi, and Kuniya Fukuda. "Measurements of Oscillator Strengths for the Transitions from the Metastable 3P Levels of Alkaline-Earth Atoms. IV. Calcium–High-n Members." *J. Phys. Soc. Jpn.*, **52**(8):2666–2672, 1983.

[UOY10] Muhammet Uyanik, Hiroaki Okamoto, Takeshi Yasui, and Kazuaki Ishihara. "Quaternary Ammonium (Hypo)iodite Catalysis for Enantioselective Oxidative Cycloetherification." *Science*, **328**(5984):1376–1379, 2010.

[Van29] J. H. Van Vleck. "On σ-Type Doubling and Electron Spin in the Spectra of Diatomic Molecules." *Phys. Rev.*, **33**:467–506, Apr 1929.

[VBH18] Robert A. VanGundy, Joshua H. Bartlett, and Michael C. Heaven. "Spectroscopy of the low-lying states of CaO+." *Journal of Molecular Spectroscopy*, **344**:17 – 20, 2018.

[VOC15] Sjoerd N Vogels, Jolijn Onvlee, Simon Chefdeville, Ad van der Avoird, Gerrit C Groenenboom, and Sebastiaan YT van de Meerakker. "Imaging resonances in low-energy NO-He inelastic collisions." *Science*, **350**(6262):787–790, 2015.

[VPH19] Robert A. VanGundy, Thomas D. Persinger, and Michael C. Heaven. "Improved vibrational constants for BaCl+ X $1\Sigma+$." *Journal of Molecular Spectroscopy*, **363**:111176, 2019.

[Vut15] Amar Vutha. "Optical frequency standards for gravitational wave detection using satellite Doppler velocimetry." *New Journal of Physics*, **17**(6):063030, 2015.

[WBZ99] John Weiner, Vanderlei S Bagnato, Sergio Zilio, and Paul S Julienne. "Experiments and theory in cold and ultracold collisions." *Reviews of Modern Physics*, **71**(1):1, 1999.

[Wie82] John R Wiesenfeld. "Atmospheric chemistry involving electronically excited oxygen atoms." *Accounts Chem. Res.*, **15**(4):110–116, 1982.

[Wit05] Curt Wittig. "The Landau–Zener Formula." *J. Phys. Chem. B*, **109**(17):8428–8430, 2005. PMID: 16851989.

[WKK12] Hans-Joachim Werner, Peter J. Knowles, Gerald Knizia, Frederick R. Manby, and Martin Schütz. "Molpro: a general-purpose quantum chemistry program package." *WIREs Computational Molecular Science*, **2**(2):242–253, 2012.

[WM55] W. C. Wiley and I. H. McLaren. "Time-of-Flight Mass Spectrometer with Improved Resolution." *Review of Scientific Instruments*, **26**(12):1150–1157, 1955.

[WOH06] G. Wilpers, C.W. Oates, and L. Hollberg. "Improved uncertainty budget for optical frequency measurements with microkelvin neutral atoms: Results for a high-stability 40Ca optical frequency standard." *Applied Physics B*, **85**(1):31–44, 2006.

[WSD95] C. D. Wallace, V. Sanchez-Villicana, T. P. Dinneen, and P. L. Gould. "Suppression of Trap Loss Collisions at Low Temperature." *Phys. Rev. Lett.*, **74**:1087–1090, Feb 1995.

[WT72] Albert F Wagner and Donald G Truhlar. "Comment on Enhancement of the Reaction Cross Section of He+ H 2+ → HeH++ H by Vibrational Excitation of H 2+ and the Treatment of Nuclear Spin by the Statistical Phase-Space Theory." *The Journal of Chemical Physics*, **57**(9):4063–4064, 1972.

[WWH16] Fabian Wolf, Yong Wan, Jan C. Heip, Florian Gebert, Chunyan Shi, and Piet O. Schmidt. "Non-destructive state detection for quantum logic spectroscopy of molecular ions." *Nature*, **530**(7591):457–460, Feb 2016.

[XLH03] Xinye Xu, Thomas H. Loftus, John L. Hall, Alan Gallagher, and Jun Ye. "Cooling and trapping of atomic strontium." *J. Opt. Soc. Am. B*, **20**(5):968–976, May 2003.

[XLS02] Xinye Xu, Thomas H. Loftus, Matthew J. Smith, John L. Hall, Alan Gallagher, and Jun Ye. "Dynamics in a two-level atom magneto-optical trap." *Phys. Rev. A*, **66**:011401, Jul 2002.

[YLC18] Tiangang Yang, Anyang Li, Gary K Chen, Changjian Xie, Arthur G Suits, Wesley C Campbell, Hua Guo, and Eric R Hudson. "Optical control of reactions between water and laser-cooled Be+ ions." *The journal of physical chemistry letters*, **9**(13):3555–3560, 2018.

[ZBR00] Götz Zinner, Tomas Binnewies, and Fritz Riehle. "Atom-interferometry constraints on dark energy." *Phys. Rev. Lett.*, **85**:2292, 2000.

[Zen32] Clarence Zener. "Non-adiabatic crossing of energy levels." *Proceedings of the Royal Society of London. Series A, Containing Papers of a Mathematical and Physical Character*, **137**(833):696–702, 1932.

[ZFT09] Zhanchun Zuo, Miho Fukusen, Yoshihito Tamaki, Tomoki Watanabe, Yusuke Nakagawa, and Ken'ichi Nakagawa. "Single atom Rydberg excitation in a small dipole trap." *Optics Express*, **17**(25):22898–22905, 2009.

[ZMM96] S. C. Zilio, L. Marcassa, S. Muniz, R. Horowicz, V. Bagnato, R. Napolitano, J. Weiner, and P. S. Julienne. "Polarization Dependence of Optical Suppression in Photoassociative Ionization Collisions in a Sodium Magneto-optic Trap." *Phys. Rev. Lett.*, **76**:2033–2036, Mar 1996.

[ZPR10] Christoph Zipkes, Stefan Palzer, Lothar Ratschbacher, Carlo Sias, and Michael Köhl. "Cold heteronuclear atom-ion collisions." *Physical review letters*, **105**(13):133201, 2010.

[ZPS10] Christoph Zipkes, Stefan Palzer, Carlo Sias, and Michael Köhl. "A trapped single ion inside a Bose–Einstein condensate." *Nature*, **464**(7287):388–391, Mar 2010.

[ZRP11] Christoph Zipkes, Lothar Ratschbacher, Stefan Palzer, Carlo Sias, and Michael Köhl. "Hybrid quantum systems of atoms and ions." In *Journal of Physics: Conference Series*, volume 264, p. 012019. IOP Publishing, 2011.

[ZRS02] X. Zhao, V. L. Ryjkov, and H. A. Schuessler. "Parametric excitations of trapped ions in a linear rf ion trap." *Phys. Rev. A*, **66**:063414, Dec 2002.

[ZW17] Dongdong Zhang and Stefan Willitsch. "Cold ion chemistry.", 2017.